Numerical modeling of the dynamics of soft particles in microchannel flows

Jinming Lyu

CENTRALE MARSEILLE

ECOLE CENTRALE DE MARSEILLE

École doctorale n°353: *Sciences pour l'Ingénieur: Mécanique, Physique, Micro et Nanoélectronique*
Laboratoire de Mécanique, Modélisation & Procédés Propres (UMR 7340)

THÈSE

présentée par

Jinming LYU

soutenance prévue le 5 juillet 2019
pour obtenir le grade de docteur de l'ECM
discipline: Mécanique et Physique des Fluides

Modélisation numérique de la dynamique de particules molles en microcanaux

Thèse dirigée par:

M. Marc JAEGER	PR ECM, Marseille	Directeur
M. Paul G. CHEN	CR CNRS, M2P2, Marseille	Co-directeur

Membres du jury:

M^{me} Annie VIALLAT	DR CNRS, CINaM, Marseille	Présidente
M. Chaouqi MISBAH	DR CNRS, LIPhy, Grenoble	Rapporteur
M. Franck NICOUD	PR Univ. de Montpellier, Montpellier	Rapporteur
M. Marc LEONETTI	CR CNRS, LRP, Grenoble	Examinateur
M. Marc JAEGER	PR ECM, Marseille	
M. Paul G. CHEN	CR CNRS, M2P2, Marseille	

Numerical modeling of the dynamics of soft particles in microchannel flows

by

Jinming Lyu

Supervisors: M. Marc Jaeger
M. Paul G. Chen

Abstract

Vesicles are a model system for understanding the dynamical behavior of a closed soft particle such as red blood cells (RBCs) in flows. The inextensible lipid bilayer membrane of a vesicle admits resistance to the bending elasticity, and its large surface-area-to-volume ratio allows the vesicle to exhibit remarkable shape changes in the dynamics even in a simple flow. Significant progress has been made over the past decades in understanding vesicle dynamics in unbounded Stokes flows. This manuscript deals with the numerical investigation of shape transition and lateral migration of 3D vesicles in wall-bounded Stokes flows by means of an isogeometric finite-element method (FEM) and boundary-element method (BEM). Starting from a previously reported isogeometric FEM-BEM simulations of the dynamics of soft particles (drops, capsule, and vesicle) in Stokes flows in free space, the original code is developed to account for microchannel walls of arbitrary cross-section. The present work focuses on the dynamics of a vesicle that is transported through a circular tube in a pressure-driven flow. First, we investigate typical vesicle shapes, different lateral migration modes, and flow structure onto vesicle membrane versus three independent dimensionless parameters, namely, the reduced volume, the confinement, and the (bending) capillary number. Shape transitions and the phase diagram of stable shapes for several reduced volumes are obtained in the (confinement, capillary number) space, showing an extension of the set of vesicle morphologies and rich vesicle dynamics owing to the intricate interplay among the tube wall, hydrodynamic stresses, and membrane bending. Secondly, we study, via an axisymmetric BEM, the hydrodynamics under high confinements in which the shape of the vesicle is expected to maintain axisymmetry. A particular emphasis is given to the prediction of the vesicle mobility and the extra pressure drop caused due to the presence of the vesicle, the latter having implications in the rheology of a dilute suspension. In addition, based on the numerical results of limiting behavior of quantities of interest near maximal confinement, we give various scaling laws to infer, for example, the vesicle velocity, its length, and the thickness of lubrication film. Finally, we present a coupled, hybrid continuum–coarse-grained model for the study of RBCs in fluid flows. This model is based on a combination of the vesicle model with a network of springs with fixed connectivity, representing the cytoskeleton. Numerical results show that this two-component vesicle–cytoskeleton model is able to extract the mechanical properties of RBCs and predict its dynamics in fluid flows.

Key words: Fluid-cell interaction, Fluid vesicles, RBCs, Boundary element method, Shape transition, Lubrication theory.

Résumé

Une vésicule est un système modèle utilisé pour comprendre le comportement dynamique en écoulement d'une particule molle fermée telle qu'un globule rouge. La membrane bicouche lipidique inextensible d'une vésicule admet une résistance d'élasticité en flexion. Lorsque dégonflée, c'est-à-dire pour un grand rapport surface sur volume, une vésicule présente des changements de formes remarquables. Des progrès significatifs ont été réalisés au cours des dernières décennies dans la compréhension de leur dynamique en milieu infini. Ce manuscrit s'intéresse à la transition de formes et à la migration latérale d'une vésicule dans des écoulements confinés. L'approche est numérique, basée sur une méthode aux éléments finis de frontière (BEM) isogéométrique. Partant d'une version existante pour les écoulements de Stokes non confiné, un code original est développé pour prendre en compte les parois de microcanaux de section transversale arbitraire. L'essentiel des études porte sur la dynamique d'une vésicule transportée par un écoulement de Poiseuille dans une conduite de section circulaire. Tout d'abord, nous examinons les formes typiques des vésicules, les différents modes de migration latérale et la structure de l'écoulement des lipides dans la membrane, en fonction des trois paramètres sans dimension caractéristiques : le volume réduit, le confinement et le nombre capillaire (de flexion). Les transitions de forme et le diagramme de phase de formes stables pour plusieurs volumes réduits sont obtenus dans l'espace (confinement, nombre capillaire). Ils montrent une extension de l'ensemble des morphologies de la vésicule. L'interaction complexe entre la paroi du tube, les contraintes hydrodynamiques et l'élasticité de flexion de la membrane conduit à une dynamique bien plus riche. Nous étudions ensuite, via une version axisymétrique du modèle, le comportement de la vésicule lorsque des conditions de confinement deviennent sévères et imposent des formes de vésicule axisymétriques. Un accent particulier est mis sur la prédiction de la mobilité de la vésicule et de la perte de charge additionnelle induite par la présence de la vésicule. Cette dernière est importante pour comprendre la rhéologie d'une suspension diluée. De plus, sur la base des résultats numériques du comportement proche du confinement maximal, nous établissons plusieurs lois d'échelle portant sur la vitesse de la vésicule et sa longueur, ainsi que sur l'épaisseur du film de lubrification. Enfin, nous présentons un modèle hybride BEM–coarse-graining permettant d'adjoindre un cytosquelette à une vésicule pour étendre nos études au cas des globules rouges. La modélisation coarse-graining du cytosquelette repose sur un réseau de ressorts identifié à l'ensemble des arêtes du maillage d'éléments finis de la membrane de la vésicule. Les résultats numériques montrent que ce modèle à deux composants vésicule–cytosquelette est capable d'extraire les propriétés mécaniques des globules rouges et de prédire sa dynamique dans les écoulements de fluide.

Mots-clés: Interaction fluide-cellule, Vésicules, Globules rouges, Méthode des éléments de frontière, Transition de formes, Théorie de lubrification.

Acknowledgments

I would like to express my sincere gratitude to my supervisor Prof. Marc Jaeger, for enlightening and guiding me with his knowledge. His attitude towards research and angle to the problem will always be beneficial in my future work.

I wish to express my warm and sincere thanks to my co-supervisor Dr. Paul G. Chen, for his indispensable guidance, encouragement, and support in the past forty months. He was always accessible and willing to help me solve all kinds of problems, academic or daily life. I will always be indebted for the scale notion that he has impressed in my head and his thorough and meticulous examination of each manuscript.

I am particularly grateful to Dr. Marc Leonetti for his guidance and timely advice from the physics point of view. I enormously thank Dr. Gwenn Boëdec for his indispensable helps on numerics. He has always been very patient in answering all my questions about the code.

I would like to thank Dr. Chaouqi Misbah and Prof. Franck Nicoud for accepting to be my reporter and for helping to improve my work with their helpful comments. I would also thank Dr. Annie Viallat for accepting to be the president of my defense committee.

I would also like to thank Richard Kotarba, Michel Pognant and the mésocentre group (at Aix-Marseille Université) for their technical support. I also thank Sarah Mostefa (ECM), Pascal Campion (ED 353) and Sophie Baudin (M2P2) for their help in administration.

Thanks to Drs. Congshan Zhou, Yongliang Feng and Lei Zhang for their helpful discussion and kind suggestions. Thanks a lot to Dr. Sudip K. Das for his detailed review and constructive advice for this dissertation.

Thanks to all members of M2P2, and especially to Juan Antonio, Carlos, Eddy, Marianna, Oleksandr, Kaili, William, Sylvain, Nicolas, Rouae, Jiupeng, Adithya, Benjamin, Muhammad, Raffaele, Song, Xi, Shaolong, Sylvia, etc.$\cdots$, for their help, discussion and happy moments after work.

Finally, I would like to thank all my family, and especially my parents, for their love and support over the past years!

I acknowledge the China Scholarship Council (CSC) and Centrale Innovation for financial support.

Contents

1 Introduction

1.1 Context

1.1.1 Complex fluids

Complex fluids are a class of materials those with internal particles or microstructures whose evolution affects the macroscopic dynamics of the fluids, especially the rheology. Unlike classical fluids, the internal particles or microstructures are substances different from the suspending fluid, which makes complex fluids cannot be described by the classical fluid mechanics. For example, blood in the human body is a complex fluid that contains many internal substances.

An important aspect of complex fluids is that the macroscopic flow properties (rheology for example) depend on the local behaviors of their components. In general, complex fluids are homogeneous at the macroscopic scale, but are disordered at the microscopic scale, and possess structure at the mesoscopic scale. Due to the existence of these mesoscale structures, complex fluids lose scale invariance. This phenomenon, called the multi-scale organization, is at the origin of the complexity of these fluids and brings difficulties in theoretical and numerical analysis.

Complex fluids, also called soft matter[36], are intermediate between conventional liquids and solids, can display both fluid-like and solid-like behaviors. For example, they can switch from a solid- to a fluid-like behavior by increasing the strength of the applied stresses [124]. No universal law has been constructed to link macroscopic properties to local behaviors (for example, the mesoscopic interfacial morphology of red blood cells in the blood flow), so it is essential to understand the dynamics of a single internal particle before dealing with macroscopic properties of complex fluids.

1.1.2 Deformable particles

The term *deformable particles* refers to suspending particles capable of changing their shape under external stresses, such as hydrodynamic stress due to the suspending fluid, thermal fluctuations, and chemical reactions.

In this work, deformable particles may include drops, capsules, vesicles and red blood cells (RBCs). Understanding of dynamic behaviors (such as deformation, orientation, and lateral migration) of such deformable particles in a flow (for example, a shear flow or a Poiseuille flow), presents both fundamental interests (a non-linear and non-stationary system) and interests in biomedical engineering. Biomedical interest is motivated not only by *in vivo* issues (such as rheology of blood and drug delivery), but also by the increasing demands for

in vitro lab-on-chip technologies (such as particles separation, Figure 1.1) [40, 119], where the separation is mainly based on the size and the deformability of the particles.

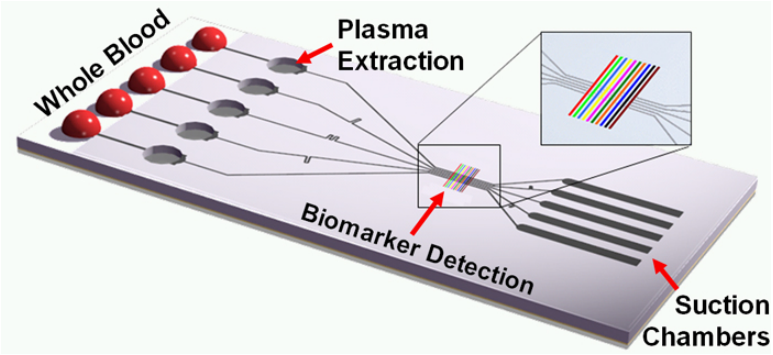

Figure 1.1: Schematic of a lab-on-chip integrating blood loading, plasma separation from whole-blood, multiple biomarker detection, and suction chambers for fluid propulsion (reproduced from [40]).

RBCs, the most complex of these four deformable particles, have fascinated many researchers because of its biological importance. RBC is encapsulated by a membrane composed essentially of a lipid bilayer supported by an underlying polymer network (in detail in Chapter 5). In this section, a brief presentation will be given for drops and capsules, that for vesicles will be detailed in the next section.

Drop, or droplet is a small quantity of liquid immersed in another immiscible fluid of different nature. The suspended liquid drop and the suspending fluid are separated by an interface having a surface tension γ, which corresponds to the energy required to increase the surface by a unit of area. Compared to the artificial one (capsule) and the biomimetic one (vesicle) of RBC, the drop is the simplest in terms of membrane structure and dynamics in external flow. But it has been the subject of many studies for a long time [144], as a fluid-structure interaction problem which itself holds rich dynamics and may give intuitions for the complex ones.

A capsule consists of an internal liquid medium (of viscosity η^i) enclosed by a thin deformable solid membrane and suspended in another liquid (of viscosity η^e). In contrast to strongly deformable fluid vesicle (Sec. 1.2), capsule membrane exhibits a finite shear elasticity (thus bears shape memory) since capsules are drops encapsulated by a network of crosslinked polymers. RBC is one of the well-known biological examples of the capsule, while artificial capsules are widely used in many industries such as pharmaceutical, cosmetic, food industries and bioengineering applications like drug targeting carriers [12].

1.2 Vesicles

Vesicles are drops encapsulated by a bilayer of lipid molecules, suspended in a fluid that can be either the same solvent as the inner or different. As shown in Figure 1.2, in aqueous

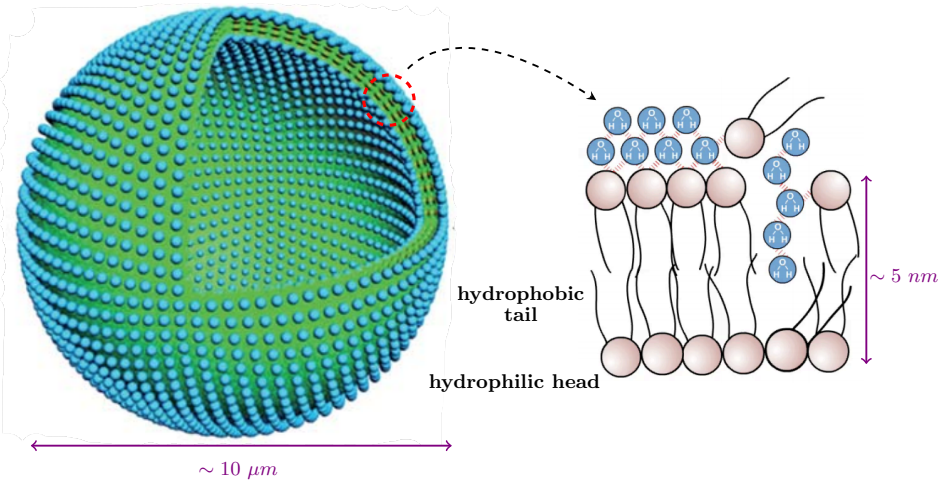

Figure 1.2: The vesicle membrane is made by a lipid bilayer. In water solution, lipid molecules spontaneously aggregate to prevent undesirable interactions between water and hydrophobic tails. Vesicles are typically about 5 μm in radius and the membrane thickness is about 5 nm [153].

solution, the lipid molecules organize themselves to form a sheet. The hydrophilic head groups interact with the aqueous medium (which is polar), while keeping the hydrophobic tails away from aqueous solution. Two sheets of such kind interact with each other forming a bilayer membrane protecting the tails. In fact, this type of configuration minimizes the membrane energy that arises from the interaction between polar and non-polar molecules.

The large scale difference between the radius and the membrane thickness[1] together with the fluidity of the membrane at room temperature make the deflated vesicle highly deformable. The area of this membrane is both locally and globally conserved since any increase or decrease in the number of lipids will require much more energy than that required for deformation. Moreover, the semipermeability keeps the enclosed volume unchanged on a time-scale of several hours, which is much longer than the typical experimental time-scale of about 10 to 15 minutes. The vesicle volume can thus be considered as constant [3]. These singular properties lead to rich behaviors when they are immersed in an external flow.

1.2.1 Deformation and energy

The motion of vesicles in an external flow is different from that of rigid particles or simple droplets because of their high deformability. Understanding the motion and the deforma-

[1] The membrane is (approximately) a 2D surface embedded in 3D space.

tion of vesicles is essential both for fundamental research and for industrial applications. The key issue is to physically describe the membrane and to determine how energy changes as a result of any membrane modification. That is, to describe or to model the dynamics of a vesicle under hydrodynamic stresses, we must first understand how the membrane energy depends on its shape, and know the response to any mechanical disturbance.

Figure 1.3 shows four classical modes of deformation for a lipid bilayer membrane. At

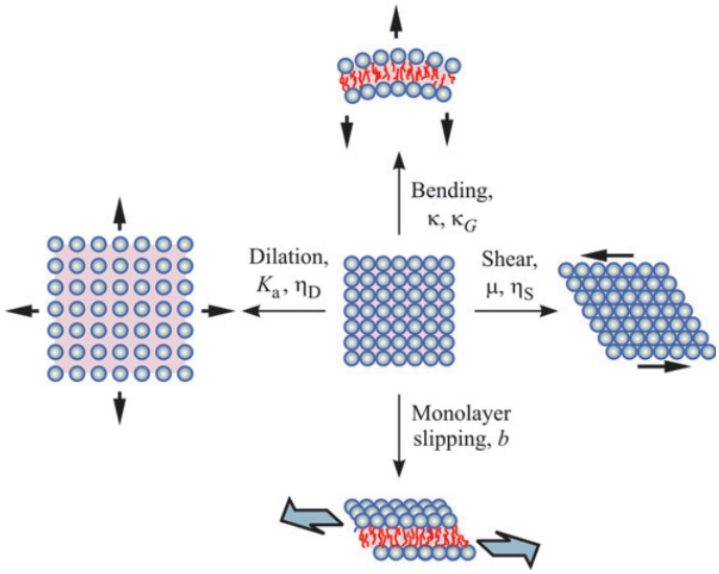

Figure 1.3: Schematic presentation of some classical modes of lipid bilayer deformations: dilation, bending, shear, and monolayer slipping. The constants characterize the response of the membrane to these deformations (reproduced from [41]).

ambient or physiological temperature, the lipid is in the liquid state, so we can neglect the shear mode by defining the elastic modulus $\mu = 0$. The viscosity between two monolayers $b \sim 10^{-9}$ Pa s which is much smaller than that of the water with $\eta \sim 10^{-3}$ Pa s, therefore, the monolayer slipping can also be neglected for giant vesicles with a size of 10 to 100 μm [19, 41, 153]. Thus, the deformation of the lipid membrane can be simplified with only two modes of deformation: dilation and bending.

From Dimova et al. [40], we have the dilation modulus $K_a \sim 240\,\mathrm{dyn/cm} \approx 53\kappa_\mathrm{B}T/\mathrm{nm}^2$, that is about $106\,\kappa_B T$ per lipid. The bending modulus $\kappa \sim 0.9\times10^{-19}$ J $\approx 20\kappa_\mathrm{B}T$. Thus, it is easier to bend a lipid membrane than to stretch it. The lipid bilayer membrane is modeled as a two-dimensional locally incompressible fluid with resistance to bending. This model takes into account the fact that when subjected to external stresses, it responds first to bending since the energy associated with bending is much lower than that with dilation. The modeling of the lipid bilayer membrane, therefore, focuses on the bending energy. Several

models on the bending energy have been reviewed by Seifert [138], here the commonly cited spontaneous curvature model is briefly presented.

The spontaneous curvature model (SC) was proposed by Helfrich [69] for the bending energy as

$$E_{\mathrm{SC}} = \frac{\kappa}{2}\int_S (2H - C_0)^2 \mathrm{d}S + \kappa_{\mathrm{G}} \int_S K \mathrm{d}S, \tag{1.1}$$

where $H = \frac{1}{2}\left(\frac{1}{R_1} + \frac{1}{R_2}\right)$ is the mean curvature (with convention that H is positive for a sphere), $K = \frac{1}{R_1 R_2}$ is the Gaussian curvature, R_1 and R_2 are the local principal radii of curvature of the surface. $\kappa \sim 20\ \kappa_{\mathrm{B}}T$ is the bending modulus which reflects the energetic expense associated with driving the mean curvature of the membrane, H, away from its preferred value, C_0. $\kappa_{\mathrm{G}} \sim -0.8\,\kappa$ is the Gaussian bending modulus which reflects the cost of imposing Gaussian curvature, K, on the surface. C_0 is the so-called spontaneous curvature, which is supposed to reflect a possible asymmetry in the membrane (e.g., due to a different chemical composition of the two monolayers). In this work, we suppose $C_0 = 0$.

Nevertheless, for a closed surface without change of topology, irrespectively of the value of the Gaussian bending modulus, the equilibrium shape is not affected since $\int_s K \mathrm{d}S$ is constant[2]. Topological changes (lysis, fusion or pore formation) are possible but rare because they are related to processes that are energetically unfavorable. In this work, topological changes are disregarded. With these two assumptions, Eq. (1.1) is simplified to

$$E^s_{\mathrm{SC}} = \frac{\kappa}{2}\int_S (2H)^2 \mathrm{d}S + 4\pi\kappa_{\mathrm{G}} = \frac{\kappa}{2}\int_S \left(c_1^2 + c_2^2\right)\mathrm{d}S + 4\pi(\kappa + \kappa_G), \tag{1.2}$$

where $c_1 = R_1^{-1}$ and $c_2 = R_2^{-1}$ are the principal curvatures of the surface. This simplified SC model differs from the minimal model [28] only by the constant term, $4\pi\kappa_{\mathrm{G}}$.

1.2.2 Equilibrium shapes

On the typical experimental time scale, both the surface area A and the volume V of vesicles are preserved, which define an important geometric parameter, the reduced volume

$$\nu = \frac{V}{\frac{4\pi}{3}\left(\frac{A}{4\pi}\right)^{3/2}} = 6\sqrt{\pi} V A^{-3/2} \tag{1.3}$$

as a ratio of the actual enclosed volume V over the volume of a sphere having the same surface area A. The reduced volume, which quantifies the geometric ability of the vesicle to deform, can range from 0 (totally deflated vesicle) to 1 (sphere). A sphere is a form of maximum volume for a given surface, or reciprocally, of minimal area for a fixed volume. A spherical vesicle is geometrically undeformable with constraints of volume and surface conservation. In order to deform this vesicle, it is necessary to deflate it, which can be measured by the reduced volume.

[2] With Gauss-Bonnet theorem, $\int_s K \mathrm{d}S = 4\pi(1 - g)$, where g is the number of pore of the surface (e.g., $g = 0$ for a classical sphere).

Alternatively, one can also use the excess area Δ as the geometric parameter, which is given by

$$A = (4\pi + \Delta)R_{\mathrm{v}}^2, \tag{1.4}$$

where $R_{\mathrm{v}} = \left(V/\frac{4\pi}{3}\right)^{1/3}$ is the radius of a sphere with the same volume V. These two parameters are linked to each other by relations:

$$\nu = \left(1 + \frac{\Delta}{4\pi}\right)^{-3/2} \quad \text{and} \quad \Delta = 4\pi\left(\frac{1}{\nu^{2/3}} - 1\right). \tag{1.5}$$

For healthy human RBCs, which have an average surface area of 135 μm^2 and a mean cellular volume of 94 μm^3 [2], thus the reduced volume can be calculated to be around 0.64.

The bending energy (1.2) was first used to determine the equilibrium shapes free of external stresses. As shown in Figure 1.4 (a), three different branches: prolates, oblates and stomatocytes are obtained by minimizing the bending energy. Each branch is a minimal lo-

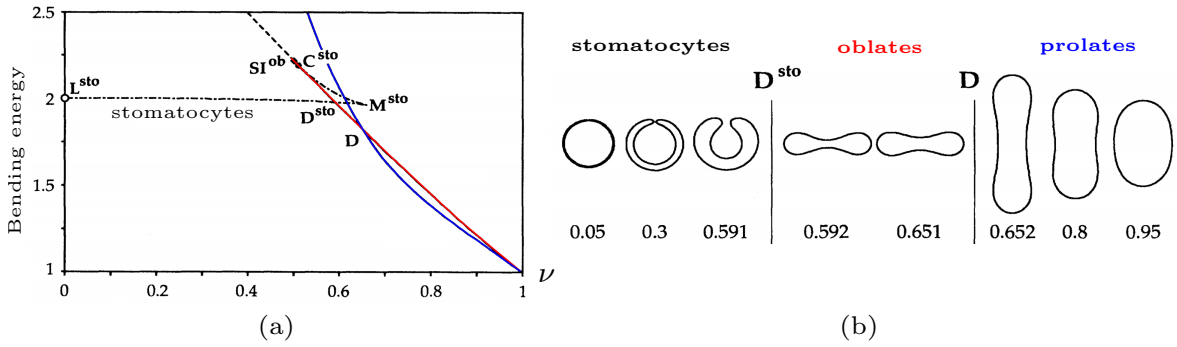

Figure 1.4: (a) Bending energy (Eq. (1.2)) corresponds to the equilibrium shapes as a function of reduced volume. Three branches are displayed: the prolate, the oblate, and the stomatocytes branches. The upper part between C^{sto} and M^{sto} corresponds to locally unstable shapes, whereas the lower part between L^{sto} and M^{sto} corresponds to locally stable shapes. The oblate branch beyond SI^{ob} corresponds to self-intersected states. (b) Equilibrium shapes for several values of ν. D and D^{sto} denote the discontinuous prolate-oblate and oblate-stomatocyte transitions. (reproduced from [139])

cal of the Helfrich bending energy, while the global equilibrium shape (with global minimal bending energy) is a function of the reduced volume ν. In other words, several solution branches can coexist, but with only one solution branch is a global minimum, which corresponds to a form of thermal equilibrium.

Comparing the Helfrich bending energy of these three branches, we observed that for $0 < \nu < \nu_D^{sto} \simeq 0.59$, the stomatocytes have the lowest energy, while for $\nu_D^{sto} < \nu < \nu_D \simeq 0.65$, the oblates have the lowest energy, and finally, for $\nu_D < \nu < 1$, the prolates correspond

to the ground state. Several shapes of the lowest bending energy are displayed in Figure 1.4 (b), which are separated by two discontinuous transitions [139].

1.2.3 Non-equilibrium shapes: dynamics in external flow

The behaviors of a single vesicle in a simple shear flow[3]

$$\boldsymbol{u} \equiv s(x\boldsymbol{e}_y + y\boldsymbol{e}_x) + \omega(x\boldsymbol{e}_y - y\boldsymbol{e}_x), \tag{1.6}$$

have been studied experimentally[1, 37, 38, 76, 77], theoretically[20, 35, 45, 82, 92, 93, 112, 117, 137], and numerically with boundary integral method (BIM)[17, 22, 158] or immersed boundary method[84], and with mesoscale techniques[115, 117], etc. All these three approaches have identified three basic dynamical behaviors, namely

- *tank-treading* (TT): the fluid membrane rotates as a tank treads about a rigid object of fixed orientation (Φ) (Figure 1.5 (a)),
- *tumbling* (TU): vesicles flipping periodically in the shear plane with its shape remains globally unchanged (Figure 1.5 (b)),
- *trembling* (TR): also called vacillating-breathing (VB) [112], an intermediate regime between TT and TU, where vesicles tremble while its long axis oscillating around the flow direction (Figure 1.5 (c)),

in a linear shear flow. Analytical models are based either on Keller-Shalak (KS) theory[82],

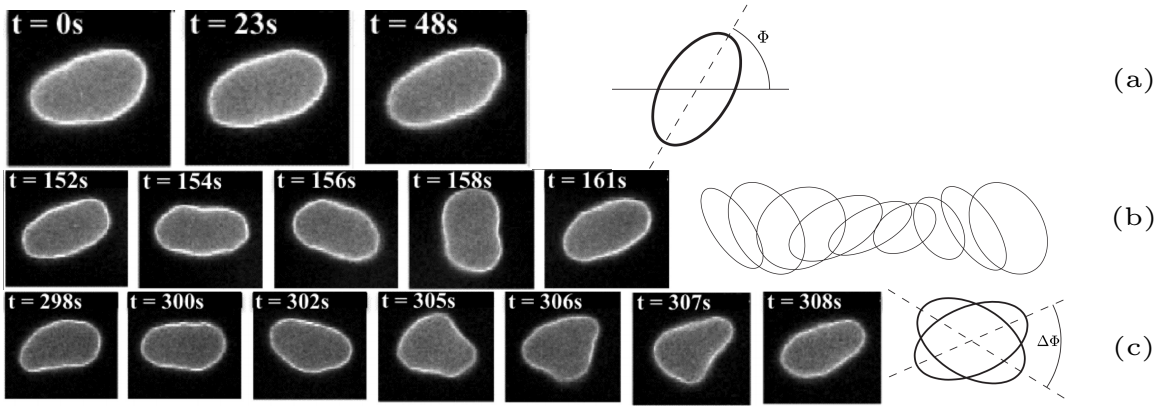

Figure 1.5: Dynamics of vesicle in general flow [37, 93]. (a) tank-treading (TT), (b) tumbling (TU) and (c) trembling (TR).

which assumes vesicles have fixed ellipsoidal shape, or on perturbation theory [45] which are limited for quasi-spherical vesicles ($\nu \approx 1$) under simple boundary conditions.

[3] It may be represented as a superposition of a purely elongational flow and a purely rotational flow, where s is a measure of the strength of the elongational flow component and 2ω is the vorticity.

Phase diagram of a vesicle in a linear flow as a function of the reduced parameters Λ and S (see [93] for their expressions) are plotted in Figure 1.6, with experimental and numerical data as well as analytical predictions.

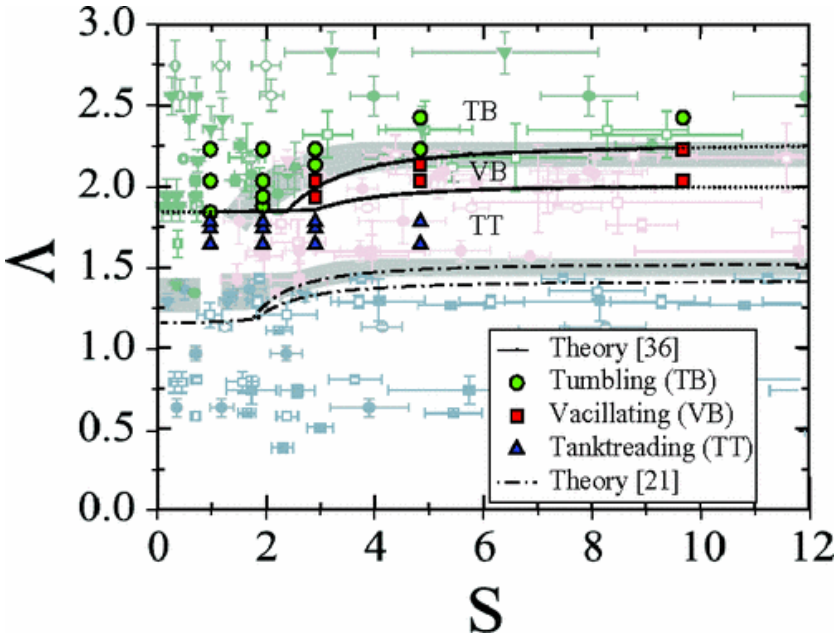

Figure 1.6: Phase diagram of the three different dynamics in linear flow (reproduced from Biben et al. [17]). The symbols with error bars are experimental data of Deschamps et al. [38]. The blue triangles, red squares, and green circles are results obtained by BIM [17] with $\nu = 0.95$. Theory[36] and Theory[21] are analytical predictions given by Farutin et al. [45] and Lebedev et al. [93], respectively.

As in quadratic Poiseuille flow, there are two major concerns: the lateral migration [33, 48, 49, 78] and the shape evolution [32, 47, 49, 80]. A single aspherical vesicle in Poiseuille flow may deform and break its upstream-downstream symmetry due to (i) the shear flow close to solid boundaries[33, 48, 79] and (ii) non-constant shear gradient[33, 48, 78, 80]. As a result of the symmetry breaking (a slipper shape, for example), vesicles undergo cross-streamline migration.

An initially symmetrical vesicle flowing in a two-dimensional unbounded Poiseuille flow, with the centroid of the vesicle being different from the flow axis, can deform into a stable asymmetric shape and can migrate either inward or outward to the flow center, as shown in Figure 1.7. It is contrary to the natural expectation that it should form a symmetrical shape in the center of the symmetrical flow.

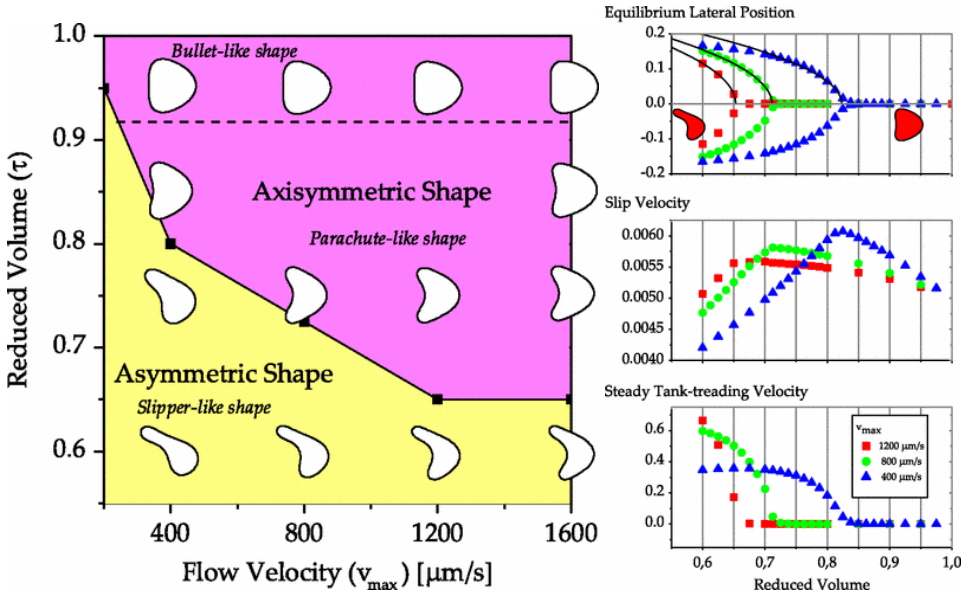

(a) (b)

Figure 1.7: Deflated vesicle in unbounded Poiseuille flow obtained by 2D simulation, reproduced from Kaoui et al. [80]. (a) Phase diagram of the stable shapes in the plane of reduced volume and maximum imposed velocity. (b) The equilibrium lateral position of the center of mass Y_G (top), the slip velocity (middle) and the tank-treading velocity (bottom) as a function of ν.

1.3 Deformable particle in a fluid flow

A vesicle[4] flowing in an external flow is fundamentally a fluid-structure interaction (FSI) problem with a moving interface. The forces induced by the fluids can deform the membrane, which results in a change in membrane forces (e.g., the bending force), and which in turn will alter the surrounding fluids. An FSI problem generally involves three aspects, for a vesicle flowing in external flow, they are

- modeling the fluid flow,
- modeling the mechanics of the lipid membrane interface,
- coupling conditions at the interface,

and will be presented separately in the following subsections.

1.3.1 Hydrodynamics: Stokes regime

Since we are currently interested in the problem of diluted suspension (a single vesicle), the inner and outer fluids of the vesicle are both described by the incompressible Navier-Stokes equations.

[4] In this section, we assume that the terms *vesicle* and *deformable particle* are interchangeable unless otherwise stated.

For a vesicle (with typical size about 10 μm) immersed in aqueous solution (with dynamic viscosity $\eta \sim 10^{-3}$ Pa s and density $\rho \sim 10^{3}$ kg m^{-3}), the Reynolds number is estimated to be $\mathrm{Re} \sim 10^{-4}$ in using a typical speed, in the capillaries, of about 10 μm s^{-1}. Thus, the control equations are simplified to the Stokes equations [127],

$$-\boldsymbol{\nabla} p + \eta \nabla^2 \boldsymbol{u} = \boldsymbol{0}, \quad \boldsymbol{\nabla} \cdot \boldsymbol{u} = 0. \tag{1.7}$$

The Stokes equations are elliptic, which means the hydrodynamic solution $(\boldsymbol{u}, p)$ in a domain D depends only on the boundary conditions imposed on its boundary ∂D. In our problems, the two boundaries are the membrane interface (refer 1.3.3) and the outer boundary of the system. The outer boundary conditions can be

$$\lim_{\boldsymbol{x} \to \partial D} \boldsymbol{u} = \boldsymbol{u}^{\infty} \tag{1.8}$$

for the open part of the outer boundary, and

$$\boldsymbol{u} \,|_{\partial D} = \boldsymbol{0} \tag{1.9}$$

for a rigid wall.

1.3.2 Membrane forces

As mentioned in subsection 1.2.1, the lipid bilayer membrane is modeled as a two-dimensional locally incompressible fluid with resistance to bending. The incompressibility of the membrane is imposed through the free of surface divergence of velocities, i.e.,

$$\boldsymbol{\nabla}_s \cdot \boldsymbol{u} = 0, \tag{1.10}$$

which is realized by adding a Lagrange multiplier γ to the Helfrich bending energy Eq. (1.2), as

$$E_{\text{vesicle}} = \int_S \left(w_s^H + \gamma \right) \mathrm{d}S, \tag{1.11}$$

where $w_s^H = \frac{\kappa}{2}(2H)^2$; the Gaussian curvature term is neglected as it does not contribute to the membrane force.

The surface density of force exerted by the membrane of vesicle $\boldsymbol{f}_{\text{v}}^m$ onto surrounding fluids is given by the first variation of its surface energy Eq. (1.11) [19],

$$\boldsymbol{f}_{\text{v}}^m = -\frac{1}{\sqrt{a}} \frac{\delta E_{\text{vesicle}}}{\delta \boldsymbol{x}} = \kappa \left[2\Delta_s H + 4H(H^2 - K) \right] \boldsymbol{n} - 2\gamma H \boldsymbol{n} + \boldsymbol{\nabla}_s \gamma, \tag{1.12}$$

where a is the determinant of the local metric. $\Delta_s = \boldsymbol{\nabla}_s \cdot \boldsymbol{\nabla}_s$ and $\boldsymbol{\nabla}_s = (\boldsymbol{I} - \boldsymbol{nn}) \cdot \boldsymbol{\nabla}$ are the surface Laplace operator (also called the Laplace-Beltrami operator) and surface gradient operator, respectively. $\boldsymbol{n}$ is the outward pointing normal vector.

For a drop with surface tension γ, it can be modeled with a surface energy density $w_s = \gamma$, or $E_{\text{drop}} = \int_S w_s \mathrm{d}S$, the surface density of force $\boldsymbol{f}_{\mathrm{d}}^m$ can be obtained in the same way [22], which reads

$$\boldsymbol{f}_{\mathrm{d}}^m = \boldsymbol{\nabla}_s \gamma - 2\gamma H \boldsymbol{n}. \tag{1.13}$$

For the hyperelastic membrane of the capsule, there are two types of constitutive law, either strain-softening (e.g., Neo-Hookean law, noted as NH) or strain-hardening (e.g., Skalak law, noted as Sk) [12, 154]. For these laws, the surface density of membrane energy is defined upon a reference configuration S^0 as,

$$\begin{cases} w_{s^0}^{NH} = \dfrac{G_s}{2}\left[I_1 - 1 + \dfrac{1}{I_2 + 1}\right] \\ w_{s^0}^{Sk} = \dfrac{G_s}{4}\left[I_1^2 + 2I_1 - 2I_2 + CI_2^2\right] \end{cases}, \tag{1.14}$$

where G_s is the surface shear modulus, C represents the relative importance of the resistance to surface dilation, and I_1, I_2 are the two strain invariants related to the principal extension ratios λ_1, λ_2, defined as

$$I_1 = \lambda_1^2 + \lambda_2^2 - 2, \qquad I_2 = \lambda_1^2 \lambda_2^2 - 1. \tag{1.15}$$

1.3.3 Coupling conditions

For an FSI problem, coupling conditions must be imposed between the surrounding fluids and the membrane. First, velocities (velocity of the internal fluid ^{i}, the external fluid ^{e} and that on the membrane $_\Gamma$) are continuous at the interface Γ

$$\boldsymbol{u}^e(\boldsymbol{x}) = \boldsymbol{u}^i(\boldsymbol{x}) = \boldsymbol{u}_\Gamma, \quad \forall \boldsymbol{x} \in \Gamma. \tag{1.16}$$

Moreover, with the assumption of no flux through the membrane, we have

$$\frac{\mathrm{D}\boldsymbol{x}}{\mathrm{D}t} = \boldsymbol{u}_\Gamma, \quad \forall \boldsymbol{x} \in \Gamma, \tag{1.17}$$

that is, the membrane has the same velocity as the fluid in the same position $\boldsymbol{x}$, where $\mathrm{D}/\mathrm{D}t$ is the material derivative. Lastly, since the inertia of the membrane being negligible, the surface density of the membrane force is balanced with the hydrodynamic stresses,

$$[\![\boldsymbol{\sigma}]\!] \cdot \boldsymbol{n} + \boldsymbol{f}^m = \boldsymbol{0}, \tag{1.18}$$

where $[\![\boldsymbol{\sigma}]\!] = \boldsymbol{\sigma}^e - \boldsymbol{\sigma}^i$, and $\boldsymbol{f}^m$ is the interfacial force densities, defined in Section 1.3.2.

1.3.4 Characteristic parameters: vesicle in capillary

The flow inside the capillary (of our interest) without deformable particle is called as Poiseuille flow

$$\boldsymbol{u}^{\infty} = U_m \left(1 - \frac{y^2 + z^2}{R_t^2}\right) \boldsymbol{e}_x, \tag{1.19}$$

where U_m, the maximum speed, is the speed at the axis of the capillary of radius R_t, and $r = \sqrt{y^2 + z^2}$ is the radial position.

- *The characteristic length*: the two relevant lengths are the radius of capillary R_t and the equivalent radius of the vesicle $R = \left(V/\frac{4\pi}{3}\right)^{1/3}$, which define a dimensionless parameter, the confinement $\beta = R/R_t$. In this work, we use R as the reference length, i.e., $l_{\text{ref}} = R$.
- *The characteristic time*: the two relevant characteristic times are the characteristic time needed by the vesicle to relax to its equilibrium shape $\tau_r = \frac{\eta^e R^3}{\kappa}$ (in the absence of imposed flow) and the characteristic time defined by the flow $\tau_f = \dot{\gamma}^{-1} = \frac{R_t^2}{2rU_m}$, which define a dimensionless parameter, the capillary number $Ca = \tau_r/\tau_f = \frac{\eta^e R^3 \dot{\gamma}}{\kappa}$. In this work, the characteristic shear rate $\dot{\gamma}_c$ is defined at $r = R/2$ for Poiseuille flow, i.e., $\dot{\gamma}_c = \dot{\gamma}(r = \frac{R}{2})$, as in [5].
- *The characteristic force*: $f_{\text{ref}} = \kappa/R^3$, the typical bending force density.

1.4 A brief review of numerical methods

In this section, we briefly present some widely used numerical methods for deformable particles suspended in external flow, respectively for the membrane and for the hydrodynamic flow, and for the algorithms to calculate the bending forces of a membrane.

1.4.1 Membrane modeling approaches

There are three basic approaches to modeling the moving interfaces by examining how the membrane is presented, namely the continuous membrane approach, the discrete membrane approach, and the implicit membrane approach [59, 61].

The continuous membrane approach

The continuous approach considers the membrane as a two-dimensional surface with known mechanical properties: such as (local) membrane incompressibility, elasticity, resistance to bending, and membrane viscosity etc [61]. The two most commonly used models are those of the constitutive laws used for capsule [11, 12, 22, 113, 129, 160] and vesicle [21, 22, 46, 113, 132, 138, 150, 158], as presented in Section 1.3.2.

In this approach, the membrane surface is explicitly discretized through triangulation [21, 22] or through spectral representation [132, 158], and the membrane stresses are directly

linked to the membrane deformation with the constitutive laws, by finite element method [21], isogeometric method [22], spectral method [132], etc.

The discrete membrane approach

Discrete modeling, or particle-based modeling, constructed in molecular level, which can explicitly include microstructural details in the model and is expected to have the ability to describe the biochemical process, such as ATP release [26, 54, 59, 97]. For this method, the membrane can generally be considered as a set of particles connected by a network of springs.

Fully particle-based modeling, such as molecular dynamics (MD), is only affordable in a small domain due to its unfavorable computational scaling [26, 53]. To work around this limitation, two approaches are proposed, the multiscale modeling and the mesoscopic method. The first solution is used with other scale methods, which together serve to simulate the entire flow, and not specialized for the membrane [53]. While the mesoscopic particle method, or coarse-grained method, each particle represents a molecular cluster rather than an individual one [97]. For example, for a typical RBC, Li et al. [95] use such a mesoscopic particle to represent each spectrin link, which is of the order of 10^5. This spectrin-level model can take into account both the lipid bilayer, the spectrin cytoskeleton and the interaction between them, and can produce macroscopic elastic modulus in agreement with the experimental observation. Such spectrin-level may probably be unnecessary, as shown by Fedosov et al. [52] and recently by our group [105]; highly coarse-grained models also give fairly acceptable results.

Among the well-known coarse-grained models used in cell simulation are dissipative particle dynamics (DPD) [51, 67], smooth dissipative particle dynamics (SDPD) [91, 114], multi-particle collision dynamics (MPCD) [63, 109], immersed boundary method (IBM) [110, 155] and lattice boltzmann method (LBM) [142].

The implicit membrane approach

For this approach, the cell membrane is presented neither by a set of elements, nor by a set of marked points, but by an auxiliary field, which assumes a certain value on the position of this membrane interface [107]. The phase field method (PF) [16, 18] and the level set method (LS) [43, 107] belong to this family.

1.4.2 Flow simulation methods

With regard to the methods used to discretize the flow equations, Freund [59] made a very impressive review by classifying into four different kinds. Here, a similar classification, but with a rather shortened version, is given.

Boundary integral methods

BIM, which is favorable for linear viscous flow (i.e., Stokes flow), benefits from the fact that only surfaces are discretized. The theory and its formulation are well documented by

Pozrikidis [127, 128], and it is now widely used in the simulation of capsule [12, 129] and vesicle [21, 22, 46]. Meanwhile, a disadvantage is that the matrix after the discretization is dense due to the slow spatial decay of Green's functions, and it becomes very difficult in calculation in the case where many cells are involved. The two most widely used methods to overcome this limitation are the particle-mesh methods and the fast multipole methods.

The particle-mesh methods decompose a potential (the Green's functions) into a rapidly decaying short-range interactions and smooth, mesh-resolvable long-range interactions [13, 58, 85]. The fast multipole methods employ multipole expansions of the Green's functions, and the long-range interactions are grouped. Unlike FFT-based methods (used in long-range interactions for particle-mesh methods), the expansion coefficients can be developed hierarchically, thus parallel implementation can be made efficient with judicious data management [59, 66, 131].

Mesh-based methods

Unlike boundary integral methods, mesh-based methods use a fixed mesh that fills the flow region but does not generally match the cell shapes. Thus interpolations are necessary, but capable for the flow with finite inertia. Both finite-difference and lattice-Boltzmann discretizations have been successfully applied for cell simulation with non-conforming meshes [59].

For example, finite difference methods are used for the simulation of deformable particles with the membrane interfaces tracked by immersed boundary method [7, 8], immersed interface method [94, 98], and level set method [31, 108] etc. Similarly, the semi-Lagrangian lattice Boltzmann methods are also used for the viscous flow simulation [4, 81] in coupling with immersed boundary method [87, 147, 156], finite element method [106],coarse-grained model [134] etc. Other mesh-based methods include the finite element method [42] and the finite volume method [91, 110, 140].

Hybrid integral-mesh methods

Kumar et Graham [88] have developed a hybrid approach that shares features of both boundary integral and mesh-based methods. In short, instead of the commonly used boundary integral (BI) formulation, an alternative BI formulation in which the velocity field is expressed in terms of single layer integral alone. The overall problem is decomposed into a local problem and a global problem, essentially by splitting the Green's function into local (singular but exponentially-decaying) and global (smooth but long-ranged) parts.

The short-range local part employs a free-space Green's function and will be solved with free-space boundary conditions (integral part). Whereas the global solution is approximated by a series (Chebyshev polynomial for non-periodic direction and Fourier series in the periodic direction), and that the Stokes equations become a set of ordinary differential equations by the application of the Galerkin method (mesh-based part). This accelerated hybrid approach is developed for multiphase flow in arbitrary geometry, thanks to the wall geometry flexibility and boundary condition convenience of mesh-based schemes [59].

Stochastic particle methods

The particle methods, as presented in Section 1.4.1 for the membrane modeling, are also used for the fluid simulation. Such methods include the dissipative particle dynamics (DPD) [51, 123] and the multiparticle collision dynamics (MPCD) [63, 109].

For more details on numerical methods, one can refer to the reviews by Li et al. [97], Freund [59], Abreu et al. [3], and Aydin et al. [6].

1.4.3 Algorithms for bending forces

Bending force is the main membrane force for vesicles and can become the dominating factor for capsules at low shear rates [12, 56]. The direct calculation of the bending force is much more difficult than the in-plane elastic force, because of the fourth-order derivative. In this section, various algorithms for calculating the bending forces, which are derived from the seminal works of Canham [28] and Helfrich [69] (Eq. (1.11) without surface tension γ), are briefly presented based on the work of Guckenberger et al [68].

In their article [68], six different algorithms (denoted by A-E and S, as shown in Table 1.1) are sorted into three different categories, depending on the variational derivative being performed before ("variational formulation") or after ("force formulation") the surface discretization. The first two algorithms, methods A and B, first discretize the surface and then perform the variational derivative by means of a direct differentiation with respect to the nodes' positions, yields the *force*. While the three methods C-E perform the discretization *after* the variational derivative and thus provide the *force density*. The last method S is somewhat set apart from the others because on the one hand the discretization is first introduced, but on the other hand, the force density is obtained by solving the weak-form integral equations discretized by means of the finite element method. As summarized in the "Result" and "Derivative" row of the Table 1.1.

	A	B	C	D	E	S
Ingredient basically from	Kantor [75]	Gompper [64]	Meyer [111]	Belkin [15]	Farutin [46]	Cirak [29] Boedec [22]
Result	Force	Force	Force density	Force density	Force density	Force density
Derivative	Nodal	Nodal	Variational	Variational	Variational	FEM
Basic idea	Normal vector discretization	Δ_s via co-tangent scheme	Δ_s via co-tangent scheme	Δ_s via heat equation	Parabolic fitting	Subdivision surface

Table 1.1: Overview of the six algorithms A-E and S [68] for computing membrane bending forces.

These algorithms also differ from the basic idea in evaluating the mean curvature or the Laplace-Beltrami operator Δ_s, if any. The results are summarized as follows:

- Method A calculates the bending energy via the normal vector and the relation $\int_S (H^2 - 2K)\mathrm{d}S = \int_S (\partial^\alpha \boldsymbol{n}) \cdot (\partial_\alpha \boldsymbol{n})\mathrm{d}S$. This method showed the largest errors and very sensitive to irregularities. Furthermore, it often requires the smallest step size in order to remain in a stable region, but on the other hand, it is the most easily implemented method.

- Method B approximates Δ_s by a variant of the so-called cotangent scheme [64]. This method turns out to be similar to Method C for homogeneous mesh, but somewhat worse for inhomogeneous triangulations regarding errors and required step size.

- Method C approximates Δ_s in the same way as Method B, except for the method of calculating the area attached to each node. Another major difference is related to the order between the discretization and the variational derivative, which allows Method C to evaluate $\Delta_s H$ also by a cotangent scheme when calculating the force density. This algorithm also has troubles with the inhomogeneous mesh. The hydrodynamical results are very similar to Methods B, D, E and S, and requires a step size comparable to B and E.

- Method D differs from Method C by the discretization of Δ_s, which is based on a kernel of the diffusion or heat equation [15]. This method is shown the most robust among all the six algorithms and working reasonably well on the inhomogeneous mesh. It also leads to the largest step size, but one evaluation scales as $O(N^2)$, where N is the number of the nodes.

- Method E evaluates the curvatures and thus the force density by a parabolic fitting scheme [46]. This method is similar to C, whereas it handled the irregular mesh better than Methods A–C but still worse than D. The required step size is comparable to Methods B and C.

- Method S is the algorithm currently used in our group, as presented in Section 2.2. The remarkable difference, compared to other algorithms, is that the force density is calculated explicitly by solving a linear system but not by approximating. This method exhibits the same behavior as Method C. Working with the mesh preservation algorithm (Section 2.5.2), this method shows its potential for various deformable particles with large deformation [22]. Moreover, it provided errors that are significantly smaller, whereas the complexity is $O(N^2)$.

Our approach is based on boundary integral equations (BIE), which are analytic for given boundary distributions, and which reduce a 3D problem into a 2D one since only boundaries/interfaces need to mesh. These two points of BIE show great advantages (in terms of accuracy and computational effort) before mesh-based methods and particle methods. To compute the mechanical source distributions raised from a single soft particle, as in our case, continuous approaches are far more accurate than particle-based modeling. The

troublesome out-of-plane bending force is alleviated from a fourth-order derivative to a second-order one by formulating the membrane equilibrium equation in weak form *and* with quadratic shape functions (Loop elements). That is, all elastic forces induced by the deformation are evaluated directly with the finite element method, and no reconstruction is necessary.

1.5 Dissertation overview

The rest of this dissertation is organized as follows.

In Chapter 2 we present the details of the numerical methods that are used in subsequent chapters to investigate the dynamics of vesicles and red blood cells in tube flow. Specifically, we first describe how a wall boundary is incorporated into a previous numerical model for soft particles (drop, capsule, and vesicle) in unbounded Stoke flows. We then present several simulation examples to validate and demonstrate the spatial and temporal convergence of the newly implemented method (Sec. 2.5.5). While the present numerical model is able to handle channel walls of arbitrary cross-section, as illustrated in the example of a capsule flowing in a rectangular microchannel (Sec. 2.5.4), the present work focuses on the dynamics of a vesicle that is transported through a circular tube in a pressure-driven flow.

Chapter 3 details the dynamics of a three-dimensional vesicle freely suspended in confined Poiseuille flow with an emphasis given to the vesicle's shape transition and different lateral migration models. Vesicles with matched viscosity of the inner and outer fluids are characterized by three dimensionless parameters, namely the reduced volume, the confinement (called also the radius ratio), and the capillary number. We show that a deflated vesicle, initially placed at an off-center position, can also migrate perpendicular to the flow direction due to both the presence of the wall boundary and the curvature of the imposed flow profile. Three general migration modes are clearly determined in Sec. 3.3.1, depending on these three control parameters. During the migration, the vesicle's shape undergoes continuous deformation due to the hydrodynamic stresses imposed by the Poiseuille flow onto the membrane. Once the lateral migration speed vanishes, a stable shape is obtained, as shown in Sec 3.3.2 and the corresponding flow structures are presented in Sec. 3.3.3. The effects of the capillary number (Sec. 3.3.4), the confinement (Sec. 3.3.5), the reduced volume (Sec. 3.3.6), and the initial conditions (H_0 and θ_0, Sec. 3.3.7) are then explored in detail.

In Chapter 4 we study, via an axisymmetric boundary element method, vesicle hydrodynamics under high confinements in which the shape of the vesicle is expected to maintain axisymmetry. We present a phase diagram of shapes, compare the simulation results with experimental observations, and give a clearly identified parachute-bullet shape transition line. Critical confinement is calculated based on the geometric constraints of vesicles – the volume and surface area are fixed on the time scale of typical experiments. We present simulation results and compare with the previous theoretical investigation when the confinement approaches its critical value. The results of this study have potential application to assess the rheology of a dilute red blood cell suspension.

Chapter 5 describes a hybrid continuum (vesicle model, see 1.3.2) and coarse-grained (FENE-POW spring model) model to study red blood cells in fluid flows. The proposed approach is compared with the classical optical tweezers experiment (Sec. 5.4.1). With the present model, both tank-treading and tumbling motions are reproduced for a red blood cell immersed in a linear shear flow (Sec. 5.4.2). The effect of the shear modulus of a red blood cell in tube flow is also investigated in Sec. 5.4.3.

Chapter 6 presents conclusions of this dissertation and outlines some future potential developments that are closely related to the present work.

Notation	Definition	Expression/Units
η	fluid viscosity	Pa s
$\eta^i(\eta^e)$	internal (external) fluid viscosity	Pa s
γ	surface tension	N m^{-1}
μ, μ_S, G_s	elastic shear modulus	N m^{-1}
K_a	dilation modulus	N m^{-1}
κ	bending modulus	N m
κ_G	Gaussian bending modulus	N m
H	mean curvature	m^{-1}
K	Gaussian curvature	m^{-2}
C_0	spontaneous curvature	m^{-1}
ν	reduced volume	Eq. (1.3)
Δ	excess area	Eq. (1.4)
$\boldsymbol{u}$	velocity	m s^{-1}
ρ	fluid density	kg m^{-3}
w_s	surface energy density	N m^{-1}
$\boldsymbol{n}$	normal vector	
$\boldsymbol{\nabla}_s$	surface gradient operator	$(\boldsymbol{I} - \boldsymbol{nn})\cdot \boldsymbol{\nabla}$
Δ_s	Laplace-Beltrami operator	$\Delta_s = \boldsymbol{\nabla}_s \cdot \boldsymbol{\nabla}_s$
R	radius of the deformable particle	m
R_t	radius of the capillary	m
β	confinement of capillary flow	$\beta = R/R_t$
$\dot{\gamma}$	shear rate	s^{-1}
Ca	(bending) capillary number	$\eta^e R^3 \dot{\gamma}/\kappa$
L_1, L_2, L_3	lengths of three principal axes	m
D	Taylor parameter	$(L_1 - L_2)/(L_1 + L_2)$
D_2	geometric parameter	$(L_2 - L_3)/(L_2 + L_3)$
θ	angle of inclination	Fig. 3.1 (b)
Y_g, Y_G	lateral position of the centroid of the particle	m
U_y	lateral migration velocity	m s^{-1}

Table 1.2: List of used notations.

Abbre.	Definition
BEM	boundary element method
BIM	boundary integral method
DPD	dissipative particle dynamics
FEM	Finite element method
FENE	finitely extensible nonlinear elastic
FSI	fluid-structure interaction
IBM	immersed boundary method
KS	Keller-Shalak theory
LBM	lattice boltzmann method
LS	level set
MD	molecular dynamics
MPCD	multi-particle collision dynamics
NH	Neo-Hookean law
PF	phase field
POW	power function
RBC	red blood cell
SDPD	smooth dissipative particle dynamics
Sk	Skalak law
T1	linear triangle element
TR	trembling
TT	tank-treading
TU	tumbling
VB	vacillating-breathing

Table 1.3: List of used abbreviations.

2 Numerical Methods

In this chapter, a three-dimensional numerical model to study the dynamics of a deformable particle suspending in a confined Poiseuille flow is presented, as shown in Figure 2.1. This model is fully based on the methods followed in our previous works for a particle suspended in a fluid without external physical boundaries [22].

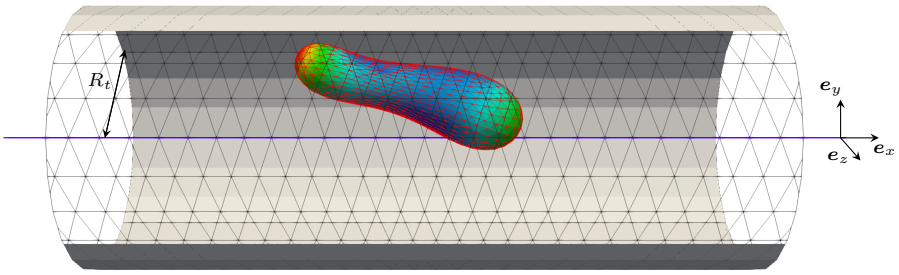

Figure 2.1: A deformable particle in flow through a cylindrical tube of radius R_t. It should be noted that the length of the tube and the mesh given here do not imply the actual length and mesh used in the simulation. The unperturbed flow is given by $\boldsymbol{u}^{\infty} = U_m\left(1 - \frac{y^2+z^2}{R_t^2}\right)\boldsymbol{e}_x$, where U_m is the speed of the flow on the centerline of the capillary, and $\boldsymbol{e}_x$ is the direction of the flow.

In the inertia-free limit (Stokes flow, Eq. (1.7)), if membrane viscosity is neglected, the evolution of the membrane interface (Eq. (1.17)) can be divided into a series of one-way coupled steps, $\boldsymbol{x} \rightarrow \boldsymbol{f} \rightarrow \boldsymbol{u} \rightarrow \partial_t \boldsymbol{x}$ [59]. The numerical methods used in this work will be presented in this way, followed by a section of validation.

2.1 Geometry description (x)

In this section, the membrane interface discretization and the physical boundary (microchannel) discretization are presented separately.

2.1.1 Interface description

To describe or to discretize the particle surface, there are several frequently used methods in the literature, such as finite element methods (FEM) [21, 22, 150], spectral methods [39, 83, 157] and particle-based methods [51, 97]. Here, a Loop subdivision [104] based isogeometric finite elements description is used [22].

For FEM, a general unstructured mesh has only C^0 continuity, and it is impossible to ensure C^1 continuity in the conventional sense where the slope is continuous across the mesh cells. While a direct computation of the membrane bending forces requires at least a C^4 representation of the membrane position since the bending forces contain fourth-order derivatives of the position $\boldsymbol{x}$. Mesh smoothness requirements can be eased from C^4 to H^2, where H^2 represents square-integrable functions whose first- and second-order derivatives are themselves square-integrable[1], by formulating the problem in weak form [29].

To circumvent the C^1 continuity limit, traditional FEM uses either a local reconstruction of elements' interface [46, 110] or designs computations of Laplace-Beltrami operator [21, 150] on C^0 mesh. While subdivision surfaces obtained by Loop scheme [104] are guaranteed to be H^2. What's more, the subdivision surfaces are used both for membrane presentation, membrane solver, and fluid solver (boundary element method) in a consistent way, which is the idea behind the isogeometric analysis [74].

The Loop subdivision surface is an assembly of linear triangle elements refined by a subdivision process. For deformable particles, homotopic to the sphere, the icosahedron can be used as an initial control mesh, in which it contains 20 equilateral triangle faces with five meeting at each of its 12 vertices. New elements are created and vertices are created or updated according to the subdivision rules.

As shown in Figure 2.2, the coordinates of newly generated vertex (level $k+1$) on the edge of the previous mesh (level k) are given by:

$$p_H^{k+1} = \frac{p_A^k + 3p_B^k + 3p_C^k + p_D^k}{8}, \tag{2.1}$$

and the old vertex is updated by

$$p_G^{k+1} = (1 - n\lambda)p_G^k + \lambda \sum_{i=1}^{n} p_{G_i}^k, \tag{2.2}$$

[1] In some cases, the terms C^1 continuity and H^2 square-integrable are interchangeable, e.g., the bounded bending force.

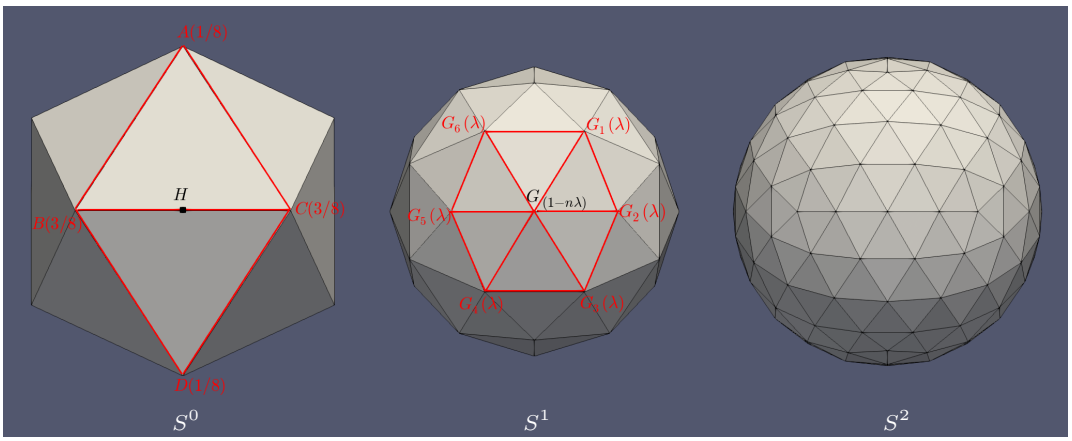

Figure 2.2: An example shows the subdivision process by Loop's rules from an initial control mesh S^0, an icosahedron, to S^1 mesh (with one refinement) and to S^2 (with two refinements). The subdivision masks for creating a new vertex H on the edges of the previous mesh is shown in S^0 and for updating a vertex G from a mesh at level k to a new mesh at level $k+1$ is shown in S^1.

where G_i, $i \in [1, n]$ are the one-ring neighbours[2] (at level k) of an existing vertex G. n, termed as *valence* of the vertex, is the number of edges incident on it [29]. The value of λ, proposed by Loop [104], is given as

$$\lambda = \frac{1}{n}\left[\frac{5}{8} - \left(\frac{3}{8} + \frac{1}{4}\cos\frac{2\pi}{n}\right)^2\right]. \tag{2.3}$$

All vertices having valence equals to six are called *regular* vertices, while vertices with valence other than six are called *irregular* vertices since the function evaluation scheme must be updated for the elements linked to it. Note that all newly generated vertices by Loop subdivision are regular vertices, while the 12 vertices (valence equals to 5) updated from the initial icosahedron mesh will remain irregular. In the limit of infinite subdivisions, the mesh converges to a limit surface which is C^2 continuous, except at the 12 irregular vertices where they degenerate to C^1 continuous.

Stam [143] shows that the limit position of any point on an element e can be obtained by

$$\boldsymbol{x}^e(s^1, s^2) = \sum_{p \in \text{one-ring}} \boldsymbol{X}^p N_p(s^1, s^2), \tag{2.4}$$

where (s^1, s^2) is a local parametrization of the element (on the basis $(\boldsymbol{e}_1, \boldsymbol{e}_2)$ as shown in Figure 2.3(a)), N_p are shape functions which span over all one-ring elements (refer to [29] or appendix B.1 for details) as shown in Figure 2.3(b). The nodal value $\boldsymbol{X}^p$ is the expansion parameters of the shape function N_p for the limit position $\boldsymbol{x}$. Similarly, every scalar function

[2] The one-ring of a vertex: immediate neighbor vertices incident to this vertex. Correspondingly, the one-ring of a element is a set of elements incident to this element, as shown in Figure 2.3 (a).

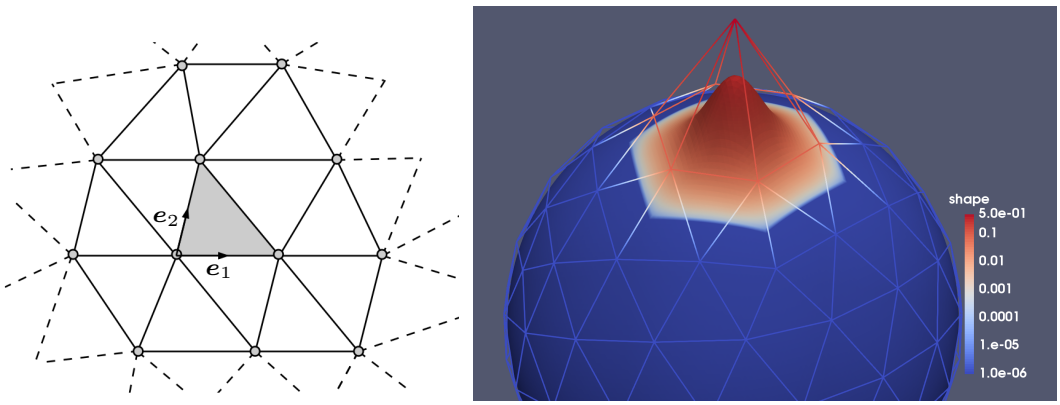

(a) (b)

Figure 2.3: (a) Schema of an element (gray triangle) and its one-ring elements (bounded by solid lines). A parameterization of any point on this element, (s^1, s^2), is built upon the basis $(\boldsymbol{e}_1, \boldsymbol{e}_2)$. (b) Representation of a shape function on a subdivision sphere interface, the wireframe shows a coarse mesh with only two subdivisions and the surface shows a mesh with six subdivisions. Unlike conventional Lagrange triangular elements, the support of the shape function of Loop scheme is spanned over the one-ring elements.

f defined on the membrane, e.g., a component of the membrane traction and velocity, can be expanded or approximated with these shape functions as [22]

$$f^e(\boldsymbol{x}) = f^e(s^1, s^2) = \sum_{p \in \text{one-ring}} F^p N_p(s^1, s^2), \tag{2.5}$$

where F^p is the p-th nodal value. Eq. (2.5) can serve to evaluate f at any point $\boldsymbol{x}$ of the membrane element e if the nodal values F^p are known. Inversely, we also need to convert the known membrane function f into its nodal values F^p, that is, given the approximation of f under the form (2.5) such that the approximation error is minimized. Using the collocation formulation, in which the known field f is collocated at vertices, that is, $f^p = f(\boldsymbol{x} = \boldsymbol{x}^p)$ is known at vertex $\boldsymbol{x}^p$

$$f^p = \sum_{q \in \text{one-ring}} F^q N_q(s^1(\boldsymbol{x}^p), s^2(\boldsymbol{x}^p)) \quad \forall p \in \{1, \cdots, N_v\}, \tag{2.6}$$

where $N_q(\boldsymbol{x}^p)$ are the shape functions evaluated in local parameter space (s^1, s^2) corresponding to the vertex $\boldsymbol{x}^p$, N_v is the total number of vertices. Assembling the linear system (2.6) in matrix form according to the index of vertices, we have

$$\{f^p\} = \boldsymbol{C}\{F^p\}, \tag{2.7}$$

where $\{f^p\} = \{f^1, f^2, \cdots, f^{N_v}\}^t$, $\{F^p\} = \{F^1, F^2, \cdots, F^{N_v}\}^t$, and $\boldsymbol{C}$ is the collocation matrix serves to transform between the limit values f^p and the nodal values F^p.

2.1.2 Microchannel description

In this thesis, the wall of the tube is considered to be rigid and satisfies no-slip and no-penetration boundary conditions. Rigidity, or without deformation, means the conventional C^0 FEM mesh is adequate as for the description of the microchannel (no need for derivative). Here, both the linear triangle elements (T1) and the subdivision elements (Loop) are implemented.

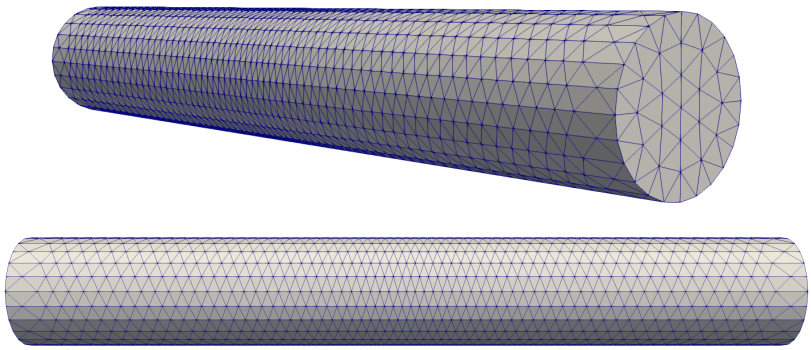

Figure 2.4: Example of a T1 tube mesh formed with linear triangle elements. Top: side view with inlet surface, bottom: full view of the wall mesh. The wall is composed of 3096 elements and the inlet/outlet is composed of 60 elements. The ratio of the length to the diameter L/D equals 7.

Figure 2.4 shows a T1 tube mesh refined at the center which is the region where we can find the soft cell[3]. The complete mesh of the tube is composed of a mesh of inlet surface, a wall mesh, and a mesh of the outlet surface. We distinguish the mesh of the wall and the meshes of the free surfaces due to the discontinuity of the normal vector when it moves from the wall to the free surface, or vice versa. That is, the normal vector is not properly defined at the intersection of these surfaces.

For linear triangle elements, every scalar function f at any point on an element e can be obtained by

$$f^e(s^1, s^2) = \sum_{p=1}^{3} F^p N_p^{t1}(s^1, s^2), \tag{2.8}$$

where N_p^{t1} are linear shape functions (refer appendix B.2 for the shape functions and the notation of control points), F^p are the expansion parameters. Unlike Loop element, the expansion parameters F^p for T1 element are exactly the value of f at control point p, that is $F^p = f^e(\boldsymbol{x}_p)$ due to the definition of the shape functions N_p^{t1}.

[3] To limit the length of the tube, the soft cell is brought back to the center (in the flow direction) after every time stepping.

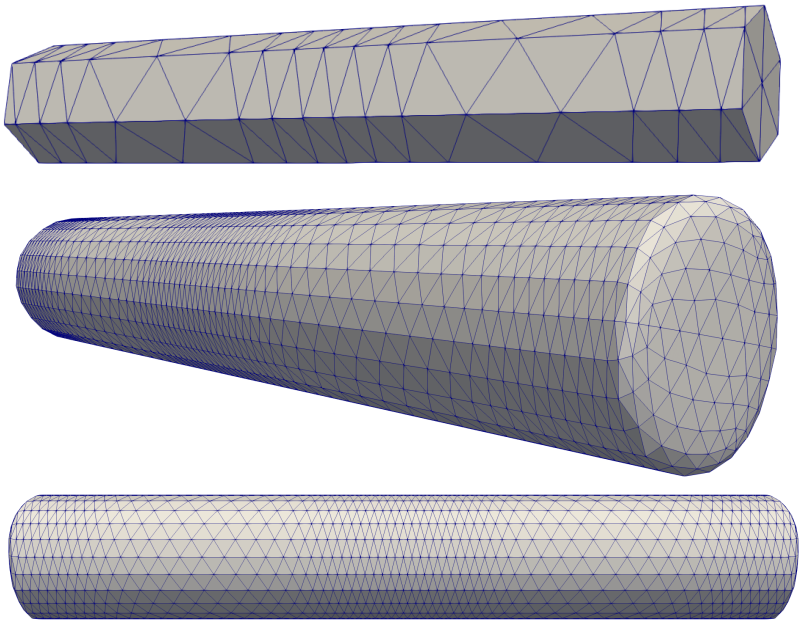

Figure 2.5: Example of a Loop tube mesh obtained by two successive subdivisions from the origin control mesh (top). Both ends are rounded by a predefined small radius circle r_c. This mesh is composed of 3360 elements. The ratio of the length to the diameter L/D equals 6, and $r_c/D = 1/16$.

Figure 2.5 shows a Loop tube mesh which is refined both at the center and its two ends. To have a Lyapunov surface, both ends are rounded by a small circle rather than separated on two. To achieve improved accuracy, the mesh must also be refined at both ends to allow a smooth description of the rounded corner.

As the T1 tube mesh is adequate for the description of the microchannel, it is used in most of the cases in this thesis, and only the perturbed flow due to the presence of the deformable particle is computed. While the Loop tube mesh may be used for microchannel other than the cylindrical tube for which the background flow is not analytically given. It is noteworthy that, in this thesis, the microchannel form of interest is the cylindrical tube, for which the analytic flow without cell is known, i.e., the Poiseuille flow.

2.2 Membrane solver (f)

The membrane solver is designed to calculate the tractions $\boldsymbol{f}^m$ applied by the membrane to the fluids. These tractions, in turn, depend on the deformation of the membrane of soft objects (described by $\boldsymbol{x}$). In our work, the isogeometric finite element method is used to evaluate the membrane tractions [22].

In order to measure the deformation of a curved surface from a reference state $\boldsymbol{x}^0(s^1, s^2)$ to a deformed state $\boldsymbol{x}(s^1, s^2)$, it is useful to introduce a local basis $(\boldsymbol{a}_1, \boldsymbol{a}_2, \boldsymbol{n})$

$$\boldsymbol{a}_1 = \frac{\partial \boldsymbol{x}}{\partial s^1}, \quad \boldsymbol{a}_2 = \frac{\partial \boldsymbol{x}}{\partial s^2}, \quad \boldsymbol{n} = \frac{\boldsymbol{a}_1 \times \boldsymbol{a}_2}{|\boldsymbol{a}_1 \times \boldsymbol{a}_2|} \tag{2.9}$$

on the deformed configuration, where $\boldsymbol{a}_1$ and $\boldsymbol{a}_2$ are tangent vectors of the parametric surface, $\boldsymbol{n}$ is the outward-pointing normal. Similarly, a local basis on the reference configuration is defined as $(\boldsymbol{a}_1^0, \boldsymbol{a}_2^0, \boldsymbol{n}^0)$, by replacing $\boldsymbol{x}$ with $\boldsymbol{x}_0$. In the rest of this section, variables' definition for the reference configuration (denoted by superindex 0) will be neglected, for brevity.

The metric tensor $a_{\alpha\beta}$ and curvature tensor $b_{\alpha\beta}$ are defined as

$$a_{\alpha\beta} = \boldsymbol{a}_\alpha \cdot \boldsymbol{a}_\beta, \quad b_{\alpha\beta} = \boldsymbol{a}_{\alpha,\beta} \cdot \boldsymbol{n} = \frac{\partial \boldsymbol{a}_\alpha}{\partial s^\beta} \cdot \boldsymbol{n}, \quad \alpha, \beta \in \{1, 2\}. \tag{2.10}$$

The elementary area $\mathrm{d}S = \sqrt{a}\mathrm{d}s^1\mathrm{d}s^2$, where $a = \det(a_{\alpha\beta})$ is the determinant of the metric tensor. The inverse metric tensor $a^{\alpha\beta}$ is defined by $a^{\alpha\gamma}a_{\gamma\beta} = \delta^\alpha_\beta$, where δ^α_β is the Kronecker symbol.

The stable equilibrium configuration of a membrane stated with the principle of virtual work for a virtual displacement of $\delta\boldsymbol{x}$ is [29]

$$\underbrace{-\int_S \left[\sigma^{\alpha\beta}\delta(E_{\alpha\beta}) + \mu^{\alpha\beta}\delta(B_{\alpha\beta})\right]\mathrm{d}S}_{\text{internal virtual work}} + \underbrace{\int_S \boldsymbol{f}^{ext} \cdot \delta\boldsymbol{x}\mathrm{d}S}_{\text{external virtual work}} = 0, \tag{2.11}$$

where $\sigma^{\alpha\beta}$ and $\mu^{\alpha\beta}$ are the effective membrane and bending stress tensors, which depend on the properties of the membrane and will be detailed later. $E_{\alpha\beta}$ is the Green-Lagrange strain tensor

$$E_{\alpha\beta} = \frac{1}{2}\left(a_{\alpha\beta} - a^0_{\alpha\beta}\right) \tag{2.12}$$

which is a measure of the membrane stretching deformation and $B_{\alpha\beta}$ is the bending strain tensor

$$B_{\alpha\beta} = b_{\alpha\beta} - b^0_{\alpha\beta} \tag{2.13}$$

which measures the out-of-plane deformation. Be aware that $\boldsymbol{f}^{ext} = -\boldsymbol{f}^m$ (Eq. (1.12)), Eq. (2.11) reads

$$\int_S \left[\frac{1}{2}\sigma^{\alpha\beta}\delta(a_{\alpha\beta}) + \mu^{\alpha\beta}\delta(b_{\alpha\beta})\right]\mathrm{d}S + \int_S \boldsymbol{f}^m \cdot \delta\boldsymbol{x}\mathrm{d}S = 0, \tag{2.14}$$

which gives a general relation between the deformations $\boldsymbol{x}$ and forces $\boldsymbol{f}^m$ of a membrane. To evaluate the forces numerically, Eq. (2.14) need to be discretized with the Loop subdivision elements as in our model.

As in Eq. (2.5), the Cartesian components of membrane forces, position, and virtual displacement can be written as

$$\begin{cases} f_i(s^1,s^2) = \sum\limits_{p\in\text{one-ring}} F_i^p N_p(s^1,s^2) \\ x_i(s^1,s^2) = \sum\limits_{p\in\text{one-ring}} X_i^p N_p(s^1,s^2) \\ \delta x_i(s^1,s^2) = \sum\limits_{p\in\text{one-ring}} \delta X_i^p N_p(s^1,s^2) \end{cases}, \quad i\in\{1,2,3\}. \tag{2.15}$$

Using Eq. (2.15), the principle of virtual work (2.14) is discretized as

$$0 = \sum_{e=1}^{N_e} \int_{S^e} \left[I_\sigma + I_M + I_{\boldsymbol{f}}\right] \sqrt{a}\mathrm{d}s^1\mathrm{d}s^2 \approx \sum_{e=1}^{N_e}\sum_{q=1}^{N_q} w_q \left[I_\sigma + I_M + I_{\boldsymbol{f}}\right]\sqrt{a}|_{(s_q^1,s_q^2)} \tag{2.16}$$

with[4]

$$\begin{cases} I_\sigma = \sum\limits_{p\in\text{one-ring}} \frac{1}{2}\sigma^{\alpha\beta}\left(N_{p,\alpha}x_{i,\beta} + N_{p,\beta}x_{i,\alpha}\right)\delta X_i^p \\ I_M = \sum\limits_{p\in\text{one-ring}} \mu^{\alpha\beta}\left(n_i N_{p,\alpha\beta} - \Gamma^\gamma_{\alpha\beta} n_i N_{p,\gamma}\right)\delta X_i^p \\ I_{\boldsymbol{f}} = \sum\limits_{p\in\text{one-ring}}\sum\limits_{m\in\text{one-ring}} N_p N_m F_i^m \delta X_i^p \end{cases}, \tag{2.17}$$

where $N_{p,\alpha} = \frac{\partial N_p}{\partial s^\alpha}$, N_e and N_q are the total number of elements and quadrature points, w_q and (s_q^1, s_q^2) are, respectively, weight and local parameters associated to the q-th quadrature point.

In Eq. (2.16), the unknowns are F_i^m, they can be formulated in matrix form as

$$\mathbf{M}\{F_i^p\} = \{\mathrm{rhs}_i^p\}, \tag{2.18}$$

where $\{F_i^p\} = \{F_1^1,\ F_2^1,\ F_3^1,\ \cdots,\ F_1^{N_v},\ F_2^{N_v},\ F_3^{N_v}\}^t$ contains the nodal values of membrane forces. $\{\mathrm{rhs}_i^p\}$ contains the sum of contributions of the local $\{\mathrm{rhs}^e\} = -\sum_{e,q} w_q\sqrt{a}(I_\sigma + I_M)$ to the i-th component of vertex p. The mass matrix $\mathbf{M}$ is an assembly of the local mass matrix $\sum_{e,q} w_q\sqrt{a}\sum_{p,m}^{\text{1-ring}} N_p N_m$.

The nodal values of membrane forces $\mathbf{F}$ can be obtained by solving Eq. (2.18) if the constitutive equations of membrane deformation $\sigma^{\alpha\beta}$ and $\mu^{\alpha\beta}$ are specified.

[4] The following relations have been used [22]:

$$\delta(a_{\alpha\beta}) = \delta\boldsymbol{x}_{,\alpha}\cdot\boldsymbol{x}_{,\beta} + \boldsymbol{x}_{,\alpha}\cdot\delta\boldsymbol{x}_{,\beta}, \qquad \delta(b_{\alpha\beta}) = \boldsymbol{n}\cdot\delta(\boldsymbol{a}_{\alpha,\beta}) - \Gamma^\gamma_{\alpha\beta}\boldsymbol{n}\cdot\delta(\boldsymbol{a}_\gamma),$$

where $\Gamma^\gamma_{\alpha\beta} = a^{\gamma\delta}\boldsymbol{a}_{\alpha,\beta}\cdot\boldsymbol{a}_\delta$ are the Christoffel symbols.

Drop

For clean drops, the surface energy, $w_s = \gamma$, does not depend on curvature, thus the bending stress $\mu^{\alpha\beta} = 0$, and the membrane stress

$$\sigma^{\alpha\beta} = \gamma a^{\alpha\beta}. \tag{2.19}$$

Capsule

For zero-thickness capsule model (for example, NH or Sk model as presented in section 1.3.2), we also have $\mu^{\alpha\beta} = 0$, and the membrane stress takes the form [154]

$$\sigma^{\alpha\beta} = \frac{2}{J_s}\frac{\partial w_s}{\partial I_1}a^{0,\alpha\beta} + 2J_s\frac{\partial w_s}{\partial I_2}a^{\alpha\beta}, \tag{2.20}$$

with $J_s = \frac{\sqrt{a}}{\sqrt{a^0}}$ be the Jacobian of the transformation from the reference to the deformed surface, and the surface energy density is given by Eq. (1.14).

Vesicle

For vesicle membrane obeying the Helfrich bending energy with the constraint of incompressibility (Eq. (1.12)), the effective membrane $\sigma^{\alpha\beta}$ and bending $\mu^{\alpha\beta}$ stresses read [22]

$$\begin{cases} \sigma^{\alpha\beta} = \dfrac{2}{\sqrt{a}}\dfrac{\partial\left(\sqrt{a}w_s^H\right)}{\partial a_{\alpha\beta}} = \dfrac{\kappa}{2}\left[4H^2a^{\alpha\beta} - 8Hb^{\alpha\beta}\right] + \gamma a^{\alpha\beta} \\ \mu^{\alpha\beta} = \dfrac{\partial w_s^H}{\partial b_{\alpha\beta}} = \dfrac{\kappa}{2}\left[4Ha^{\alpha\beta}\right] \end{cases}. \tag{2.21}$$

For these three different particles, one may need to compute the inverse metrics $a^{\alpha\beta}$ and curvature $b^{\alpha\beta}$ (for vesicle) tensors, and the local coefficients of γ, H, J_s, $\frac{\partial w_s}{\partial I_1}$, and $\frac{\partial w_s}{\partial I_2}$ at the quadrature points.

2.3 Fluid solver (u)

Once obtained the membrane force $\boldsymbol{f}^m$, we can solve the creeping flow equations

$$\boldsymbol{\nabla}\cdot\boldsymbol{u} = 0, \quad \boldsymbol{\nabla}\cdot\boldsymbol{\sigma} = -\boldsymbol{\nabla}p + \eta\nabla^2\boldsymbol{u} = \boldsymbol{0}, \tag{2.22}$$

where $\boldsymbol{\sigma} = -p\boldsymbol{I} + \eta\left[\boldsymbol{\nabla}\boldsymbol{u} + (\boldsymbol{\nabla}\boldsymbol{u})^t\right]$, η is the fluid viscosity.

As reviewed in [3, 59, 97], there are roughly two approaches[5] to solve numerically this viscous fluid-structure (deformable particles) interaction problems, the continuum-based modeling and the particle-based modeling.

[5] See Sec. 1.4.2 for a more detailed classification.

Continuum-based models directly solve Eq. (2.22) to study problems involving the hydrodynamics. The boundary integral method (BIM) [127] uses Green's tensor of Stokes flow to calculate the velocity fields induced by the membrane forces. Once the Green's functions exist[6], with which the formulated velocity fields obey the Stokes equations by definition. With spectral methods [83, 89, 157], the accuracy of BIM simulations has been further increased. While the immersed boundary method (IBM) [140], which can include inertial effects, models this fluid-cell interaction problem as an incompressible viscoelastic membrane (represented on a Lagrangian coordinate) immersed in an incompressible fluid (represented on a Eulerian coordinate).

Particle-based models define effective particles, which interact with each other, for both fluid and membrane. Particle-based modeling explicitly includes details of the microstructure, can describe the biochemical process, but affordable only for simple cases [26]. The multiscale modeling, coarse-graining of particle-based modeling, has shown the capability in modeling RBC with accurate mechanics, rheology, and dynamics [50, 51].

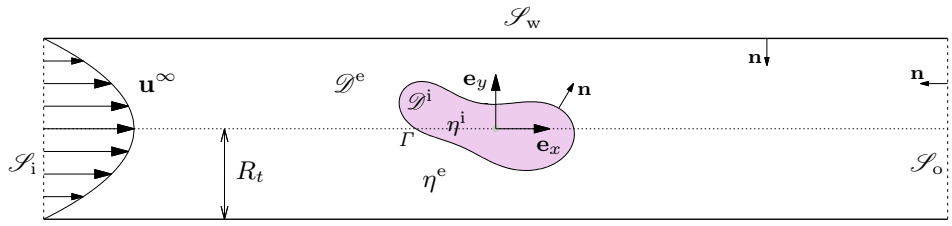

Figure 2.6: Two dimensional schematic presentation of a deformable particle in a bounded Poiseuille flow $\boldsymbol{u}^\infty$ (schematic model of Figure 2.1). $\mathscr{S}_\mathrm{i}$, $\mathscr{S}_\mathrm{o}$ and $\mathscr{S}_\mathrm{w}$ denote the inlet , outlet and wall surface of the tube. R_t denotes the radius of the tube, Γ is the membrane of the deformable particle, and η^i (η^e) is the viscosity of the internal (external) fluid of the particle.

In this thesis, an isogeometric BIM is used to study the dynamics of a vesicle flowing inside a capillary, as schematically shown in Figure 2.6. The BIM simplifies greatly the coupling of fluid and membrane solvers since it only requires the discretization of the boundary of the particles and the physical boundaries in case of bounded flows.

2.3.1 The free-space Green's function

The Green's functions of Stokes flow (2.22) are solutions of the singularly forced Stokes equation

$$\boldsymbol{\nabla}\cdot\boldsymbol{u} = 0, \quad -\boldsymbol{\nabla}p + \eta\nabla^2\boldsymbol{u} + \boldsymbol{g}\delta(\boldsymbol{x}-\boldsymbol{x}_0) = \boldsymbol{0} \tag{2.23}$$

[6] limited to viscous flow and difficult to include the inertial effects.

for the singular force with strength $\boldsymbol{g}$ acting at an arbitrary point $\boldsymbol{x}_0$, $\delta(\boldsymbol{x}-\boldsymbol{x}_0)$ is the delta function. Using the Green's functions, Pozrikidis [127] writes the solution of Eq. (2.23) in the form

$$\begin{cases} u_i(\boldsymbol{x}) = \dfrac{1}{8\pi\eta} G_{ij}(\boldsymbol{x},\boldsymbol{x}_0) g_j \\ p(\boldsymbol{x}) = \dfrac{1}{8\pi} p_j(\boldsymbol{x},\boldsymbol{x}_0) g_j \\ \sigma_{ik}(\boldsymbol{x}) = \dfrac{1}{8\pi} T_{ijk}(\boldsymbol{x},\boldsymbol{x}_0) b_j \end{cases}, \tag{2.24}$$

where $\boldsymbol{x}_0$ is called the *source point*, and $\boldsymbol{x}$ is the *field point*.

Taking divergence $\boldsymbol{\nabla}\cdot$ of the second equation of (2.23) and using the expression

$$\delta(\widehat{\boldsymbol{x}}) = -\frac{1}{4\pi}\nabla^2\left(\frac{1}{r}\right), \tag{2.25}$$

where $r = |\widehat{\boldsymbol{x}}|$, $\widehat{\boldsymbol{x}} = \boldsymbol{x} - \boldsymbol{x}_0$, we have

$$p = -\frac{1}{4\pi}\boldsymbol{g}\cdot\boldsymbol{\nabla}\left(\frac{1}{r}\right). \tag{2.26}$$

Substituting (2.25) and (2.26) into (2.23), we obtain

$$4\pi\eta\nabla^2\boldsymbol{u} = \left[\nabla^2\left(\frac{1}{r}\right)\boldsymbol{I} - \boldsymbol{\nabla}\boldsymbol{\nabla}\left(\frac{1}{r}\right)\right]\cdot\boldsymbol{g}. \tag{2.27}$$

Expressing $\eta\boldsymbol{u} = \boldsymbol{g}\cdot\left(\boldsymbol{\nabla}\boldsymbol{\nabla} - \boldsymbol{I}\nabla^2\right)H$ and substituting into Eq. (2.27), we obtain

$$\left(\boldsymbol{\nabla}\boldsymbol{\nabla} - \boldsymbol{I}\nabla^2\right)\left[4\pi\nabla^2 H + \frac{1}{r}\right] = 0. \tag{2.28}$$

Thus H is solution of the biharmonic equation $\nabla^4 H = \delta(\widehat{\boldsymbol{x}})$, that is $H = -\frac{r}{8\pi}$ and

$$u_i(\boldsymbol{x}) = \frac{1}{8\pi\eta} G_{ij}(\widehat{\boldsymbol{x}}) g_j, \tag{2.29}$$

where[7]

$$\begin{aligned} G_{ij}(\widehat{\boldsymbol{x}}) &= \left(\delta_{ij}\frac{\partial^2}{\partial x_k^2} - \frac{\partial}{\partial x_i}\frac{\partial}{\partial x_j}\right) r \\ &= \frac{\delta_{ij}}{r} + \frac{\widehat{x}_i\widehat{x}_j}{r^3} \end{aligned} \tag{2.30}$$

is the free-space Green's function, also called the *Stokeslet*.

[7] The following relations are used:

$$\frac{\partial r}{\partial x_i} = \frac{\widehat{x}_i}{r}, \quad \nabla^2 r = -8\pi\nabla^2 H = \frac{2}{r}.$$

The free-space Green's function for pressure

$$p_i(\widehat{\boldsymbol{x}}) = -2\frac{\partial}{\partial x_i}\left(\frac{1}{r}\right) = 2\frac{\widehat{x}_i}{r^3}, \tag{2.31}$$

and for stress

$$T_{ijk}(\widehat{\boldsymbol{x}}) = -\delta_{ik}p_j + \frac{\partial G_{ij}}{\partial x_k} + \frac{\partial G_{kj}}{\partial x_i} = -6\frac{\widehat{x}_i\widehat{x}_j\widehat{x}_k}{r^5}. \tag{2.32}$$

2.3.2 The boundary integral equation

Starting from the Lorentz reciprocal identity[8], the velocity induced by the sources and/or forces on the boundary Ω is [126, 127]

$$u_j^D(\boldsymbol{x}) = -\frac{1}{8\pi\eta^e}\int_\Omega f_i^D(\boldsymbol{x}_0)G_{ij}(\boldsymbol{x},\boldsymbol{x}_0)\mathrm{d}S(\boldsymbol{x}_0) + \frac{1}{8\pi}\int_\Omega u_i^D(\boldsymbol{x}_0)T_{ijk}(\boldsymbol{x},\boldsymbol{x}_0)n_k(\boldsymbol{x}_0)\mathrm{d}S(\boldsymbol{x}_0), \tag{2.34}$$

where the superscript D denotes a disturbance variable, $\boldsymbol{x}$ lies inside the control volume $\mathscr{D}^e$ bounded by the boundary $\Omega = \Gamma \cup \mathscr{S}_i \cup \mathscr{S}_w \cup \mathscr{S}_o$, and $\boldsymbol{n}$ directed towards $\mathscr{D}^e$, as shown in Figure 2.6.

Now assuming the rigid tube is long enough such that the disturbance velocity induced by the cell virtually vanishes on the inlet surface $\mathscr{S}_i$ and outlet surface $\mathscr{S}_o$. That is $\boldsymbol{f}^D|_{\mathscr{S}_i} \simeq -p_i^D\boldsymbol{n}$ and $\boldsymbol{f}^D|_{\mathscr{S}_o} \simeq -p_o^D\boldsymbol{n}$.[9] Setting $p_i^D = 0$, and applying no-slip and no-penetration velocity boundary conditions on the wall, Eq. (2.34) reduces to

$$\begin{aligned} u_j^D(\boldsymbol{x}) = &-\frac{1}{8\pi\eta^e}\left[\int_{\mathscr{S}_w,\Gamma^+} f_i^D(\boldsymbol{x}_0)G_{ij}(\boldsymbol{x},\boldsymbol{x}_0)\mathrm{d}S - p_o^D\int_{\mathscr{S}_o} n_i(\boldsymbol{x}_0)G_{ij}(\boldsymbol{x},\boldsymbol{x}_0)\mathrm{d}S\right] \\ &+\frac{1}{8\pi}\int_\Gamma u_i^D(\boldsymbol{x}_0)T_{ijk}(\boldsymbol{x},\boldsymbol{x}_0)n_k(\boldsymbol{x}_0)\mathrm{d}S, \quad \boldsymbol{x}\in\mathscr{D}^e, \end{aligned} \tag{2.35}$$

where the superscript $+$ denotes the exterior surface Γ of the deformable particle.

Applying the reciprocal theorem (2.33) firstly for the unperturbed flow $\boldsymbol{u}^\infty$ without cell and the Stokeslet (solution of singularly forced Stokes flow), we obtain

$$\int_\Gamma G_{ij}(\boldsymbol{x},\boldsymbol{x}_0)f_i^\infty(\boldsymbol{x}_0)\mathrm{d}S = \eta^e\int_\Gamma u_i^\infty(\boldsymbol{x}_0)T_{ijk}(\boldsymbol{x},\boldsymbol{x}_0)n_k(\boldsymbol{x}_0)\mathrm{d}S, \quad \boldsymbol{x}\in\mathscr{D}^i. \tag{2.36}$$

[8] For two flows $\boldsymbol{u}$ and $\boldsymbol{u}'$, which are solutions of the Stokes equations, the reciprocal identity reads

$$\int_\Omega(\boldsymbol{u}'\cdot\boldsymbol{f} - \boldsymbol{f}'\cdot\boldsymbol{u})\mathrm{d}S = 0, \tag{2.33}$$

where $\boldsymbol{f} = \boldsymbol{\sigma}\cdot\boldsymbol{n}$ and $\boldsymbol{f}' = \boldsymbol{\sigma}'\cdot\boldsymbol{n}$ are the corresponding surface forces exerted on Ω, the boundary of the control volume. By identifying $\boldsymbol{u}'$ and $\boldsymbol{f}'$ as the solutions of the singularly forced Stokes equations (2.24), one can obtain $\boldsymbol{u}(\boldsymbol{x})$ at a point $\boldsymbol{x}$ inside Ω.

[9] We suppose the pressure disturbance p_i^D (p_o^D) is a constant over the inlet (outlet) surface.

And then applying the reciprocal theorem for the flow inside the cell and the Stokeslet, we have

$$\int_{\Gamma^-} G_{ij}(\boldsymbol{x},\boldsymbol{x}_0) f_i^D(\boldsymbol{x}_0)\mathrm{d}S = \eta^i \int_{\Gamma} u_i^D(\boldsymbol{x}_0) T_{ijk}(\boldsymbol{x},\boldsymbol{x}_0) n_k(\boldsymbol{x}_0)\mathrm{d}S, \quad \boldsymbol{x}\in\mathscr{D}^i, \tag{2.37}$$

where the superscript $-$ denotes the interior surface Γ of the deformable particle.

From Eq. (2.35) and (2.37), we have an integral representation for the exterior flow

$$\begin{aligned} u_j(\boldsymbol{x}) = u_j^\infty(\boldsymbol{x}) &- \frac{1}{8\pi\eta^e}\int_{\Gamma} \Delta f_i(\boldsymbol{x}_0) G_{ij}(\boldsymbol{x},\boldsymbol{x}_0)\mathrm{d}S \\ &- \frac{1}{8\pi\eta^e}\int_{\mathscr{S}^w} f_i^D(\boldsymbol{x}_0) G_{ij}(\boldsymbol{x},\boldsymbol{x}_0)\mathrm{d}S \\ &+ \frac{p_o^D}{8\pi\eta^e}\int_{\mathscr{S}^o} n_i(\boldsymbol{x}_0) G_{ij}(\boldsymbol{x},\boldsymbol{x}_0)\mathrm{d}S \\ &+ \frac{1-\lambda}{8\pi}\int_{\Gamma} u_i^D(\boldsymbol{x}_0) T_{ijk}(\boldsymbol{x},\boldsymbol{x}_0) n_k(\boldsymbol{x}_0)\mathrm{d}S \end{aligned} \quad \boldsymbol{x}\in\mathscr{D}^e, \tag{2.38}$$

where $\Delta\boldsymbol{f} = \boldsymbol{f}^+ - \boldsymbol{f}^- = \left(\boldsymbol{\sigma}^+ - \boldsymbol{\sigma}^-\right)\cdot\boldsymbol{n}$ is the membrane traction discontinuity, $\lambda = \eta^i/\eta^e$ is the viscosity contrast.

From Eq. (2.38), we approach the field point $\boldsymbol{x}$ to the membrane interface Γ, we obtain[10]

$$\begin{aligned} \frac{1+\lambda}{2} u_j(\boldsymbol{x}) = u_j^\infty(\boldsymbol{x}) &- \frac{1}{8\pi\eta^e}\int_{\Gamma} \Delta f_i(\boldsymbol{x}_0) G_{ij}(\boldsymbol{x},\boldsymbol{x}_0)\mathrm{d}S \\ &- \frac{1}{8\pi\eta^e}\int_{\mathscr{S}^w} f_i^D(\boldsymbol{x}_0) G_{ij}(\boldsymbol{x},\boldsymbol{x}_0)\mathrm{d}S \\ &+ \frac{p_o^D}{8\pi\eta^e}\int_{\mathscr{S}^o} n_i(\boldsymbol{x}_0) G_{ij}(\boldsymbol{x},\boldsymbol{x}_0)\mathrm{d}S \\ &+ \frac{1-\lambda}{8\pi}\int_{\Gamma}^{\mathscr{PV}} u_i^D(\boldsymbol{x}_0) T_{ijk}(\boldsymbol{x},\boldsymbol{x}_0) n_k(\boldsymbol{x}_0)\mathrm{d}S \end{aligned} \quad \boldsymbol{x}\in\Gamma, \tag{2.39}$$

[10] The following relation has been used [127, p. 27]:

$$\lim_{\boldsymbol{x}\to\Gamma^+}\int_{\Gamma} u_i(\boldsymbol{x}_0) T_{ijk}(\boldsymbol{x},\boldsymbol{x}_0) n_k(\boldsymbol{x}_0)\mathrm{d}S = 4\pi u_j(\boldsymbol{x}) + \int_{\Gamma}^{\mathscr{PV}} u_i(\boldsymbol{x}_0) T_{ijk}(\boldsymbol{x},\boldsymbol{x}_0) n_k(\boldsymbol{x}_0)\mathrm{d}S,$$

where the superscript $\mathscr{PV}$ denotes an improper (principal value) double-layer integral when the point $\boldsymbol{x}$ is right on the boundary Γ.

Similarly, approaching $\boldsymbol{x}$ to the tube boundaries $\mathscr{S}^{\text{tube}} = \mathscr{S}^i \cup \mathscr{S}^w \cup \mathscr{S}^o$ and applying the appropriate boundary conditions, we have

$$\begin{aligned} 0 = &-\frac{1}{8\pi\eta^e}\int_\Gamma \Delta f_i(\boldsymbol{x}_0)G_{ij}(\boldsymbol{x},\boldsymbol{x}_0)\mathrm{d}S \\ &-\frac{1}{8\pi\eta^e}\int_{\mathscr{S}^w} f_i^D(\boldsymbol{x}_0)G_{ij}(\boldsymbol{x},\boldsymbol{x}_0)\mathrm{d}S \\ &+\frac{p_o^D}{8\pi\eta^e}\int_{\mathscr{S}^o} n_i(\boldsymbol{x}_0)G_{ij}(\boldsymbol{x},\boldsymbol{x}_0)\mathrm{d}S \\ &+\frac{1-\lambda}{8\pi}\int_\Gamma u_i^D(\boldsymbol{x}_0)T_{ijk}(\boldsymbol{x},\boldsymbol{x}_0)n_k(\boldsymbol{x}_0)\mathrm{d}S \end{aligned} \qquad \boldsymbol{x}\in\mathscr{S}^{\text{tube}}, \tag{2.40}$$

In summary, Eq. (2.37), (2.38) and (2.39), (2.40) are valid when point $\boldsymbol{x}$ is located in $\mathscr{D}^i$, $\mathscr{D}^e$ and on Γ, $\mathscr{S}^{\text{tube}}$. In this thesis, we are only interested in the matching viscosity case, i.e., $\lambda = 1$, for a bounded flow. Thus both Eq. (2.38) and (2.39) are simplified as

$$\begin{aligned} u_j(\boldsymbol{x}) = u_j^\infty(\boldsymbol{x}) &-\frac{1}{8\pi\eta^e}\int_\Gamma \Delta f_i(\boldsymbol{x}_0)G_{ij}(\boldsymbol{x},\boldsymbol{x}_0)\mathrm{d}S \\ &-\frac{1}{8\pi\eta^e}\int_{\mathscr{S}^w} f_i^D(\boldsymbol{x}_0)G_{ij}(\boldsymbol{x},\boldsymbol{x}_0)\mathrm{d}S \\ &+\frac{p_o^D}{8\pi\eta^e}\int_{\mathscr{S}^o} n_i(\boldsymbol{x}_0)G_{ij}(\boldsymbol{x},\boldsymbol{x}_0)\mathrm{d}S \end{aligned} \qquad \boldsymbol{x}\in\mathscr{D}^e\cup\Gamma, \tag{2.41}$$

and Eq. (2.40) is simplified as

$$\begin{aligned} \int_{\mathscr{S}^w} f_i^D(\boldsymbol{x}_0)G_{ij}(\boldsymbol{x},\boldsymbol{x}_0)\mathrm{d}S = &-\int_\Gamma \Delta f_i(\boldsymbol{x}_0)G_{ij}(\boldsymbol{x},\boldsymbol{x}_0)\mathrm{d}S \\ &-\Delta p_a^D\int_{\mathscr{S}^o} n_i(\boldsymbol{x}_0)G_{ij}(\boldsymbol{x},\boldsymbol{x}_0)\mathrm{d}S \end{aligned} \qquad \boldsymbol{x}\in\mathscr{S}^{\text{w}}, \tag{2.42}$$

where the disturbance pressure drop [126]

$$\Delta p_a^D = -p_o^D = \frac{1}{Q}\int_\Gamma \Delta f_i u_i^\infty \mathrm{d}S \tag{2.43}$$

with Q is the flow rate which is assumed not disturbed by the presence of the cell, i.e., $Q = Q^\infty$.

Singularity treatment

When the field point $\boldsymbol{x}$ approaches the source point $\boldsymbol{x}_0$, numerical treatment should be applied to the integrals in Eq. (2.41) to regularize the singularity due to the singular behavior of the Stokeslet kernel $\boldsymbol{G}$. By subtraction of exact identities for the terms involving the normal and the tangential components of the force on a closed surface (first equation of (2.45)),

Farutin et al. [46] proposed the singularity subtraction (SS) technique, which can deal with the singularities both in normal and tangential directions. The single-layer integral on the cell membrane can be formulated with

$$\int_\Gamma \boldsymbol{G}(\boldsymbol{x},\boldsymbol{x}_0)\cdot\boldsymbol{f}(\boldsymbol{x}_0)\mathrm{d}S(\boldsymbol{x}_0)=\int_\Gamma \boldsymbol{G}\cdot\tilde{\boldsymbol{f}}(\boldsymbol{x},\boldsymbol{x}_0)\mathrm{d}S-\frac{\boldsymbol{n}(\boldsymbol{x})\times\boldsymbol{f}(\boldsymbol{x})}{4\pi}\times\int_\Gamma \boldsymbol{R}(\boldsymbol{x},\boldsymbol{x}_0)\mathrm{d}S, \tag{2.44}$$

where

$$\begin{aligned}\tilde{\boldsymbol{f}}(\boldsymbol{x},\boldsymbol{x_0})&=\boldsymbol{f}(\boldsymbol{x}_0)-\boldsymbol{n}(\boldsymbol{x}_0)(\boldsymbol{f}(\boldsymbol{x})\cdot\boldsymbol{n}(\boldsymbol{x}))+\boldsymbol{n}(\boldsymbol{x}_0)\times(\boldsymbol{n}(\boldsymbol{x})\times\boldsymbol{f}(\boldsymbol{x}))\\ \boldsymbol{R}(\boldsymbol{x},\boldsymbol{x}_0)&=\frac{[\widehat{\boldsymbol{x}}\cdot\boldsymbol{n}(\boldsymbol{x}_0)]}{r^3}\widehat{\boldsymbol{x}}\end{aligned}. \tag{2.45}$$

Surface incompressibility constraint

For a vesicle, the surface incompressibility constraint (Eq. (1.10)) is satisfied by the surface tension γ, a Lagrange multiplier, which is the solution of:

$$\boldsymbol{\nabla}_s\cdot\boldsymbol{u}(\boldsymbol{x})=\boldsymbol{\nabla}_s\cdot\boldsymbol{u}^\infty(\boldsymbol{x})+\boldsymbol{\nabla}_s\cdot\boldsymbol{u}^\kappa(\boldsymbol{x})+\boldsymbol{\nabla}_s\cdot\boldsymbol{u}^\gamma(\boldsymbol{x})+\boldsymbol{\nabla}_s\cdot\boldsymbol{u}^w(\boldsymbol{x})=0, \tag{2.46}$$

where $\boldsymbol{u}^\infty$, $\boldsymbol{u}^\kappa$ are the imposed external velocity and bending induced velocity, $\boldsymbol{u}^\gamma$ is the velocity due to surface tension γ, $\boldsymbol{u}^w$ is the velocity due to the microchannel wall (such as the third term of Eq. (2.41)). $\boldsymbol{u}^\kappa$ and $\boldsymbol{u}^w$ are determined entirely by the shape of the membrane, thus Eq. (2.46) is actually linear with the unknown surface tension γ,

$$\mathbf{D}^\gamma\{\Gamma\}=-\{\boldsymbol{\nabla}_s\cdot\boldsymbol{u}^\infty(\boldsymbol{x})+\boldsymbol{\nabla}_s\cdot\boldsymbol{u}^\kappa(\boldsymbol{x})+\boldsymbol{\nabla}_s\cdot\boldsymbol{u}^w(\boldsymbol{x})\}, \tag{2.47}$$

where $\boldsymbol{D}^\gamma$ is a linear operator which transforms the nodal values of tension $\{\Gamma\}$ to the limit value of the surface divergence of the velocity field due to surface tension $\boldsymbol{\nabla}_s\cdot\boldsymbol{u}^\gamma(\boldsymbol{x})$. Eq. (2.47) is iteratively solved by GMRES [14, 135] with a preconditioner to remedy the ill-conditioned matrix $\boldsymbol{D}^\gamma$.

2.3.3 Discretization and linear system

Assuming that the nodal values of membrane force $\{\boldsymbol{F}\}$ is known (solved with Eq. (2.18)) , there are two basic steps to calculate the velocity field on the membrane.

1. Calculation of the nodal values of perturbed force $\left\{\boldsymbol{F}_w^D\right\}$ on the wall of the tube
   As in Figure 2.6, we use Γ, w, o denote the surface of cell, wall and outlet of the tube. Using the same shape functions as in Eq. (2.5), Eq. (2.42) can be formulated as

   $$\boldsymbol{S}^{ww}\left\{\boldsymbol{F}_w^D\right\}=-\boldsymbol{S}^{w\Gamma}\{\boldsymbol{F}\}-\Delta p_a^D\boldsymbol{S}^{wo}\{\boldsymbol{N}_o\}, \tag{2.48}$$

   where $\boldsymbol{S}^{\alpha\beta}$ is the matrix formulated by the single-layer integral, the superscript $^{\alpha\beta}$ means the field point $\boldsymbol{x}$ is evaluated on the surface $\mathscr{S}^\alpha$ from the source on surface

$\mathscr{S}^\beta$, $\{\boldsymbol{N}_o\}$ is the nodal values of the normal on the outlet surface $\mathscr{S}^o$, and Δp_a^D is computed with Eq. (2.43).

2. Calculation of the velocity on the membrane surface $\{\boldsymbol{u}_\Gamma\}$
   The limit values of velocity field on the membrane surface are derived from Eq. (2.41)

$$\{\boldsymbol{u}_\Gamma\} = \{\boldsymbol{u}_\Gamma^\infty\} - \frac{1}{8\pi\eta^e}\left[\boldsymbol{S}^{\Gamma\Gamma}\{\boldsymbol{F}\} + \boldsymbol{S}^{\Gamma w}\left\{\boldsymbol{F}_w^D\right\} + \Delta p_a^D \boldsymbol{S}^{\Gamma o}\{\boldsymbol{N}_o\}\right]. \tag{2.49}$$

2.4 Time stepping ($\partial_t \mathbf{x}$)

Two time stepping schemes have been implemented in order to update the position of membrane interface given by the semi-discrete forme (2.50) (Eq. (1.17)) , an high-order explicit scheme and an implicit scheme.

$$\frac{\mathrm{d}\boldsymbol{x}(t)}{\mathrm{d}t} = \boldsymbol{g}(t, \boldsymbol{x}). \tag{2.50}$$

At discretized time t_n, the membrane surface position is given by $\boldsymbol{x}_n$, thus the membrane forces $\{\boldsymbol{F}\}$ can be obtained by Eq. (2.18), and then the membrane velocity $\boldsymbol{u}_n$ can be obtained by solving Eq. (2.48) and (2.49), which is possiblely accompanied a projection stage (Eq. (2.47)) to compute the Lagrange tension γ and to satisfy the local surface incompressibility constraint of the membrane. The time stepping schemes are aiming to compute the new membrane position $\boldsymbol{x}_{n+1}$ at time $t_{n+1} = t_n + \mathrm{d}t$.

2.4.1 Runge-Kutta-Fehlberg scheme

The explicit time stepping implemented is a Runge-Kutta Fehlberg fourth-fifth (RKF45) stage scheme [55]. This high-order scheme allows dynamically adapting the time step $\mathrm{d}t = h_n$ by measuring the difference between fourth and fifth results and allows very good conservation of invariants such as the enclosed fluid volume.

The fourth and fifth stage formulations are given as

$$\boldsymbol{x}_{n+1}^{(4)} = \boldsymbol{x}_n + \frac{25}{216}\boldsymbol{k}_1 + \frac{1408}{2565}\boldsymbol{k}_3 + \frac{2197}{4101}\boldsymbol{k}_4 - \frac{1}{5}\boldsymbol{k}_5 \tag{2.51}$$

$$\boldsymbol{x}_{n+1}^{(5)} = \boldsymbol{x}_n + \frac{16}{135}\boldsymbol{k}_1 + \frac{6656}{12858}\boldsymbol{k}_3 + \frac{28651}{56430}\boldsymbol{k}_4 - \frac{9}{50}\boldsymbol{k}_5 + \frac{2}{55}\boldsymbol{k}_6, \tag{2.52}$$

and the parameters at the intermediate stage are

$$\begin{aligned}
\boldsymbol{k}_1 &= h_n \cdot \boldsymbol{g}(t_n, \boldsymbol{x}_n) \\
\boldsymbol{k}_2 &= h_n \cdot \boldsymbol{g}(t_n + \frac{1}{4}h_n, \boldsymbol{x}_n + \frac{1}{4}\boldsymbol{k}_1) \\
\boldsymbol{k}_3 &= h_n \cdot \boldsymbol{g}(t_n + \frac{3}{8}h_n, \boldsymbol{x}_n + \frac{3}{32}\boldsymbol{k}_1 + \frac{9}{32}\boldsymbol{k}_2) \\
\boldsymbol{k}_4 &= h_n \cdot \boldsymbol{g}(t_n + \frac{12}{13}h_n, \boldsymbol{x}_n + \frac{1932}{2197}\boldsymbol{k}_1 - \frac{7200}{2197}\boldsymbol{k}_2 + \frac{7296}{2197}\boldsymbol{k}_3) \\
\boldsymbol{k}_5 &= h_n \cdot \boldsymbol{g}(t_n + h_n, \boldsymbol{x}_n + \frac{439}{216}\boldsymbol{k}_1 - 8\boldsymbol{k}_2 + \frac{3680}{513}\boldsymbol{k}_3 - \frac{845}{4104}\boldsymbol{k}_4) \\
\boldsymbol{k}_6 &= h_n \cdot \boldsymbol{g}(t_n + \frac{1}{2}h_n, \boldsymbol{x}_n - \frac{8}{27}\boldsymbol{k}_1 + 2\boldsymbol{k}_2 - \frac{3544}{2565}\boldsymbol{k}_3 + \frac{1859}{4104}\boldsymbol{k}_4 - \frac{11}{40}\boldsymbol{k}_5)
\end{aligned} \quad . \tag{2.53}$$

The dynamic time step is realized by comparing the difference of fourth and fifth stage results $\epsilon_n = \max |\boldsymbol{x}_{n+1}^{(4)} - \boldsymbol{x}_{n+1}^{(5)}|$ with two presetting tolerances $\varepsilon_{\max}$ and $\varepsilon_{\min}$

$$\begin{cases}
h_n = \left(\dfrac{\varepsilon_{\max}}{2\epsilon_n}\right)^{1/4} h_n & \text{if } \epsilon_n > \varepsilon_{\max} \\
h_{n+1} = \left(\dfrac{\varepsilon_{\min}}{2\epsilon_n}\right)^{1/4} h_n & \text{if } \epsilon_n < \varepsilon_{\min} \\
h_{n+1} = h_n & \text{else}
\end{cases} . \tag{2.54}$$

2.4.2 Trapezoidal scheme

For capsules without bending, the stability condition $\Delta t \leq O(\Delta x / G_s)$ allows a reasonable time step to be selected for an explicit time scheme, while for vesicles, the stability condition $\Delta t \leq O(\Delta x^3 / \kappa)$, where the time step should be inferior to the characteristic time of bending deformation, limits the use of an explicit time scheme in practical.

The implicit time scheme implemented in our code is the trapezoidal time scheme. For a given position and tension $(\boldsymbol{x}_n, \gamma_n)$ at time t_n, the new state $(\boldsymbol{x}_{n+1}, \gamma_{n+1})$ at t_{n+1} is computed by

$$\begin{cases}
\boldsymbol{x}_{n+1} = \boldsymbol{x}_n + \dfrac{\Delta t}{2}[\boldsymbol{u}(\boldsymbol{x}_n, \gamma_n) + \boldsymbol{u}(\boldsymbol{x}_{n+1}, \gamma_{n+1})] \\
\boldsymbol{\nabla}_s \cdot \boldsymbol{u}(\boldsymbol{x}_{n+1}, \gamma_{n+1}) = 0
\end{cases} . \tag{2.55}$$

These equations are solved iteratively. Assume the state at r-th iteration $(\boldsymbol{x}_{n+1}^{(r)}, \gamma_{n+1}^{(r)})$ is given, the residuals of this state read

$$\begin{cases}
\mathrm{res}_{\boldsymbol{x}} = \boldsymbol{x}_{n+1}^{(r)} - \left[\boldsymbol{x}_n + \dfrac{\Delta t}{2}\Big(\boldsymbol{u}(\boldsymbol{x}_n, \gamma_n) + \boldsymbol{u}(\boldsymbol{x}_{n+1}^{(r)}, \gamma_{n+1}^{(r)})\Big)\right] \\
\mathrm{res}_{\gamma} = \boldsymbol{\nabla}_s \cdot \boldsymbol{u}(\boldsymbol{x}_{n+1}^{(r)}, \gamma_{n+1}^{(r)})
\end{cases} . \tag{2.56}$$

If both residuals $\mathrm{res}_{\boldsymbol{x}}$ and res_{γ} are less than a prescribed tolerance, the iteration finishes. Otherwise, a correction $(\delta\boldsymbol{x}, \delta\gamma)$ is seeked by GMRES iterations such that $(\boldsymbol{x}_{n+1}^{(r)}+\delta\boldsymbol{x}, \gamma_{n+1}^{(r)}+\delta\gamma)$ satisfies the linearization of Eq. (2.55) [11]:

$$\begin{cases} \left[\boldsymbol{I} - \dfrac{\Delta t}{2} J^{\boldsymbol{x}}\right]\delta\boldsymbol{x} - \dfrac{\Delta t}{2}\boldsymbol{u}^{\gamma}(\boldsymbol{x}_{n+1}^{(r)}, \delta\gamma) = -\mathrm{res}_{\boldsymbol{x}} \\ \boldsymbol{\nabla}_s\cdot(J^{\boldsymbol{x}}\delta\boldsymbol{x}) + \boldsymbol{\nabla}_s\cdot\boldsymbol{u}^{\gamma}(\boldsymbol{x}_{n+1}^{(r)}, \delta\gamma) = -\mathrm{res}_{\gamma} \end{cases}, \tag{2.57}$$

where $\boldsymbol{u}^{\gamma}$ is the velocity solely due to surface tension, $J^{\boldsymbol{x}}$ is Jacobian with respect to position $\boldsymbol{x}$. Eq. (2.57) is solved with the Jacobian-free Newton–Krylov methods [86], and in GMRES iterations, rather than calculating directly the Jacobian, only its action on a vector $\delta\boldsymbol{x}$ is computed

$$J^{\boldsymbol{x}}\delta\boldsymbol{x} \approx \frac{\boldsymbol{u}(\boldsymbol{x}_{n+1}^{(r)} + \varepsilon\delta\boldsymbol{x}, \gamma_{n+1}^{(r)}) - \boldsymbol{u}(\boldsymbol{x}_{n+1}^{(r)}, \gamma_{n+1}^{(r)})}{\varepsilon}, \tag{2.58}$$

where ε is a small parameter.

In summary, the implicit trapezoidal scheme (2.55) is solved iteratively through Eq. (2.56) with possible corrections $(\delta\boldsymbol{x}, \delta\gamma)$ (Eq. (2.57)) if the residuals $(\mathrm{res}_{\boldsymbol{x}}, \mathrm{res}_{\gamma})$ are too large. This scheme is detailed in Algorithm 1.

2.5 Validation

Our code is validated for deformable particles, such as drop, capsule, and vesicle, flow in linear flow without confinement [22, 65]. In this section, validations will focus primarily on the implementation of microchannels. More precisely, the influence of tube mesh, includes its length and refinement, will be first discussed. And then, benchmark tests are carried out to verify the code and to show the overall resolution.

2.5.1 Tube mesh: length & refinement

Two different microchannel meshes have been implemented as shown in the aforementioned section 2.1.2. The Loop tube mesh, which requires more cell elements to properly describe the corner, is designed to study more complicated channel where analytical background flow is not available. For a fluid vesicle flow in a cylinder tube, which is the most important subject of this thesis, the T1 tube mesh is used.

[11] Since the tension-induced velocity $\boldsymbol{u}^{\gamma}$ is linear with γ, i.e., $\boldsymbol{u}(\boldsymbol{x}_{n+1}^{(r)}, \gamma_{n+1}^{(r)} + \delta\gamma) = \boldsymbol{u}(\boldsymbol{x}_{n+1}^{(r)}, \gamma_{n+1}^{(r)}) + \boldsymbol{u}(\boldsymbol{x}_{n+1}^{(r)}, \delta\gamma)$, we thus have

$$J^{\gamma}\delta\gamma = \left.\frac{\partial\boldsymbol{u}}{\partial\gamma}\right|_{(\boldsymbol{x}_{n+1}^{(r)}, \gamma_{n+1}^{(r)})} = \frac{\boldsymbol{u}(\boldsymbol{x}_{n+1}^{(r)}, \gamma_{n+1}^{(r)} + \delta\gamma) - \boldsymbol{u}(\boldsymbol{x}_{n+1}^{(r)}, \gamma_{n+1}^{(r)})}{\delta\gamma}\delta\gamma = \boldsymbol{u}(\boldsymbol{x}_{n+1}^{(r)}, \delta\gamma) = \boldsymbol{u}^{\gamma}.$$

Algorithm 1: compute one step with trapezoidal scheme

Data: mesh m with position $\boldsymbol{x}_n$ and surface tension γ_n at n-th time step, t_n
Result: all data on mesh m at time step n+1, t_{n+1}

compute the precondition matrix $\boldsymbol{D}^{\gamma}$ in Eq. (2.47);
preconditioner for system (2.57);
back up the position $\boldsymbol{x}_n$ and the tension γ_n of t_n;
/* guess values for new time step are computed as: $(\boldsymbol{x}_n, \gamma_n) \rightarrow \boldsymbol{f}_n \rightarrow \boldsymbol{u}_n \rightarrow$ correct γ_n to satisfy incompressibility, $\gamma^0_{n+1} \rightarrow$ corrected velocity $\boldsymbol{u}^0_{n+1}$ */
compute the membrane velocity $\boldsymbol{u}^0_{n+1}$ and membrane tension γ^0_{n+1} (with $\boldsymbol{\nabla}\cdot\boldsymbol{u}_s = 0$) as the predictions for time step n+1, t^0_{n+1};
first guess on the new position $\boldsymbol{x}^0_{n+1} = \boldsymbol{x}_n + \boldsymbol{u}^0_{n+1}\cdot \mathrm{dt}$;
/* solve the system (2.57) by GMRES iteration, r */
$r = 0$;
do
  if r=0 then
    compute the membrane velocity $\boldsymbol{u}^r_{n+1}$; // $(\boldsymbol{x}^r_{n+1}, \gamma^r_{n+1}) \rightarrow \boldsymbol{f}^r_{n+1} \rightarrow \boldsymbol{u}^r_{n+1}$
    compute the surface divergence of velocity $[\mathrm{divS}]^r_{n+1} = \boldsymbol{\nabla}_s\cdot\boldsymbol{u}^r_{n+1}$;
  /* formulate the error vector for GMRES iteration (the right hand side of (2.57)) */
  calculate the estimation error for position $\mathrm{res}_{\boldsymbol{x}} = \boldsymbol{x}_n + \frac{\mathrm{dt}}{2}\left(\boldsymbol{u}_n + \boldsymbol{u}^r_{n+1}\right) - \boldsymbol{x}^r_{n+1}$;
  error for surface tension $\mathrm{res}_{\gamma} = -[\mathrm{divS}]^r_{n+1}$;
  solve Eq. (2.57) for $(\delta\boldsymbol{x}, \delta\gamma)$ by GMRES;
  update $\boldsymbol{x}^{r+1}_{n+1} = \boldsymbol{x}^r_{n+1} + \delta\boldsymbol{x}$ and $\gamma^{r+1}_{n+1} = \gamma^r_{n+1} + \delta\gamma$;
  compute the new membrane velocity $(\boldsymbol{x}^{r+1}_{n+1}, \gamma^{r+1}_{n+1}) \rightarrow \boldsymbol{u}^{r+1}_{n+1}$;
  compute $[\mathrm{divS}]^{r+1}_{n+1} = \boldsymbol{\nabla}_s\cdot\boldsymbol{u}^{r+1}_{n+1}$;
  update error $\mathrm{res}_{\boldsymbol{x}} = \boldsymbol{x}_n + \frac{\mathrm{dt}}{2}\left(\boldsymbol{u}_n + \boldsymbol{u}^{r+1}_{n+1}\right) - \boldsymbol{x}^{r+1}_{n+1}$ and $\mathrm{res}_{\gamma} = -[\mathrm{divS}]^{r+1}_{n+1}$;
  $\mathrm{res} = \max\left(\sqrt{\mathrm{res}_{\boldsymbol{x}}\cdot\mathrm{res}_{\boldsymbol{x}}}, \sqrt{\mathrm{res}_{\gamma}\cdot\mathrm{res}_{\gamma}}\right)$;
  r++;
while res $> \varepsilon$;

In this section, the flow without cell is first calculated via BEM with Loop tube mesh, and then a study on the influence of T1 tube mesh is carried out with a drop flow in a moderate confined capillary ($\beta = 0.8$).

Loop tube mesh

The first validation is carried out for the Loop tube mesh by calculating the Poiseuille flow via BEM. In this test, a Poiseuille flow boundary condition [133] on the inlet and outlet of the tube is prescribed as:

$$\boldsymbol{u} = U_m \left(1 - \frac{r^2}{R_t^2}\right) \boldsymbol{e}_x, \tag{2.59}$$

where R_t is the radius of the tube. The friction force density (wall shear stress) on the tube wall, the pressure drop, and the velocity inside the tube can be obtained by BEM and are compared to the analytical expressions[12], by varying the length of the tube.

L/D	f_x^w/η	$\Delta p/(\eta L)$
1	8.7958	4.9885
2	8.3303	4.4362
3	8.1922	4.2083
4	8.1281	4.1064
5	8.0920	4.0436
6	8.0689	4.0009
analytical	8.0	4.0

Table 2.1: Friction force density and pressure drop obtained by BEM for the different ratio of the tube length L and the diameter D. In this test, we have set $R_t = 4$ and $U_m = R_t^2 = 16$. The wall friction force density f_x^w is taken from the middle of the tube and surface pressure is taken as the average pressure on the inlet/outlet surface.

Table 2.1 shows the friction force density (at the middle of the tube) and the pressure drop for different lengths of the tube. On increasing the length of the tube, the values of friction force density and pressure drop converge to the analytical values. Similarly, from Figure 2.7

[12] The friction force density on the tube wall for the given Poiseuille flow (2.59) is

$$f_x^w = \eta \frac{\partial u_x}{\partial r}|_{r=R_t} = -\frac{2\eta U_m}{R_t},$$

and the pressure drop is

$$\Delta p = \frac{4\eta U_m L}{R_t^2}.$$

we found that the wall shear stress (away from the end) become indistinguishable when the ratio L/D is larger than three. Due to the rounding effect, this force on the outlet surface, which is the pressure on this surface in absolute value, is not a constant, but the average value converges to a constant value (Table 2.1). Although the ends have been rounded, fluctuations (or overshoots) remain due to the limited number of cells applied in this region where the normal vector varies rapidly (Figure 2.5).

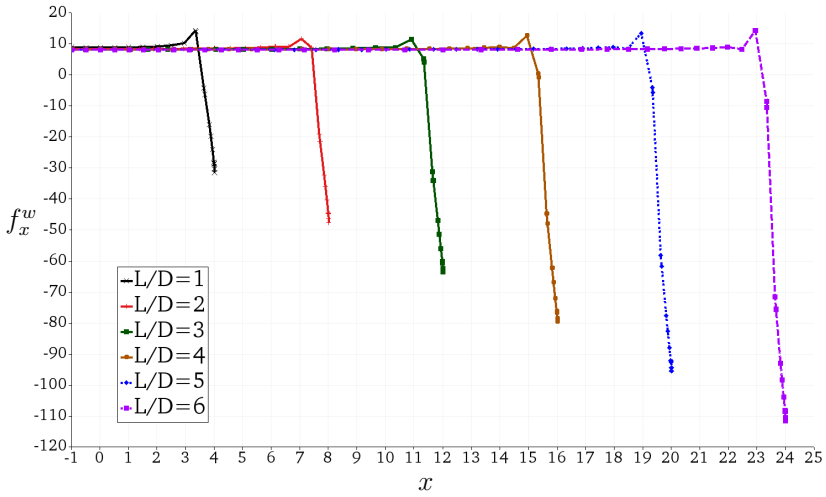

Figure 2.7: The axial force density of the tube (on the line intersected by a plane passing through the axis of the capillary and with the normal vector $\boldsymbol{n} = (0, 0, 1)$) with different lengths. Only the right half of the curves are displayed due to symmetry.

Figure 2.8 (a) shows the axial velocity at the center of the tube for different values of L/D. The normalized axial velocity converges to a constant 1.02 as increasing L/D. This minor deviation from 1.0 is due to fluctuation at both ends. Figure 2.8 (b) shows that the axial velocity on the surface cut the tube at $x = 0$.

T1 TUBE MESH

The cylinder capillary meshed with T1 elements, as used in this case, suffices to calculate the disturbed flow due to the presence of the drop, and the background flow is given as Poiseuille flow.

First, let's summarize some parameters used to describe the mesh of the tube, as shown in Figure 2.4. The ratio of the equivalent radius of the deformable particle R to the radius of the cylinder tube R_t defines a dimensionless parameter, the confinement $\beta = R/R_t$. The half length of the tube L_t is set as $L_t = \zeta R_t = \frac{\zeta}{\beta} R$. During the simulation, we keep the cell in the middle of the tube to avoid the use of a very long tube or periodic boundary conditions. Thus, for the wall, only the central part requires a relatively fine mesh. The grid in the axial direction is generated from the middle (the minimum size $l_{\min}$) to the two ends

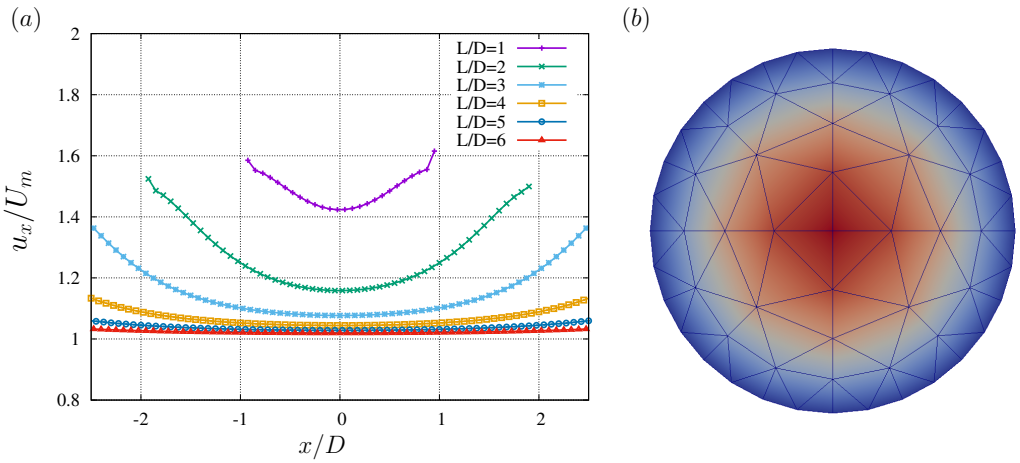

Figure 2.8: (a) The axial velocity at the center of the tube u_x, normalized by U_m, for various tube lengths L/D. (b) The axial velocity plotted on the surface $x = 0$ for $L/D = 6$.

by a progressively coarse process (control by a scale ratio $\iota = 1.05$ for example). The grid in the circumferential direction is equally divided to $m \times 2^n$ arcs, where m is the number of arcs on the innermost circle, n is the number of divisions of the tube radius. For example, $m = n = 4$ as shown in Figure 2.8 (b).

In implementing the flow in capillary with T1 tube mesh, we have assumed that the tube is sufficiently long such that the velocity perturbations on the inlet and outlet surfaces are negligible [126]. As aforementioned in section 2.3.3, we first compute the perturbed force on the capillary due to the presence of the drop with Eq. (2.48), and then update the position of the membrane of the drop via Eq. (2.49). In the calculation of the disturbed force on the capillary, the following force continuity conditions are applied at intersections, namely

$$\begin{cases} \boldsymbol{f}^w \cdot \boldsymbol{e}_x = \pm \boldsymbol{f}^{i,o} \cdot \boldsymbol{e}_r \\ \boldsymbol{f}^w \cdot \boldsymbol{e}_r = \pm \boldsymbol{f}^{i,o} \cdot \boldsymbol{e}_x \,, \\ \boldsymbol{f}^w \cdot \boldsymbol{e}_\theta = \quad \boldsymbol{f}^{i,o} \cdot \boldsymbol{e}_\theta \end{cases} \tag{2.60}$$

where ^{w}, ^{i} and ^{o} represent the wall, inlet and outlet surface of the capillary, $(\boldsymbol{e}_x, \boldsymbol{e}_r, \boldsymbol{e}_\theta)$ are the basis vectors for cylindrical coordinates. $+$ and $-$ apply on the inlet and outlet intersections, respectively.

Figure 2.9 shows the perturbed shear stress $f_{\mathrm{x}}^{\mathrm{w}}$ in the flow direction on the line intersected by a plane (with the normal vector $(0, 1, 0)$) passes through the axis of the capillary, for L_t varies from 5 to 20. The inset shows the stable shapes cut by the same plane. In this case, with L_t as the only variable, we observed that both the perturbed stress due to the presence of the drop, $f_{\mathrm{x}}^{\mathrm{w}}$ and the stable shapes are indistinguishable.

In fact, the boundary of the wall can be replaced by a certain distribution of forces, which act to "neutralize" the velocity distribution on the wall induced by the presence of the drop. From Figure 2.9, we observed that these forces are concentrated at the region $(-2.5, 2.5)$, where we can find the drop.

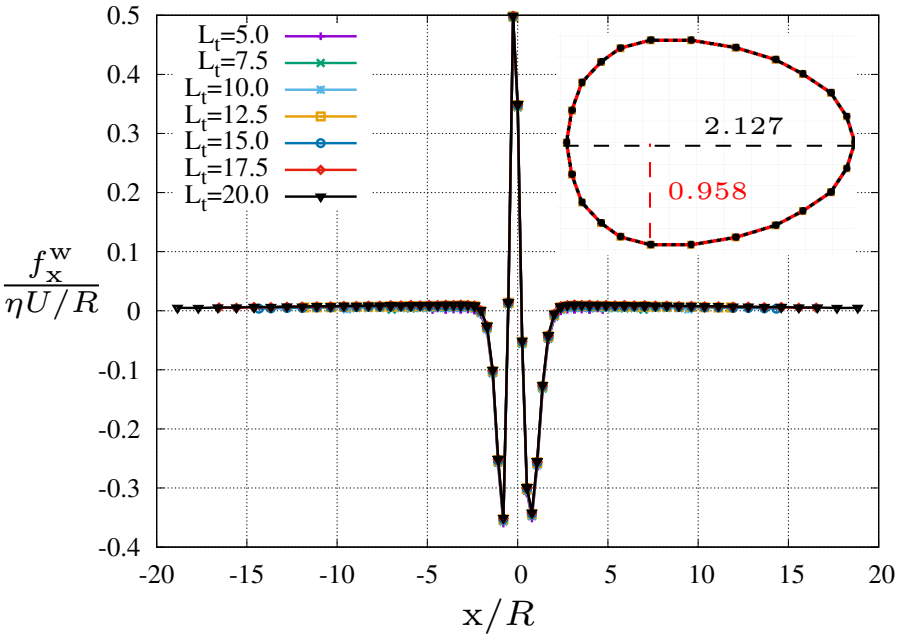

Figure 2.9: The perturbed shear stress of the wall $f_{\mathrm{x}}^{\mathrm{w}}$ on the line intersected by a plane passes through the axis of the capillary and with the normal vector $\boldsymbol{n} = (0, 1, 0)$ for $Ca = 0.1, \beta = 0.8, l_{\min} = 0.25$, with different tube lengths L_t. The inset shows the curves of the intersection with the drop by the same plane for these different cases.

For a vesicle flowing in a capillary, as shown in Figure 2.10, no distinguishable differences are observed as we vary the tube length from $L_t = 12$ to $L_t = 28$[13].

We then work on the influences of the refinement of the tube mesh, with $Ca = 0.5$ and $\beta = 0.8$. Since both the flow and the drop are axisymmetric in this case, we fixed the grid's distribution in the circumferential direction, and only vary the grids in the flow direction, which is controlled by the minimal length $l_{\min}$ and the size increase ratio ι. Here, we set $\iota = 1.05$, and the results are shown in Table 2.2 and Figure 2.11 for different $l_{\min}$.

Table 2.2 shows the additional pressure drop Δp^a due to the presence of the drop and the displacement velocity U_x for $l_{\min}$ varying from 0.025 to 0.7, and also the results of Lac [90] given by spectral method.

Similar to Figure 2.9, the shear stresses f_x^w and stable shapes are displayed in Figure 2.11 for five distinct sizes with $\zeta = 7.5$. We observed the difference of the shape is imperceptible for $l_{\min} \leq 0.5$, and the shear stresses are concentrated at the region $(-3.0, 3.0)$, where we can find the drop. For the case with the coarsest mesh $l_{\min} = 0.7$, even though the peak of shear stresses is not captured due to the limited grid distribution, but the stresses obtained on its grid points are very close to those obtained by finer meshes.

[13] For all simulations in Chapter 3, we have used $\zeta \geq 5$, namely $L_t \geq 5/\beta$.

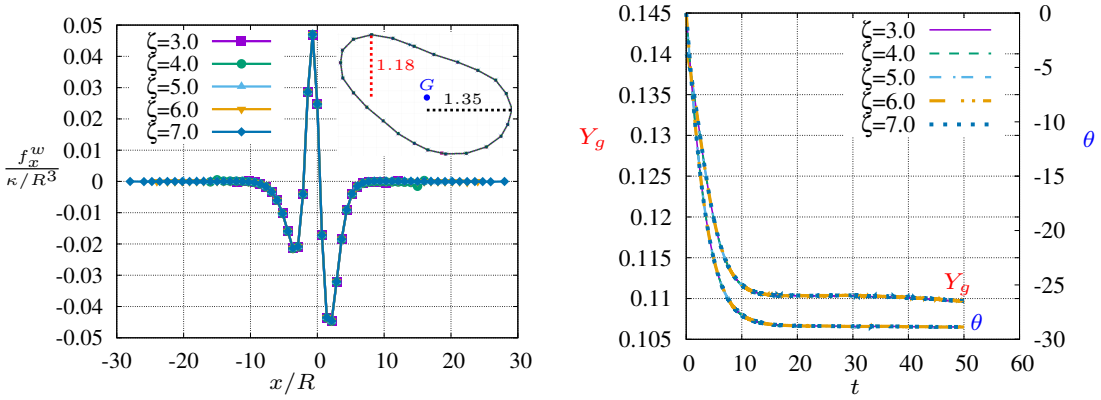

(a) (b)

Figure 2.10: Influence of the length of the tube L_t for vesicle ($\nu = 0.9$) flowing in a capillary ($\beta = 0.25$, $Ca = 1$ and $l_{\min} = 0.7$). (a) The perturbed shear stress of the wall f_x^w on the line intersected by a plane passes through the axis of the capillary and with the normal vector $\boldsymbol{n} = (0, 0, 1)$, for different tube lengths $L_t = \zeta/\beta = 4\zeta$. The inset shows the curves of the intersection with the vesicle by the same plane for these different cases, G is the centroid. (b) Evolution of the centroid (Y_g, dimensionless by R) and inclination angle (θ, in degree).

$l_{\min}$	$\frac{\Delta p^a}{\eta U/R}$	$\frac{U_x}{U}$
0.7	0.5008	1.6970
0.6	0.5011	1.6984
0.5	0.4951	1.6997
0.4	0.4921	1.7007
0.3	0.4907	1.7011
0.2	0.4913	1.7010
0.05	0.4991	1.6989
0.025	0.4981	1.6989
Lac(2009)[90]	0.4867	1.7022

Table 2.2: Effect of the mesh refinement $l_{\min}$ of the capillary on the additional pressure drop Δp^a and the drop translational velocity U_x for a drop flowing along the centerline ($Ca = 0.5, \beta = 0.8, \zeta = 7.5$).

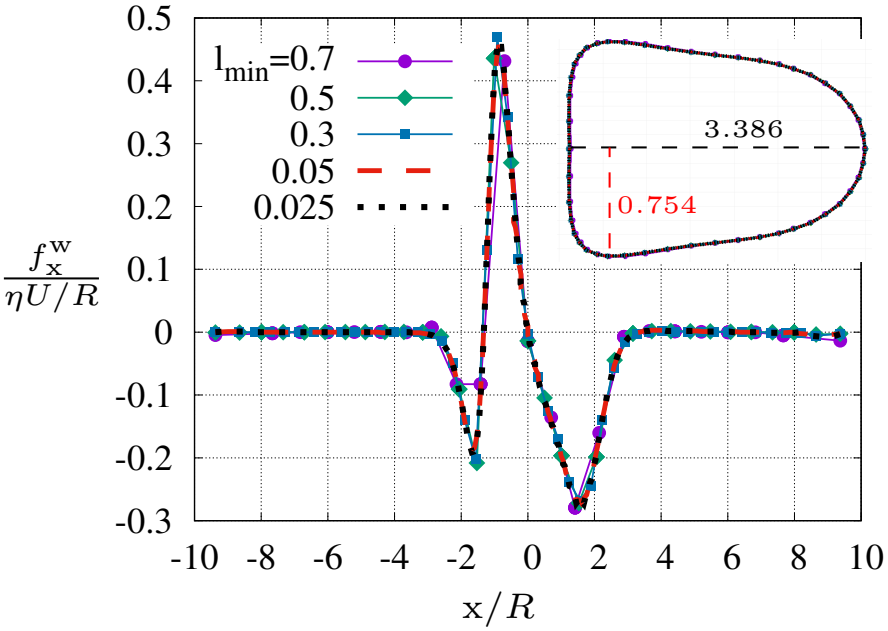

Figure 2.11: The shear stress of the wall f_x^w on the line intersected by a plane passes through the axis of the capillary and with the normal vector $\boldsymbol{n} = (0, 1, 0)$ for $Ca = 0.5, \beta = 0.8$. Five of the eight cases in Table 2.2 are displayed. The inset shows the curves of the intersection with the drop by the same plane for these different cases.

2.5.2 Remeshing

A mesh quality preserving algorithm, termed as *remeshing* in this thesis, has been designed and implemented in our code [22]. Here, the basic idea is firstly presented, and then a guide on the use of this algorithm is given by numerical experiments.

Vesicles and droplets cannot withstand shear, i.e, an infinitesimal shear stresses will deform them, thus there is no tangential reference configuration. The lack of tangential reference configuration means that it is possible to move the grid along the membrane surface in order to improve the quality of the mesh, without affecting the physics. The idea of our algorithm is to treat the mesh as a network of springs since the position of the grid nodes may be updated by tangential displacements controlled by various local characteristics of the grid, such as the local length of the edge, the local area, and the local curvature. The displacement of the i-th node is controlled by

$$\mu \boldsymbol{u}^{\mathrm{r}}(\boldsymbol{x}_i) = (\boldsymbol{I} - \boldsymbol{nn}) \cdot \boldsymbol{f}^{\mathrm{r}}(\boldsymbol{x}_i), \tag{2.61}$$

where $\boldsymbol{u}^{\mathrm{r}}$ is the tangential velocity adopted by the nodes for their *r*edistribution, μ is a fictitious viscosity and $\boldsymbol{f}^{\mathrm{r}}(\boldsymbol{x}_i)$ is the sum of forces due to the network of springs (namely, the

nodes connected by one edge to the current node i), acting on the node with position $\boldsymbol{x}_i$. The nodes redistribution force is computed as

$$\boldsymbol{f}_i^{\mathrm{r}} = \boldsymbol{f}^{\mathrm{r}}(\boldsymbol{x}_i) = \sum_{j \in \text{one-ring}} \left[(k_i + k_j)(l_{ij} - l_{ij}^0) \frac{\boldsymbol{t}_{ij}}{l_{ij}} \right], \tag{2.62}$$

where $\boldsymbol{t}_{ij} = \boldsymbol{x}_j - \boldsymbol{x}_i$, $l_{ij} = ||\boldsymbol{t}_{ij}||$ and l_{ij}^0 is the equilibrium length which is defined as $l_{ij}^0 = c_{\mathrm{L}} L_{ij}$, with L_{ij} the distance between node i and j at the beginning of the time step. The constant k_j are defined as

$$k_j = \frac{c_{\mathrm{A}}}{\widehat{A}} \sum_{e \in E_j} \frac{A_e}{3} + \frac{c_{\mathrm{H}}}{\widehat{(2H)^2}} \sum_{e \in E_j} \frac{(2H)_e^2}{3}, \tag{2.63}$$

where A_e is the area of e-th element connected to the node j, $(2H)_e^2$ is the curvature energy of this element, and

$$\widehat{A} = \frac{1}{N} \int_S \mathrm{d}S, \quad \widehat{(2H)^2} = \frac{1}{N} \int_S (2H)^2 \mathrm{d}S$$

are the average value of membrane area and curvature energy by node, with N is the total number of nodes in the mesh. The node position is then updated with

$$\frac{\mathrm{d}\boldsymbol{x}}{\mathrm{d}t^*} = \boldsymbol{u}^{\mathrm{r}}, \tag{2.64}$$

which is integrated in fictitious time t^* until the residual of redistribution forces $\sum_i ||\boldsymbol{f}_i^{\mathrm{r}}||$ is below a prescribed parameter ε_{r}.

Including ε_{r}, the algorithm has four user-defined parameters,

- $c_{\mathrm{L}} \leq 1$ used to define the equilibrium length l_{ij}^0 of the edges. $c_{\mathrm{L}} < 1$ allows nodes displacement even if the shape remains unchanged, vesicle in tank-treading motion, for example;
- c_{A} tends to make the mesh to have uniform distribution of area of elements (first term at the right hand side of Eq. (2.63));
- c_{H} tends to make the mesh to have more elements in highly curved regions (second term at the right hand side of Eq. (2.63)).

According to our previous studies, using ($c_{\mathrm{L}} = 0.9$, $c_{\mathrm{A}} = 1.0$, $c_{\mathrm{H}} = 1.0$, $\varepsilon_{\mathrm{r}} = 0.05$) gives good results in most situations.

The effects of remeshing are compared and shown in Figure 2.12 for an initially oblate vesicle (with reduced number ν=0.65) flows in a bounded (with confinement $\beta = R/R_t = 0.25$) Poiseuille flow, $Ca = 1$, with 320 elements. The case launched without remeshing becomes very difficult to converge (at $t \approx 3.2$) with the same parameters as those used for the case with remeshing, because of poor quality of the mesh as shown at $t = 3$. Using the aforementioned parameters, it is observed, Figure 2.12 (a), that both the length of edges

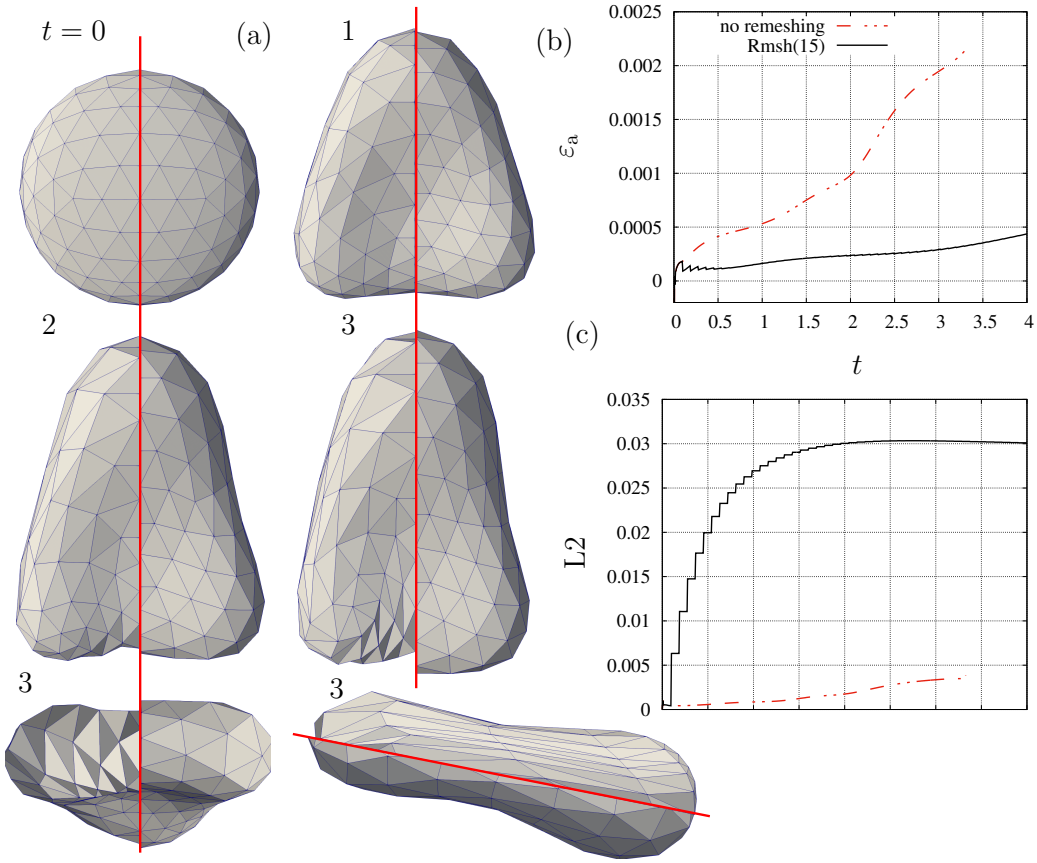

Figure 2.12: Effects of mesh quality preserving algorithm on a vesicle flows in a bounded Poiseuille flow $Ca = 1, \nu = 0.65, \beta = 0.25$, with 320 elements. (a) Snapshots of the shape and the mesh at different dimensionless times, results without (left or top) and with (right or bottom) remeshing are separated by red lines. At $t = 3$, the front, rear and side views are all displayed. (b) Relative error of the membrane area $\varepsilon_a = A/A_0 - 1$ as a function of time for results without remeshing and with remeshing, where $A_0 = A(t = 0)$ and *Rmsh(15)* means the mesh quality preserving algorithm is called every 15 time steps. (c) The local cell error $L2 \equiv \frac{1}{N_e}\sqrt{\sum_i |A_i/A_i^0 - 1|^2}$ as a function of time, where A_i is the area of the i-th element and $A_i^0 = A_i(t = 0)$.

and the area of elements are well controlled, and the membrane surface remains smooth. Remeshing is an overdamped process, Figure 2.12 (c) shows that the L2 error of the local area of elements are much greater in comparison with that without remeshing, but the overall relative error of the membrane area is much smaller, Figure 2.12 (b). This is because the mesh quality preserving algorithm will distribute more nodes in regions with higher curvature.

How the remeshing frequency will influence an initially prolate vesicle ($\nu = 0.95$) flowing in a bounded ($\beta = 0.1$) Poiseuille flow ($Ca = 1$) are compared and shown in Figure 2.13, by the relative error of the membrane area (2.13 (a)) and the relative cross-streamline migration velocity (2.13 (b)). When the mesh quality preserving algorithm is called every 50 time

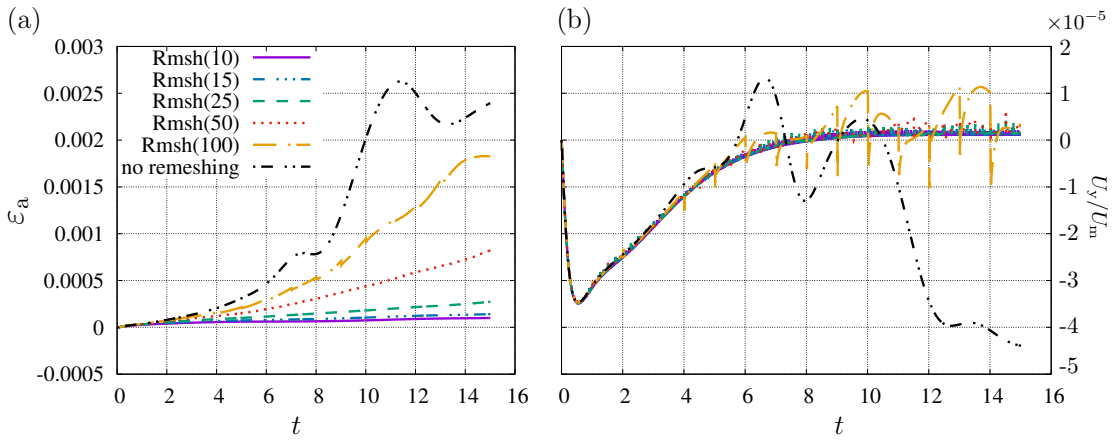

Figure 2.13: Effects of the remeshing frequency on a vesicle flows in a bounded Poiseuille flow $Ca = 1, \nu = 0.95, \beta = 0.1$, with 320 elements. The results of (a) relative error of the membrane area ε_a and (b) relative cross-streamline migration velocity U_y/U_m are compared for applying remeshing every 10, 15, 25 50, 100 and ∞ time steps.

steps or even more, the relative errors become remarkable (2.13 (a)) and the dynamics of lateral migration is influenced (2.13 (b)). Numerical iterations on Eq. (2.64) require about 5% of the whole time needed in a time step of this case. What's more, remeshing introduces dissipation, thus we can activate the remeshing every 20 time steps, for example.

The above two examples involve either significant deformation 2.12 or membrane sliding 2.13, but for a vesicle reaching a steady state without tank-treading, the call of the mesh quality preserving algorithm should be relaxed.

2.5.3 Drop in a capillary flow

Lac and Sherwood [90] numerically studied the motion of an axisymmetric drop along the centerline of a cylindrical capillary. This problem is very similar to the main problem of this thesis, a vesicle flows in a microchannel (refer to Chapter 3), although asymmetry is a major feature for the latter case.

It is known that the presence of a drop in the capillary changes the pressure difference by Δp^a, termed additional pressure drop, in order to maintain a given flow rate Q. They analyzed the displacement velocity U_x and the additional pressure drop Δp^a by varying the capillary number $\mathrm{Ca} = \frac{\eta^e \overline{U}}{\gamma}$, the confinement $\beta = R/R_t$, and the viscosity contrast $\lambda = \eta^i/\eta^e$, where $\overline{U} = U_m/2$ is the average velocity of a Poiseuille flow, γ is the surface tension. The drop size is characterized by the radius R of the sphere with the same volume of the drop $\mathscr{V}$.

By lubrication analysis, they found that at a high capillary number Ca, a drop moves with velocity

$$2 - U^* \sim \mathrm{Ca}^{-2/3}, \tag{2.65}$$

for $\lambda = 1$, where $U^* = U_x/\overline{U}$, and induces an additional pressure drop

$$\frac{R_t}{\eta^e \overline{U}} \Delta p^a \sim \mathrm{Ca}^{-5/3}. \tag{2.66}$$

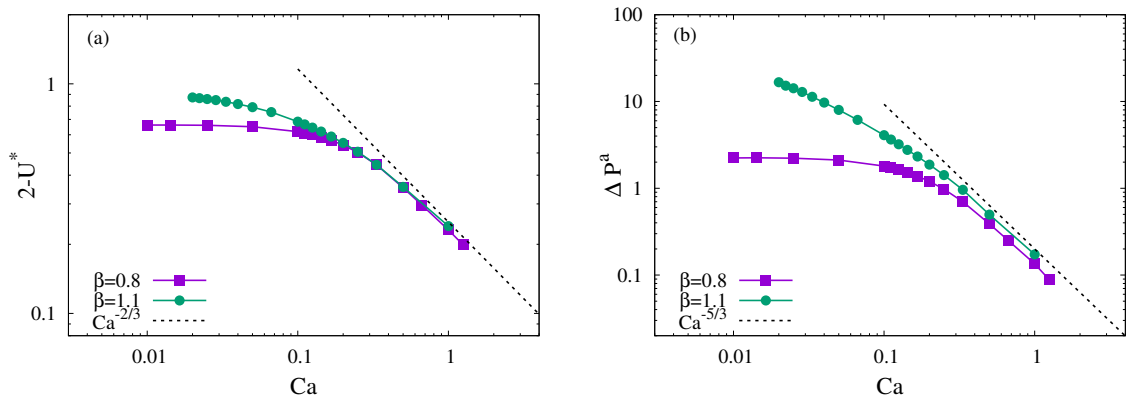

Figure 2.14: Variations of (a) translational velocity $2 - U^*$ and (b) additional pressure drop Δp^a as a function of the capillary number Ca for $\beta = 0.8$ and $\beta = 1.1$.

Figure 2.14(a) shows two curves with different confinements, which represent the translational velocity $2 - U^*$, decrease and converge when the capillary number is increased. Figure 2.14(b) shows the additional pressure drop Δp^a between the extremities of the capillary as a function of Ca for these same confinements β. In both figures, the curves adopt same behaviors with the increasing of the capillary number, and match well with analytical predictions, Eq. (2.65) and (2.66). As for the confinement, we observed that the curve with stronger confinement ($\beta = 1.1$) matches better with the analytical predictions than the weaker one ($\beta = 0.8$), which is consistent with the lubrication hypothesis.

For a vanishingly small droplet moving along the centerline of a capillary, the nondimensional displacement velocity is given as [90]

$$U^* = 2 - \frac{4\lambda}{2+3\lambda}\beta^2 + O(\beta^3), \tag{2.67}$$

and the additional pressure drop is given as

$$\frac{\Delta p^a}{\eta^e \overline{U}/R_t} = \frac{16}{27}\frac{(2+9\lambda)^2 - 40}{(1+\lambda)(2+3\lambda)}\beta^5 + O(\beta^{10}). \tag{2.68}$$

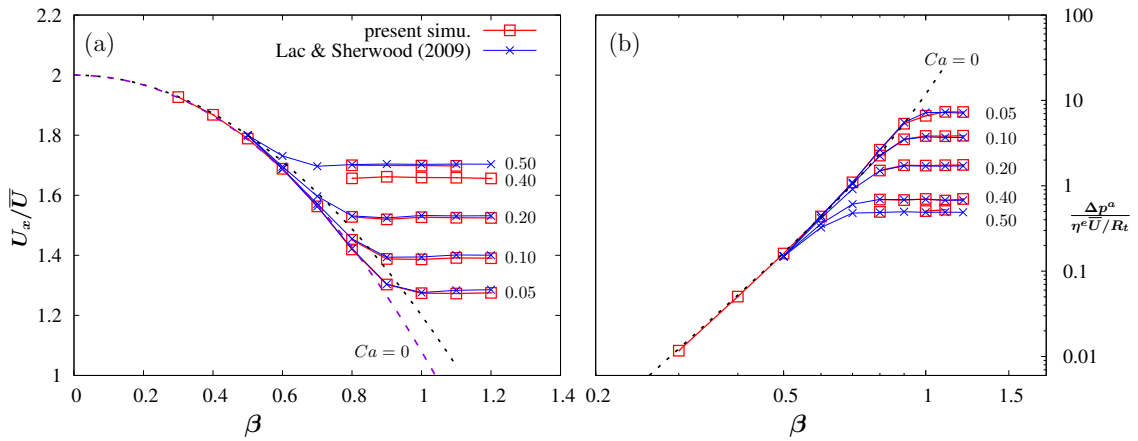

Figure 2.15: Effect of the drop size on (a) the translational velocity and (b) the additional pressure drop for different capillary number. The dashed lines for $\mathrm{Ca} = 0$ are given by Eq. (2.67), (2.68) and its high-order fitting.

The drop translational velocity U_x is shown in Figure 2.15(a) as a function of confinement β for different capillary numbers Ca. The additional pressure due to the presence of a drop for different Ca is shown in Figure 2.15(b). Our results, obtained by fully three-dimensional simulation, are compared with Lac's results which are based on axisymmetric hypothesis, and a good agreement is observed. With the decreasing of the capillary number, we observed the results obtained from simulation converge with the asymptotic prediction for $\mathrm{Ca} = 0$ at a low confinement β. For a vanishingly small droplet moving along the centerline of a capillary, both the displacement velocity and pressure drop follow the asymptotical predictions given at $Ca = 0$, which is identical to an undeformable particle. While for stronger confinements, $\beta \geq 1$ for example, the results show a plateau and no longer depend on β.

2.5.4 Elastic capsule in a square channel

The validation of our procedure of a deformable particle flowing in a microchannel (presented in Section 2.3) is continued here by an elastic capsule flowing in a square channel, as shown in Figure 2.16.

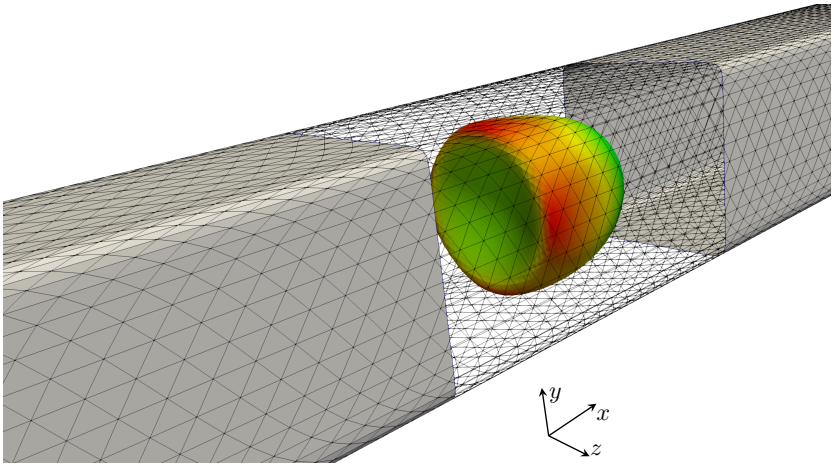

Figure 2.16: An example showing a capsule flowing in a rectangular microchannel. Capsule's membrane is coded by the membrane force of the x-component, i.e., f_x^m. The channel mesh is generated by the Loop subdivision process and rounded with an arc of the circle.

Far from the capsule, the flow approachs the undisturbed flow in a channel $\boldsymbol{u}^\infty = (u_x^\infty, 0, 0)$ which is given as [89],

$$\frac{u_x^\infty}{\Upsilon} = \left(l_z^2 - z^2\right) + \sum_{m=1}^{\infty} B_m \cosh\left(\frac{b_m y}{l_z}\right) \cos\left(\frac{b_m z}{l_z}\right), \tag{2.69}$$

where

$$\Upsilon = -\frac{1}{2\eta}\frac{\mathrm{d}p}{\mathrm{d}x}, \quad b_m = \frac{(2m-1)\pi}{2}, \quad B_m = \frac{(-1)^m 4\, l_z^2}{b_m^3 \cosh\left(\frac{b_m l_y}{l_z}\right)}, \tag{2.70}$$

and l_y and l_z are the widths of the rectangular channel in the directions y and z, respectively. By integrating over the channel's cross-section, the volumetric flow rate Q is given by

$$\frac{Q}{\Upsilon} = \frac{8 l_y l_z^3}{3} + \sum_{m=1}^{\infty} B_m \left(\frac{2l_z}{b_m}\right)^2 \sinh\left(\frac{b_m l_y}{l_z}\right) \sin(b_m). \tag{2.71}$$

In our simulations, we truncated the infinite but convergent series in Eq. (2.69) when m=40, like the one used by Kurikose et Dimitrakopoulos [89]. According to Eq. (2.69), we know

that the channel is not limited to the square section, but it may be a more general rectangular channel.

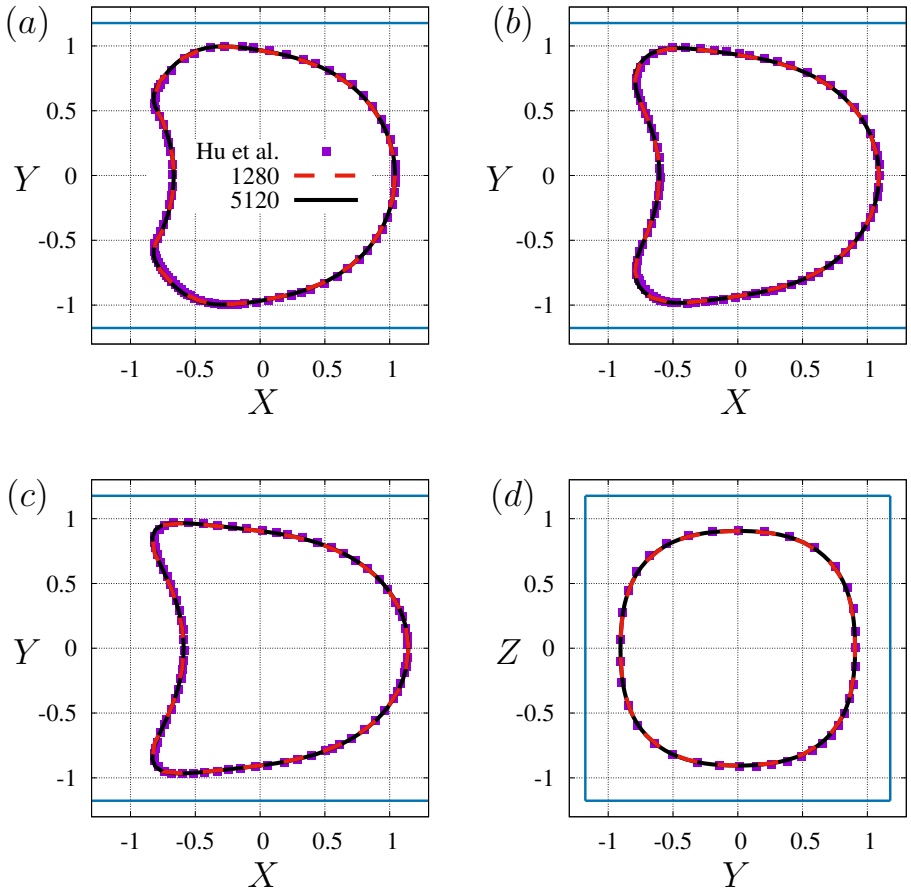

Figure 2.17: Comparison of the steady-state deformed shape of a capsule flowing in a square cross-section channel with those obtained by Hu et al. [72, 73] in the Stokes regime for a confinement $\beta = 0.85$ and (a) $Ca = 0.02$, XY-plane, (b) $Ca = 0.05$, XY-plane, (c) $Ca = 0.1$, XY-plane, (d) $Ca = 0.1$, YZ-plane. The blue lines indicate the limits of the microchannel.

In this test, the strain-hardening Sk law (Eq. (1.14)) with $C = 1$ (as in [73]) has been applied for the confinement $\beta = 0.85$ and for three different capillary number $Ca = \eta U/G_s = 0.02, 0.05$, and 0.1, where $U = Q/S$ and S is the area of the cross section. As shown in Figure 2.17, two different meshes have been adopted for the capsule, with 1280 and 5120 elements, and the benchmark results of Hu et al. [72, 73] are obtained with the freely available tool WebPlotDigitizer[14].

The steady-state shapes obtained for $Ca = 0.02, 0.05$, and 0.1 are plotted in Figure 2.17 (a)-(c) in the plane $z = 0$ and in Figure 2.17 (d) in the plane $x = 0$ (for $Ca = 0.1$ only).

[14] https://automeris.io/WebPlotDigitizer/

These results, first, show that the difference is negligible for our numerical results obtained with 1280 elements and 5120 elements, and second, all these results match well with those of Hu et al [72, 73].

2.5.5 Convergence

A convergence study on the model developed in this thesis is carried out for space discretization of the membrane surface and for time discretization. The number of elements of a membrane mesh, created by Loop subdivision, quadruples once a subdivision is applied. Therefore, our code becomes very slow (and impossible in practical case) for a vesicle with four subdivisions (resulting 5120 elements) from an icosahedron. Thus, in this section, in order to show the convergence, the droplet will be chosen as the deformable particle flowing in the microchannel. At the same time, the influence of the number of elements for a vesicle will also be shown.

The effects of space discretization of the membrane are studied with a drop flowing along the centerline of a capillary ($Ca = 0.05, \beta = 0.8$), as shown in Figure 2.18. First, evolution of

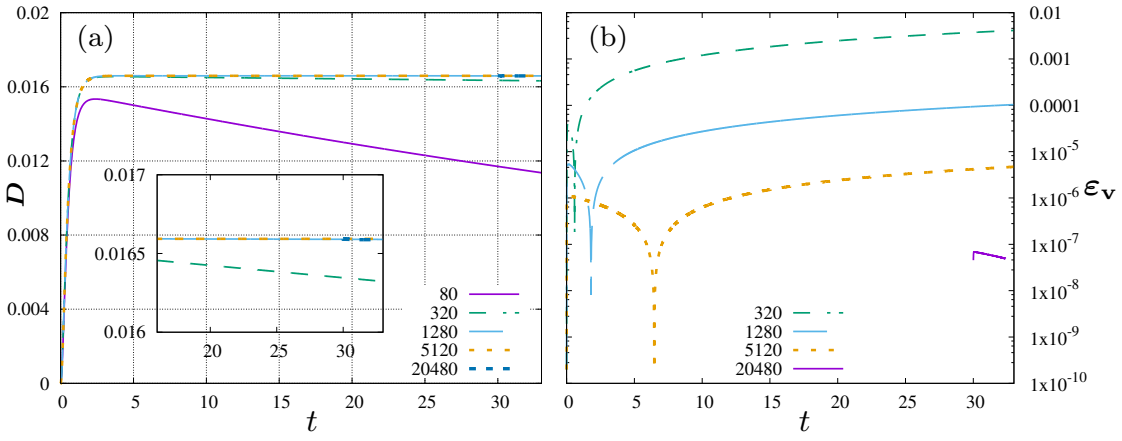

Figure 2.18: Evolution of (a) the Taylor parameter D and (b) the relative error of the enclosed volume $\varepsilon_v = V/V_0 - 1$ of a drop in a capillary flow ($\mathrm{Ca} = 0.05,\ \beta = 0.8$) as a function of time, for different number of elements. A case with 20480 elements is refined from the case with 5120 elements. Inset shows a zoom-in of the Taylor number. RKF45 is used in all these cases for time stepping.

the Taylor parameter[15] $D = \frac{L-l}{L+l}$ is plotted, in Figure 2.18 (a), as a function of dimensionless time for various number of elements, which is varied from 80 to 20480. For the first four cases, the spherical drop is used as the initial form, while the case with 20480 is launched from an existing state of the case with 5120 elements. Inset shows a zoom-in of the Taylor

[15] where L and l are semi-axis of the ellipsoid having the same tensor of inertia.

parameter except for the coarsest case (with 80 elements). It is showing the difference on D becomes rather small except for the coarsest case.

The influence of mesh discretization is further studied for the four cases which give consistent results, by inspecting the relative error of the enclosed volume $\varepsilon_v = \frac{V(t)-V_0}{V_0}$, as shown in Figure 2.18 (b), where V_0 is the initial volume for each case. This figure shows that multiplying the number of elements by four (one subdivision) allows more than one order of magnitude gaining in volume conservation. For example, the relative error is about 0.4% after a dimensionless time of $t = 30$ for the case with 320 elements, a quite acceptable result.

The convergence order of space discretization is then estimated with the relative error of the Taylor parameter $\epsilon = \frac{D-D_{\text{ref}}}{D_{\text{ref}}}$, where D_{ref} is the reference Taylor parameter given by the case with 20480 elements. This error is represented as a function of the number of elements in Figure 2.20 (a), which is second order in number of elements $O(N^{-2})$. It's shown, by Boedec et al [22], that this second-order convergence is not affected by the inclusion of bending rigidity for a Capsule flowing in a linear shear flow. This also gives us the vision of having a second-order convergence for a vesicle flowing in a capillary, even if we do not conduct such numerical study.

Now, the effects of temporal discretization are also considered for a drop as above, with 1280 elements and with the conditions $Ca = 0.05$ and $\beta = 0.8$. As shown in Figure 2.19,

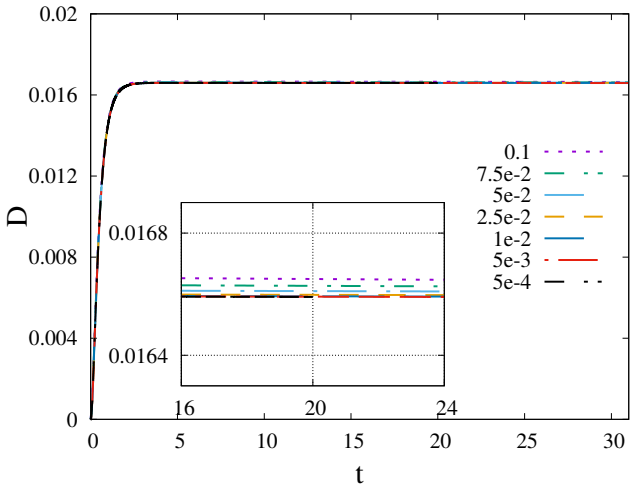

Figure 2.19: Evolution of the Taylor parameter of a drop (with 1280 elements) flowing in a capillary flow (Ca $= 0.05$, $\beta = 0.8$) as a function of time, for different time steps. Inset shows a zoom-in of the Taylor number. The implicit fixed time step trapezoidal scheme is chosen.

the evolution of the Taylor parameter is plotted against the dimensionless time for different time steps $\Delta t = 0.1,\ 0.075,\ 0.05,\ 0.025,\ 0.01,\ 5E\text{-}3$, and $5E\text{-}4$, with the implicit fixed time step trapezoidal scheme. The difference is very small and can only be seen in zoom-in plots.

Similar to the estimation of the convergence order of space discretization, using the result obtained with $\Delta t = 1E\text{-}4$ as the reference Taylor parameter, the convergence order of temporal discretization is also plotted as a function of time steps, as in Figure 2.20 (b). As expected, the relative error of the Taylor parameter converges as $O(\Delta t^2)$ when using the

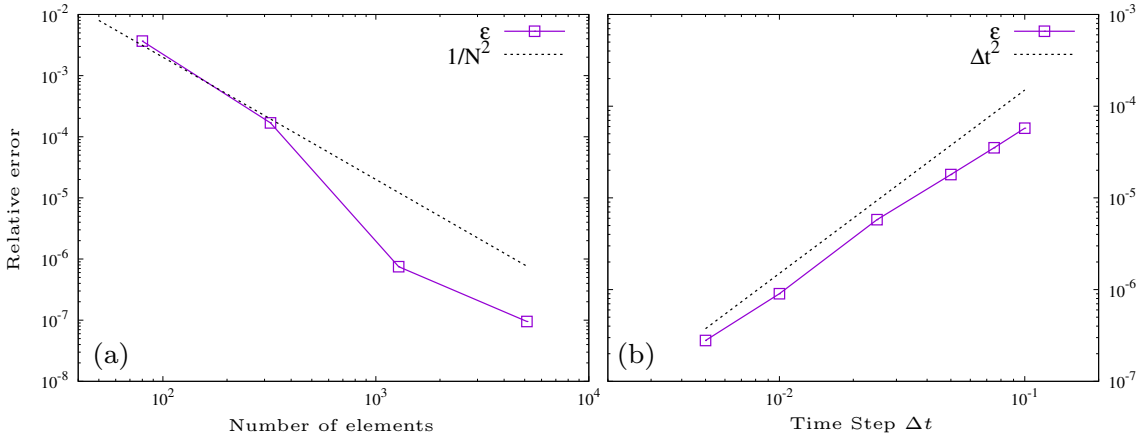

Figure 2.20: Convergence study of the numerical algorithm: relative error on the steady state value of the Taylor parameter of a drop in a capillary flow ($\mathrm{Ca} = 0.05,\ \beta = 0.8$) with respect to (a) the number of elements and (b) the time step size. For spatial convergence (a), the RKF45 scheme is used, and the reference value is computed with 20480 elements. For temporal convergence (b), the trapezoidal scheme is used, the drop is discretized by 1280 elements, and the reference value is computed with a time step $\Delta t = 5e - 4$.

trapezoidal scheme.

A second-order convergence is shown for both the discretization of the membrane and the discretization of time by a droplet flowing along the centerline of a capillary. The previous study shows that this convergence will not degrade by adding a bending rigidity to the Capsule membrane [22]. As aforementioned at the beginning of this subsection, simulation of a vesicle with four subdivisions is not practical, but the influences of the number of elements are compared and shown in Figure 2.21 for a little deflated vesicle ($\nu = 0.9$) flowing in a microchannel with $Ca = 1$ and $\beta = 0.2$.

The evolution of the inclination angle θ with axis of the flow is displayed in Figure 2.21 (a) as a function of the dimensionless time t for three different numbers of element: 80, 320, and 1280. We have observed that the difference between the case with 320 elements and 1280 elements becomes imperceptible, but the result obtained with 80 elements shows a remarkable difference compared to the two finer cases. It is clear that the result with 80 elements can be questionable as the relative volume error reaches to $\sim$ 7% at the dimensionless time $t = 25$, while those for the two finer cases are less than 0.2%.

This test may also suggest that for a vesicle with $\nu \geq 0.9$, the results obtained with 320 elements should, in general, be reliable.

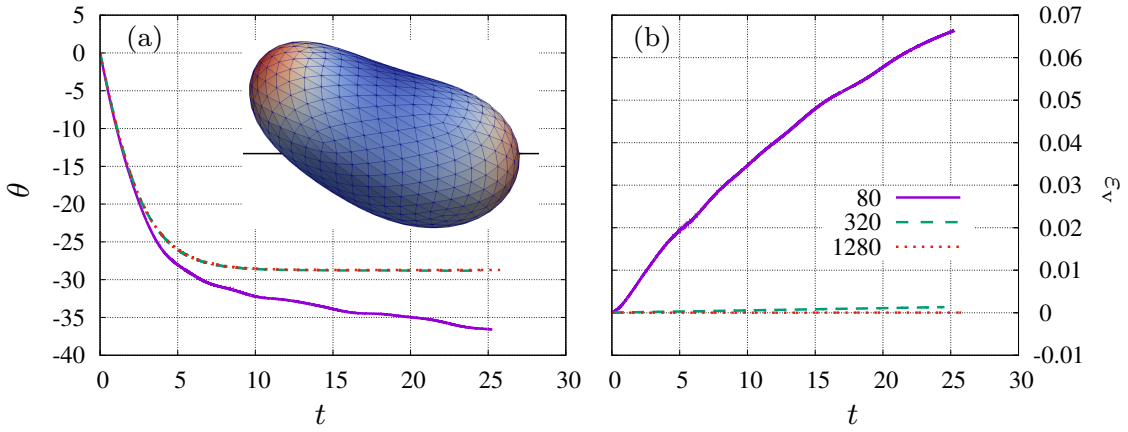

Figure 2.21: Evolution of (a) the inclined angle θ (in degree) and (b) the relative error of the enclosed volume ε_v of a vesicle flowing in a microchannel ($Ca = 1, \nu = 0.9, \beta = 0.2$) as a function of the dimensionless time, for three different numbers of element: 80, 320 and 1280. The inset displays a stable shape, colored by the mean curvature, obtained with 1280 elements, where the axis of the microchannel is indicated by the solid black line.

2.6 Summary

In this chapter, first, the subdivision scheme is introduced, which is used to discretize and present the membrane (i.e., its position $\boldsymbol{x}$). This scheme can also be used for the channel mesh, although we do not need to evaluate derivative on this mesh, sec. 2.1.

Then the membrane force density is obtained, using the subdivision formulation, by solving the linear system derived from the finite element method, sec. 2.2. The force density $\boldsymbol{f}$ obtained is highly reliable except for the initial 12 irregular vertices of the icosahedron, which increase the global error [68].

The procedure for calculating the membrane velocity $\boldsymbol{u}$ of a deformable particle flowing in a channel is presented in Section 2.3. This procedure is also based on the subdivision method. Whereas the time stepping schemes, for $\partial_t \boldsymbol{x}$, are presented in Section 2.4.

Finally, verification and validation for the procedure are presented. We, first, verify our numerical procedure by checking its consistency in varying the mesh of the channel (cases without external boundaries have already done in [22]). We, then, validate this procedure by two benchmarks, one for the drop and the other for the capsule. The convergence is also shown, with the drop and vesicle, in the last example of Section 2.5.

3 Motion and Shape Transition of 3D Vesicles in Confined Flows

3.1 Introduction

Vesicles are large membrane 'bubbles' formed by bending and closing up a bilayer of lipid molecules, suspended in a fluid that can be either the same solvent as the inner or different [138]. This bilayer is often in a liquid phase at room temperature and has a fixed number of lipids which makes the vesicle highly deformable, while its membrane surface is conserved, both locally and globally. The semipermeability of the membrane helps to maintain the enclosed volume unchanged on a time-scale of several hours, which is much longer than the typical experimental time-scale of about 10 to 15 minutes. The vesicle volume can thus be considered as constant [3]. Since its volume V and surface area A are both constant, the non-sphericity is measured by a non-dimensional number, the reduced volume $\nu = 6\sqrt{\pi}VA^{-3/2} \leq 1$.

Vesicles have been, and remain, the subject of extensive studies not only due to their resemblance to anucleate cells such as red blood cells (RBCs) but also because of their importance in different industries such as pharmaceutical carriers [149]. Aspherical vesicles can exhibit, in an external flow, an amazing variety of shapes (parachute, bullet, peanut, croissant, and slipper) [3, 32, 80] and different types of dynamical behavior (tank-treading, tumbling, trembling, and cross-streamline migration) [3, 49, 77, 79, 112, 118]. The study on these behaviors is important to understand the suspensions of deformable particles, such as blood. Thus how a single vesicle behaves in an external flow is significant, but the analysis is rather challenging. This is due to the coupling between the vesicle deformation and the flow that leads to a free-boundary hydrodynamic problem, where the vesicle shape is not given a priori but is determined dynamically from a balance between interfacial forces and fluid stresses [76].

The behaviors of a single vesicle in simple shear flow have been studied experimentally[1, 76, 77], theoretically[35, 82, 92, 93, 112, 117, 137], and numerically with boundary integral method[17, 21, 22, 158] or immersed boundary method[84], and with mesoscale techniques[115, 117]. All the three approaches have identified the three basic dynamical behaviors, namely tank-treading (the fluid membrane rotates as a tank tread about a fixed orientation angle), tumbling (vesicles flipping periodically in the shear plane) and trembling (also called vacillating-breathing, an intermediate regime between tank-treading and tumbling, where vesicles tremble while its long axis oscillating around the flow direction) in shear flow. Analytical models

are either based on the Keller-Shalak (KS) theory[82], which assumes vesicles have fixed ellipsoidal shape, or the perturbation theory [45], which are limited to quasi-spherical vesicles ($\nu \approx 1$) under simple boundary conditions. Here, we are interested in a single fluid vesicle, from quasi-spherical to quite deflated, flowing in microchannels of different sizes.

Two major concerns for vesicles in Poiseuille flow are the lateral migration[33, 48, 49, 78] and the shape evolution[32, 47, 49, 80]. A single aspherical vesicle in Poiseuille flow may deform and break its upstream-downstream symmetry due to (i) the shear flow close to solid boundaries[33, 48, 79] and (ii) non-constant shear gradient[33, 48, 78, 80]. As a result of the symmetry breaking (for example a slipper), vesicles undergo cross-streamline migration. Numerical studies in these directions are mostly in two-dimensional or unbounded three-dimensional cases. Three-dimensional simulations are very resource consuming[49, 79], especially for vesicles with small reduced volume. The direct inclusion of the wall is a necessary step to mimic the realistic RBC dynamics in capillary since the effects of the walls and the flow curvature are coupled in a nonlinear manner[33, 79].

In this chapter, shape transition and migration of three-dimensional vesicles in a confined Poiseuille flow are numerically studied with the method coupling BEM and FEM (refer to Chapter 2 for details).

3.2 Problem formulation

A vesicle flowing in a bounded Poiseuille flows (Eq. (1.19))

$$\boldsymbol{u}^{\infty} = U_m \left(1 - \frac{y^2 + z^2}{R_t^2}\right) \boldsymbol{e}_x$$

with matched viscosity ($\lambda = 1$) of inner and outer fluids (refer Figure 2.1 and 2.6) is a fluid structure interaction (FSI) problem with deformable interface (refer Section 1.3).

Vesicles immersed in an external flow suffer stresses, which can lead to deformations. These deformations of the two-dimensional incompressible membrane interface which can resist bending are modeled by the Helfrich energy with a Lagrange multiplier (γ), Eq. (1.11). The surface density of force exerted by the membrane of vesicle $\boldsymbol{f}^m$ onto surrounding fluids is given by Eq. (1.12)

$$\boldsymbol{f}^m = \kappa\big[2\Delta_s H + 4H(H^2 - K)\big]\boldsymbol{n} - 2\gamma H\boldsymbol{n} + \boldsymbol{\nabla}_s\gamma.$$

Due to the length and time scales involved, the inertia can be neglected, and therefore the hydrodynamic flows fall into the Stokes flow regime (Eq. (1.7))

$$-\boldsymbol{\nabla}p + \eta\Delta\boldsymbol{u} = \boldsymbol{0}, \quad \boldsymbol{\nabla}\cdot\boldsymbol{u} = 0.$$

Since the viscous effects are much faster than a moving boundary can change its position ($Re \ll 1$), the fluid rapidly, or instantaneously in the ideal limit, establish a velocity distribution for a given geometry of the boundaries [145]. Thus, the coupling conditions of

velocities and stresses between the hydrodynamic flow and the membrane can be applied, as presented in Section 1.3.3.

This flow problem is characterized by three dimensionless parameters (refer Section 1.3.4),

- the reduced volume $\nu = 6\sqrt{\pi}VA^{-3/2}$, which quantifies the geometric ability of the vesicle to deform,
- the confinement $\beta = R/R_t$, which is the ratio of the vesicle size $R = (3V/4\pi)^{1/3}$ and the radius of the microchannel R_t,
- the Capillary number $Ca = \frac{\eta\alpha R^4}{\kappa}$, which is the ratio of the flow stress and the bending force density, where $\alpha = \frac{U_m}{R_t^2}$ is the flow curvature.

To complete the presentation of this boundary value problem with the evolution of the membrane, initial conditions must also be provided. In this chapter, vesicles are initially given in the form of *prolate* (Figure. 3.1 (a)) or *oblate* (Figure 3.1 (b)) characterized by the reduced volume ν. These vesicles are initially released at a height H_0 away from the flow axis

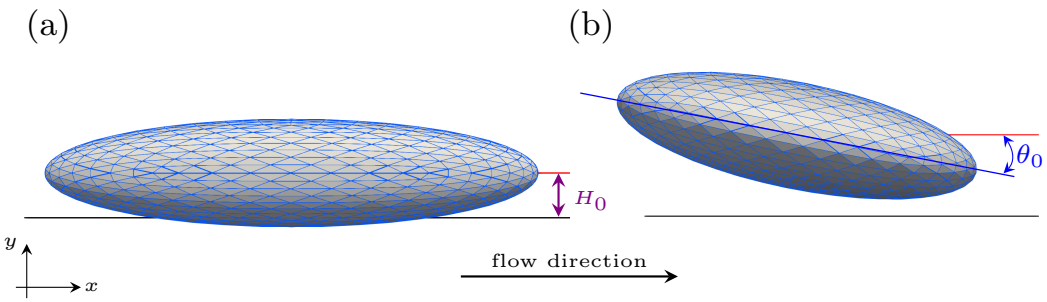

Figure 3.1: Vesicle with $\nu = 0.65$ in the form of (a) prolate and (b) oblate. Black and red solid lines indicate the flow axis and the line $y = 0$ that passes through the centroid of the vesicles, respectively. H_0 is the initial position of the vesicle measured from its centroid to the axis of flow. θ_0 is the initial inclined angle compared with the flow direction.

and with an inclination angle θ_0 with the direction of flow, as shown in Figure 3.1.

3.3 Results and discussions

In this section, the analysis is done for the vesicles discretized with 1280 Loop elements unless otherwise stated. The initial position of the centroid of the vesicle is given with $(0, H_0, 0)$, and the flow is in x direction (Figure 3.1). The implicit trapezoidal time stepping scheme is used to update the shape of the vesicles.

3.3.1 Kinematics: lateral migration

Unlike a neutrally buoyant rigid spherical particle, which can not migrate in the direction transverse to the flow lines when immersed in a creeping flow, an initially centrosymmetric and deflated vesicle has the ability to migrate cross-streamline at vanishing Reynolds number provided that the symmetry of the Stokes flow is broken [48, 60]. Highly deformable vesicles flowing in a confined Poiseuille flow may deform due to the complex interplay between its membrane, the wall, and the Poiseuille flow, which in turn leads to upstream-downstream asymmetry of the vesicle.

Cross-streamline migration under flow plays a key role in suspensions of soft matter, and therefore in several industrial and medical applications. Such as the Fåhræus-Lindqvist effect in the blood flow, which is the result of lateral migration. A vesicle placed away from the centerline of the Poiseuille flow can migrate either towards the center, or outwards until it reaches a wall, or stop at an intermediate position [48]. In this subsection, the kinematics of cross-stream migration of an initially off-center prolate vesicle ($H_0 \neq 0$ and $\theta_0 = 0$) in a confined Poiseuille flow ($Ca = 1$) are presented.

Inward migration

Figure 3.2 shows an example of inward migration. As shown in Figure 3.2(a), an initially prolate vesicle (①) released at height $H_0 = 0.05$ migrates to the center of the flow with a bullet shape (⑧) at the end, and its centroid performs a damped oscillation around the center of the microchannel.

More specifically, starting from an initial prolate state, the vesicle quickly deforms to a slipper shape with its major axis aligned with the flow profile. This asymmetrical shape will only be slightly deformed during its migration to the flow center (②). When the vesicle arrives at the flow center, it keeps on moving due to the asymmetricity of its shape. When the vesicle is located below the flow center, it starts to re-deform in order to adapt the inverse flow profile. An almost symmetrical shape is obtained at the lowest position (③), this state is not stable because the flow at this position (observed from the centroid of the vesicle) is not symmetrical. Thus it continues to deform and adpts a new asymmetrical shape with its major axis, once again aligns the flow profile (④). This deformation to align the flow profile is accompanied by an inward migration (but with an inverse direction in comparison with the former one). As before, it will continue moving when it reaches the flow center for the second time (④). The vesicle will continue this inward and outward migration but with gradually reduced strength (⑤, ⑥ and ⑦) until it attains the stable state, a symmetrical bullet with $\mathrm{Y_G} = 0$ (⑧).

Figure 3.2(b) shows the lateral migration velocity U_y as a function of Y_G, with the initial state indicated by a blue dot. It is shown that both U_y and Y_G decrease with time, and converge to the point $(0, 0)$, which has vanished shear rate. The red triangles, which correspond to the states with relative extreme values of the radial position Y_G (as ③, ⑤, ⑥ and ⑦ in Figure 3.2(a)), represent the states having zero instantaneous velocity and almost symmetrical shapes, but these states are not stable and can be broken by the surrounding flow.

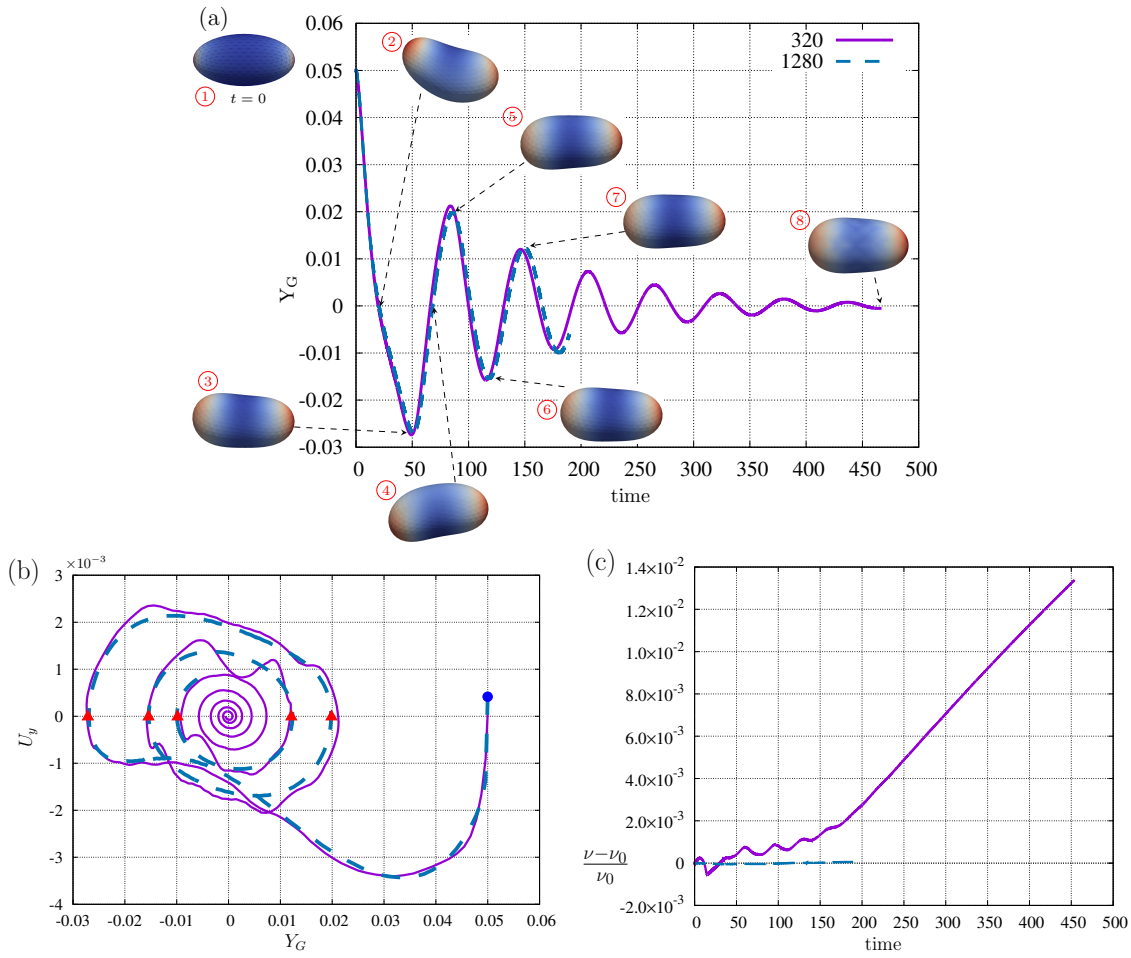

Figure 3.2: The dynamics of deflated vesicles ($\nu = 0.9$) in a microchannel ($R_t = 1/\beta = 3$), for the meshes with 320 and 1280 elements. (a) The instantaneous radial height Y_G of the centroid of the vesicle as a function of dimensionless time, the insets (Oxy plane) are instantaneous vesicle shapes during the migration, colored by the mean curvature of the membrane. (b) Evolution of the migration velocity U_y as a function of Y_G, the blue dot indicates the initial state. (c) Evolution of the relative variance of the reduced volume ν.

Figure 3.2(c) shows the relative variance of the reduced volume as a function of time. It is shown that the case with finer mesh accumulates much smaller error than the coarse one. For the case with 320 elements, the gradual increase in error may interpret the discrepancy appeared in Figure 3.2(a), namely, the gradually increasing phase difference between these two curves. Here, we observed an inward migration with oscillation, but it can also, without surprise, be a migration without oscillation, such as the example presented in Figure 3.6.

Centered snaking

As for the dynamics of a vesicle in a confined flow, the term *snaking* may be introduced by Kaoui et al. [79], for the first time. This dynamic of motion corresponds to the motion where the centroid position oscillates periodically over time, as shown in Figure 3.3(a). In their works, both the centered (where the mean value of Y_G is zero) and the off-centered (where the mean value of $Y_G \neq 0$) snaking are observed for a highly deflated vesicle ($\nu = 0.6$), in the two-dimensional simulation.

Figure 3.3 shows a centered snaking for (i) $\nu = 0.85, R_t = 2.8$ and (ii) $\nu = 0.8, R_t = 2.5$. For the case (i), the simulation is first launched with 320 elements, and the mesh is refined to 1280 elements at $t \approx 500$. Neither like the inward migration, for which vesicles finally adopt an axisymmetric form and remain on the axis of the channel (such as the bullet shape), nor the migration to an off-center position, for which the stable vesicles take a slipper shape and its centroid is radially displaced from the flow axis, the centroid of vesicles varies periodically during the snaking motion, as shown in Figure 3.3(a), like the locomotion of snake. The insets show some typical instantaneous vesicle shapes, which are very similar to those obtained by Kaoui et al. [79, Fig.3]. In coherence with Figure 3.2, the vesicle is much deformed when it passes through the axis of the microchannel than when it reaches its extreme position.

Figure 3.3(b) shows the evolution of the migration velocity U_y as a function of Y_G, which is also termed as Poincaré map [23]. We found that once the oscillation becomes stable, these maps are very similar, like that reported by Boujja et al. [23, Fig. 2(d)] for $\nu = 0.6$ and $\beta = 0.55$. Figure 3.3(c) shows the variance of the angle of inclination θ, like that of the centroid position Y_G, which varies periodically.

Migration to an off-center position

As reported by Kaoui et al. [80], the initially axisymmetric vesicles flowing in a symmetric two-dimensional unbounded Poiseuille flow may have asymmetric stable shapes, called *slipper*, with their center of gravity deviated from the flow axis. We confirm this by a fully three-dimensional simulation, as shown in Figure 3.4, an example of migration to the final stable position located away from the flow center, $\mathrm{Y_g^*} \approx 0.047$. In this thesis, the centroid position of a stable slipper Y_g^* is meaningful in the following sense, when a vesicle is initially placed at a height H_0, it migrates inwards and stops at some position, and this position has height Y_g^*. This inward migration does not conclude that H_0 must larger than Y_g^*, actually,

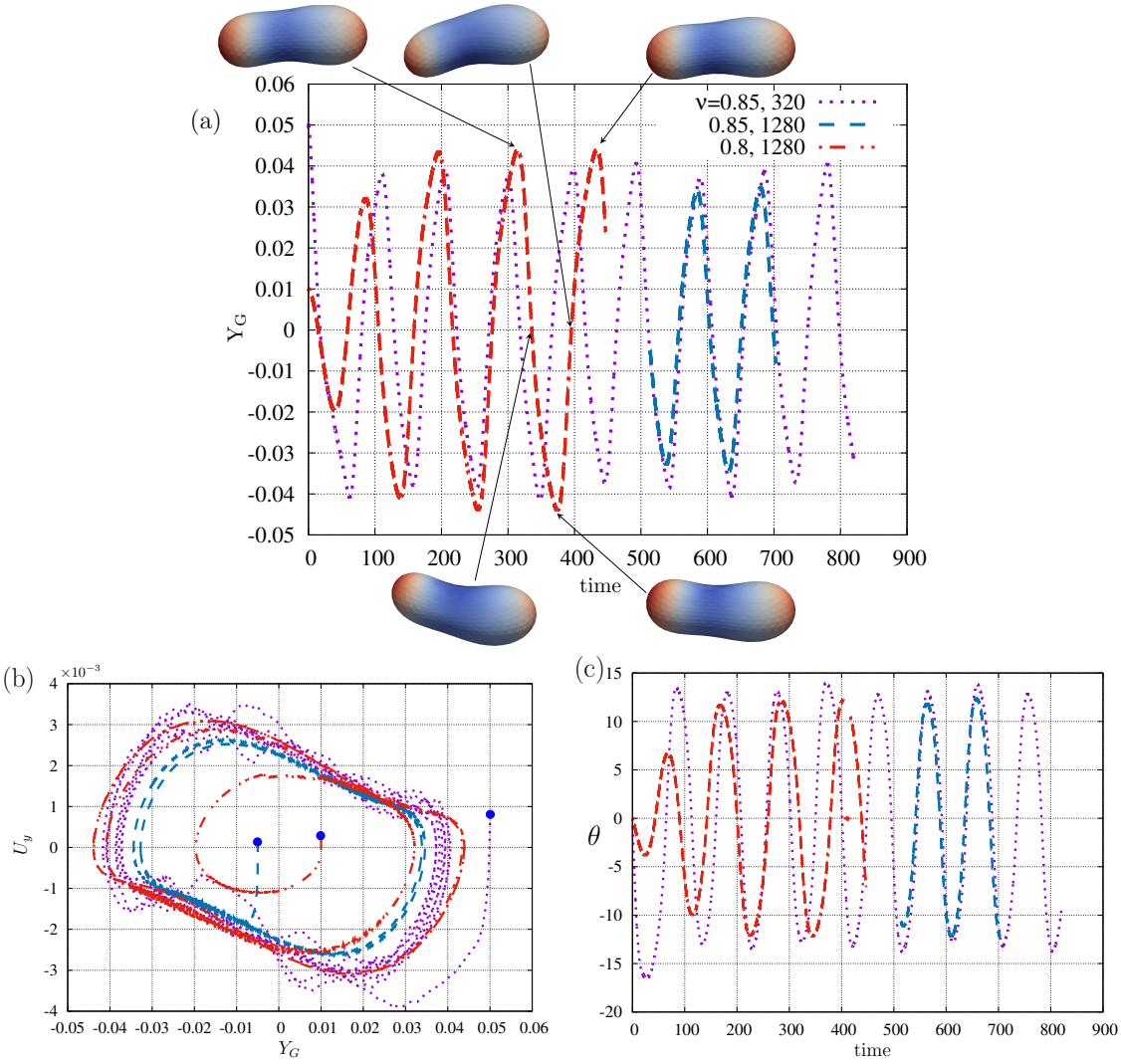

Figure 3.3: The dynamics of deflated vesicles in a microchannel for three different cases: (1) $\nu = 0.85$, $R_t = 2.8$, 320 elements; (2) $\nu = 0.85$, $R_t = 2.8$, 1280 elements; (3) $\nu = 0.8$, $R_t = 2.5$, 1280 elements. (a) The instantaneous radial height Y_G as a function of dimensionless time, the insets (Oxy plane) are instantaneous vesicle shapes during the migration for $\nu = 0.8$. (b) Evolution of the migration velocity U_y as a function of Y_G, the blue dots indicate the initial states. (c) Evolution of the inclination angle θ (in degree) of the major axis of the vesicle relative to the axis of flow.

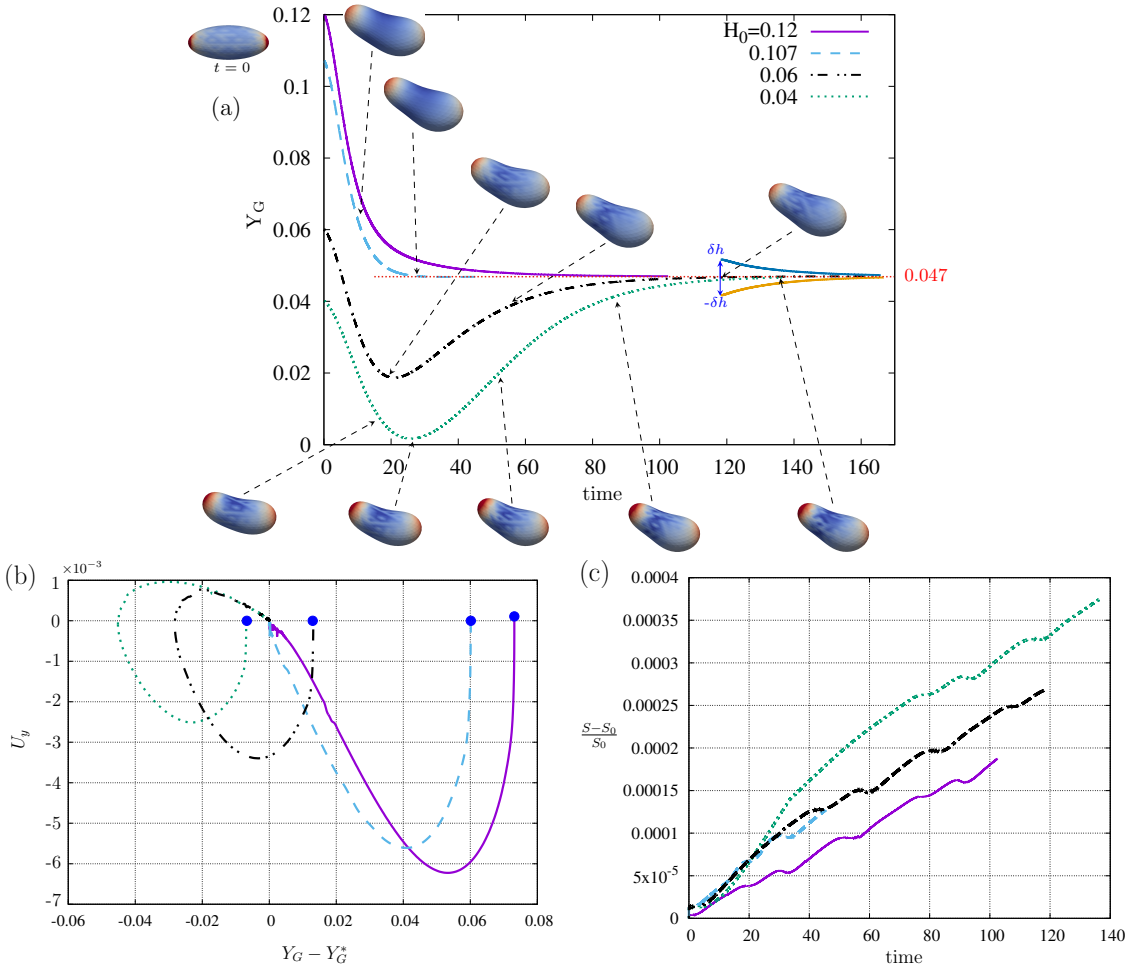

Figure 3.4: The dynamics of deflated vesicles ($\nu = 0.85$) in a microchannel ($R_t = 3$) with different initial heights $H_0 = 0.12, 0.107, 0.06$ and 0.04. (a) The instantaneous radial height Y_G as a function of dimensionless time, the final stable position Y_G^* is indicated by the horizontal red dotted line. The insets (Oxy plane) are instantaneous vesicle shapes during the migration. (b) Evolution of the migration velocity U_y as a function of the distance measured from the centroid to the final stable position. (c) Evolution of the relative variance of the membrane area.

a vesicle initially placed at a position $H_0 < Y_g^*$ can migrate first inwards then outwards, eventually reaches the same stable position, as shown in Figure 3.4(a).

In Figure 3.4(a), the prolate vesicles are initially released at four different heights H_0. For the case with $\mathrm{H_0}$ close to $\mathrm{Y_g^*}$ (0.04 and 0.06), the vesicle first migrate inwards and then outwards. The one with $\mathrm{H_0} = 0.107$ which is greater than $\mathrm{Y_g^*}$, merely experiences the inward/outward oscillation before fast reaching to the stable state. If the initial height is even larger ($H_0 = 0.12$), a vesicle migrates inwards without experiencing oscillation, but the migration is rather slow when it is closed in the stable position Y_g^*. Whereas all these three cases share the same final state, an off-center slipper. This asymmetric stable state is thought to be the common result of the complex interplay of flow curvature, the wall, and membrane forces [48, 60]. What's more, given a positive or negative positional perturbation on a stable state with strength $\delta h = 0.005$, the off-stable state vesicle will move back to the original stable state. All the shapes shown in the insets, unlike those of Figure 3.2(a), experience the same direction of inclination, since Y_G is always greater than zero.

Figure 3.4(b) shows the lateral migration velocity U_y as a function of $Y_g - Y_g^*$, with the initial states are indicated by the blue dots. The slope represents the acceleration, as they approach the final stable position; the case with $H_0 = 0.107$ has bigger acceleration (in absolute value) than the three others. We are audacious to say that a vesicle with $H_0 \in [0.04, 0.12]$, while with other parameters remain unchanged, the final stable state is a slipper with $Y_G^* = 0.047$, and there should be an initial height H_0^c from which the vesicle can reach the stable position most quickly.

Figure 3.4(c) shows the relative variance of the membrane area, in the dynamics for different initial heights $\mathrm{H_0}$. For all the cases, the relative variances of the area are less than 0.1%, suggests that the constraint of surface incompressibility is well preserved.

3.3.2 Morphology: possible stable shapes

Because of the interplay between the vesicle shape and the external flow, vesicles flowing in the microchannel bear a rather rich set of morphologies, which vary from the full axisymmetric shape (such as the bullet) to the off-centered nonsymmetric one (such as the slipper). Here, all observed stable shapes are classified by the number of planes of symmetry, that is, ∞-, two- and one-plane of symmetry. In this analysis, the initial inclination angle θ_0 is set to zero unless otherwise stated.

Infinity planes of symmetry

Stable shapes that have infinite planes of symmetry are axisymmetric, which includes bullet shape, parachute shape, and peanut shape. Figure 3.5 shows a case that attains a stable *bullet* shape, an axisymmetric form with a convex rear end, under given parameters, $Ca = 3, \nu = 0.9, R_t = 2.0$ and $H_0 = 0.03$. The prolate vesicle is initially placed at $H_0 = 0.03 \ll R_t$, which is very close to the center of the flow; at first, it migrates inwards to the center and crosses the centerline with a slipper shape. This slipper shape continues the lateral migration until a position with a maximum negative height Y_G is reached, here the vesicle resumes

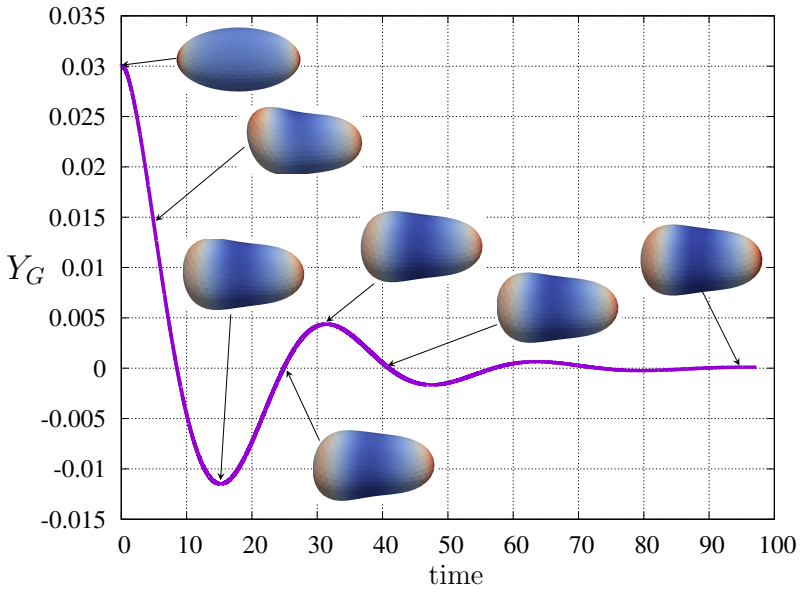

Figure 3.5: Evolution of the centroid Y_G for $Ca = 3, \nu = 0.9, R_t = 2.0$ and $H_0 = 0.03$. The insets (Oxy plane), colored by mean curvature, present the instantaneous shapes, starting from a prolate form and it becomes a stable bullet form at the end of the simulation.

an axisymmetric shape. This axisymmetric shape re-enters the migration in the direction opposite to the previous one and with a smaller amplitude. The evolution of the centroid Y_G behaves thus like a damped oscillation.

Figure 3.6 shows a case that has a stable *parachute* shape, an axisymmetric form with a concave rear end, under given parameters, $Ca = 50, \nu = 0.9, R_t = 6.0$ and $H_0 = 0.05$. Starting from a prolate shape, the case presented here does not enjoy the oscillation process, and it becomes a parachute shape whose axis coincides with that of the flow.

The last observed axisymmetric shape, the *peanut*, is shown in Figure 3.7 under given parameters, $Ca = 1, \nu = 0.7, R_t = 1.5$ and $H_0 = 0.0$. Peanut is an axisymmetric shape with its two ends larger than the middle part. It can be a generalization of the dumbbell shape since the two ends usually have different size. Starting from a prolate form, initially placed at $H_0 = 0.0$, the volume of the stout middle part is first transferred symmetrically to the rear and the front. And then a neck part occurred which separates two convex ends with different sizes.

Two planes of symmetry

The shape with two planes of symmetry is the one with the two perpendicular planes of symmetry, and the line of intersection of these two planes coincides with the axis of the microchannel.

The first one reported here is called the *croissant* [49], as shown in Figure 3.8, for which the rear end is convex in one direction but concave in the perpendicular one. Figure 3.8 shows the evolution of the centroid Y_G and the geometric parameter $D_2 \equiv \frac{L_2 - L_3}{L_2 + L_3}$ (the relative difference of the two major axes in the plane perpendicular to the flow direction) as a

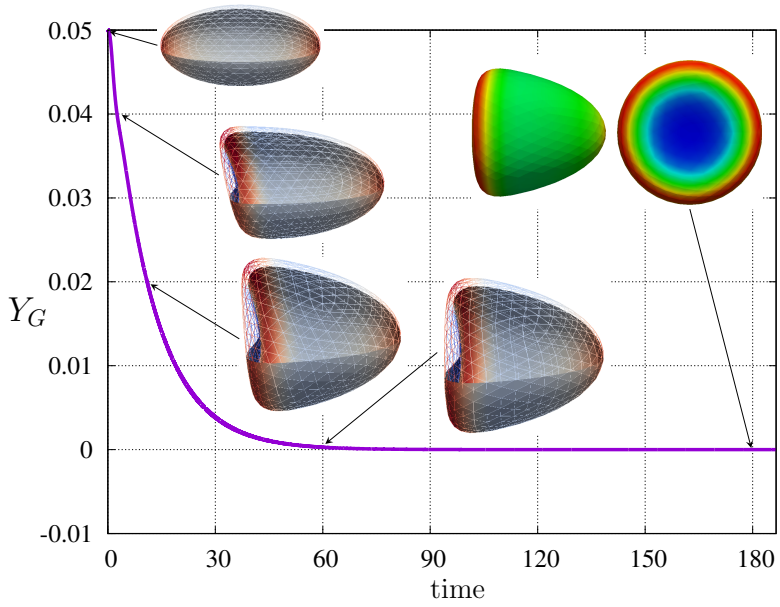

Figure 3.6: Evolution of the centroid Y_G for $Ca = 50, \nu = 0.9, R_t = 6.0$ and $H_0 = 0.05$. The insets (side view in the Oxy plane and rear view in the Oyz plane), colored by mean curvature, present five instantaneous shapes, starting from a prolate form and it becomes a stable parachute form at the end of the simulation.

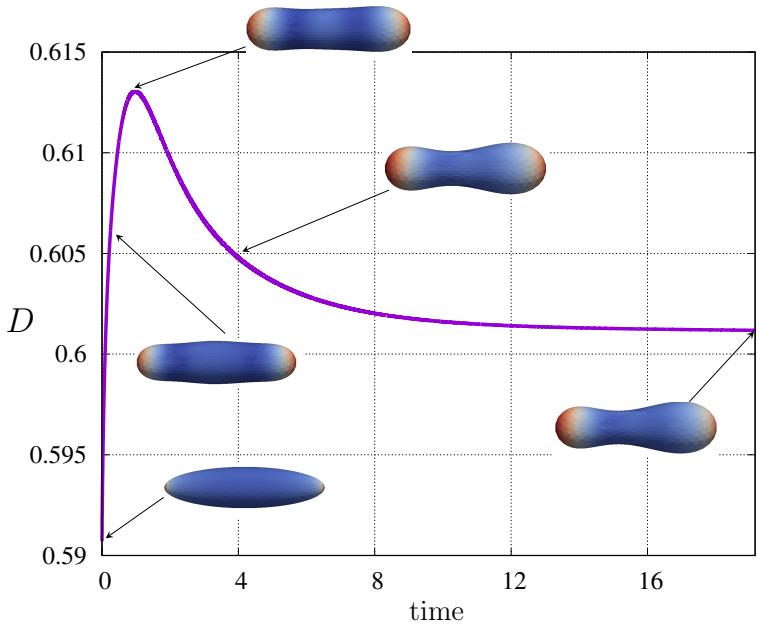

Figure 3.7: Evolution of the Taylor parameter D for $Ca = 1, \nu = 0.7, R_t = 1.5$ and $H_0 = 0.0$. The insets (Oxy plane), colored by mean curvature, present five instantaneous shapes, starting from a prolate form and it becomes a stable peanut form at the end of the simulation.

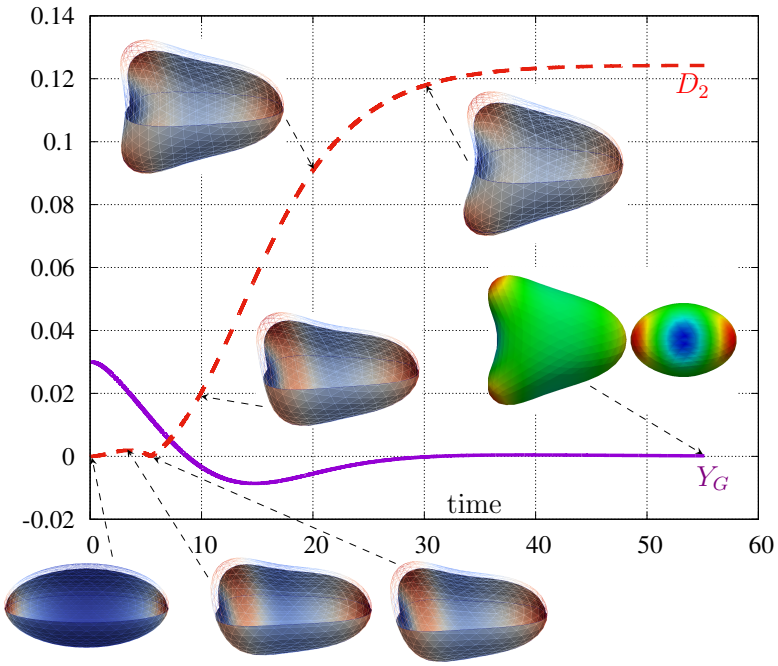

Figure 3.8: Evolution of the centroid Y_G and geometric parameter D_2 for $Ca = 5, \nu = 0.9, R_t = 2.5$ and $H_0 = 0.03$. The insets (side view in the Oxy plane and rear view in the Oyz plane), colored by mean curvature, present the instantaneous shapes, starting from a prolate form and it becomes a stable croissant form at the end of the simulation.

function of dimensionless time, under given parameters, $Ca = 5, \nu = 0.9, R_t = 2.5$ and $H_0 = 0.03$. The geometric parameter $D_2 \equiv \frac{L_2 - L_3}{L_2 + L_3}$, like the Taylor parameter $D \equiv \frac{L_1 - L_2}{L_1 + L_2}$, is used to characterize the deformation in the plane perpendicular to the flow direction, where L_2 and L_3 are the length of the two major axes in the plane perpendicular to the flow.

Similar to Figure 3.5 and 3.6, the initial prolate vesicle, placed at an off-center position with $H_0 = 0.03$, deforms first to a slipper form during its lateral migration to the center of the flow. While the transition from the slipper shape to the croissant shape is achieved mainly during the inverse lateral migration from the maximum negative position to the flow center. All snapshots are colored with the mean curvature, while the last one is mapped with a different color scheme, called blue to red rainbow, to emphasize extreme values of the mean curvature (also in the previous Figure 3.6).

Another example of two planes of symmetry is shown in Figure 3.9, which is characterized by two concave regions in its two flatter surfaces. It is a combination of the biconcave disk shape and the croissant shape, we may term it here as *biconcave-croissant* shape. This kind of form is only observed for highly deflated vesicles (for example, $\nu = 0.65$ and $\nu = 0.6$ in our ever launched simulations) having an initial oblate shape.

Figure 3.9(a) shows the centroid Y_G and the geometric parameter D_2 as a function of dimensionless time, under given parameters, $Ca = 1, \nu = 0.6, R_t = 3.0, H_0 = 0.35$ and $\theta_0 = -7°$. The oscillation of Y_G is quickly damped out, and its centroid locates on the flow axis for $t > 100$. Figure 3.9(b) shows the evolution of the inclination angle between the major axis and the axis of the microchannel. From the last snapshot, we observe that the two

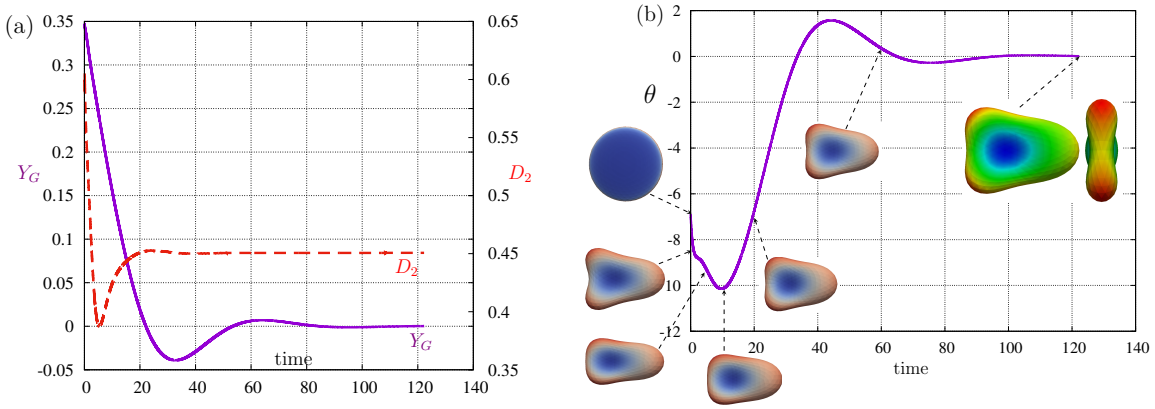

Figure 3.9: Evolution of (a) the centroid Y_G, geometric parameter D_2 and (b) the inclination angle θ for $Ca = 1, \nu = 0.6, R_t = 3.0, H_0 = 0.35$ and $\theta_0 \approx -7°$ (or -0.12 rad). The insets (top view in the Oxz plane and rear view in the Oyz plane), colored by mean curvature, present the instantaneous shapes, starting from a oblate form and it becomes a stable biconcave-croissant form at the end of simulation.

planes of symmetry are perpendicular and that the intersection of these two planes coincides with the axis of the flow, like those for the croissant shape.

One plane of symmetry

The slipper shape in the cylinder channel has one plane of symmetry. For a vesicle initially placed at a position H_0 (assumed in the y direction), and in a flow in the x direction, this plane of symmetry is Oxy, as shown in Figure 3.1.

As pointed out by Kaoui, Biros, and Misbah [80], a slipper shape is accompanied by a tank-treading membrane, and thus by flow circulation inside the vesicle, which means a slipper is not favored from the point of view of dissipation. They also show that the establishment of a slipper will help reduce the difference between the vesicle velocity and that of the bare imposed flow. As a consequence, the slipper becomes a favorable shape.

Figure 3.10 shows a stable slipper shape with two different initial configurations: a prolate ($H_0 = 0.555$ and $\theta_0 = 0$) and an oblate ($H_0 = 0.6$ and $\theta_0 \approx -11.5$), under given conditions, $Ca = 1, \nu = 0.7$ and $R_t = 6.0$. Figure 3.10(a) shows the evolution of the centroids Y_G, which converge to a common value $Y_G^* \approx 0.508$, as indicated by the dashed black line. When a vesicle approaches the stable position, the migration velocity decreases rapidly, as shown in Figure 3.4(b). In order to decrease the time required to reach the steady state, we dynamically update the lateral position according to the current migration velocity U_y. For example, in this case, when $U_y > 0$, we update the new centroid value of the vesicle by adding a small positive number, as shown in Figure 3.10(a) and Figure 3.10(b). It is shown that this operation did not influence the final equilibrium state, for example, given a small perturbation on the lateral position of the centroid Y_G (Figure 3.4(a)), the equilibrium state is unaffected. And also see Appendix D.1 for more examples of manual alert of the radial position to accelerate the convergence.

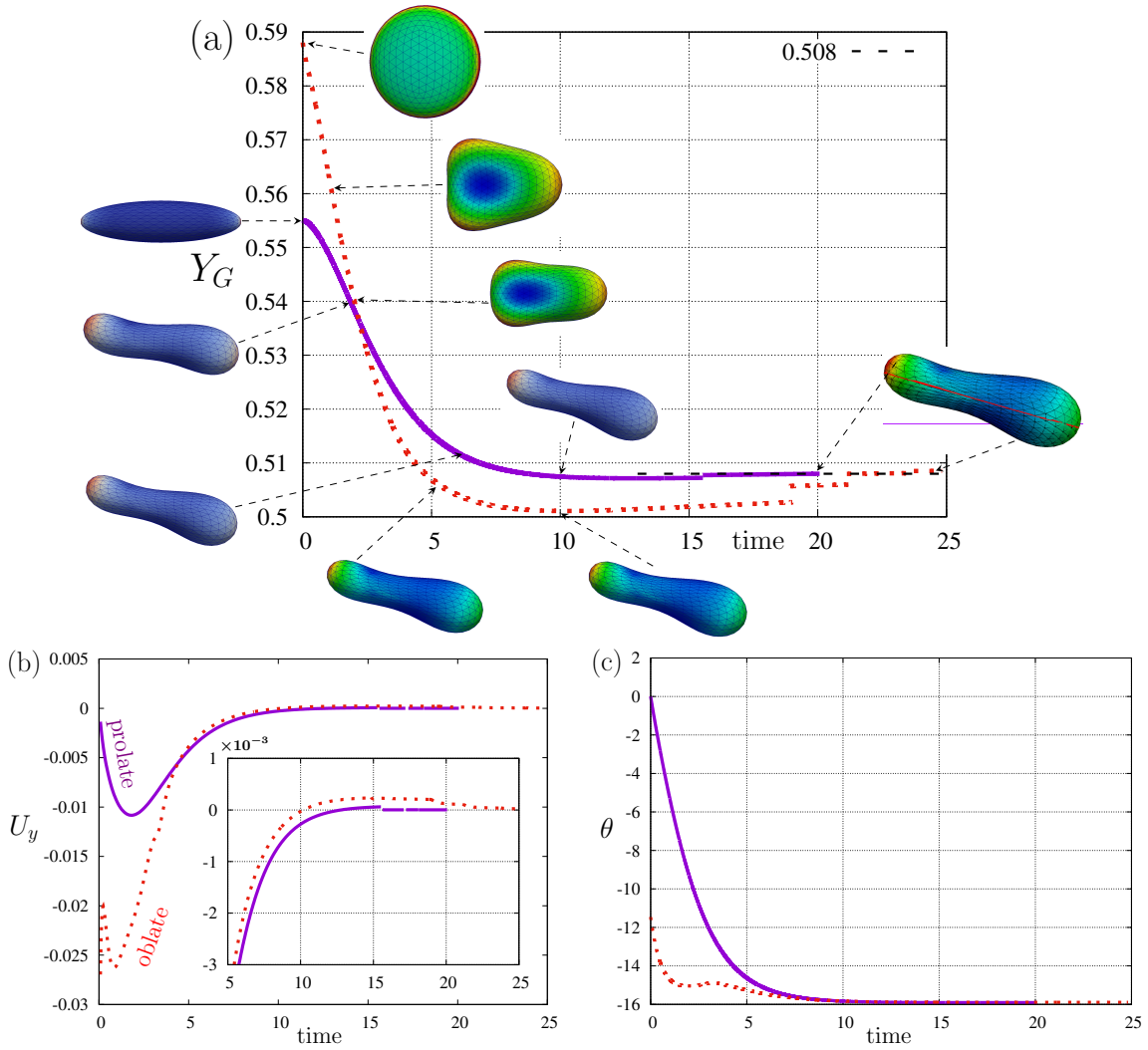

Figure 3.10: Evolution of (a) the centroid Y_G, (b) the migration velocity U_y and (c) the inclination angle θ for $Ca = 1, \nu = 0.7, R_t = 6.0$, with $H_0 = 0.555, \theta_0 = 0°$ for an initially prolate form and with $H_0 = 0.6, \theta_0 \approx -11.5°$ (or -0.2 rad) for an initially oblate form. The insets (side view in the Oxy plane and top view in the Oxz plane), colored by mean curvature, present the instantaneous shapes, starting from prolate and oblate form respectively, and they become a stable slipper form at the end of the simulation. The last snapshot is a combination of these two cases, separated by the red inclined line, the upper comes from the prolate form and the lower is from the oblate one. The horizontal purple line shows the axis of the microchannel.

The snapshots in Figure 3.10 (a) show some instantaneous shapes for an initial prolate and oblate form. Although the evolution process is very different, their stable shapes are perfectly matched, as shown in the last snapshot, which is a combination of these two cases, separated by a red line, where the upper half comes from the prolate form and the lower half comes from the oblate one. Figure 3.10(b) and its enlarged subplot show the evolution of the migration velocity. It is shown that at the end of the simulation, where a stable form is obtained, there is no more lateral migration. Figure 3.10(c) shows the evolution of the inclination angle θ, in this case, the slippers have a common stable inclination angle about -16 degrees.

3.3.3 Membrane flow and surrounding fluid flow

In this section, the fluid flow on the membrane of the vesicles and for the surrounding fluid are presented for a stable form with five examples, among which two are a slipper, one is a peanut shape, and the other two are shapes with two planes of symmetry. Be aware that the velocities presented in this section are all velocities relative to the centroid of the vesicle, i.e., in the reference frame moving with the steady vesicle. To calculate the flow of the surrounding fluid, a fluid box mesh is generated with freely available python scripts and Gmsh (refer to the Appendix C).

For an axisymmetric stable form, for example, a peanut, as indicated in Figure 3.11, the membrane has no slipping, i.e., there is no membrane velocity. Putting the camera on the vesicle, the fluid moving globally in the direction $-x$[1], as shown in Figure 3.11, the fluid located away from the axis moves from the front of the vesicle to the rear, and the streamlines remain parallel, which is nearly unaffected even in the region of vesicle. While as the fluid approaches the axis, it is hindered, and the streamlines are diverted, the fluid flows in the totally opposite direction at the axis of the flow. Thus, there are two vortex regions in the form of a ring, at the front and the rear of the vesicle.

Two different tank-treading modes are presented in Figure 3.12, the left one with $\beta = 0.1$ ($R_t = 10$, less confined) has a single axis of rotation, and the right one with $\beta = 0.3745$ ($R_t = 2.67$, more confined) has two distinctive axes of rotation. It should be noted that for the less confined case, the stable radial position $Y_G^* \approx 0.608$ (all vertices have coordinates $y \in [-0.407, 1.655]$), and that of the more confined case is about 0.0122 (all vertices have coordinates $y \in [-0.963, 1.075]$). Thus, the vesicle with $\beta = 0.1$ has its major part of the body above the axis (as indicated by the dashed blue line), and the membrane slides globally with a single axis, which is driven by the imposed flow. While, the vesicle with $\beta = 0.3745$ is almost equally separated by the axis of the flow, and the membrane slides in opposite directions with two different axes[4], one above the flow axis and the other under the flow axis. These two circulations meet at the shared region (in the middle of the vesicle) flowing in the same direction. The strength of maximal sliding velocity for the latter case is much smaller than the former.

[1]The vesicle translates at a speed $U_x^{\mathrm{v}} \approx 3.647$, while the maximum velocity of the unperturbed flow is 4. We define the relative velocity lag as $\delta_u = (U_m - U_x^{\mathrm{v}})/U_m$, here we have $\delta_u \approx 8.83\%$.

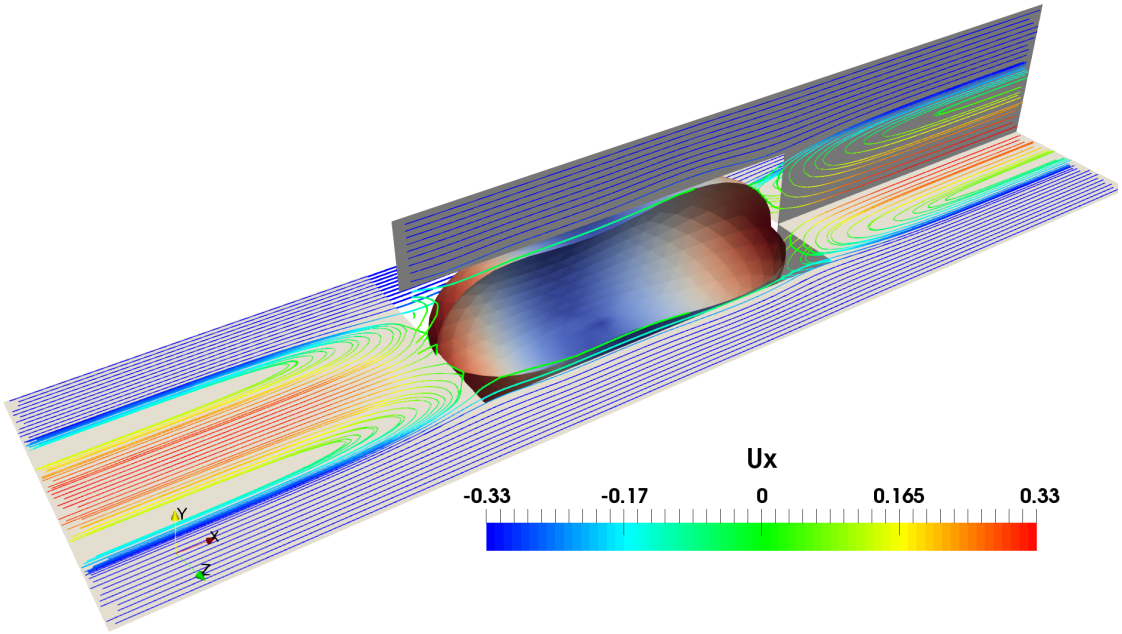

Figure 3.11: Streamlines in the $y = 0$ and $z = 0$ planes around a peanut-shaped vesicle for $Ca = 1, \nu = 0.8$ and $\beta = 0.5$. The vesicle membrane is colored by the mean curvature and the streamlines are colored with the axial velocity u_x. For the flow direction to be clearer, the color legend is set with the same upper and lower limits, the lower limit of the flow is actually much bigger than the upper one.

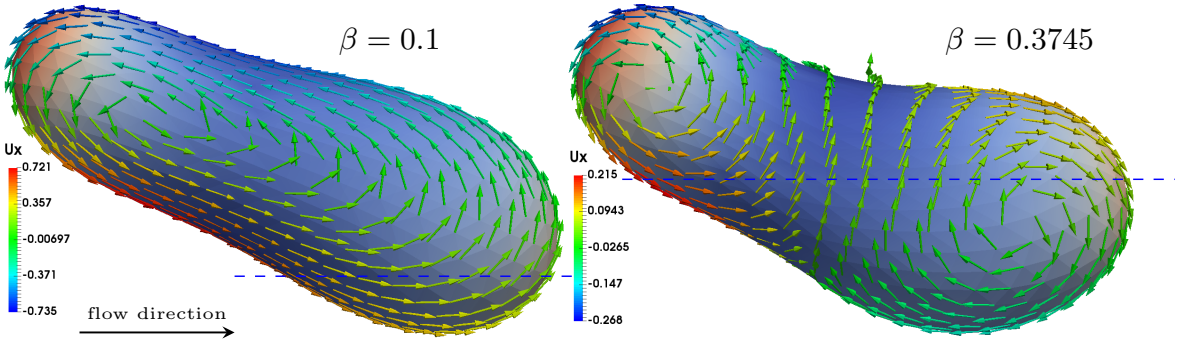

Figure 3.12: Stable slipper shape with fluid velocities at the membrane for $Ca = 1, \nu = 0.8$ and for two different confinement $\beta = 0.1$ and 0.3745. The membranes are colored by mean curvature of the surface and the arrows are colored by the strength of circulation velocities in the x-direction, u_x. The two dashed blue lines indicate the axis of the flow.

The streamlines of the surrounding fluid for these two cases are presented in Figure 3.13. Comparing with those of the axisymmetric case, as shown in Figure 3.11, a major differ-

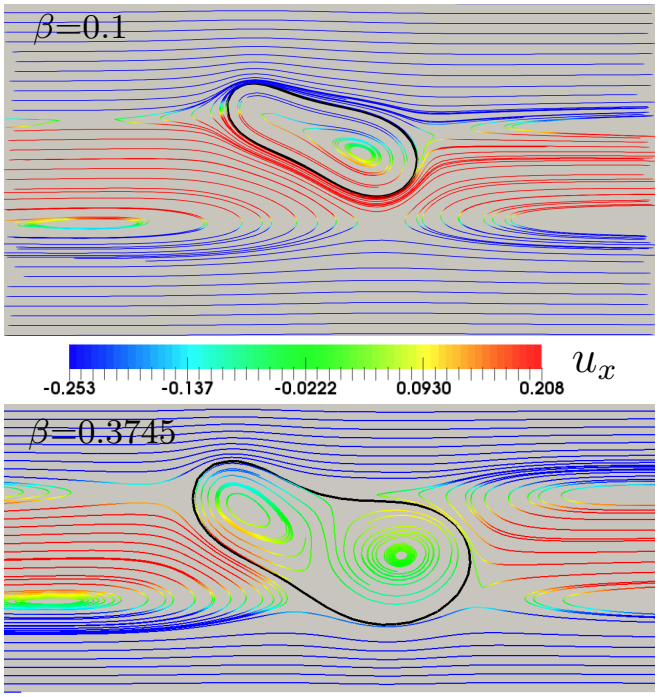

Figure 3.13: Streamlines in the $z = 0$ plane for the two cases shown in Figure 3.12. The black line indicates the position of the membrane in this plane.

ence is that the fluid inside the vesicle is no longer stationary. Actually, the fluid flows synchronously with the adjacent flow outside the vesicle, but with a strength slightly lower.

The fluid outside of the vesicle moves globally from the positive direction to the negative direction of the flow axis[2], if one observes from the vesicle. For the less confined case ($\beta = 0.1$), there exists a stagnation point just below the vesicle, but this point disappears at a higher confinement, and there are only two rings (one before the vesicle and the other after the vesicle) where the velocities equal to zero. The fluid inside the vesicle behaves in the same way as the membrane flow, which is reasonable because the sliding of the membrane is the driving force of the internal flow.

Figure 3.14 and 3.15 show the flow structure of the stable croissant shape and biconcave-croissant shape, respectively. Both the cases exhibit membrane sliding, the tank-treading speed is greater in the case of biconcave-croissant shape ($Ca = 1$) than that of the croissant shape ($Ca = 20$ for this example and for the other croissant shapes in Figure 3.23 and 3.24). While, a posteriori check on the membrane sliding velocity for $Ca = 1, \nu = 0.65$ and $R_t = 3.2$ (Figure 3.28) shows an almost equal strength for the biconcave-croissant shape and the slipper shape.

[2]The relative velocity lag δ_u are 0.9% and 6.67%, respectively for $\beta = 0.1$ and 0.3745.

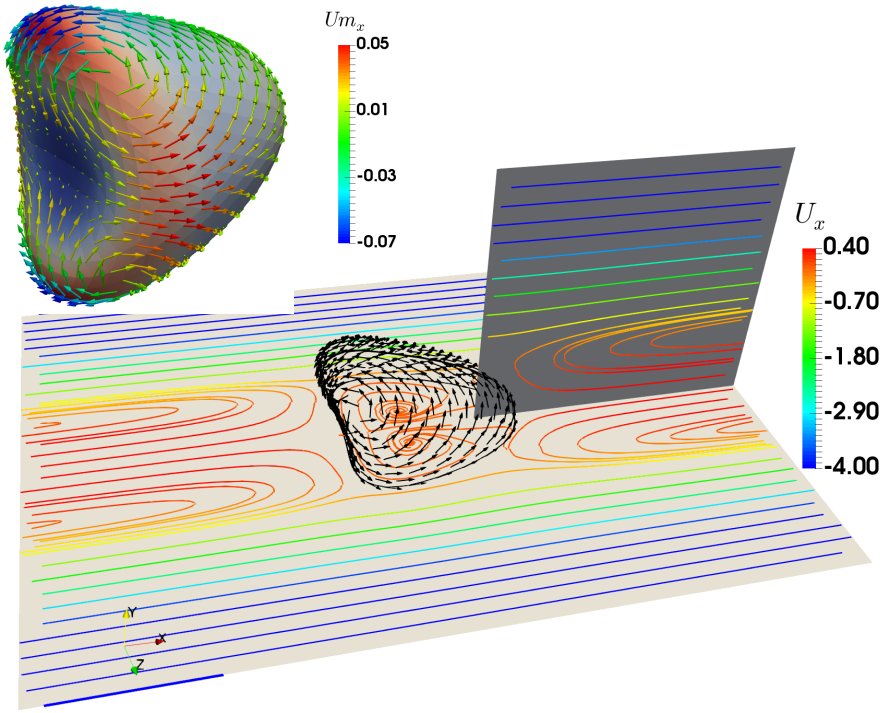

Figure 3.14: Streamlines (colored by translational velocities in x direction, u_x) in planes $y = 0$ and $z = 0$ for $Ca = 20, \nu = 0.9$ and $R_t = 5$. The black arrows show the tank-treading of the membrane. The inset in the upper left corner shows a stable croissant shape colored by the mean curvature, and the arrows are colored by the membrane tank-treading velocities in the x-direction.

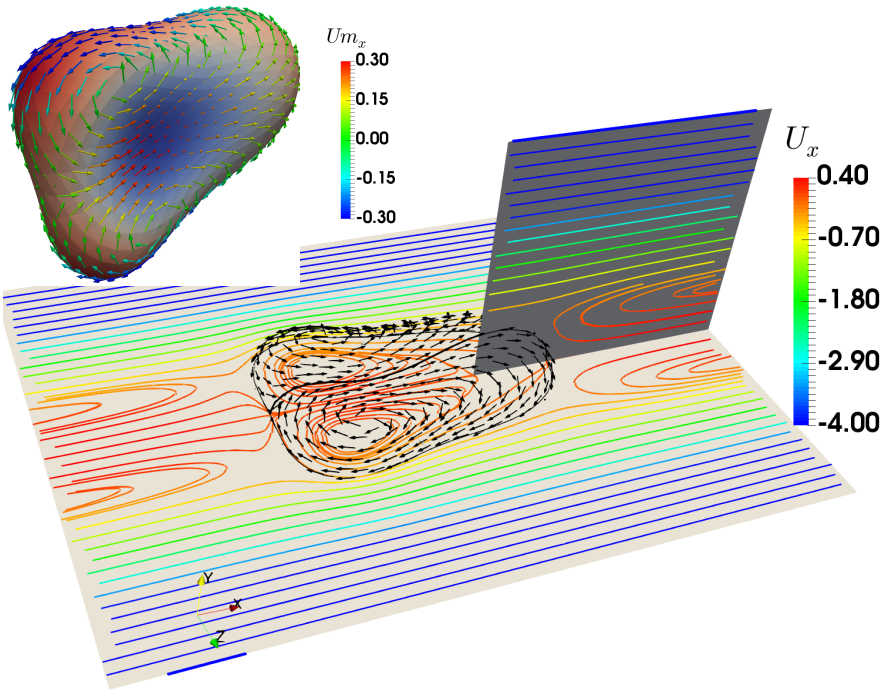

Figure 3.15: Streamlines in planes $y = 0$ and $z = 0$ for $Ca = 1, \nu = 0.65$ and $R_t = 3.2$. The black arrows show the tank-treading of the membrane. The inset in the upper left corner shows a stable biconcave-croissant shape colored by the mean curvature.

It is also seen that, for both cases (Figure 3.14 and 3.15) in the plane $y = 0$, there are two vortices (interior of the vesicle) rotating in the opposite directions. Whereas, the streamlines around the vesicles are globally comparable to those of the peanut shape [3].

3.3.4 Effect of Ca

In this section, the effect of the capillary number Ca, or the bending rigidity $\kappa = 1/Ca$ is qualitatively presented. The evolution of the vesicle shape as a function of the capillary number, for fixed reduced volume $\nu = 0.9$ and confinement $\beta = 0.25$ is shown in Figure 3.16. The simulations are performed with 1280 elements, while the vesicles presented here are refined to 20480 elements to better represent the stable shape. A dramatic change in morphology is found as increasing Ca: from slipper ($Ca = 0.1, 1.0$ and 3.0) to croissant ($Ca = 10.0$ and 20.0), and eventually parachute ($Ca = 50.0$) shapes. This tendency can be more pronounced for more deflated vesicle, for example when $\nu < 0.7$, as reported by Kaoui, Biros and Misbah [80]. This property may be used as a potential diagnostic for detecting RBC pathologies, such as malaria, which are characterized by an increase in membrane rigidity.

All the shapes in Figure 3.16 are sliced by the plane $z = 0$ and plotted in the same figure, as shown in Figure 3.17(a). Starting from $Ca = 0.1$, an off-centered, inclined and almost prolate shape deforms to a slipper form, in accompanying with a decrease of the centroid

[3] The relative velocity lag δ_u is 2.77% for the croissant shape and 4.95% for the biconcave-croissant shape.

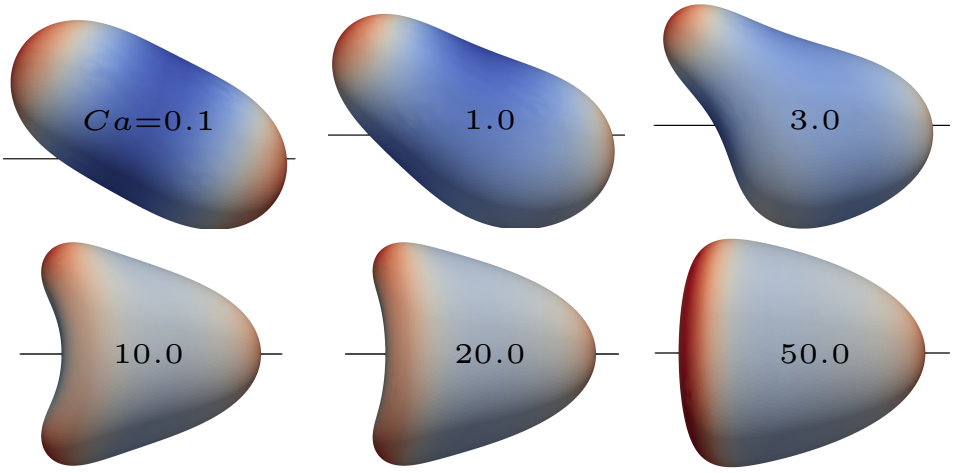

Figure 3.16: Evolution of the morphology as a function of the capillary number for $\nu = 0.9$ and $\beta = 0.25$. The membranes are colored by the mean curvature and the axis of the microchannel is indicated by the black line.

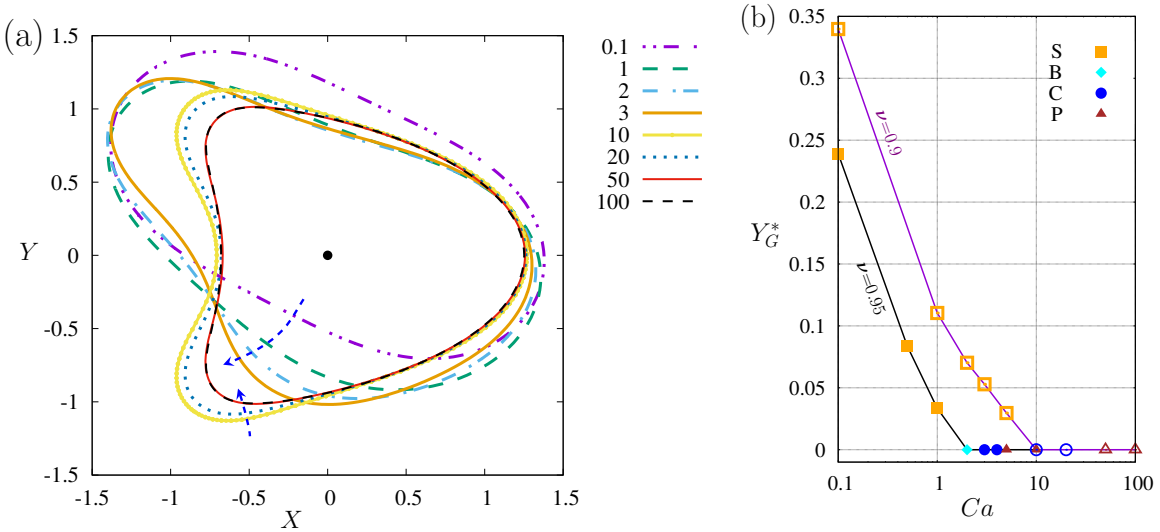

Figure 3.17: (a) Evolution of the projected morphology in the plane of XY as a function of the capillary number for $\nu = 0.9$ and $\beta = 0.25$. The two dashed blue arrows indicate the direction in which Ca increases, for the slipper shape and for the symmetric shape (croissant and parachute), respectively. (b) Evolution of the stable centroid position Y_G^* as a function of Ca for $\beta = 0.25$, where S, B, C, and P stand for slipper, bullet, croissant, and parachute, respectively. In this figure, results are presented for two reduced volumes, $\nu = 0.95$ (filled symbols) and $\nu = 0.9$ (empty symbols).

position when Ca is increased to 3. Further increasing the capillary number, for example to $Ca = 10$, leads to the vesicle transits to a croissant shape with its centroid located at the axis of the flow. This croissant shape is not stable, which then transforms into a fully axisymmetric parachute shape, for example, when $Ca = 50$, we obtain a stable parachute shape.

Figure 3.17(b) shows the evolution of the stable centroid position Y_G^* as a function of the capillary number Ca for $\beta = 0.25$ and two different reduced volume $\nu = 0.95$ (filled symbols) and 0.9 (empty symbols). Once again, we found that the vesicle first has its centroid located away from the center of the flow, and it has an asymmetric slipper shape. The position of the centroid decreases as we increase the capillary number. When the capillary number is bigger than some critical values, Ca_c, the stable centroid position $Y_G^* \to 0$, and the vesicle attains an axisymmetric or a croissant shape. The selection of the final shape is dependent on the values of ν and Ca. It should be noted that the bullet shape appears only for $\nu = 0.95$ for confinement is not strong ($\beta = 0.25$). Furthermore, according to this figure, it seems that the decrease in reduced volume ν will delay this transition.

3.3.5 Effect of β

The explicit inclusion of a wall boundary for a fully three-dimensional vesicle flowing in a Poiseuille flow is marked as a significant difference from previous numerical studies on vesicle dynamics in (quadratic) Poiseuille flow, as briefly discussed at the beginning of this chapter. In this section, the effects of the confinement β are discussed in the following sequence: (i) the influences on the asymmetric slipper are presented first, then (ii) the transition to the axisymmetric shape, and (iii) the effects on the snaking motion are lastly revealed.

A vesicle, with reduced volume $\nu = 0.9$, flowing in a capillary flow with $Ca = 1$, will have slipper as the final stable shape for a capillary with appropriate size, for example a capillary with radius $R_t \geq 3.2$, as shown in Figure 3.18. In this figure, the final stable slippers are presented for an unbounded Poiseuille flow ($\beta = 0$) and capillary flow with five different sizes, ranging from $R_t = 10$ to $R_t = 3.2$. In fact, the value of the stable lateral position of the centroid decreases from 0.33 to 0.03 as we increase the confinement β from 0 to 0.3125. That is, the vesicle migrates to the center of the capillary as the effect of confinement increases. On further increase in confinement, an axisymmetric form is obtained ($Y_g^* = 0$), which will soon be involved.

With regard to the geometric shape of these vesicles, it seems that a region (the upper central part of the membrane) with inverted curvature is appeared and becomes more pronounced in increasing the confinement β. Also, the membrane sliding transits correspondingly from a whole (with a single axis of rotation) to a form with two separate parts, each having their own axis of rotation. As shown in the last figure, these two vortices rotate in opposite directions, like the counter-rotating propellers[4].

Figure 3.19 shows the transition from a slipper to a axisymmetric bullet in detail for $\nu = 0.97, 0.95$ and 0.9 via (i) the evolution of the stable centroid position Y_g^* of the membrane,

[4]Refer the schematic animation in wikipedia page for counter-rotating propellers, https://en.wikipedia.org/wiki/Counter-rotating_propellers.

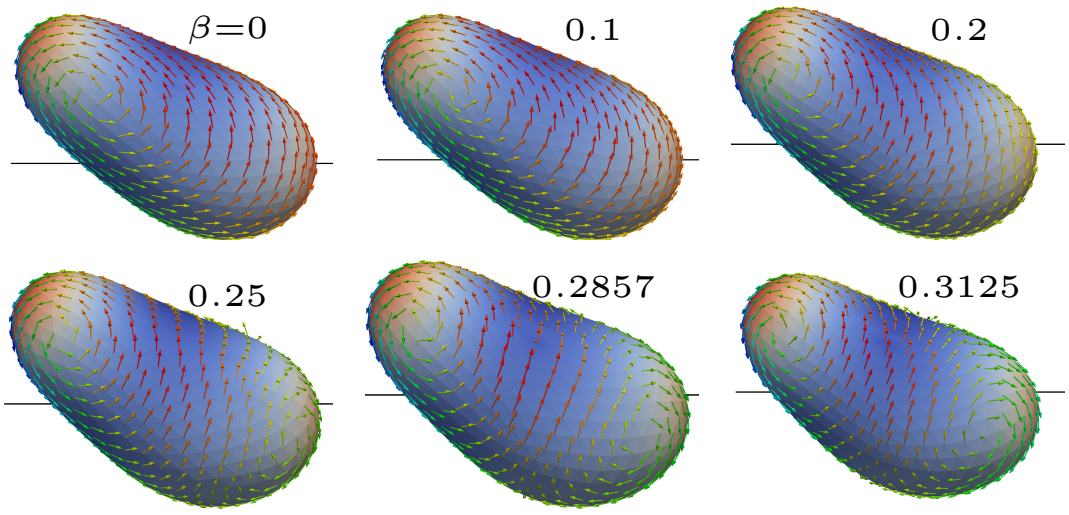

Figure 3.18: Evolution of vesicle slipper state (shape and radial position) and its membrane velocity as a function of the confinement β for $Ca = 1$ and $\nu = 0.9$. The membrane is coded by the mean curvature and the arrow is coded by the membrane velocity in the y-direction, namely u_y^m. The axis of the capillary is indicated by the black line.

(ii) the maximum value, in magnitude, of the tank-treading velocity for a stable form $U_{tt} = \max_{\text{all vertices}} \{\|\mathbf{u}_i - \mathbf{U}_{\text{mig}}\|\}$, (iii) the velocity lag, and (iv) the stable inclination angle θ, measured from the axis of the flow to the major axis of the vesicle. Here, the velocity lag is defined as the difference between the unperturbed velocity at the centroid position of the vesicle $U_l^\infty = u^\infty(Y_g^*)$ and the translation velocity of the vesicle U_x when it reaches at the stable state.

The evolutions of the stable centroid position Y_g^* as a function of the radius of the capillary R_t are shown in the first row of Figure 3.19 for three different reduced volume ν. Starting from a common large capillary, $R_t = 10$ for those three different ν, the value of Y_g^* decreases simultaneously with the decrease in the size of the capillary, and it eventually decreases to zero when R_t is less than a critical value R_c, the slipper shape transit correspondingly to an axisymmetric one, a bullet. There are two obvious differences in these very similar transitions, the first is that the value of Y_g^* is different for a capillary of the same size, the more the vesicle is deflated, the higher the value of Y_g^* is; the second difference is the value R_c, the critical value where the transition takes place, which seems that a more deflated vesicle can support the slipper shape in more confined Poiseuille flow.

Conversely, if we observe these curves from left (smaller R_t) to right (larger R_t), the vesicle transit from an axisymmetric bullet shape to an off-center slipper shape. That is, when R_t is rather small, the strong confinement makes the bullet shape stable against various perturbations, but when R_t is larger than the critical value R_c, instability develops and the bullet shape evolves into another stable state–the slipper shape, which is characterized by the loss of up-down symmetry. Thus a fit is shown in these figures (dashed black curves) in order

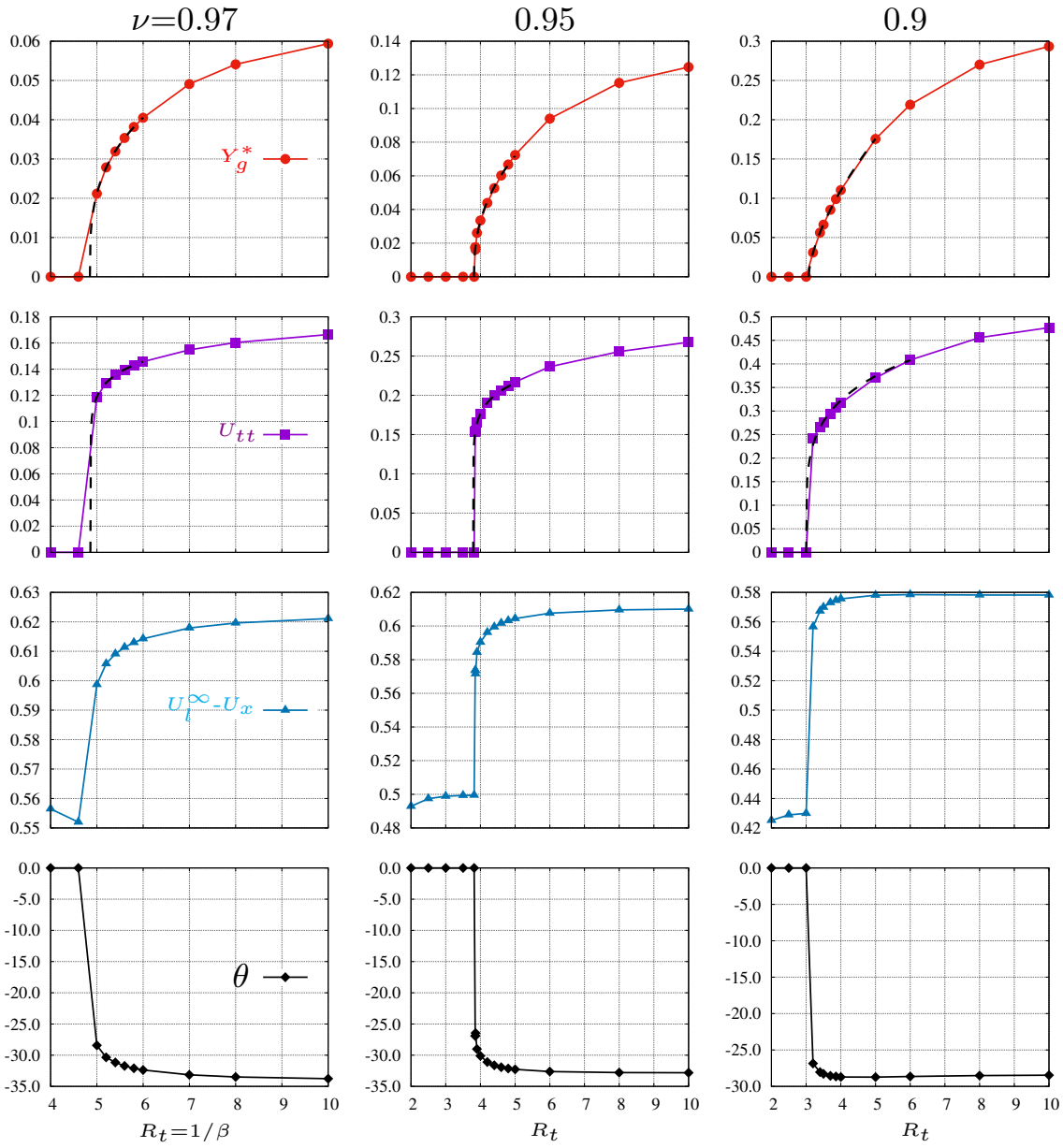

Figure 3.19: Effects of the confinement β on a vesicle flowing in microchannel with $Ca = 1$ and three different reduced volumes: (i) $\nu = 0.97$ (left panels), (ii) $\nu = 0.95$ (middle panels) and (iii) $\nu = 0.9$ (right panels), for the stable centroid position Y_g^*, the maximum sliding speed U_{tt}, the velocity lag $U_l^\infty - U_x$ and the stable inclination angle θ.

to have a reduced dynamical description near the bifurcation point R_c, actually, we assume that the points close to R_c can be fitted with the common formula

$$Y_g^f = a(R_t - R_c)^b. \tag{3.1}$$

The fitting results show the sets (R_c, b) are $(4.8499, 0.32)$, $(3.8136, 0.42)$ and $(3.0271, 0.65)$ for $\nu = 0.97, 0.95$ and 0.9, respectively. These fitted exponential number b together with the transition curves suggest an analogy between this transition and the classical supercritical pitchfork bifurcation [34, 80]

$$\partial_t Y_g^* = (R_t - R_c)Y_g^* - Y_g^{*3}, \tag{3.2}$$

which has a pair of nontrivial stable solutions

$$Y_g^* = \pm\sqrt{R_t - Rc}, \quad \text{for } R_t > R_c. \tag{3.3}$$

We then plot the maximum tank-treading speed U_{tt} as a function of R_t. At first glance, we notice that membrane sliding takes place only for the asymmetrical slipper shape and that there is no movement of the membrane for the axisymmetric bullet shape. Therefore, it is rational to see that the critical value of the capillary radius R_c, from which a vesicle without tank-treading passes to a vesicle with tank-treading in increasing the control parameter R_t, equals to that for the transition of stable lateral position Y_g^*. A major difference is that the behavior near the transition point R_c for U_{tt} is much faster than that for Y_g^*. This means that the difference of membrane tank-treading velocity for a slipper at different states is much smaller than that of the slipper shape and the bullet shape.

The fitting curves with the data near the transition point are also plotted in these figures (the second row of Figure 3.19), as indicated by the dashed black lines. For these curves, the same formula (3.1) was used, and by which the sets (R_c, b) are $(4.8603, 0.1)$, $(3.792, 0.11)$ and $(2.7187, 0.27)$ for $\nu = 0.97, 0.95$ and 0.9, respectively.

Results show the evolution of the velocity lag $(U_l^\infty - U_x)$ in the direction of the flow and the inclination angle θ between the axis of the flow and the major axis of the vesicle are then continued (in the last two rows of Figure 3.19). They overall have similar behaviors in comparison with those of U_{tt} (We may replace θ with $\mid \theta \mid$ for the θ–R_t curves.). Whereas, in comparison with the other two cases, a major difference is that they are much less sensitive when the radius of the capillary R_t is rather larger than the critical value R_c.

Figure 3.19 shows a consistent transition for a vesicle from the axisymmetric bullet shape to the asymmetric slipper shape when varying the control parameter, the confinement β, via the inspection of Y_g^*, U_{tt}, $U_l^\infty - U_x$ and θ. It is also worth mentioning the influences of deflation: the scope of the existence of the slipper shape is, in general, extended for a vesicle with smaller reduced volume ν, which has much stronger deformability. We may, therefore, estimate the plentiful picture for a vesicle with an equal reduced volume of the normal RBC of human (~ 0.64).

Evolution of the stable lateral position Y_g^* of the slipper shape as a function of the confinement β is presented in Figure 3.20 for deflated vesicles ($\nu = 0.95, 0.9$) flowing in the microchannels with the capillary number $Ca = 0.1, 1$ and 10 (only for $\nu = 0.9$), where $\beta = 0$ corresponds to the unbounded case. From our simulations for $\nu \geq 0.9$, we found the

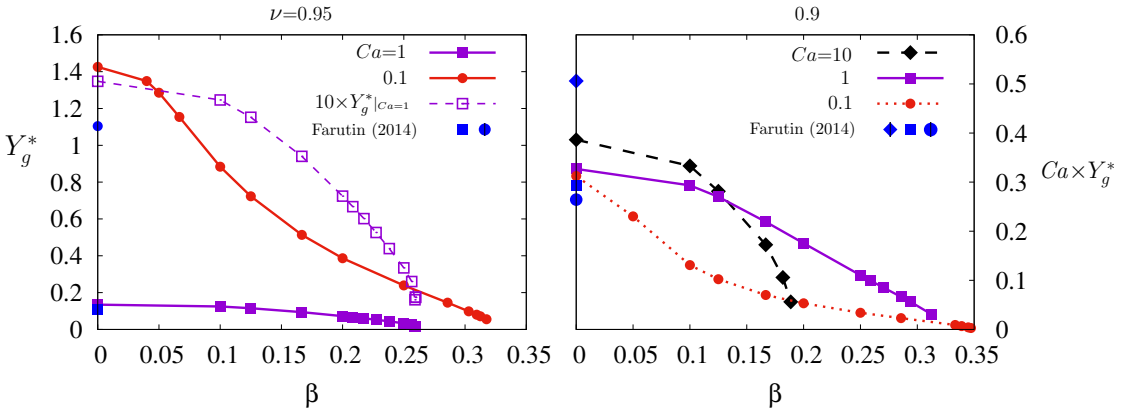

Figure 3.20: Effects of the confinement β on a vesicle flowing in microchannel for $Ca = 0.1, 1, 10$ and for reduced volumes $\nu = 0.95, 0.9$. Numerical results of a vesicle in an unbounded ($\beta = 0$) Poiseuille flow are also plotted [49] (obtained with WebPlotDigitizer).

stable lateral position Y_g^* is approximately inversely proportional to the capillary number Ca when the confinement β is very weak (similar to Farutin & Misbah [49, FIG. 7]). Therefore, for better representation, we draw, in Figure 3.20 (b), the curves for Y_g^* multiplied by the capillary number, i.e., $Ca \times Y_g^*$, to show the similarities and the differences.

First, for each individual curve, we again found the intuitive result that the stable lateral position decreases as the confinement β increases, but this behavior was different for $Ca = 1$ in comparison to $Ca = 0.1$ and $Ca = 10$. Secondly, the transition from the slipper shape to the axisymmetric shape is delayed for $Ca = 0.1$ when compared with $Ca = 1$, and the latter is more delayed in comparison to $Ca = 10$. As shown in Figure 3.23, there is no stable slipper shape in the case of $\nu = 0.95$ and $Ca = 10$, thus the results of $Ca = 10$ are only presented for $\nu = 0.9$. Thirdly, the inversely proportional relation between Y_g^* and Ca seems to work roughly well in case of very weak confinement, but as confinement β increases, the higher the capillary number Ca (the stronger of the flow) is, the faster the variance of the stable lateral position Y_g^*. Lastly, in comparison with the results of Farutin & Misbah [49], our results for unbounded cases ($\beta = 0$) match very well for $Ca = 1$. As for the discrepancy for $Ca = 0.1$, our results seem reasonable regarding to the evolutionary trend of the confinement.

Figure 3.18, 3.19 and 3.20 mainly concern the slipper shape, while a richer morphological dynamic for a vesicle ($\nu = 0.9$) in a capillary flow ($Ca = 10$) is presented in Figure 3.21. In such flow conditions, we vary the capillary size R_t from 5.0 to 3.0, 1.5 and finally to 1.2, the initial slipper shape transforms first into the croissant shape, then to the parachute shape and finally to the bullet shape, which is a evolution of increasing of the number of plane of

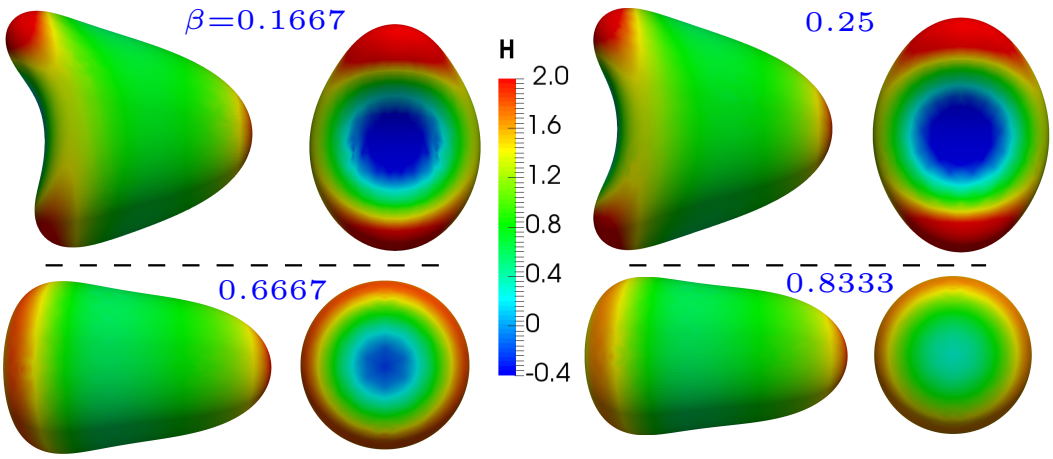

Figure 3.21: Evolution of the morphology as a function of the confinement β for $Ca = 10$ and $\nu = 0.9$. The membrane (discretized with 1280 elements) is coded by the mean curvature with the same legend.

symmetry. Conversely, as the confinement decreases, the restriction from the circumferential wall weakens, which allows the bullet shape with convex rear transit to the parachute shape with concave rear. By further reducing the confinement, the parachute shape transforms into the croissant shape that has only two planes of symmetry. Instability continuously develops and the croissant shape transforms into the asymmetric slipper shape as the confinement further decreases.

Before closing this subsection, we present the last example that shows the effect of confinement on the snaking motion, as shown in Figure 3.22. Basically, as confinement β in-

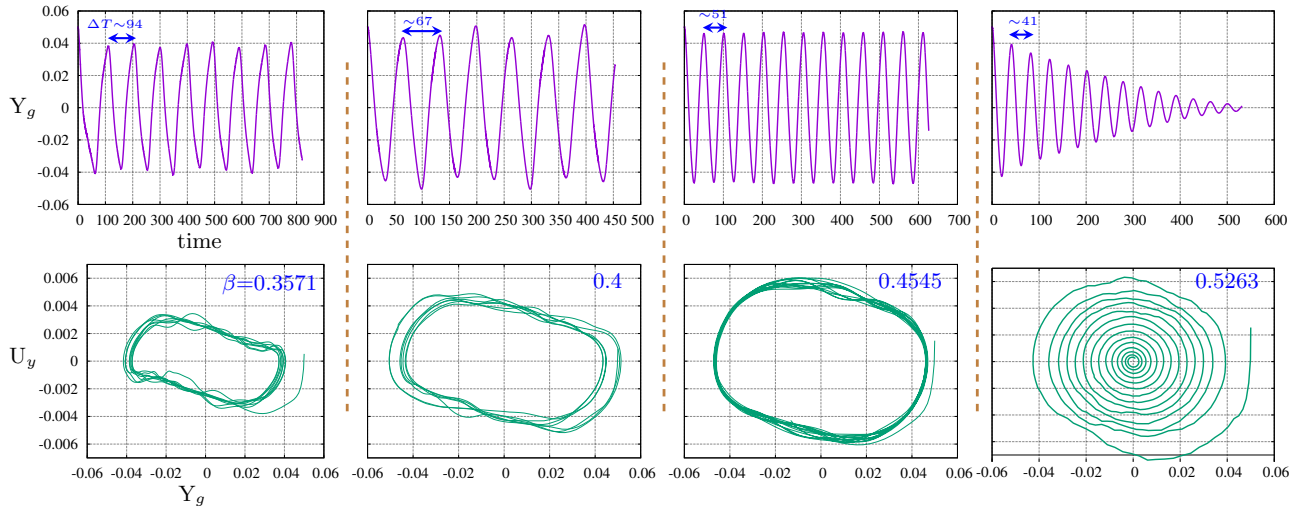

Figure 3.22: Effects of the confinement β on a vesicle flowing in microchannel with $Ca = 1$, $\nu = 0.85$ and with 320 elements. (top panel) Evolution of the lateral position of the centroid, (bottom panel) Poincaré maps.

creases, the snaking motion oscillates more rapidly and becomes a damped oscillation when the confinement exceeds a critical value. As for $Ca = 1$ and $\nu = 0.85$, it becomes a damped oscillation when $\beta \geq 0.5263$, and a bullet shape is obtained once this solution becomes stable. The noncircular limit cycles, shown in the bottom panel of Figure 3.22, means that the oscillation of the vesicle motion is not harmonic. In fact, this inharmonic oscillation is also accompanied by periodic deformation of the vesicle shape as demonstrated in the insets of Figure 3.3 (a).

From the Poincaré maps, it is seen that for a non-damped snaking motion ($\beta = 0.3571, 0.4$ and 0.4545), the size of the periodic orbit increases with the confinement β. That is, for a given lateral position Y_g, the corresponding lateral migration speed is greater if the effect of the confinement is more important. Since the local shear rate is given by $\dot{\gamma}(Y_g) = -2Y_g$, confinement (or the wall) is the only global factor[5] responsible for this effect.

3.3.6 Diagram for different ν

A systematic analysis of the phase diagram for relatively low deflation is made by varying the capillary number Ca and the confinement β, as displayed in Figure 3.23 for $\nu = 0.95$ and Figure 3.24 for $\nu = 0.9$. In the unbounded limit ($\beta \to 0$), our results behave consistently with those of Farutin & Misbah [49, FIG. 8] except in some cases such as $Ca = 20$ and 50, for $\nu = 0.9$.

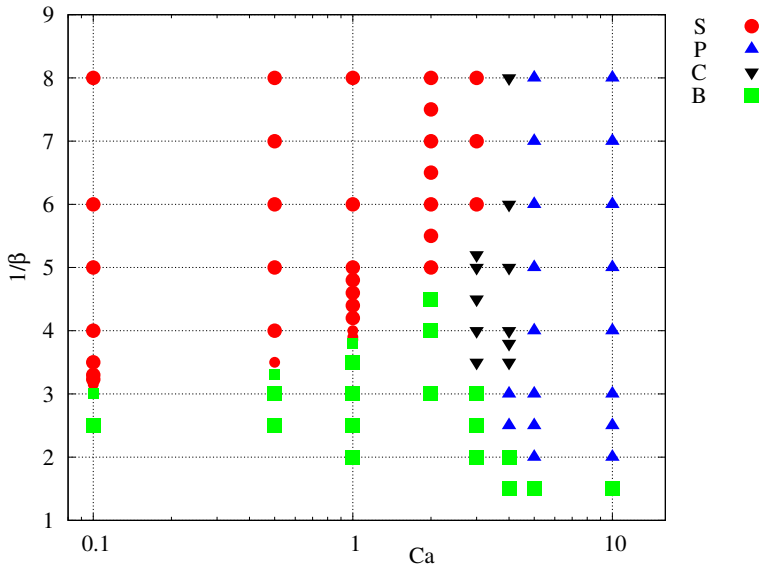

Figure 3.23: Phase diagram of steady states of vesicles for $\nu = 0.95$ in the variables $R_t = 1/\beta$ and Ca. S, slipper; P, parachute; C, croissant; B, bullet.

[5] The term *global factor* means that if we approximate the whole vesicle as a single point at its centroid, confinement is the only factor causing this difference – U_y of the snaking motions are varied for a vesicle at the same off-center position Y_g in microchannels of different size R_t. But due to the deformability, it becomes much more complicated. (see Figure D.4)

It is seen that, for both cases, the general tendency is that high β favors bullet shape, while at small β, slipper shape prevails at low Ca and parachute shape prevails at high Ca. Whereas, the croissant shape appears at the intersection region of the three previous steady shapes.

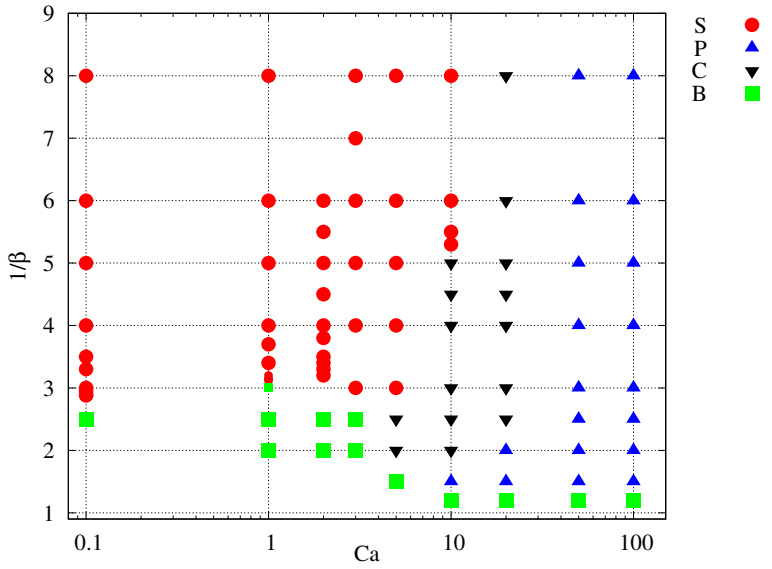

Figure 3.24: Phase diagram of steady states of vesicles for $\nu = 0.9$ in the variables $R_t = 1/\beta$ and Ca. S, slipper; P, parachute; C, croissant; B, bullet.

From these phase diagrams (Figure 3.23 and 3.24), the effects of Ca (horizontal view with R_t fixed) and β (vertical view with Ca fixed) on shape transitions can be directly identified without effort. That is, the number of planes of symmetry of the steady shape increases when Ca or β is increased.

3.3.7 Effect of the initial configuration

In this last section, the effects of the initial configuration, including shape (prolate and oblate), height H_0 and inclination angle θ_0, are discussed for very deflated vesicles, $\nu = 0.65$ and 0.6, which are close to that of RBC (~ 0.64) and have the oblate shapes as the unstressed equilibrium shapes (Figure 1.4).

The effect of the initial inclination angle θ_0 (Figure 3.1 (b)) between the major axis of an oblate shape and the axis of the flow is first briefly addressed, as shown in Figure 3.25 and 3.26. Figure 3.25 shows the evolution of the inclination angle θ, the radial position of the centroid Y_g, and the lateral migration velocity U_y of the vesicle initially placed at height $H_0 = 0.2$ with different inclination angles θ_0. The case with $\theta_0 = 0.0$ rad converges to a stable state, both in the inclination angle θ (3.25 (a)) and the radial position of its centroid Y_g (3.25 (b)). The black solid curves represent the calculations with manual adjustment of the radial position Y_g of the vesicle for the case with $\theta = 0.0$. These finite perturbations

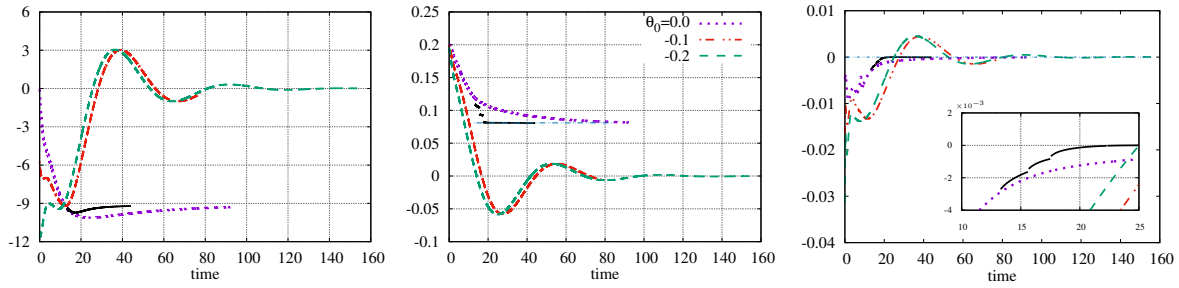

(a) θ (b) Y_g (c) U_y

Figure 3.25: Time histories of (a) the inclination angle θ (in degree), (b) the lateral position of the centroid Y_g and (c) the lateral migration velocity U_y for $Ca = 1, \nu = 0.65, 1/\beta = 3.0$ and the initially oblate shapes are placed at $H_0 = 0.2$ with three different inclination angles: $\theta_0 = 0.0, -0.1$ and -0.2 rad ($\approx -11.46°$). The black curves correspond to the simulations with manual adjustment of the lateral position of the centroid.

(on Y_g) are performed according to the lateral migration velocity. As shown in Figure 3.25 (c), the adjustment is made to accelerate the decrease of the lateral migration velocity. This technique is very useful in seeking the stable lateral position Y_g^* when Y_g is close to Y_g^* due to the slowing down effect [146]. In addition, numerical examples have shown that this finite perturbation on the lateral position will not influence the final stable radial position Y_g^* (also refer to Figure 3.4, 3.10 and Appendix D.1). While the cases with $\theta_0 = -0.1$ and -0.2 rad experience totally different dynamics, namely, a damped oscillation both for the inclination angle θ and for the centroid position Y_g.

Figure 3.26 shows the evolution of the shape for two cases with different θ_0, mainly in the preliminary phase. The oblate, with θ_0 equals to 0, deforms and becomes more and more elongated, until reaching the final stable slipper shape, while the other one with θ_0 equals to -0.2 rad is first stretched in the flow direction, the stretch then relaxes and the deformation in the flow direction weakens, and finally, obtains a biconcave-croissant shape.

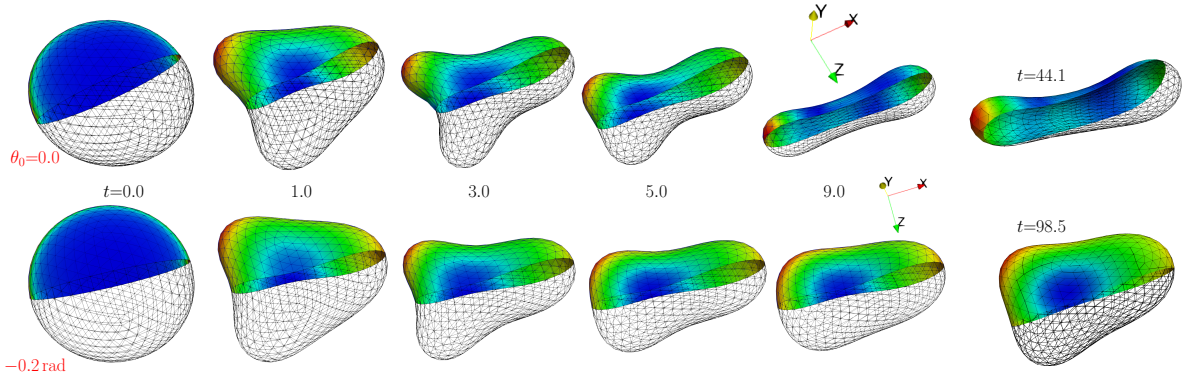

Figure 3.26: Snapshots of two of the three cases presented in Figure 3.25, membranes are colored by mean curvature.

Figure 3.25 and 3.26 do show the dependence of the initial inclination angle θ_0 on the dynamics of vesicle flowing in a capillary flow, hereinafter, we focus on the effects of the initial radial height H_0, and the initial inclination angle θ_0 is set to some values between -0.2 rad and -0.12 rad to make the initial shape synergistic with the local flow profile. The value of θ_0 is, in fact, also inspired by the final stable inclination angle obtained with prolate as the initial shape.

In Figure 3.10, examples with respectively prolate and oblate as the initial shapes show a common final stable shape, a slipper[6]. That example has $\nu = 0.7$, to better show the effect of the initial shape on the dynamics of vesicle flowing in capillary flow, vesicle should be chosen with $\nu \in (0.592, 0.651)$ (see Figure 1.4). As summarized in Table 3.1, some detail simulations with prolate and oblate as the initial shapes, but converge both to a stable slipper shape are presented. It is shown that the difference in the final centroid radial position Y_g^* due to different initial conditions is very limited. While, hereinafter, we show that the value of H_0

	prolate		oblate	
R_t	H_0	Y_g^*	H_0 (θ_0, rad)	Y_g^*
6.0	0.75; 1.1†	0.5121; 0.5151	0.7 (-0.2)	0.5164
5.0	0.7	0.4003	0.6 (-0.18)	0.4008
4.0	0.4; 0.6	0.2605; 0.2620	0.5 (-0.17)	0.2568
3.0	0.13†	0.0792	0.35 (-0.16)	0.0811
2.0	0.045†	0.0444	0.1 (-0.15)	0.0479

Table 3.1: Simulations have slipper as the final stable shape with respectively prolate and oblate as the initial shape for $Ca = 1$, $\nu = 0.65$ and different capillary sizes R_t. The upper index † means that the simulation is started from an existing state, not from a prolate shape.

has a significant influence on the dynamics of an initially oblate vesicle flowing in capillary flow.

The dependence of the initial position H_0 on the dynamics of an oblate vesicle flowing in a capillary is typically illustrated in Figure 3.27. That is, when H_0 is greater than a critical value H_0^c, the vesicle deforms and evolves into a slipper shape as the final stable shape, whereas if H_0 is less than this critical value, it deformes into a biconcave-croissant shape in accompanying with slowly damped oscillation. For a deflated vesicle ($\nu = 0.65$) flowing in capillary ($Ca = 1$ and $R_t = 3.2$), as shown in Figure 3.27, a slipper shape is obtained for $H_0 = 0.4$ and 0.35. For these large values of H_0, the evolution (shape and lateral position) becomes progressively slower as they approach the final steady state, as illustrated by

[6] Although H_0 is different, from Figure 3.4 and many other simulations, we can anticipate that the prolate shape with H_0 equals to 0.6 or 0.555 should converge to the same final state. Thus we can say in this example that the initial shape, prolate or oblate, is the only variable (small θ_0 for prolate will only slightly affect the total time to the final state).

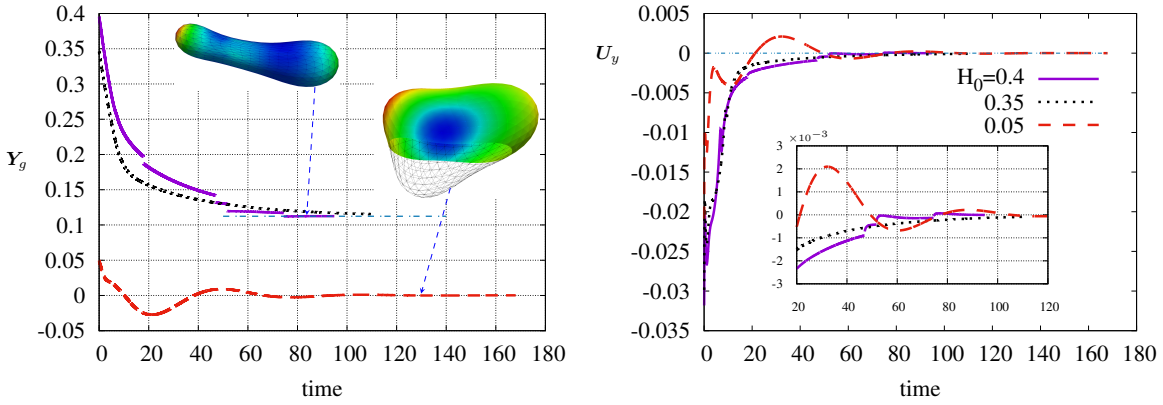

(a) (b)

Figure 3.27: Time histories of (a) the centroid radial position Y_g and (b) the lateral migration velocity U_y for $Ca = 1, \nu = 0.65, 1/\beta = 3.2$ and the initially oblate shapes are placed at three different heights $H_0 = 0.4, 0.35$ and 0.05 with the inclination angle $\theta_0 = -0.15$ rad. The insets (in (a), coded by mean curvature) show the final stable shapes, slipper, and biconcave-croissant, respectively.

the lateral migration velocity (Figure 3.27 (b)). By inspecting the migration velocity, we accelerate this slow evolution by manually changing the lateral position of the centroid of a finite value, as shown in Figure 3.27 (a) for $H_0 = 0.4$ and in Figure 3.25 (b). This kind of modification has shown no effect on the final stable state of slipper. Whereas for $H_0 = 0.05$, the biconcave-croissant shape is selected as the final stable shape.

By inspecting the evolution of the vesicle shape, the biconcave-croissant shape (for $H_0 < H_0^c$) seems to be due to the limited migration path (limited distance where the sign of the shear rate remains unchanged). But by examining the shape evolution of a vesicle flowing in an unbounded Poiseuille flow (see Figure D.5), for which it deforms first into a biconcave-croissant shape, which suggests that the presence of the capillary wall should be the major factor.

A systematic study of the effect of H_0 for $Ca = 1$ and $\nu = 0.65$ is carried out, and the resulting phase diagram is presented in Figure 3.28. It is shown that for relatively large capillaries ($R_t \geq 3.6$), the critical value H_0^c is almost constant, which corresponds to a value in between 0.35 and 0.4. For intermediate capillaries ($3.6 \geq R_t \geq 2.5$), this critical value H_0^c decreases with a decrease in size R_t of the capillary. While for relatively small capillaries ($2.5 > R_t \geq 2.0$), the results with a finer mesh (1280 elements) show only a slipper shape.

The discrepancy shown for the small capillaries between the fine mesh and the coarse mesh may be questioned as to the sensitivity to the error on the preservation of the membrane surface. Take the case with $R_t = 2.25$ and $H_0 = 0.2$ as an example, the relative errors of the membrane surface and the reduced volume are 0.3% and 0.51% for mesh with 320 elements, and those for mesh with 1280 elements are 0.008% and 0.02%, respectively (at the same instant $t \approx 10$).

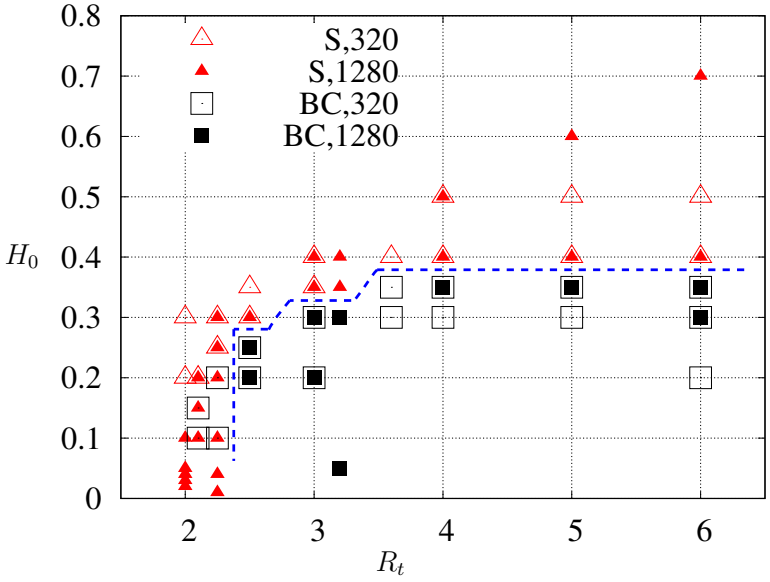

Figure 3.28: Phase diagram for $Ca = 1, \nu = 0.65$ in the variables H_0 and R_t. S and BC stand for slipper and biconcave-croissant shape, respectively. The full symbols represent results obtained with 1280 elements, while empty symbols with 320 elements. The dashed blue line is a guide for the eyes.

A similar phase diagram for $Ca = 1$ and $\nu = 0.6$ is presented in Figure 3.29. The results presented in this figure are mainly obtained with 320 elements, further simulations with 1280 elements should be performed to have a more reliable phase diagram.

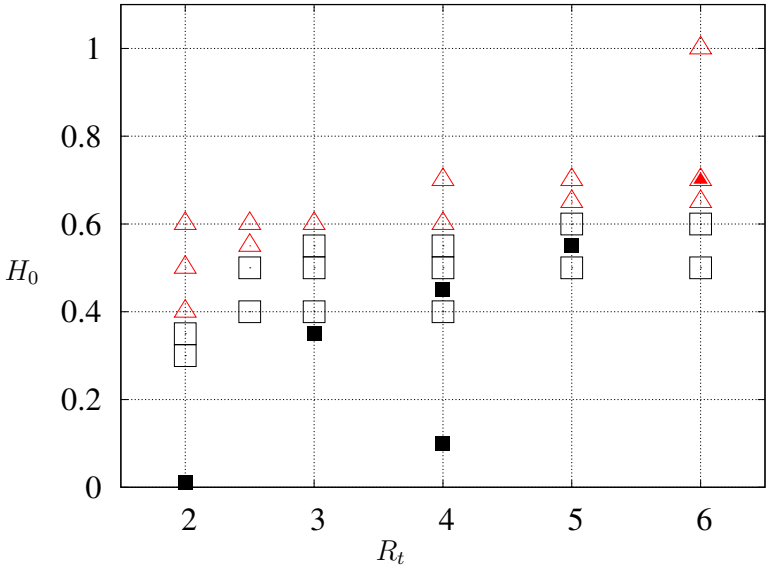

Figure 3.29: Phase diagram for $Ca = 1, \nu = 0.6$ in the variables H_0 and R_t. Preliminary results using the same notation as in Figure 3.28.

3.4 Summary

In this chapter, the dynamics (shape transition and lateral migration) of a three-dimensional fluid vesicle in a microchannel of different sizes is studied numerically via the BEM in a rather wide range of dimensionless parameters space of (ν, β, Ca), i.e., the reduced volume, the confinement, and the capillary number.

Because of the complex nonlinear interplay between the membrane, the external flow, and the solid boundaries, a rich variety of stable shapes have been explored, as presented in Sec. 3.3.2, which includes the widely reported axisymmetric bullet (Fig. 3.5), parachute (Fig. 3.6) and peanut (Fig. 3.7) shapes, the unconventional slipper shape (Fig. 3.10), and also the intermediate ones: the croissant (Fig. 3.8) and the biconcave-croissant (Fig. 3.9) shapes. Break up of the upstream-downstream symmetry due to the shape deformation will lead to the cross-streamline migration, as presented in Sec. 3.3.1, which can be the migration to the centerline of the flow (Fig. 3.2), the periodically centered snaking motion (Fig. 3.3) or the migration to the off-center position (Fig. 3.4). The exact sort of migration is closely related to the three dimensionless parameters. Normally, the inward migration can lead both to an axisymmetric stable shape or to the (biconcave-)croissant shape, whereas the migration to an off-center position corresponds to the slipper shape.

The flow structures of the surrounding flow and the fluid lipid bilayer are then presented in Sec. 3.3.3, with a special distinction in the case of the slipper shape (Fig. 3.12 and 3.13), the classical tank-treading motion or the counter-rotating propellers like motion[4].

The effect of the capillary number Ca and the transition from the slipper shape to an axisymmetric one are presented in Sec. 3.3.4. The general result is that: the increase in the capillary number lowers the centroid Y_g^* (Fig. 3.17) and increases the degree of symmetry (Fig. 3.16).

The next section (Sec. 3.3.5) deals with the effect of confinement β, in which the membrane flow of the slipper shape and its transition are first presented (Fig. 3.18). Then the shape transition from a slipper to an axisymmetric bullet shape is presented for three different reduced number $\nu = 0.97, 0.95$, and 0.9. By fitting the results of stable lateral centroid position Y_g^* and the maximum speed of tank-treading U_{tt}, a supercritical pitchfork like bifurcation is revealed (Fig. 3.19). This effect of β on the slipper shape is then compared for different capillary number (Fig. 3.20). Furthermore, the effect of β on the snaking motion is shown in Fig. 3.22.

The penultimate section 3.3.6 shows us the phase diagram of steady states of vesicles for $\nu = 0.95$ and 0.9 in the (R_t, Ca) plane. Lastly, the effect of the initial conditions is shown in Sec. 3.3.7, including the initial shape (prolate or oblate), the initial height H_0, and the initial inclination angle θ_0. The biconcave-croissant shape is found when an initial oblate vesicle ($\nu = 0.65, 0.6$) is placed at a height below a certain critical value H_0^c (Fig. 3.27, 3.28, 3.29).

4 Vesicle hydrodynamics in highly confined flows

This chapter is devoted to the steady motion and deformation of a lipid-bilayer vesicle moving along the axis of a circular tube in low Reynolds number pressure-driven flow. Though the subject is described in the preceding chapters, particular emphasis is given here to vesicle hydrodynamics in highly confined flows. Under such circumstances, three-dimensional simulations of vesicle motion become computationally expensive due to the necessity to resolve the stronger hydrodynamic interaction between the vesicle surface and the wall boundary. On the other hand, as shown in the previous chapter, it is expected that the vesicle shape retains axisymmetry when it is highly confined. It's therefore legitimate for us to pursue this study numerically by means of a previously reported axisymmetric boundary element method. Since the present chapter is composed of a manuscript in preparation, the presentation is self-contained, allowing for some duplications with the previous chapters and different notations being used. For the sake of brevity, we shall not elaborate the subject any further in a conventional introduction section; let us move on to the mathematical formulation – a fluid-structure interaction problem.

4.1 Problem formulation

4.1.1 Hydrodynamics

We consider a neutrally buoyant vesicle that is transported in a pressure-driven flow through a straight, circular tube of radius R. Fluid flows at an imposed, constant volumetric flow rate Q ($\equiv \pi R^2 U$, giving a mean bulk velocity U) driven by a pressure difference between inlet and outlet cross-sections. A schematic description of the problem is shown in Figure 4.1 with axisymmetric cylindrical basis $(\mathbf{e}_x, \mathbf{e}_r, \mathbf{e}_\phi)$. The suspending fluid and the fluid inside the vesicle membrane are incompressible and Newtonian with dynamic viscosity η and $\bar{\eta}$, respectively. We assume that the Reynolds numbers for both interior and exterior fluids are sufficiently small compared with unity, so that the inertial terms in the equations of motion may be neglected, the governing equations thereby reduce to the Stokes equations for creeping motion. Under these circumstances, experimental evidence [151] shows (and we will assume) that the flow and vesicle shapes are axisymmetric and that a vesicle initially positioned at the tube axis will translate with a steady velocity $V\mathbf{e}_x$ (which is unknown *a priori*) along the axis of the tube.

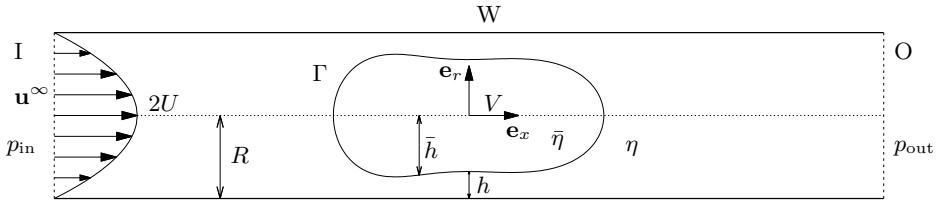

Figure 4.1: Schematic illustration of a vesicle flowing along the centreline of a circular tube of radius R in a pressure-driven flow. The system is rotationally symmetric about the x-axis. The boundaries of the control volume (D) are the inlet and outlet sections I and O, the solid surface of the tube wall W, and the membrane/medium interface Γ, i.e., $\partial D \equiv I \cup O \cup W \cup \Gamma$. The vesicle shape and the gap size between the membrane and the tube wall are denoted by $\bar{h}$ and $h(\equiv R - \bar{h})$, respectively. The vesicle enclosed volume is denoted by Ω.

In the absence of any vesicle, we obtain an unperturbed Poiseuille flow with a parabolic velocity profile:

$$\mathbf{u}^\infty(\mathbf{x}) = 2U\left(1 - \frac{r^2}{R^2}\right)\mathbf{e}_x, \qquad \mathbf{x} \in \mathrm{D}, \tag{4.1a}$$

$$\text{with} \qquad U = \frac{G^0 R^2}{8\eta}, \quad \Delta p^0 = \frac{8\eta U L_w}{R^2}, \quad R_H^0 = \frac{8\eta L_w}{\pi R^4}, \tag{4.1b}$$

where G^0 is the negative (uniform) pressure gradient applied along a tube of length L_w, namely, $G^0 = \Delta p^0 / L_w$, Δp^0 is the pressure difference or pressure drop required for the Poiseuille flow, and R_H^0 is the hydraulic resistance ($\equiv \Delta p^0 / Q$).

The presence of a vesicle causes a change in the hydraulic resistance of the system (i.e., tube + vesicle): it increases, meaning that to maintain the same volumetric flow rate $\pi R^2 U$, it is necessary to increase the pressure difference by a quantity Δp^+ called extra pressure drop. Finding that extra pressure drop, together with the vesicle shape deformation and its mobility, is the essential part of the investigations in the present work.

In the creeping-flow regime, the motion of the fluid inside and outside the vesicle is governed by the Stokes equations,

$$\nabla \cdot \mathbf{u} = 0, \quad \nabla \cdot \boldsymbol{\sigma} = -\nabla p + \eta \nabla^2 \mathbf{u} = \mathbf{0}, \qquad \mathbf{x} \in \mathrm{D} \setminus \Omega, \tag{4.2}$$

where $\mathbf{u}$, $\boldsymbol{\sigma}$ and p denote the exterior fluid velocity, stress tensor and pressure, respectively. Similar equations hold for the interior fluid velocity $\bar{\mathbf{u}}$, stress tensor $\bar{\boldsymbol{\sigma}}$ and $\bar{p}$ for $\mathbf{x} \in \Omega$. The fluid motion is coupled with the interface motion via the kinematic boundary condition,

$$\mathbf{u}(\mathbf{x}) = \bar{\mathbf{u}}(\mathbf{x}) = \frac{\mathrm{d}\mathbf{x}}{\mathrm{d}t} = \mathbf{u}_\Gamma, \qquad \mathbf{x} \in \Gamma, \tag{4.3}$$

where $\mathbf{x}$ is the membrane position. The dynamic boundary condition at the interface establishes a *nonlinear interaction* between the ambient flow and membrane mechanics,

$$\Delta\mathbf{f} + \mathbf{f}^m = \mathbf{0}, \qquad \mathbf{x} \in \Gamma, \tag{4.4}$$

wherein we assume the membrane is in quasi-static mechanical equilibrium; the membrane force density $\mathbf{f}^m$ balances the net traction $\Delta\mathbf{f}$ ($\equiv (\boldsymbol{\sigma} - \bar{\boldsymbol{\sigma}}) \cdot \mathbf{n}$) exerted on the membrane by the bulk fluids. Here and throughout this chapter, the unit normal vector of a surface $\mathbf{n}$ is pointing inward into the suspending fluid.

Additional boundary conditions for the velocity field include the no-slip condition at the tube wall,

$$\mathbf{u}(\mathbf{x}) = \mathbf{0}, \qquad \mathbf{x} \in W, \tag{4.5}$$

and vanishing far-field flow perturbation,

$$\mathbf{u}(\mathbf{x}) = \mathbf{u}^\infty(\mathbf{x}), \qquad \mathbf{x} \in I \cup O. \tag{4.6}$$

The velocity of the vesicle center of mass is given by

$$V = \frac{1}{\Omega}\int_\Omega \bar{u}_x \mathrm{d}^3\mathbf{x} = \frac{1}{\Omega}\int_\Gamma x(\mathbf{u}_\Gamma \cdot \mathbf{n})\mathrm{d}S(\mathbf{x}). \tag{4.7}$$

The enclosed volume

$$\Omega = \int_\Omega \mathrm{d}^3\mathbf{x} = \frac{1}{3}\int_\Gamma (\mathbf{x} \cdot \mathbf{n})\mathrm{d}S(\mathbf{x}) \tag{4.8}$$

is fixed, as the vesicle membrane is considered to be impermeable, at least on typical experimental time scales. The axial coordinate of the vesicle center of mass is defined by

$$x_G = \frac{1}{\Omega}\int_\Omega x\mathrm{d}^3\mathbf{x} = \frac{1}{2\Omega}\int_\Gamma x^2(\mathbf{n} \cdot \mathbf{e}_x)\mathrm{d}S(\mathbf{x}). \tag{4.9}$$

4.1.2 Membrane mechanics

A biomembrane is invariably a phospholipid bilayer, which is classically described as a two-dimensional, incompressible fluid elastic. This means that there exist a surface tension and bending energy associated with the "out-of-the-plane" motions of the membrane. Its elastic energy due to the Helfrich energy functional [69] is given by

$$E = \int_\Gamma \left[2\kappa H^2(\mathbf{x}) + \gamma(\mathbf{x})\right]\mathrm{d}S(\mathbf{x}), \tag{4.10}$$

where κ ($\sim 10^{-19}$ J) is the bending modulus, H is the local mean curvature (with the convention that curvature is equal to 1 for a unit sphere), and γ is the membrane tension, which is,

in fact, identical with the Lagrange multiplier used to enforce the surface incompressibility condition,

$$\nabla_{\mathrm{S}} \cdot \mathbf{u}_\Gamma = 0, \qquad \mathbf{x} \in \Gamma, \tag{4.11}$$

where $\nabla_{\mathrm{S}} = (\mathbf{I} - \mathbf{nn}) \cdot \nabla$ is the surface gradient.

The membrane force density $\mathbf{f}^m$, by the principle of virtual work, is the variational derivative of Eq. (4.10) with respect to small deformations of the surface [159],

$$\mathbf{f}^m = -\frac{\delta E}{\delta \mathbf{x}} = \mathbf{f}^b + \mathbf{f}^\gamma, \qquad \mathbf{x} \in \Gamma, \tag{4.12a}$$

$$\text{with} \quad \mathbf{f}^b = 2\kappa\big[\Delta_{\mathrm{S}} H + 2H(H^2 - K)\big]\mathbf{n}, \quad \mathbf{f}^\gamma = -2\gamma H\mathbf{n} + \nabla_{\mathrm{S}}\gamma, \tag{4.12b}$$

where $\mathbf{f}^b$ denotes the bending surface force density, which is purely normal, $\mathbf{f}^\gamma$ is the tension surface force density, K is the Gaussian curvature, and $\Delta_{\mathrm{S}} H = \nabla_{\mathrm{S}} \cdot \nabla_{\mathrm{S}} H$ is the Laplace-Beltrami operator of the mean curvature, which contains the fourth derivative of the surface position, posing serious algorithmic and numerical challenges to compute the bending forces [68].

4.1.3 Dimensionless parameters

The volume Ω and surface area A of a vesicle remain constant and define a volume-based radius $R_0 \equiv (3\Omega/(4\pi))^{1/3}$ and an area-based radius $R_A \equiv (A/(4\pi))^{1/2}$, respectively. Together with the tube radius R, the system geometry is completely parametrized by two dimensionless parameters which are independent of the flow conditions: the reduced volume ν (alternatively, the excess area Δ) and the confinement λ,

$$\nu \equiv \frac{\frac{4}{3}\pi R_0^3}{\frac{4}{3}\pi R_A^3} = \left(\frac{R_0}{R_A}\right)^3 = 6\sqrt{\pi}\Omega A^{-3/2}, \tag{4.13a}$$

$$\Delta \equiv 4\pi\left(\frac{4\pi R_A^2}{4\pi R_0^2} - 1\right) = 4\pi\left(\frac{1}{\nu^{2/3}} - 1\right), \tag{4.13b}$$

$$\lambda \equiv \frac{R_0}{R}. \tag{4.13c}$$

Here, we use the volumetric radius R_0 as the reference length. The reduced volume ($0 < \nu \leq 1$) or the excess area ($\Delta \geq 0$), characterizing the ability for the vesicle to deform and change shape, is commonly used in the literature, and they are related to each other by (4.13b). The confinement measures the size of the vesicle relative to the radius of the tube. Natural scales for velocities and time are the mean velocity U of the ambient flow and R_0/U, respectively. Pressure and hydrodynamic stress are scaled by the typical viscous stress $\eta U/R_0$, and membrane tension is scaled by ηU. The relative importance of membrane bending force density and viscous traction in the balance of normal stress on the membrane (Eqs. (4.4) and (4.12b)) defines the bending-based capillary number $\mathrm{Ca}_{\mathrm{B}} \equiv \eta U R_0^2/\kappa$. Finally, there is no viscosity contrast between the fluid inside and outside the vesicle as we are interested in the stationary axisymmetric shapes which do not depend upon the inner viscosity [27, 136]. Hence, the

vesicle motion is determined by three independent dimensionless parameters: the reduced volume ν, the confinement λ, and the (bending) capillary number $\mathrm{Ca_B}$. We note that while ν is a fixed quantity for a given vesicle, namely independent of which reference length is used, the other two parameters depend on that length. However, solutions under different scalings are easily converted from one to another in terms of ν and λ. For example, the surface area-based confinement $\lambda_A \equiv R_A/R = \lambda/\nu^{1/3}$, and the tube's radius-based capillary number $\mathrm{Ca_R} \equiv \eta U R^2/\kappa = \mathrm{Ca_B}/\lambda^2$. Occasionally, we nondimensionalize physical quantities using the scalings of cited references in order to facilitate the comparison with those results.

4.2 Boundary element method simulation

The fluid-cell membrane interaction problem described in Section 4.1 is solved using an axisymmetric boundary element method (BEM) [150], which is based on the numerical method for 3D model [21], therefore, only the complementary information is provided below.

First, in view of the linearity of the Stokes equations, we decompose the total velocity field around the vesicle into an undisturbed component $\mathbf{u}^\infty$ and a disturbance component $\mathbf{u}^+$ due to the presence of the vesicle, namely, $\mathbf{u} = \mathbf{u}^\infty + \mathbf{u}^+$. The disturbance velocity at a point $\mathbf{x}_0$ that lies inside the control volume D or on its boundaries ∂D can be represented as a boundary integral equation [126, 127],

$$\mathbf{u}^+(\mathbf{x}_0) = -\frac{1}{8\pi\eta}\int_{\partial D} \mathbf{G}(\mathbf{x}_0,\mathbf{x})\cdot\mathbf{f}^+(\mathbf{x})\mathrm{d}S(\mathbf{x}), \tag{4.14}$$

where $\mathbf{G}$ is the free-space Green's function, $\mathbf{f}^+ \equiv \boldsymbol{\sigma}^+\cdot\mathbf{n}$ is the disturbance surface traction. Since the perturbation flow generated by a point-force distribution decays exponentially with distance from the vesicle [102, 150], if the inlet and outlet are sufficiently far from the vesicle, then the flow perturbation near the inlet and outlet sections virtually vanishes. Furthermore, if we consider axisymmetric flow configuration only, the surface integrals can be explicitly integrated in the azimuthal direction with $\mathrm{d}S = r\mathrm{d}\phi\mathrm{d}l$, where $\mathrm{d}l$ is the differential arc length of the trace of the boundary ∂D in the x-r azimuthal plane [127, 150]. Finally, we obtain a more specific form to Eq. (4.14), yielding the total velocity field as follows:

$$\begin{aligned} u_\alpha(\mathbf{x}_0) \;=\; & u_\alpha^\infty(\mathbf{x}_0) + \frac{1}{8\pi\eta}\left[\int_\Gamma M_{\alpha\beta}(\mathbf{x}_0,\mathbf{x})f_\beta^m(\mathbf{x})\mathrm{d}l(\mathbf{x}) - \int_W M_{\alpha\beta}(\mathbf{x}_0,\mathbf{x})f_\beta^w(\mathbf{x})\mathrm{d}l(\mathbf{x})\right. \\ & \left. + p_{\mathrm{in}}^+\int_I M_{\alpha x}(\mathbf{x}_0,\mathbf{x})\mathrm{d}l(\mathbf{x})\right], \end{aligned} \tag{4.15}$$

where the Greek subscripts α and β are either x or r, representing the axial and radial components respectively, $\mathbf{x} = x\mathbf{e}_x + r\mathbf{e}_r$, $\mathbf{M}$ is the free-surface axisymmetric Green's function [127, 150], $\mathbf{f}^w(\equiv f_x^w\mathbf{e}_x + f_r^w\mathbf{e}_r)$ stands for the disturbance stress distribution at the tube wall with

the shear stress f_x^w and the normal stress $f_r^w (= -p^+, \mathbf{x} \in W)$, and p_{in}^+ the disturbance pressure over the inlet while setting, without loss of generality, $p_{\text{out}}^+ = 0$ for the disturbance pressure over the outlet.

Application of Eqs. (4.5) and (4.15) leads to an additional integral boundary equation that allows the calculation of the disturbance wall stress $\mathbf{f}^w$,

$$\begin{aligned} \int_W M_{\alpha\beta}(\mathbf{x}_0, \mathbf{x}) f_\beta^w(\mathbf{x}) \mathrm{d}l(\mathbf{x}) &= \int_\Gamma M_{\alpha\beta}(\mathbf{x}_0, \mathbf{x}) f_\beta^m(\mathbf{x}) \mathrm{d}l(\mathbf{x}) \\ &\quad + p_{\text{in}}^+ \int_I M_{\alpha x}(\mathbf{x}_0, \mathbf{x}) \mathrm{d}l(\mathbf{x}), \qquad \mathbf{x}_0 \in W. \end{aligned} \tag{4.16}$$

The extra pressure drop can be obtained using the reciprocal theorem [126] of the Stokes flow; it is expressed in terms of the membrane load and the ambient velocity field,

$$\begin{aligned} \Delta p^+ \equiv p_{\text{in}}^+ - p_{\text{out}}^+ &= -\frac{1}{Q} \int_\Gamma \mathbf{f}^m(\mathbf{x}) \cdot \mathbf{u}^\infty(\mathbf{x}) \mathrm{d}S(\mathbf{x}) \\ &= -\frac{4}{R^2} \int_\Gamma r \left(1 - \frac{r^2}{R^2}\right) f_x^m(\mathbf{x}) \mathrm{d}l(\mathbf{x}). \end{aligned} \tag{4.17}$$

The membrane is discretized by N^m piecewise linear 2D elements, consisting of a collection of points of $\{\mathbf{x}_n(t), n \in 0 \dots N^m\}$. The points are distributed according to the magnitude of the membrane's mean curvature H, thereby allowing the local mesh refinement in high-curvature regions. This is important given large deformations of vesicles involved in flows. The mesh points at the tube wall, composed of N^w linear elements, are uniformly distributed. The differential surface operators, which are involved in the calculation of surface incompressibility (4.11) and bending forces (4.12b), are computed on each element of the membrane with a parametrization (Γ, ϕ) of the surface.

Starting from some initial configuration of the vesicle shape, the preceding three integral equations, together with the membrane incompressibility condition (4.11), allow the computation of Δp^+, $\mathbf{f}^w$, the interfacial velocity $\mathbf{u}_\Gamma$ and the membrane tension γ at each time step via the boundary element method, as described in [21, 150]. The vesicle translational velocity V is computed from (4.7).

The vesicle interface is advected according to

$$\frac{\mathrm{d}\mathbf{x}(t)}{\mathrm{d}t} = u_n(\mathbf{x}) \mathbf{n}(\mathbf{x}), \tag{4.18}$$

where $\mathbf{x}$ is an interface node and $u_n = \mathbf{u}_\Gamma \cdot \mathbf{n}$ is given by (4.15). This means the movements of the bilayers in the normal and tangential directions are treated differently, namely in Lagrangian fashion for the former and with a Eulerian description for the latter. Indeed, the tangential movement of nodes, which does not change the membrane shape, offers the possibility of a redistribution of nodes–remeshing along the membrane. At each time we employ a keeping-the center-of-mass strategy that the vesicle is re-centered at the origin by

subtracting the vesicle center of mass $(x_G, 0)$ from the membrane position. Since this process, which is equivalent to replacing u_n by $u'_n = u_n - \mathbf{V} \cdot \mathbf{n}$ in (4.18), does not modify the stress field, the vesicle shape remains unchanged. Equation (4.18) is solved numerically by a semi-implicit time stepping scheme [21] in which the bending forces are computed at the advected, new position of the membrane and, therefore improving long term stability of the algorithm. A steady state is obtained when the maximum absolute normal velocity $|u'_n|/U$ is less than a chosen tolerance ($\sim 10^{-5}$), with N^m ranging from 130 to 300, and N^w from 300 to 1000, depending upon the reduced volume ν and the confinement λ. The tube has a total length of $L_w = O(10R_0)$, so the outlet and inlet sections are located at a distance $x = \pm L_w/2$ from the vesicle center of mass. The dimensionless time step $U\Delta t/R_0$ ($\sim 5 \times 10^{-3} - 5 \times 10^{-5}$) decreases as ν decreases and as either N^m or λ increases. Since both the volume and surface area of the vesicle are conserved, the change in the enclosed volume and surface area during simulations provides an indication of the accuracy of the computations. The relative volume and surface area variations were found to be $\sim 0.01\% - 0.1\%$ over a typical full simulation ($\sim 10^4 - 10^5$ time steps).

While several studies have already been conducted in [150] in order to validate the axisymmetric BEM code, the validation of a prediction for the hydrodynamical quantities V and Δp^+ has not been reported so far. Therefore, we first considered the well-known example of the motion of a liquid drop in a circular tube and compared our numerical results with those reported in Ref. [90]. The drop is free of bending stiffness ($\kappa = 0$) and has a constant surface tension γ. The motion of the drop for a given confinement λ is determined by the surface tension-based capillary number $\mathrm{Ca} = \eta U/\gamma$. The comparison in Table I shows excellent agreement.

	V/U		$\Delta p^+/(\eta U/R)$	
Ca	Present work	Ref. [90]	Present work	Ref. [90]
0.05	1.4218	1.42	2.6591	2.65
0.1	1.4543	1.45	2.2532	2.25
0.2	1.5311	1.53	1.4981	1.50
0.3	1.5999	1.60	1.0063	1.01
0.5	1.7021	1.70	0.4889	0.49

Table 4.1: Comparison of droplet relative velocity V/U and dimensionless extra pressure drop $\Delta p^+/(\eta U/R)$ as a function of the capillary number $\mathrm{Ca} = \eta U/\gamma$ for $\lambda = 0.8$ to those reported in Ref. [90].

Additionally, we have checked in two ways whether a numerical discretization, in terms of the number of elements (of both N^m and N^w), was fine enough to sufficiently resolve the drainage fluid of thin liquid film between the membrane and the tube wall: (i) can a stationary solution be achieved ? and most importantly (ii) is the steady velocity ratio V/U larger than unity? An insufficient discretization was found to result in significantly large viscous

and confinement-dependent friction on the membrane and therefore a smaller velocity ratio V/U, which sometimes is much less than unity. Under high confinement, especially for highly deflated vesicles (i.e., $\nu \leq 0.7$) when λ approaches its critical value, a substantially large number of elements, say $N^m = O(300)$ and $N^w = O(1000)$ for $\nu = 0.6$, is needed to accurately resolve the vesicle shape and membrane traction. Our numerical experiments suggest an empirical relationship between the mesh size and the film thickness h:

$$\delta x^m \approx h, \quad \delta x^w \approx \frac{1}{2}h, \tag{4.19}$$

where δx^m and δx^w denote a typical mesh size (i.e., element length) on the membrane and at the tube wall, respectively, in the region of the liquid film.

4.3 Results and discussion

4.3.1 Phase diagram of shapes and shape transition

In aqueous solution, lipid vesicles exhibit a large variety of shapes and shape transformations [100, 139], in particular, they can exhibit a biconcave shape typical of red blood cells. The equilibrium shape of a vesicle is determined by minimization of the Helfrich energy (4.10) of the membrane, resulting in different families of solutions with respect to the reduced volume ν. The global minimum is for a prolate if $\nu \in [0.652 : 1]$, an oblate if $\nu \in [0.592 : 0.651]$, and a stomatocyte if $\nu \in [0.05 : 0.591]$. When confined in capillary tubes subject to a pressure-driven flow, however, vesicles assume complex shapes and behave in different ways due to the nonlinear interplay between bending elasticity, hydrodynamic stresses, and confinement. For the axisymmetric case being considered in this study, there are two commonly steady-state shapes which are classified as bullet-like and parachute-like shapes, the latter being characterized by a concave (negative curvature) rear part.

Figure 4.2 shows steady-state shapes for a vesicle of $\nu = 0.84$ confined in a tube flow with unity radius ratio (i.e., $\lambda = 1$) for increasing flow rates characterized by the bending capillary number $\mathrm{Ca_B}$. Two limiting cases are clearly illustrated in Figure 4.2. One is no flow ($\mathrm{Ca_B} = 0$), in which the equilibrium shape – symmetric between the front and the rear – is determined solely by the minimization of the bending energy. The other is $\mathrm{Ca_B} \to \infty$, which corresponds to an infinitely small bending resistance. For this particular combination of parameter groups, the rear part of the vesicle becomes almost flat (i.e., zero curvature). This result is interesting because, for a given vesicle in a tube, its steady-state shape lies between these two limiting profiles. Another noticeable feature is that when $\mathrm{Ca_B} \geq 50$, the shape is virtually independent of $\mathrm{Ca_B}$. This property allows us to fix $\mathrm{Ca_B} = 50$ while studying the motion and deformation of a confined vesicle at high flow rates (i.e., $U/(2R) > 50\,\mathrm{s}^{-1}$) [130, 136]. A zero-bending elasticity or equivalently an infinity $\mathrm{Ca_B}$ is, however, not permitted because of small radii of curvature occurring at the trailing edge, especially for highly deflated vesicles.

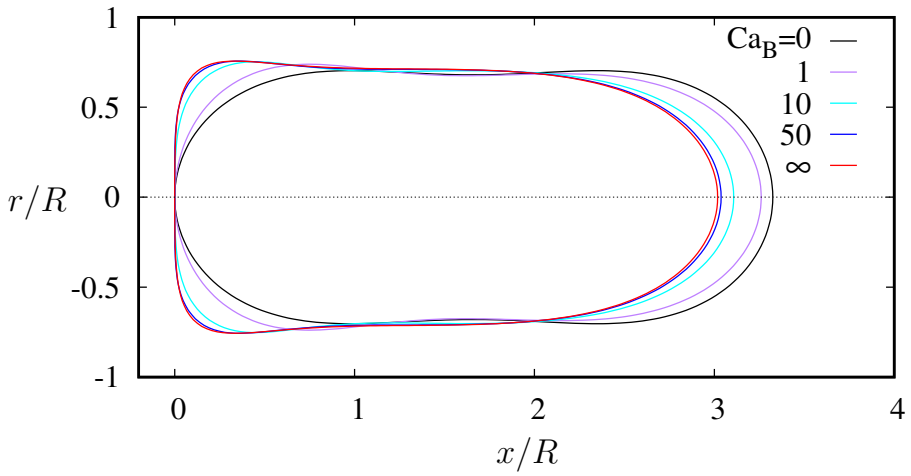

Figure 4.2: Steady-state vesicle profile as a function of the bending capillary number $\mathrm{Ca_B}$ for $\nu = 0.84$ and $\lambda = 1$.

Steady-state vesicle shapes for the reduced volume ranging from 0.98 to 0.6 are shown in Figure 4.3 at different degrees of confinement. A near-spherical vesicle (i.e., $\nu = 0.98$) always exhibits a bullet-like shape, whereas shapes undergo a transition from parachute to bullet as the confinement increases (i.e., large λ). The shapes with $\nu = 0.6$, which are particularly relevant to red blood cells, mark a transition starting from a bell shape and ending in a sphero-cylinder. Clearly, increasing λ increases the length of the vesicle but reduces the size of the gap between the vesicles and the tube. At high confinement, the vesicles tend to attain a sphero-cylinder consisting of a long cylindrical main body and two hemispherical endcaps.

A phase diagram of steady-state shapes is presented in Figure 4.4, together with experimental results of Ref. [32] obtained in a square cross-section channel. Increasing λ makes the transition shifted towards lower values of reduced volume, which means a bullet-like shape is favored at high confinement. The present numerical results are in good agreement with the experimental observations, suggesting the geometry of the channel might not affect too much the parachute-bullet transition. Interestingly, there is a clear separation between the bullet region and parachute region in the (ν, λ) space, as revealed in Figure 4.5(a). Bullet-like and parachute-like shapes are identified according to the curvature of the rear part of vesicles; a flat rear marks as a transition point in the (ν, λ) space. Remarkably, the transition point decreases almost linearly with increasing confinement when $\lambda \geq 0.6$. A linear fitting to the transition points gives a correlation

$$\nu_{\mathrm{T}} = 1.126 - 0.29\lambda, \qquad \text{for} \quad \nu \leq 0.93, \tag{4.20}$$

which are obtained at $\mathrm{Ca_B} = 50$. A careful examination of numerical results suggests this relationship is valid even for a small bending capillary number since steady shapes are virtually independent of $\mathrm{Ca_B}$ under high confinement. The transition from a parachute shape

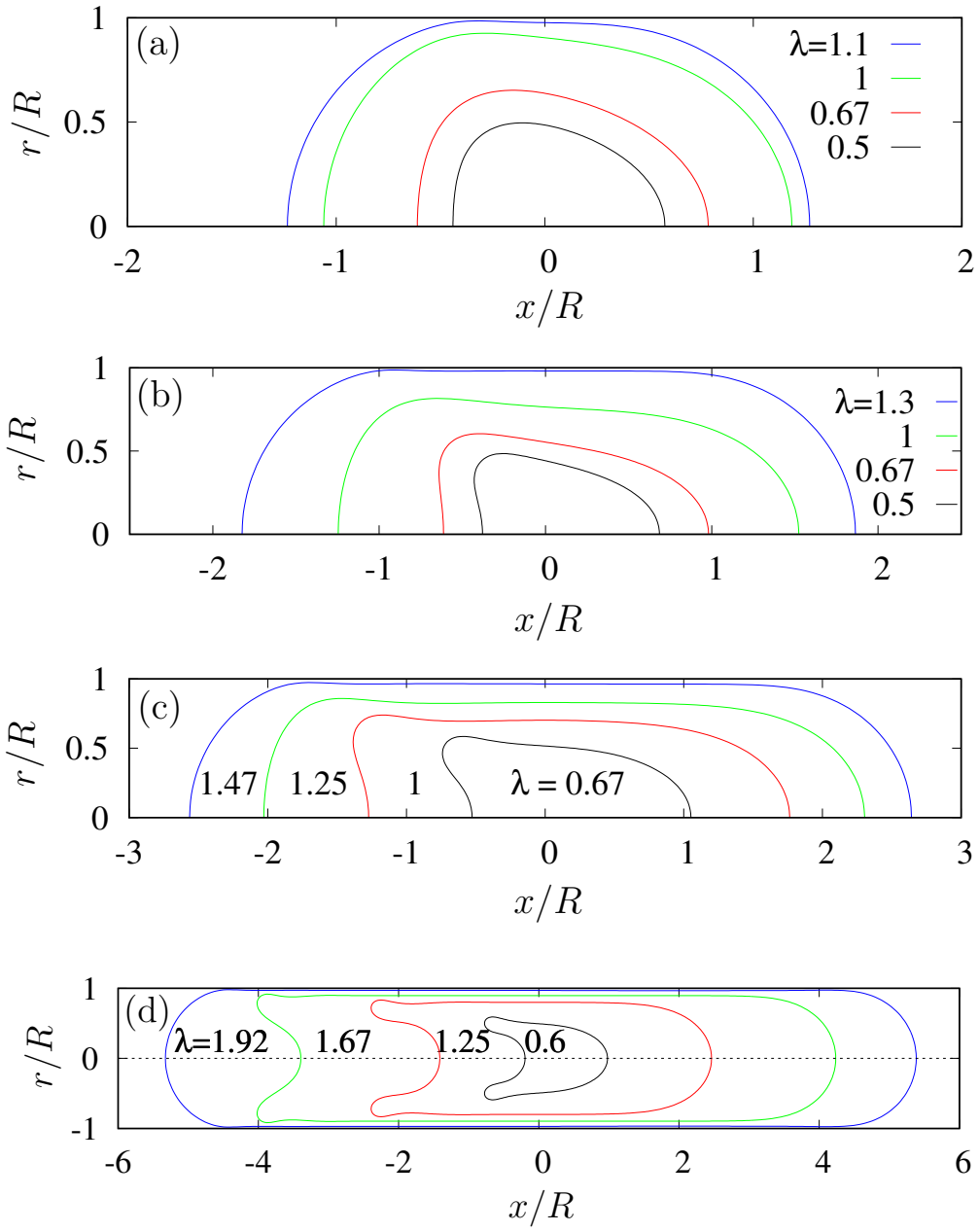

Figure 4.3: Steady-state vesicle shapes as a function of the confinement λ for a wide range of reduced volumes ν ($\mathrm{Ca_B} = 50$): (a) $\nu = 0.98$, (b) $\nu = 0.9$, (c) $\nu = 0.8$ and (d) $\nu = 0.6$.

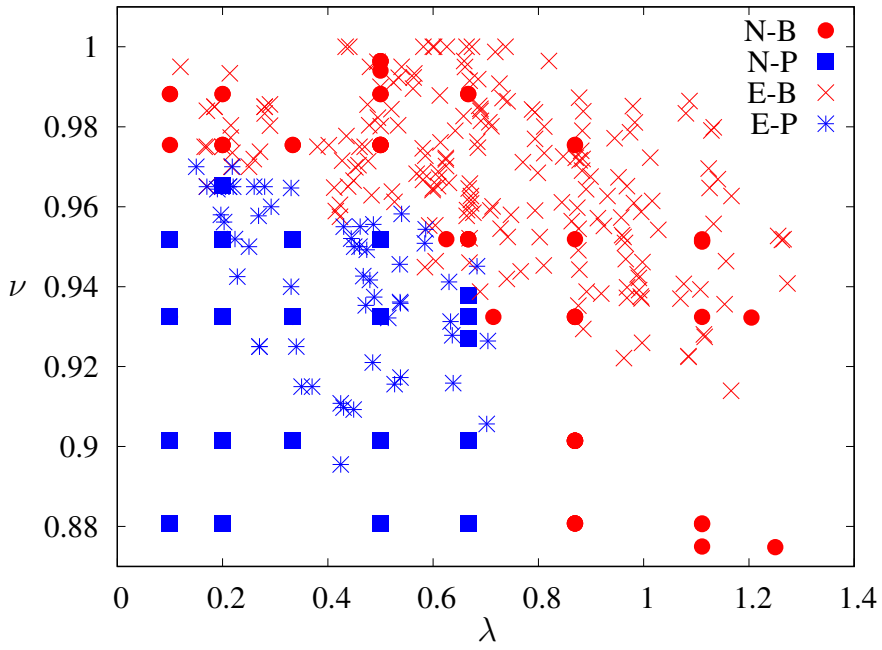

Figure 4.4: Parachute-bullet phase diagram in the (ν, λ) space. Filled symbols denote the present numerical results (● for bullet-like shape, ■ for parachute-like shape), crosses represent experimental data of Ref. [32] (× for bullet-like shape, ∗ for parachute-like shape). Capillary number varies over four orders of magnitude ($10^1 < \mathrm{Ca_B} < 10^4$).

to a bullet one for a vesicle having the same reduced volume of red blood cells takes place at very high confinement, i.e., $\lambda_\mathrm{T}(\nu = 0.6) \simeq 1.8$. The shape at the transition point, as shown in Figure 4.5(b), consists of a long cylindrical body and a front endcap, leaving a narrow vesicle-wall gap of $\sim 7\%$ of the tube's radius.

4.3.2 Critical confinement

Both the volume and surface area of a vesicle are conserved at least on the time scale of typical experiments. These geometric constraints impose a critical confinement λ_c ($\equiv 2R_0/d_c$) corresponding to a lower limit d_c to the diameter of the tubes through which the vesicle may pass intact. The critical confinement is calculated by assuming that the two hemispherical endcaps are tightly fitting the tube cross-section; its relation with the reduced volume ν is given by a cubic equation

$$2\lambda_c^3 - 3\nu^{-2/3}\lambda_c^2 + 1 = 0, \tag{4.21}$$

whose solution is

$$\lambda_c = \frac{1}{2\nu^{2/3}}\left[1 + \left(1 - 2\nu^2 + 2\nu\sqrt{\nu^2 - 1}\right)^{1/3} + \left(1 - 2\nu^2 + 2\nu\sqrt{\nu^2 - 1}\right)^{-1/3}\right]. \tag{4.22}$$

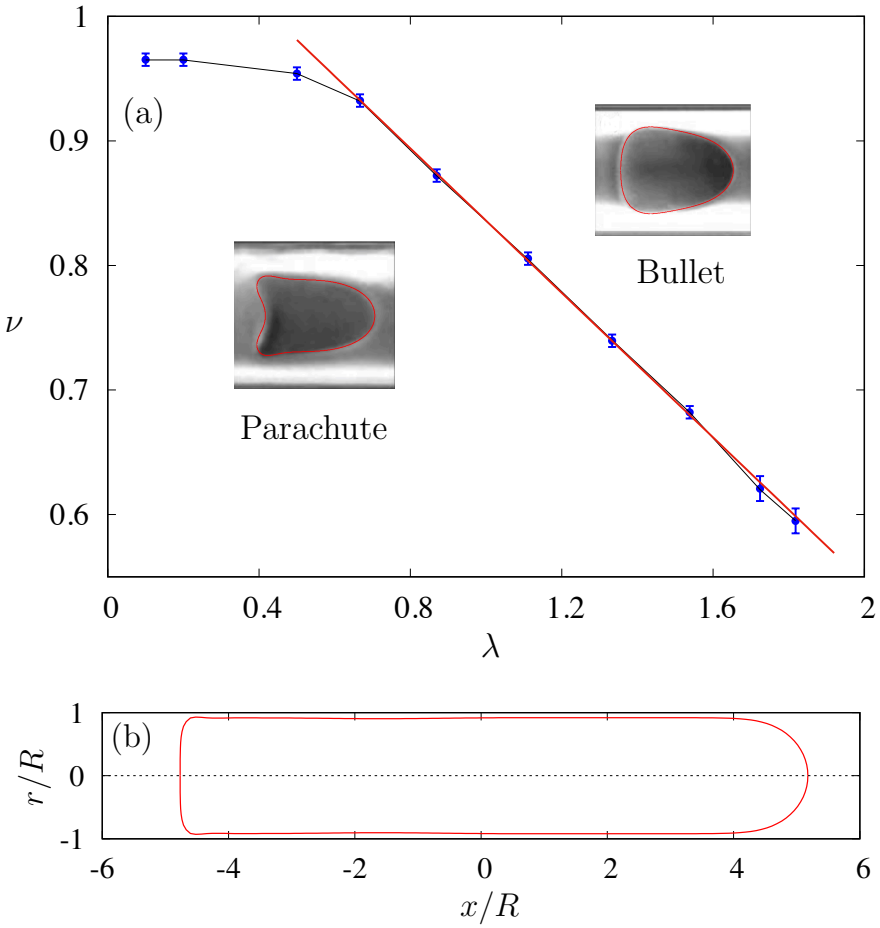

Figure 4.5: (a) Shape transition line from parachute (low limit in error bars) to bullet (up limit in error bars) in the (ν, λ) space ($\mathrm{Ca_B} = 50$). Vesicles are flowing from left to right. The two typical vesicles are characterized, respectively, by $\nu = 0.95$, $\lambda = 0.8$ and $\mathrm{Ca_B} = 5$ for the bullet-like shape, and $\nu = 0.83$, $\lambda = 0.67$ and $\mathrm{Ca_B} = 15$ for the parachute-like shape. Insets show the comparison of the computed shapes (red line) with the reported ones in an experimental study [151]. (b) The shape at the parachute-bullet transition of a vesicle with the same typical deflation of red blood cells ($\nu = 0.6$) flowing through a narrow capillary tube ($\lambda \simeq 1.8$).

This critical confinement defines an upper limit ℓ_c to the reduced vesicle length $\ell\ (\equiv L/R)$

$$\ell_c \equiv \frac{2L_c}{d_c} = 2\nu^{-2/3}\lambda_c^2. \tag{4.23}$$

The variation of λ_c with ν ranging from 0.6 to 1 is plotted in Figure 4.6, together with the parachute-bullet transition line given by $\lambda_T = 3.88 - 3.45\nu$ (c.f., Eq. (4.20)). When $\lambda > \lambda_c$, the vesicle cannot pass through the tube without rupturing the membrane. Assuming red blood cells have a typical volume $\Omega = 90\ \mu\text{m}^3$, which gives a volumetric radius $R_0 \simeq 2.8\ \mu$m, one then obtains a critical cylindrical diameter of normal human erythrocyte $d_c = 2R_0/\lambda_c \simeq 2.8\ \mu$m ($\lambda_c \simeq 1.98$ for $\nu = 0.6$) and the maximum length of cells $L_c \simeq 15.4\ \mu$m ($\ell_c \simeq 11$). This means that a normal human erythrocyte can squeeze through capillaries that are smaller than half the diameter of a red blood cell ($\simeq 8\ \mu$m).

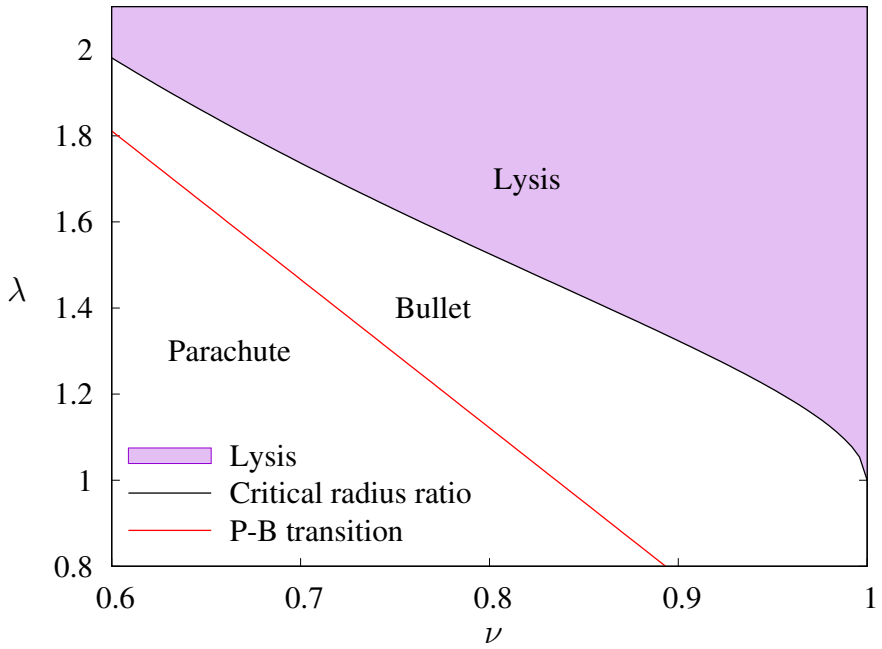

Figure 4.6: Critical confinement λ_c as a function of the reduced volume ν. Membrane lysis occurs when $\lambda > \lambda_c$. The red line denotes the shape transition from parachute to bullet.

4.3.3 Lubrication film thickness

As shown in Figure 4.3, under high confinement, a liquid film of nearly uniform thickness is formed between the front and rear endcaps. Let h denote a typical film thickness of the gap separating the vesicle membrane and tube wall, the narrow-gap theory in Appendix A

yields an asymptotic behavior of the clearance parameter $\delta(\equiv h/R)$ in terms of a small perturbation parameter $(1-\lambda/\lambda_c) << 1$,

$$\delta = 1 - \lambda/\lambda_c + O\left[(1-\lambda/\lambda_c)^2\right]. \tag{4.24}$$

Numerical results of δ for ν ranging from 0.98 to 0.6 are plotted in Figure 4.7 and compared with its asymptotic behavior given by (4.24). Despite a wide range of the reduced volumes being considered, Figure 4.7 makes it clear that when $1-\lambda/\lambda_c < 0.1$ – namely in the small-gap regime, the numerical results approach the prediction (4.24); minimal thickness are about 2–5% of the tube's radius when $\lambda/\lambda_c \simeq 0.98$.

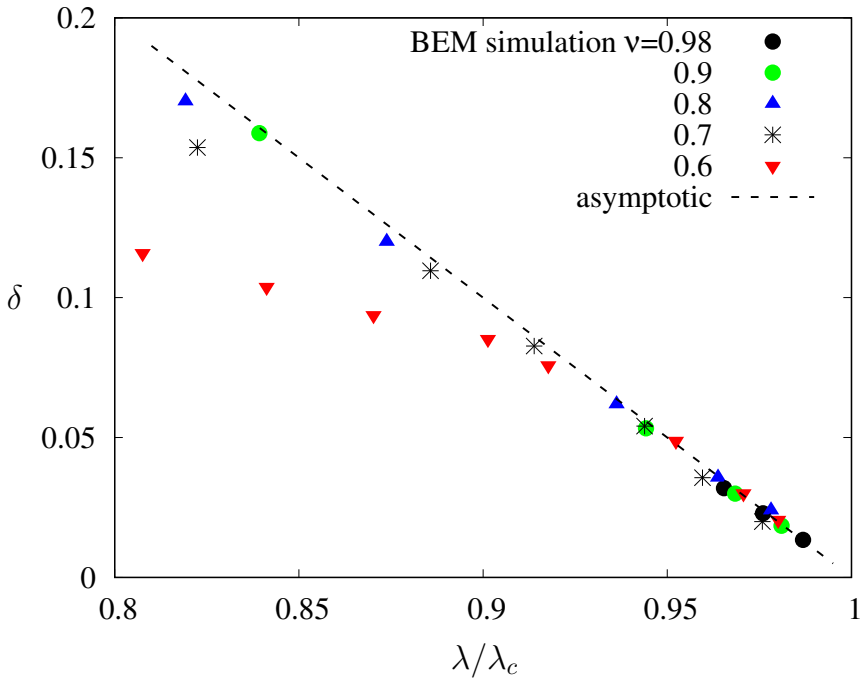

Figure 4.7: The dimensionless thickness of the lubrication layer δ plotted as a function of the reduced radius ratio λ/λ_c for a wide range of reduced volumes ν ($\mathrm{Ca_B} = 50$), together with the asymptotic prediction (4.24).

As derived in the appendix, the film thickness is controlled by the membrane tension γ in the lubrication layer. The clearance size is found to be proportional to the 2/3 power of the capillary number $\mathrm{Ca_v}$

$$\delta \simeq c_0 {\mathrm{Ca_v}}^{2/3}, \tag{4.25}$$

where the vesicle tension-mobility-based capillary number $\mathrm{Ca_v} = \eta V/\gamma_F$, γ_F is the membrane's frontal tension, also the highest tension in the membrane. We note that the numerical prefactor c_0 differs slightly in the literature; $c_0 \simeq 2.123$ in Ref. [136] while $c_0 \simeq 2.05$ in Ref. [27]. A fitting to the present numerical results yields $c_0 \simeq 2$ for $\mathrm{Ca_v} < 10^{-2}$, as

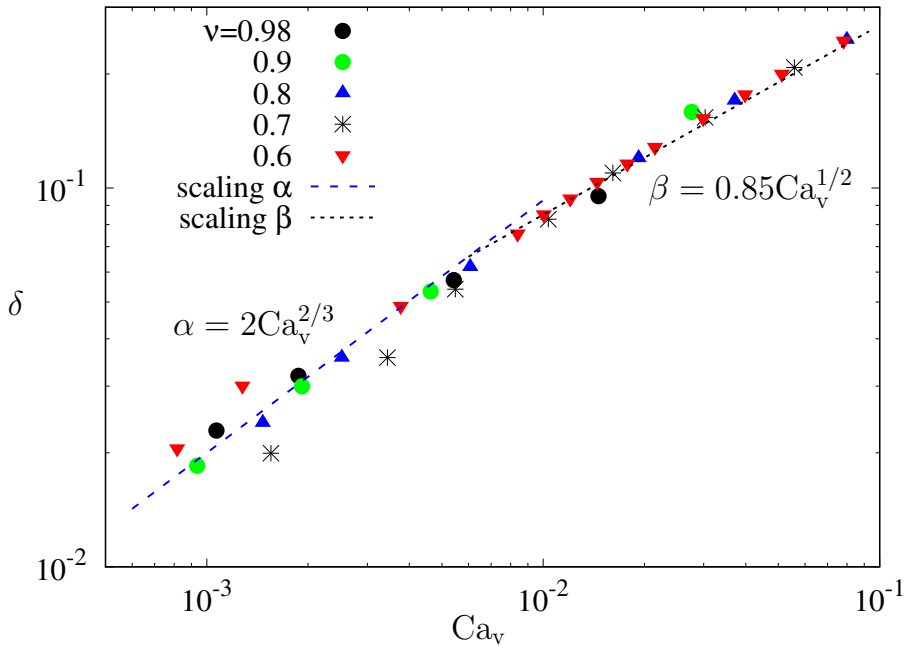

Figure 4.8: The dimensionless thickness of the lubrication layer δ plotted as a function of the capillary number $\mathrm{Ca_v} = \eta V/\gamma_\mathrm{F}$ for a wide range of reduced volumes ν, together with two scalings.

shown in Figure 4.8. In addition, Figure 4.8 reveals a characteristic change in power scaling from the 2/3 power regime for small $\mathrm{Ca_v}$ to the 1/2 power regime for large $\mathrm{Ca_v}$. The separation of the two regimes occurs at $\mathrm{Ca_v} \simeq 6 \times 10^{-3}$. Therefore, our numerical results support one of the findings of Ref. [27] that the thickness of the lubrication layer, at high flow rates, is independent of the bending energy and is determined solely by the membrane tension. It should be emphasized that the 2/3 power law regime found in the case of a long bubble in tubes [25] stems from the different underlying mechanisms compared to vesicles; a stress-free surface for the former while a "no-slip" hydrodynamic boundary condition for vesicles.

The mechanical tension of a membrane is identical with the Lagrange multiplier tension γ that enforces a certain, fixed membrane area [101]. For the lipid bilayers, the rupture tension, which represents the largest mechanical tension that can be applied to the membrane, is of the order of a few mN/m. It is, therefore, interesting to examine whether our BEM simulations are indeed able to predict a mechanical tension approaching that limit. For $\nu = 0.6$ typical of red blood cells and under the maximum possible confinement that we have reached, i.e., $\lambda = 1.94$ ($\lambda_c \simeq 1.98$), the maximum dimensionless tension is found to be $\gamma_\mathrm{max} \simeq 1.2 \times 10^3$, which gives rise to a dimensional mechanical tension about 1.5 mN/m. Here the tension is scaled by $\gamma_\mathrm{ref} = \eta U = \kappa \mathrm{Ca_B}/R_0^2 = 1.28\,\mu$N/m, with $\mathrm{Ca_B} = 50$, $\kappa = 2 \times 10^{-19}$ J and $R_0 = 2.8\,\mu$m. The predicted mechanical tension at the proximity of the maximum confinement is actually of the order of the rapture tension.

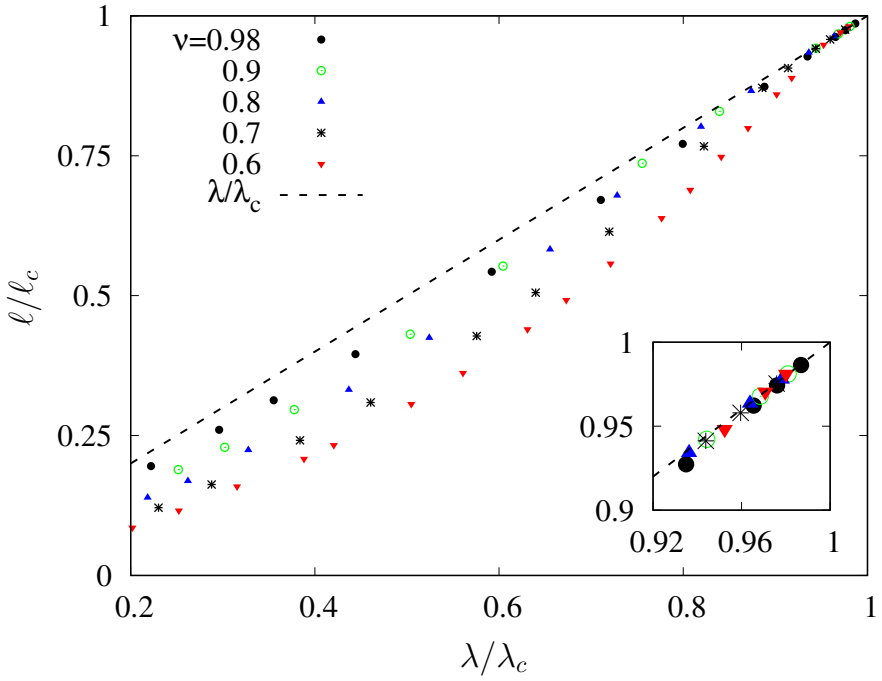

Figure 4.9: Normalized vesicle length ℓ/ℓ_c versus the reduced radius ratio λ/λ_c for a wide range of reduced volumes ν ($\mathrm{Ca_B} = 50$), together with the linear scaling $\ell/\ell_c = \lambda/\lambda_c$ (Eq. (4.26)).

The reduced vesicle length ℓ is an important geometric parameter that characterizes the vesicle deformation when flowing in a tube. It is also an easily accessible parameter in tube-flow experiments. In addition, it was found that there is an upper limit to the reduced vesicle length, given by Eq. (4.23). Figure 4.9 shows the normalized vesicle length ℓ/ℓ_c as a function of the reduced radius ratio λ/λ_c for a wide range of reduced volumes ν. It is quite clear that the simulated vesicle lengths tend towards its limiting behavior as $\lambda \to \lambda_c$. The correlation

$$\ell = \ell_c \frac{\lambda}{\lambda_c} = 2\nu^{-2/3}\lambda_c^2 \frac{\lambda}{\lambda_c}, \tag{4.26}$$

suggests an estimated vesicle length for given ν and λ. It is also noticed that this relation gives a more precise estimate of the length for less deflated vesicles. This is because the shape transition point decreases with increasing confinement, as shown in Figure 4.5(a). For comparison, the asymptotic theory of Ref. [10] showed that $\ell = \ell_c + O(1 - \lambda/\lambda_c)$ as $\lambda \to \lambda_c$, which is effectively equivalent to Eq. (4.26) when $\lambda = \lambda_c$. But the proposed correlation in the present study allows not only precisely predicting the vesicle length under high confinement but also giving an estimate of the length at different degrees of confinement.

4.3.4 Vesicle mobility and extra pressure drop

Vesicle mobility, measured in the relative velocity V/U, and dimensionless extra pressure drop $\Delta p^+ R_0/(\eta U)$ are the most important hydrodynamical quantities of interest. Espe-

cially, the dimensionless extra pressure drop is involved in the determination of the relative apparent viscosity of a vesicle suspension in tube flow (see Sec. 4.3.5). Unlike in an unperturbed Poiseuille flow in which the mean flow velocity U is a linear function of the pressure drop Δp^0, V and Δp^+ are strongly nonlinear coupled due to the vesicle's deformation. Prediction of V/U and $\Delta p^+ R_0/(\eta U)$ has been recently reported in Ref. [9] but limited to the reduced volume up to 0.7, presumably due to the difficulty of dealing with the reduced volume of 0.6 in a 3D computation. The present BEM simulations provide a whole range of these quantities in terms of the reduced volume ν and the confinement λ, thus extending previous studies of vesicle hydrodynamics in tube flows. The results are shown in Figure 4.10 for the relative velocity and in Figure 4.11 for the dimensionless extra pressure drop. It is clear that vesicles with $\nu = 0.6$ (mimicking red blood cells) exhibit distinct features.

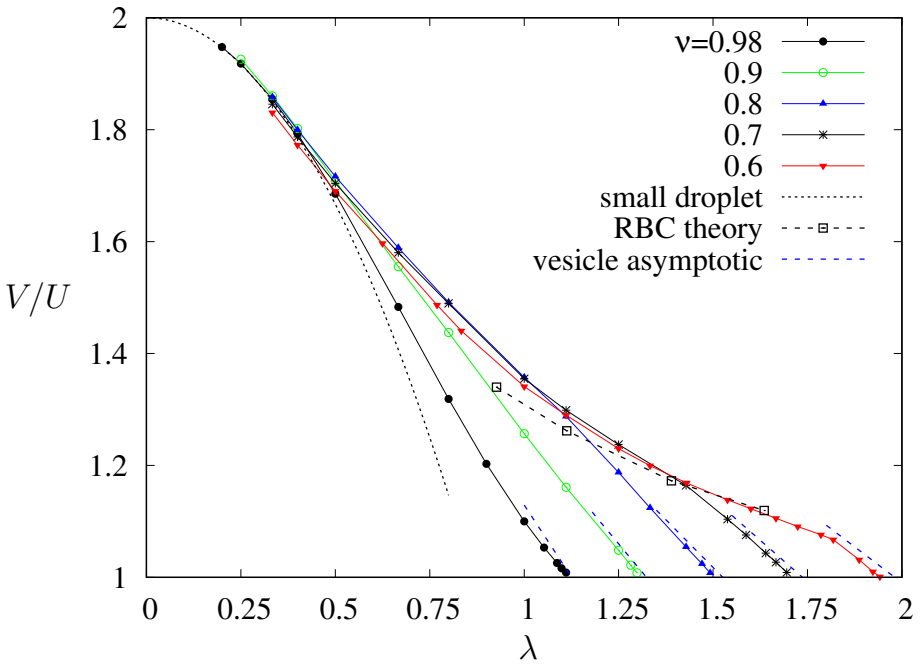

Figure 4.10: Variation of the relative velocity V/U as a function of the confinement λ for a wide range of reduced volumes ν ($\mathrm{Ca_B} = 50$), together with asymptotic predictions. The dotted curve shows the asymptotic prediction for a small spherical droplet moving along the centreline of a tube (4.27a). The dashed curves are the asymptotic predictions for highly confined vesicles (4.28a). Also shown is the prediction of a lubrication model for red blood cells [136].

The relative velocity lies between 2 and 1. The former represents an infinitely small vesicle traveling along the tube axis with the centerline maximum flow velocity, and the latter, for a tightly fitting vesicle moving at the mean flow velocity as a "piston" through the tube. The dimensionless extra pressure drop, however, exhibits astonishing variations – six orders of

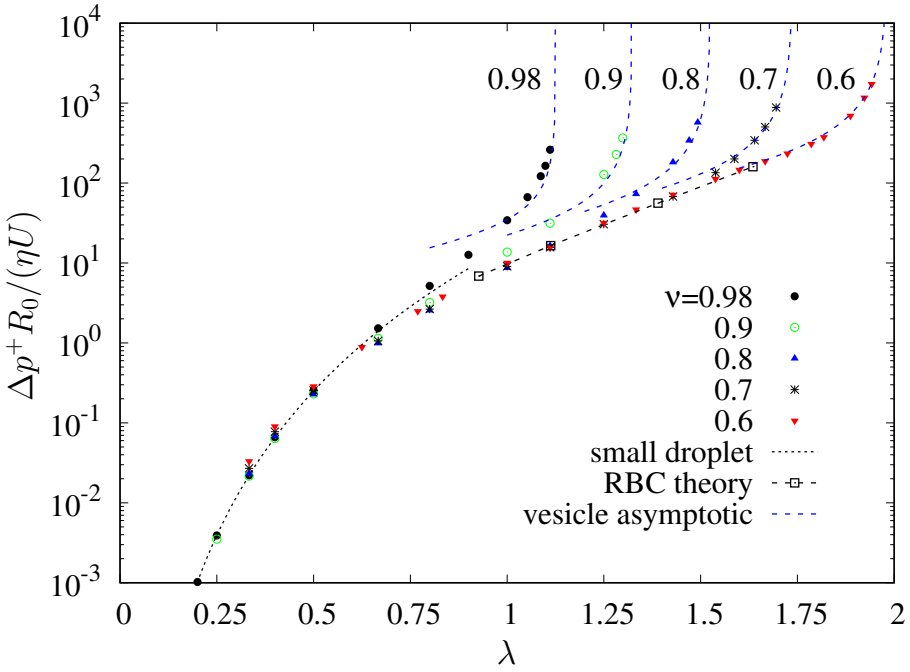

Figure 4.11: Variation of the dimensionless pressure drop $\Delta p^+ R_0/(\eta U)$ as a function of the confinement λ for a wide range of reduced volumes ν ($\mathrm{Ca_B} = 50$), together with asymptotic predictions. The dotted curve shows the analytical prediction for a small spherical droplet (4.27b). The dashed curves are the asymptotic predictions for highly confined vesicles (4.28b). Also shown is the prediction of a lubrication model for red blood cells [136].

magnitude. Under weak confinement (i.e., small λ), the simulation results are in excellent agreement with the theoretical predictions for a small spherical droplet flowing along the centreline of a tube [24, 70], given by

$$\frac{V}{U} = 2 - \frac{4}{3}\lambda^2 + O(\lambda^3), \tag{4.27a}$$

$$\frac{\Delta p^+ R_0}{\eta U} = 16\lambda^6 + O(\lambda^{11}). \tag{4.27b}$$

For instance, when $\lambda < 0.5$, the relative errors as compared to the theoretical predictions are less than 1%, particularly for nearly spherical vesicles. The case of $\nu = 0.6$ is an exception; a decreased mobility and an enhanced pressure drop are clearly visible. These are attributed to the large deformations inherent to the bell-shaped morphology (c.f., Figure 4.3(d)). The experimental measurements of V/U reported in Ref. [151] are not shown herein for the comparison because the measured V/U for vesicles in circular tubes with $\nu = 0.924$–0.999 are scattered around the curve (4.27a).

As the confinement increases, the dimensionless groups V/U and $\Delta p^+ R_0/(\eta U)$ undergo a considerable variation with the reduced volume. Such a high sensitivity to the vesicle's deflation stems from significant changes in vesicle deformations at increasing confinement. Indeed, for a given vesicle, namely a given ν, increasing λ results in two combined effects: the vesicle tends to become more elongated, forming a nearly uniform viscous film between the vesicle and the tube wall, as shown in Figure 4.3 and in Figure 4.9, and the gap size becomes smaller, as illustrated in Figure 4.7. These two effects enhance the confinement-induced viscous friction on the vesicle surface, thus increasing extra pressure drop across the vesicle, and hindering vesicle mobility. Note that, as derived in Appendix A, the shear stress exerted on the membrane is balanced by the tension gradient in the membrane. This is in contrast with a clean drop (i.e., stress-free surface) transported in a pressure-driven flow wherein there appears a plateau value of V/U and $\Delta p^+ R_0/(\eta U)$ as the confinement increases. Comparisons of the present results with a lubrication model of Ref. [136] for red blood cells are also shown in these two figures; very good agreements are found when $\lambda > 1.4$. For smaller cells (i.e., small λ), the parallel-flow approximation of the lubrication model produces relatively smaller values of V/U and higher values of $\Delta p^+ R_0/(\eta U)$, which is clearly visible in Figure 4.10 but indistinguishable in Figure 4.11 due to logarithmic scales used. When $\lambda \to \lambda_c$, the asymptotic theory of Ref. [10] produced, in our notation, the following predictions

$$\frac{V}{U} = 1 + \frac{4}{3}\left(\frac{3\lambda_c^2\nu^{-2/3} - 2}{4\lambda_c^2\nu^{-2/3} - 3}\right)\left(1 - \frac{\lambda}{\lambda_c}\right) + O\left[\left(1 - \frac{\lambda}{\lambda_c}\right)^2\right], \tag{4.28a}$$

$$\frac{\Delta p^+ R_0}{\eta U} = 4\lambda\left(\lambda_c^2\nu^{-2/3} - 1\right)\left(1 - \frac{\lambda}{\lambda_c}\right)^{-1} + \lambda\left(\frac{4\sqrt{2}\pi}{4\lambda_c^2\nu^{-2/3} - 3}\right)\left(1 - \frac{\lambda}{\lambda_c}\right)^{-1/2} + O(1), \tag{4.28b}$$

The limiting behaviors are well captured in the simulations. We note that the numerical results of V/U are slightly less than those predicted by the theory as $\lambda \to \lambda_c$, it is due to the fore-aft symmetry of a sphero-cylindrical vesicle that is assumed when calculating the critical confinement λ_c. In fact, the frontal endcap is relatively smaller than the rear endcap, as shown in Figure A.1, resulting in a slightly larger theoretical λ_c. Another noticeable feature is a sudden change of slope in V/U; it becomes visible for $\nu = 0.8$ and 0.7, and that feature is quite noticeable for $\nu = 0.6$. It is found that the points where the curves of V/U vs. λ display a remarkable change in slope correspond exactly to the parachute-bullet transition points in the (ν, λ) space, as discussed above. This result is not surprising given that vesicle mobility is dictated by the vesicle shape and its interplay with the surrounding fluid. Indeed, the competition between geometric constraints and confinement-induced viscous friction determines the speed at which a vesicle is transported in a pressure-driven flow.

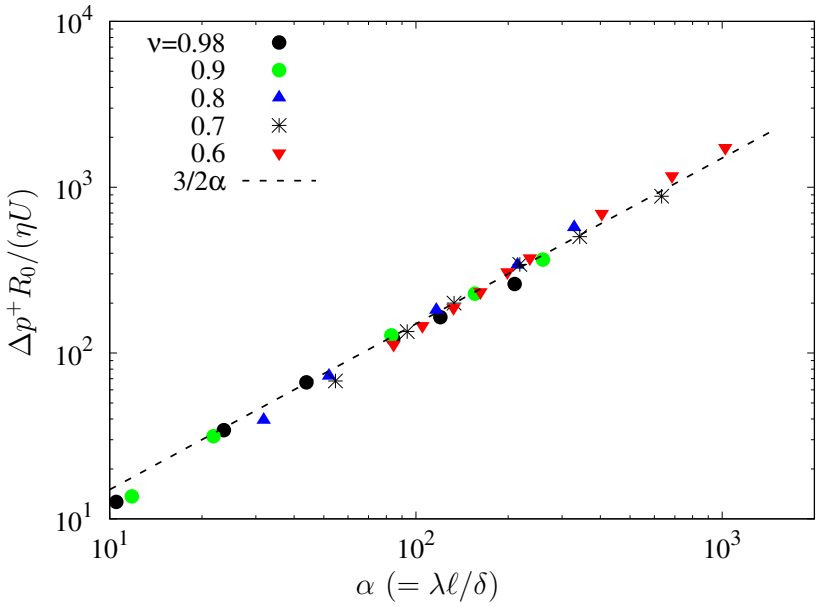

Figure 4.12: Dimensionless pressure drop $\Delta p^+ R_0/(\eta U)$ plotted as a function of $\alpha\ (=\ \lambda\ell/\delta)$ for highly confined vesicles (i.e., $\lambda \to \lambda_c$). The dashed line shows the scaling $3\alpha/2$.

When $\lambda \to \lambda_c$, the asymptotic theory of Ref. [10] shows a scaling of the dimensionless extra pressure drop $\Delta p^+ R_0/(\eta U) \sim O(\lambda\ell/\delta)$; the dimensionless extra pressure drop is proportional to the reduced vesicle length but inversely proportional the clearance size. The compilation of the present simulation results allows a precise correlation $\Delta p^+ R_0/(\eta U) \simeq 3/2(\lambda\ell/\delta)$, as illustrated in Figure 4.12. This is a significant improvement, given that a wide range of reduced volumes is involved. More importantly, this correlation holds implications that may help devise and interpret tube-flow experiments. Specifically, based on the vesicle length and its translational velocity which are the most easily accessible quantities in experiments, the simulated results presented in Figs. 4.9 and 4.10, together with scaling laws

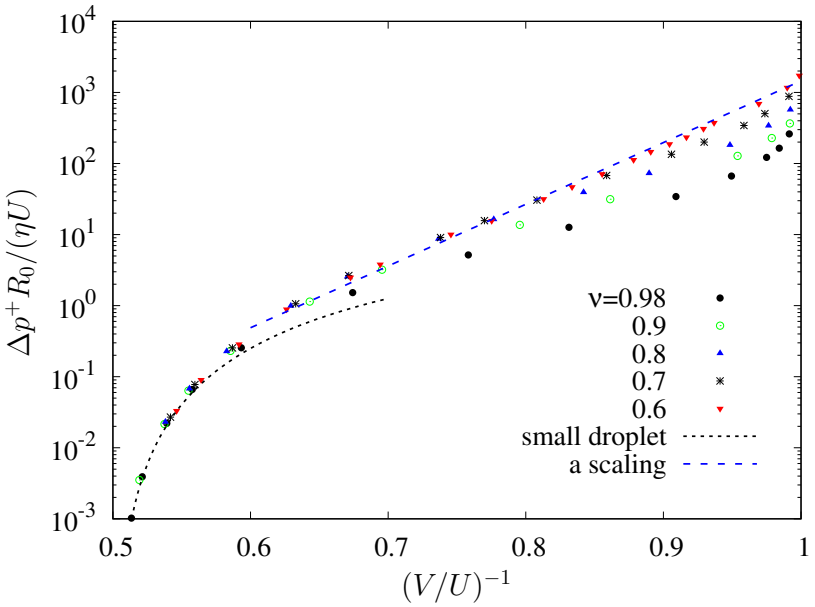

Figure 4.13: Dimensionless pressure drop $\Delta p^+ R_0/(\eta U)$ versus the reciprocal of the relative velocity V/U. The dotted curve shows the analytical prediction for a small spherical droplet (4.29). The dashed line is the best fitting (4.30) to $\nu = 0.6$ in the range of $0.6 < (V/U)^{-1} < 0.995$.

obtained from this study allow an estimate of the reduced volume ν (hence λ_c) and the film thickness, from which the dimensionless extra pressure drop $\Delta p^+ R_0/(\eta U)$ can be inferred. Directly measuring these parameters is no simple task. It often requires advanced imaging methods and instrumentation, with an added difficulty arising from the fact that the extra pressure drop is highly sensitive to the reduced volume. The estimated extra pressure drop should be contrasted with Figure 4.11 for consistency. An iterative process may be required to obtain a consistent result. Finally, an estimate of the maximum tension in the membrane can also be obtained using the scaling laws shown in Figure 4.8.

Before closing this subsection, we highlight the strong coupling behavior in the dimensionless groups $\Delta p^+ R_0/(\eta U)$ and V/U. Even for a vanishing small spherical droplet, Eqs. (4.27a) and (4.27b) give a highly nonlinear relationship

$$\frac{\Delta p^+ R_0}{\eta U} = \frac{27}{4}\left(2 - \frac{V}{U}(\lambda)\right)^3 + O(\lambda^3). \tag{4.29}$$

The theoretical prediction is shown in Figure 4.13, where the dimensionless pressure drop $\Delta p^+ R_0/(\eta U)$ is plotted against the reciprocal of the relative velocity V/U. The reason for using $(V/U)^{-1}$, instead of V/U, is quite simple and it is to illustrate how the coupling behaves as the vesicle size – equivalently the confinement for a given tube diameter – increases. While both the relative velocity and dimensionless extra pressure drop are notably sensitive to the reduced volume as the confinement increases, Figure 4.13 makes it clear that the sensitivity becomes relatively weaker as compared to Figure 4.11. Nevertheless, finding a correlation

between the dimensionless groups $\Delta p^+ R_0/(\eta U)$ and V/U, under high confinement, is by no means trivial because $\Delta p^+ R_0/(\eta U)$ diverges like $(1-\lambda/\lambda_c)^{-1}$. So here we put forward only a fitting to $\nu = 0.6$, given by

$$\frac{\Delta p^+ R_0}{\eta U} \simeq 3 \times 10^{-6} \exp\left[20\left(\frac{V}{U}\right)^{-1}\right]. \tag{4.30}$$

We conclude that the dimensionless groups $\Delta p^+ R_0/(\eta U)$ and V/U are strongly nonlinear coupled in tube flows.

4.3.5 Implications for the rheology of dilute red blood cell suspensions

The hematocrit measures the volume of red blood cells (RBCs) compared to the total blood volume (red blood cells and plasma). Its normal value in humans is approximately 45% but can be largely less in small vessels. Consider now the hematocrit, denoted by H_T, in a capillary of length L, and assuming RBCs flow in single file through the capillary with a characteristic length l_v between two neighbors (i.e., the distance between their centers of mass), then the ratio L/l_v is the number of RBCs inside the capillary, the total volume of the RBCs is $(L/l_v)\Omega$ (Ω the volume of a single RBC) and the hematocrit H_T equals to $(\Omega L/l_v)/(\pi R^2 L)$, which gives a mean distance between RBCs

$$l_v = \frac{\Omega}{\pi R^2 H_T}. \tag{4.31}$$

Poiseuille's law defines an apparent viscosity in terms of the overall pressure drop across the capillary tube

$$\eta_{\text{app}} = \left(\Delta p^0 + \Delta p^+\right)\frac{\pi R^4}{8LQ} = \eta + \frac{R^2}{8UL}\Delta p^+. \tag{4.32}$$

We then obtain, by setting $L = l_v$,

$$\eta_{\text{app}} = \eta\left[1 + \frac{3}{32}\left(\frac{R}{R_0}\right)^4\left(\frac{R_0}{\eta U}\Delta p^+\right)H_T\right] = \eta(1 + K_T H_T), \tag{4.33}$$

where the dimensionless parameter K_T is called apparent intrinsic viscosity. This single-file flow model allows recovering an apparent viscosity which depends linearly on the local hematocrit H_T, as in a lubrication model for red blood cells [136]. In capillaries with diameters up to about 8 μm, the single-file flow model is appropriate as RBCs frequently flow in single file and interactions between cells may be negligible.

Finally, the apparent intrinsic viscosity is given by

$$K_T = 9.53 \times 10^{-5} d^4 \left(\frac{R_0}{\eta U} \Delta p^+ \right), \qquad \text{for} \quad d > d_c, \tag{4.34}$$

where d denotes the diameter of tubes, d_c the critical diameter ($\simeq 2.8\ \mu$m) (c.f., § 4.3.2). The dimensionless extra pressure drop $\Delta p^+ R_0/(\eta U)$ for $\nu = 0.6$ is plotted in Figure 4.11 as a function of the confinement $\lambda = R_0/(d/2)$ with $R_0 \simeq 2.8\ \mu$m. Relative apparent viscosity which is the ratio of apparent viscosity to suspending medium viscosity can be written in terms of tube diameter d in μm, dimensionless extra pressure drop, and hematocrit H_T as

$$\eta_{\text{rel}} = \frac{\eta_{\text{app}}}{\eta} \simeq 1 + 9.53 \times 10^{-5} d^4 \left(\frac{R_0}{\eta U} \Delta p^+ \right) H_T, \qquad d \text{ in } \mu\text{m}. \tag{4.35}$$

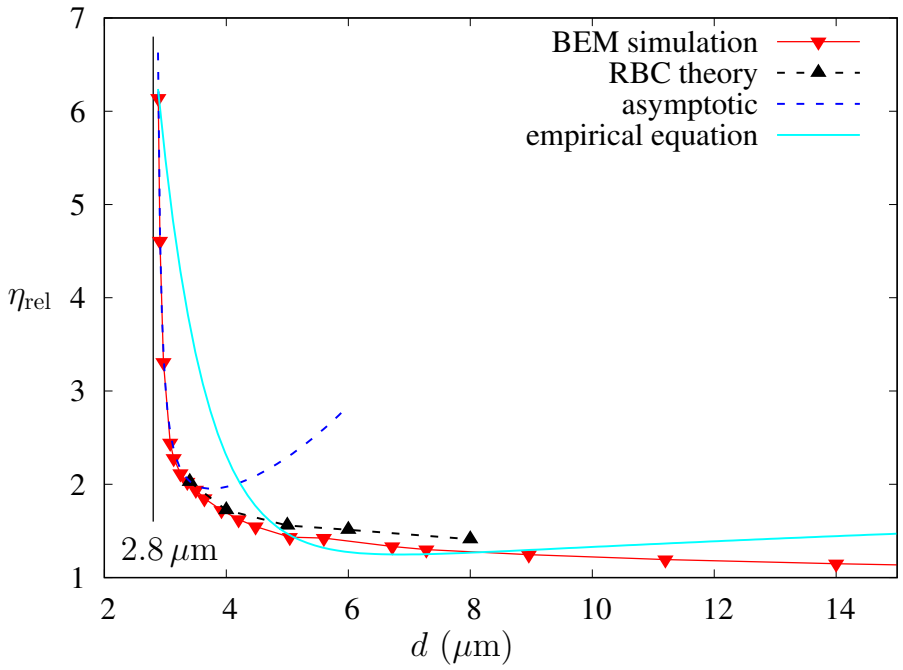

Figure 4.14: Variation of relative apparent blood viscosity η_{rel} with tube diameter d in μm for a hematocrit H_T of 0.45. Curve –▼– represents simulation results based on single-file fluid model, and curve –▲– represents lubrication model of RBCs [136]. Dashed line in blue shows asymptotic theory for dimensionless extra pressure drop [10] (Eq. (4.28b)). Solid curve in cyan represents a fitting empirical equation to *in-vitro* experimental data [130]. The vertical line (black) indicates a lower limit ($d_c \simeq 2.8\ \mu$m) to the diameter of tubes beyond which normal red blood cells cannot pass through without rapture.

As an example, simulated relative apparent viscosity with a hematocrit of 0.45 as a function of tube diameter is shown in Figure 4.14. There is a small decrease in η_{rel} as the tube diameter increases when $d \geq 5\ \mu$m (i.e., $\lambda \leq 1.11$). The value of η_{rel} for $d = 5.6\ \mu$m ($\lambda = 1$) is slightly less than 2% of the value for $d = 5\ \mu$m. At smaller diameters, say $d < 4\ \mu$m, relative apparent viscosity rises rapidly and becomes substantially higher as the tube diameter approaches the critical diameter d_c. The dramatical rise is attributed to a significantly large resistance to flow as reflected from the behavior of extra pressure drop at nearly maximum confinement. This feature is remarkably captured in the asymptotic theory of Ref. [10] for the tube diameters less than $3.5\ \mu$m. The numerical results are compared with those obtained from a lubrication model of red blood cells at high shear rates ($U/d > 50\ \mathrm{s}^{-1}$) [136]. It is shown that apparent viscosity is almost independent of flow rate in this regime but increases with decreasing flow rate at lower shear rates [130, 136]. At a bending capillary number $\mathrm{Ca_B} = 50$, our BEM simulations always lie in a high-flow-rate regime as an estimate of $U/d = \kappa \mathrm{Ca_B} \lambda/(2\eta R_0^3) > 50\ \mathrm{s}^{-1}$ even at a very weak confinement $\lambda = 0.3$. While the model of Ref. [136] includes a shear elasticity of the RBC membrane but neglects the bending elasticity, our numerical predictions of η_{rel} are in excellent agreement with the lubrication theory when $d \leq 4\ \mu$m. Indeed, under high confinement, bending resistance has a negligible contribution to the hydrodynamic force balance; the isotropic tension in the membrane (see Appendix A) resists the flow in the lubrication layer. When $d > 5\ \mu$m, the parallel-flow approximation of Ref. [136] yields relatively higher values of η_{rel} as compared to our BEM simulation results.

Based on a compilation of *in-vitro* experimental data, an empirical equation describing the dependence of relative apparent viscosity on tube diameter has been put forward in Ref. [130] and is also plotted in Figure 4.14. Given the paucity of experimental measurements in the range of smaller tube diameters, we may say that the predicted relative apparent viscosities are in reasonable agreement with experimental data for tube diameters ranging between 2.9 and 14 μm. Nevertheless, it should be mentioned that while the present single-file vesicle model provides some insight into how apparent blood viscosity behaves for tube diameters in the range of ~ 2.8–$14\ \mu$m, the model due to its axial symmetry nature is not able to make reliable predictions for tube diameters beyond that range as the confinement ($\lambda < 0.4$) becomes too weak for vesicles to preserve axisymmetry. Also, the limitation of a single-file flow model (i.e., $d < 8\ \mu$m) makes the model unreliable for the prediction of relative apparent viscosity for larger tube diameters; the simulated results presented in Figure 4.14 for tube diameters larger than 8 μm are for illustrative purposes only.

4.4 Summary

We have presented a numerical investigation of the motion and deformation of a vesicle freely suspended inside a circular tube in a pressure-driven flow. The numerical simulations of this fluid-structure interaction problem have been carried out by using a previously reported axisymmetric boundary element method. The results were presented for the reduced volumes ν ranging from 0.98 (i.e., nearly spherical vesicles) to 0.6 (i.e., red blood cell-

mimicking vesicles) at different degrees of confinement up to near its critical value λ_c. The critical confinement of a vesicle in cylindrical tube flow, as well as its critical length, was calculated on the basis of the geometric constraints of fixed volume and surface area while assuming the fore-aft symmetry of a sphero-cylindrical vesicle. It turned out that this maximum confinement was overestimated by about one percent due to the symmetry that was usually assumed in the calculation.

The results of the present study allowed us to build a phase diagram of vesicle shapes in good agreement with the most comprehensive experimental data [32]. Carefully controlled simulations let us propose a linear shape transition line separating the two commonly observed shapes, namely parachute-like and bullet-like shape regions in the (λ, ν) space. We found that this transition is accompanied by a change in the behavior of the mobility of vesicles, especially for low-reduced-volume vesicles (i.e., $\nu \leq 0.7$). The present work focused on highly confined vesicles, which required high-resolution simulations to account for the hydrodynamic interaction between the tube wall and vesicle surface. These simulations enabled us to examine the limiting behavior of several quantities of interest, particularly the vesicle mobility and the extra pressure drop due to the presence of the vesicle in the tube. The results obtained lend support to a recently reported asymptotic theory [10].

Aiming to help interpret the numerical results when the confinement approaches its critical value, we have also presented a lubrication theory combining two approaches reported in the literature. While the balance between viscous, bending, and tension forces controls the vesicle motion and deformation, we showed that bending elasticity plays a minor role in the hydrodynamic force balance in the lubrication layer. It is the isotropic tension in the membrane that resists the confinement-induced viscous friction, thus controlling the size of the gap between the tube wall and the vesicle surface. We also showed that the predicted mechanical tension at the proximity of the critical confinement for red blood cell-mimicking vesicles is of the order of the rupture tension. In addition, based on a single-file flow model, an attempt has been made to predict the rheology of dilute red blood cell suspensions. Simulated relative apparent viscosity of a vesicle suspension in small capillary tubes yielded a consistent and complementary result as compared with experimental data and highlighted the role of confinement in the rapid rise in the relative viscosity of red blood cells when passing through small vessels. However, there is a severe limitation to such a model since it is relevant only for capillary diameters up to about 8 μm.

5 Hybrid continuum–coarse-grained modeling of RBCs

5.1 Introduction

The human red blood cells (RBCs) are normally biconcave discocytes with a diameter of approximately 8 μm and a thickness of about 2 μm. The mean volume is about 94 μm^3 and the average surface area around 135 μm^2, a value larger than the surface area of a sphere with the same volume. The RBC membrane ($\sim$10 nm in thickness) is composed of a lipid bilayer supported from inside by a two-dimensional (2D) triangular spectrin network of cytoskeletal proteins, as shown in Figure 5.1. A highly elastic membrane, together with a high surface-to-volume ratio (reduced volume $\nu \sim 0.64$), provides RBCs with the ability of large reversible deformation when passing through capillaries. This composite bilayer-spectrin membrane (Figure 5.1(b)) may be treated as an elastic thin shell. Based on this simplified elastic description and the assumption of flat membrane, two fundamentally different approaches have been proposed to study RBCs in fluid flows: one, more traditional, founded on continuum mechanics, and the other, founded on molecular details, see for recent reviews [59, 97, 152, 153].

The classical continuum approach, which was largely inspired by numerical methods developed in mechanical engineering, considers the suspending fluids as well as the RBC membrane itself as a continuous medium. A number of well-established continuum methods have been developed, including boundary integral/element method (BIM/BEM) and several interface tracking methods widely employed in multi-phase flows. These methods have been used to simulate the dynamics of a single RBC in external flows as well as the collective behavior of an ensemble of them [59]. From this point of view, the RBC is most often modeled as a hyperelastic capsule (made of the polymerized membrane, Figure 5.1(d)) [59, 153]. However, the fluid nature of the cell membrane was systematically lacking; the near incompressibility of the membrane was generally taken into account through a high dilatational modulus. Numerical simulations with vesicles (made of a lipid bilayer, Figure 5.1(c)) with bending rigidity can provide insight into the shapes taken by RBCs, either at equilibrium – the typical biconcave shape of RBCs or in external flows – bullet, parachute, and slipper shapes [153], but shear elasticity and shape memory that are the fundamental mechanical properties of RBCs are missing.

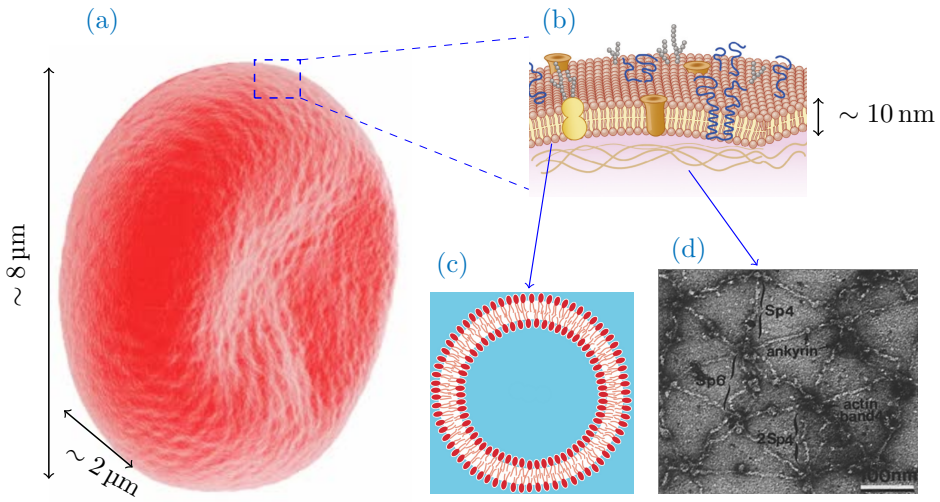

Figure 5.1: A single RBC and schematic view of its membrane. (a) an RBC with a typical biconcave discoid shape; (b) a schematic view of the membrane and the general disposition of its lipid and protein constituents; (c) a drawing of a small spherical vesicle seen in cross-section; (d) a spectrin network (the cytoskeleton) shown by high-resolution negative staining electron microscopy [103].

Discrete modeling exploits the microstructural properties of RBCs. Any medium is seen as a huge number of molecules, submitted to thermal agitation and to intermolecular forces. However, to be able to resolve much larger space and time scales involved in the transport of RBCs in fluid flows, coarse-graining of spectrin-level models has to be used, and the level of coarse-graining characterizes the crudeness with which the molecular level of the medium is represented [52]. Mesoscale (whole cell) particle-based methods [95] consider both the lipid bilayer and the spectrin cytoskeleton and the interaction between them. Some cell scale particle-based models keep the trace of the two contributions in the form of a two-component whole cell model [96, 116]. In this way, the detachment of the cytoskeleton from the lipid bilayer, which, for example, can occur in the micropipette aspiration experience or the flow through a constriction, has been successfully simulated [96].

One could regard the continuum approach as the ultimate state of coarse-graining; however, in that ultimate state, the molecular structure is fully integrated and forgotten. There is a need for developing new numerical methods combining the two approaches, thus being able to benefit from the advantages of both of them. Indeed, the idea of representing the cytoskeleton as a discrete 2D structure made of a large number of connected springs is very attractive. This is the starting point of the present contribution. Actually, particle-based and continuum-based models work all on the same principle: one mesh (or two coupled meshes if we distinguish between the bilayer and the cytoskeleton) made of triangular elements to represent the RBC membrane. In the particle-based model, the mesh is seen as a discrete network of springs, which tends to be a good representation of the spectrin cytoskeleton when the number of vertices reaches the real cytoskeleton structure. In the continuum-based model, the mesh is understood as a finite element discretization of the membrane,

in which a two-dimensional mesh, embedded in a 3D domain, is defined by a set of vertices connected by edges. Therefore, the same ingredients are present, providing very similar modeling possibilities in these two approaches.

In this chapter, we propose to explore the idea of whether the combination of a spring network with a vesicle model could give rise to an accurate and reliable hybrid discrete-continuum RBC model. It is a first attempt to couple a 3D vesicle model with a discrete description of the cytoskeleton. From purely mechanical considerations, such a model could extract the essential mechanical properties of the RBC membrane: fluidity and bending rigidity of the lipid bilayer, and shear elasticity of the cytoskeleton while maintaining surface-area and volume conservation constraint. This is also computationally feasible, thanks to an existing continuum vesicle model [19, 22, 150]. The argument is that, in the vesicle model, the movements of the bilayer in the normal and tangential directions are treated differently, namely in Lagrangian fashion for the former and with a Eulerian description for the latter. Therefore the tangential movement of mesh vertices (or nodes in a finite element context), which does not change the membrane shape, is fully independent of the tangential movement of the lipids. Actually, the possibility of prescribing the tangential velocities of mesh vertices to any convenient set is used to preserve the mesh quality in a vesicle simulation context. Our idea for an extension towards RBCs is then to prescribe this velocity set to that of the vertices of a spring network. In doing so, the movement of the mesh vertices is constrained to slide along the bilayer. However, this constraint is automatically ensured by the fact that the same mesh is used both for the bilayer and the cytoskeleton, and that the nodes of the bilayer finite-element mesh are also the vertices connected by the edges of spring network. As far as numerical aspects are concerned, one of the major developments involves assigning a spring behavior law to the edges and a drag friction law (based on the lipid/node relative velocity) to the vertices, as well as a way how to incorporate these additional forces into the vesicle model.

In the following sections, we first describe the RBC membrane model and outline the numerical methods. We then present three numerical examples to evaluate the proposed hybrid model, followed by a summary of this chapter.

5.2 Cytoskeleton elasticity

The membrane model consists of a collection of points $\{\mathbf{x}_n, n \in 1 \dots N\}$, which are the vertices of the RBC surface triangulation, representing the cytoskeleton. The length of the link connecting vertices n and p is defined as $l_{np} = |\mathbf{x}_n - \mathbf{x}_p|$. The spring network induces on each node (or vertex) n of the surface mesh a resulting force given by

$$\mathbf{f}_n = \sum_p \mathbf{f}_{np} = \sum_p K_{np}(\mathbf{x}_p - \mathbf{x}_n) \tag{5.1}$$

where the summation is over all the vertices p connected to the node n by an edge np, i.e. spring np.

In Eq. (5.1), $\mathbf{f}_{np}$ denotes the force exerted by the node p on the node n, and K_{np} represents the stiffness coefficient of the spring np, connecting the node n at the position $\mathbf{x}_n$ to the node p at the position $\mathbf{x}_p$. In the case of a linear spring with the spring stiffness k_{np}, the force $\mathbf{f}_{np}$, as a function of the spring length l_{np} and its value at rest l^0_{np}, is given by

$$\mathbf{f}_{np} = k_{np}\frac{l_{np} - l^0_{np}}{l_{np}}(\mathbf{x}_p - \mathbf{x}_n) = k_{np}(1 - l^0_{np}/l_{np})(\mathbf{x}_p - \mathbf{x}_n) = K_{np}(\mathbf{x}_p - \mathbf{x}_n) \tag{5.2}$$

Since the aim of this work is not to compare different spring laws but rather to test the idea described in the introduction, we only consider one of the constitutive laws proposed in [52], namely the finitely extensible nonlinear elastic (FENE) spring in combination with a repulsive force defined as a power function (POW). It is worth mentioning that compared to the linear spring model, i.e. Eq. (5.2), the FENE-POW spring model has been widely used for modeling the shear resistance of the cytoskeleton, especially for large deformations of RBCs. The elastic energy of the spring np is then the sum of an attractive part and a repulsive one

$$U_{np} = -\frac{k_a}{2}(l^{max}_{np})^2 \log(1 - x^2_{np}) + \frac{k_r}{(\alpha - 1)l^{\alpha-1}_{np}} \tag{5.3}$$

where k_a and k_r are, respectively, the FENE (attractive) and the repulsive spring constants, α is the repulsive exponent assumed as a constant value.

This expression uses the normalized spring length (or separation distance) $x_{np} = l_{np}/l^{max}_{np} \in (0, 1]$. So, the spring's behavior law can be adjusted by fixing three physical parameters: the maximum spring length l^{max}_{np}, and the attractive and repulsive spring constants k_a and k_r. The total stiffness coefficient K_{np} is given by

$$K_{np} = \frac{k_a}{1 - x^2_{np}} - \frac{k_r}{(l^{max}_{np}x_{np})^{\alpha+1}} \tag{5.4}$$

Eq. (5.4) defines a spring with non-zero equilibrium length l^0_{np} given by $\mathbf{f}_{np} = -\delta U_{np}/\delta \mathbf{x}_n = 0$ for $x^0_{np} = l^0_{np}/l^{max}_{np}$. The equilibrium length l^0_{np} corresponds to the length of the spring in the reference shape, i.e. stress-free mesh. For simplification, we use hereinafter x_0 and l_0 to denote, respectively x^0_{np} and l^0_{np}. The two spring constants k_a and k_r can be related by

$$k_r = k_a\frac{l^{\alpha+1}_0}{1 - x^2_0} \tag{5.5}$$

Thanks to the Virial theorem [52], the elastic shear modulus of the spring network μ_s can be expressed in terms of k_a and k_r as follows:

$$\mu_s = \frac{\sqrt{3}}{4}\left(\frac{2k_a x^2_0}{\left(1 - x^2_0\right)^2} + \frac{k_r(\alpha + 1)}{l^{\alpha+1}_0}\right) \tag{5.6}$$

Combining Eq. (5.4) with Eq. (5.5) and Eq. (5.6) yields finally the spring force at node n by an edge np

$$\mathbf{f}_{np} = K_{np}(\mathbf{x}_p - \mathbf{x}_n) = \frac{4\mu_s}{\sqrt{3}\left(\frac{2x_0^2}{1-x_0^2} + \alpha + 1\right)}\left(\frac{1-x_0^2}{1-x_{np}^2} - \frac{x_0^{\alpha+1}}{x_{np}^{\alpha+1}}\right)(\mathbf{x}_p - \mathbf{x}_n). \tag{5.7}$$

As in [52], we set $\alpha = 2$ and the ratio $x_0 = 1/2.05$. For a given shear modulus μ_s, which is in the range of 2–6 μN/m for a normal RBC [155], and on the basis of the triangulation of cell membrane ($x_{np} = l_{np}x_0/l_0 = l_{np}x_0/l_{np}^0$) and its stress-free mesh ($l_0 = l_{np}^0$), the elastic force $\mathbf{f}_{np}^e$ at node n by the edge np exerted by the spring network on the lipid bilayer can be obtained from Eq. (5.7) since $\mathbf{f}_{np}^e$ is simply equal to $\mathbf{f}_{np}$, and subsequently incorporated into the bilayer-cytoskeletal interaction as described below.

5.3 Cytoskeleton-bilayer interaction

In this chapter, interest is focused on the membrane model, thus a free space case without physical boundaries will be used to complete the description of the model.

In [21, 22], the boundary element method is used to resolve the lipid's flow on the vesicle membrane, which can be formulated as

$$\boldsymbol{u}^{\text{lip}} = \boldsymbol{u}^{\infty} + \mathbf{G}\boldsymbol{f}, \quad \boldsymbol{f} = \boldsymbol{f}^b + \boldsymbol{f}^{\gamma} \tag{5.8}$$

where the exponent "lip" stands for the lipid's velocity field and "∞" indicates the imposed background bulk fluid flow. $\mathbf{G}$ is the Green operator due to the Stokeslet, $\boldsymbol{f}^b(\boldsymbol{y})$ is the bending force field induced by the lipid bilayer in response to deformations and $\boldsymbol{f}^{\gamma}(\boldsymbol{y})$ is the surface-tension-like force resulting from the Lagrange multiplier γ of the surface divergence-free constraint on the lipid's flow

$$\boldsymbol{\nabla}_S \cdot \mathbf{u}^{\text{lip}} = 0. \tag{5.9}$$

For an RBC we have to add the elastic force $\boldsymbol{f}^{\text{e}}(\boldsymbol{y})$ (Eq. 5.7) exerted by the spring network on the lipid bilayer. This spring elastic action is transmitted to the lipid bilayer in the normal direction directly and in the tangential plan indirectly via the drag forces $\boldsymbol{f}^{\text{d}}(\boldsymbol{x})$ that the lipids exert on the cytoskeleton

$$\mathbf{f}^{\text{d}} = \text{C}_{\text{f}}\Pi_{\text{tg}}(\mathbf{u}^{\text{lip}} - \mathbf{u}^{\text{cyt}}) = \Pi_{\text{tg}}\mathbf{f}^{\text{e}} \tag{5.10}$$

where the exponent "cyt" stands for cytoskeleton and C_{f} is the friction coefficient. The operator $\Pi_{\text{tg}} = Id - \Pi_n$ is the projector onto the tangent plane of the membrane surface, with $\Pi_n = \mathbf{n} \otimes \mathbf{n}$ the projector in the normal direction given by the normal vector $\mathbf{n}$ pointing toward the outside bulk fluid.

From the kinematic point of view, the sliding of the cytoskeleton is taken into account, thanks to the mixed Lagrangian-Eulerian updating of the mesh node's position,

$$\boldsymbol{x}(t+\mathrm{d}t) = \boldsymbol{x}(t) + \mathrm{d}t\boldsymbol{u} = \boldsymbol{x}(t) + \mathrm{d}t\,\Pi_n\boldsymbol{u}^{\mathrm{lip}} + \mathrm{d}t\,\Pi_{\mathrm{tg}}\boldsymbol{u}^{\mathrm{cyt}}. \tag{5.11}$$

Thus, the mesh nodes move with the lipid's velocity in the normal direction only, whereas it moves tangentially with the cytoskeleton's ones. Using Eq. (5.10), Eq. (5.11) writes also

$$\boldsymbol{x}(t+\mathrm{d}t) = \boldsymbol{x}(t) + \mathrm{d}t\boldsymbol{u}^{\mathrm{lip}} - \mathrm{d}t\frac{1}{\mathrm{C_f}}\Pi_{\mathrm{tg}}\boldsymbol{f}^{\mathrm{e}}. \tag{5.12}$$

Using the Stokes-Einstein relation and measured values of the translational diffusivity of band 3 and glycophorin C in the lipid bilayer, the drag force and thus the values of the friction coefficient can be deduced [120]. While these values are relevant only in the context of a spectrin scale modeling or in the case involving a dynamic process. In the present study, the value of $\mathrm{C_f}$ affects only numerical efficiency; $\mathrm{C_f} \to 0$ is equivalent to minimizing the elastic energy at each time step, whereas a finite value leads to a relaxation of the cytoskeleton stresses. We set $\mathrm{C_f} = 0.194\ \mathrm{pN\,\mu m^{-1}\,s}$ in most of our computations, as in [120], but the final stationary RBC shape remains the same for all the examples we have considered, whatever its value [105].

Before presenting our numerical examples, the properties of RBC and the blood flow in the human body are listed in Table 5.1 for reference.

Property (units)	used values (variability)
Surface area, A (μm^2)	135 [2]
Volume, V (μm^3)	94 [2]
Effective diameter, $D_{eff} = \sqrt[3]{6\,V/\pi}$ (μm)	5.64
Bending rigidity, κ ($\times 10^{-19}$ J)	2.4 (1–7) [52, 91, 116, 120, 155]
Shear modulus, μ_s (μN m^{-1})	2–10 (2–12) [2, 52, 155]
Bilayer-cyto friction coeff., C_f (pN μm^{-1} s)	0.194 [120, 121]
Plasma viscosity, η^e ($\times 10^{-3}$ Pa s)	1.2 [120]
Shear rate, $\dot{\gamma}$ (s^{-1})	100–300 (mean 270, peak 1640) [120]

Table 5.1: Summary of the properties of RBC and plasma in human body.

5.4 Numerical examples

Here, we present three simulation examples to evaluate the proposed approach.

(a) Stretching of an RBC in the optical tweezers experiment [148], which is the most classic validation of RBC models.

(b) Motion of a single RBC in a simple shear flow.

(c) Motion of a single RBC in a capillary.

In all these three examples, the initial shape of RBC is a biconcave discoid, and the geometry can be obtained using the following expression [44]

$$y = \pm D\sqrt{1 - \frac{4(x^2+z^2)}{D^2}}\left[a_1 + a_2\frac{x^2+z^2}{D^2} + a_3\frac{\left(x^2+z^2\right)^2}{D^4}\right], \tag{5.13}$$

where $D = 7.82\,\mu\text{m}$ is the cell diameter, $a_1 = 0.0518$, $a_2 = 2.0026$ and $a_3 = -4.491$. The volume and surface area of the corresponding RBC are respectively $94\,\mu\text{m}^3$ and $135\,\mu\text{m}^2$, giving a reduced volume $\nu = 0.64$. Figure 5.2 shows the shape generated with this expression, which has 1280 elements, created by the Loop subdivision. In this chapter, all results are obtained with 1280 elements unless otherwise stated.

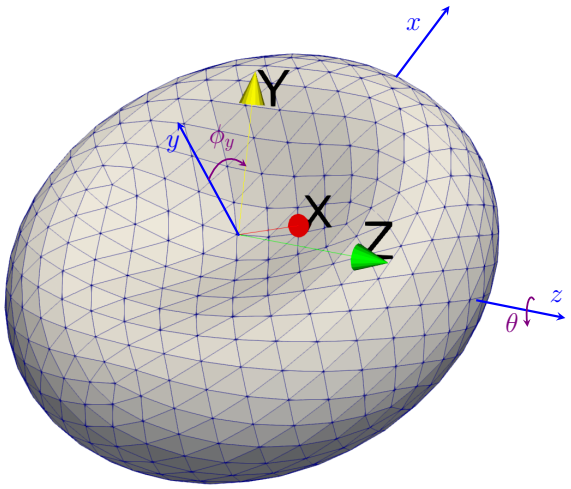

Figure 5.2: RBC with a biconcave discoid shape generated with Eq. (5.13). The triangular mesh is composed of 642 nodes and 1280 elements. $\{X, Y, Z\}$ is the fixed Cartesian coordinate system and the flow is in the X direction. $\{x, y, z\}$ is the Cartesian coordinate system rotates with the RBC. The pitch angle θ represents the rotation of the cell around the z axis, ϕ_y measures the angle between the minor axis of RBC and Y.

For the coarse-grained model used for cytoskeletal proteins, the reference shape is another indispensable ingredient to compute the elastic force, as in Eq. (5.7). However, it must be stressed that there is no universal consensus on the reference shape that should be adopted to describe the real deformation of an RBC under external solicitations, even though it is

an essential characteristic to consider in order to correctly estimate the actual stress in the membrane during large deformations [2]. In most of the previous studies, the initial shape, i.e., a biconcave discocyte is used as the stress-free reference shape. But recently, an oblate, which is close to a sphere (ν=0.95 $\sim$ 0.997), with equal surface area to the RBC is chosen as the stress-free configuration [2, 30, 122]. The nearly spherical oblate shape is used in the hope of recovering some experimental observations under strong external stresses, to make up the deficiency in using the biconcave shape. In this chapter, both the biconcave and the oblate shape are used as the stress-free configuration. But we do not have many arguments on why we use such a shape as reference shape, it may be interesting to make a quantitative comparison of their effects.

Before presenting the numerical results, it is useful to recall the characteristic parameters appeared in our current system. We use the cell radius as the reference length, i.e., $L_{\text{ref}} = R = D_{eff}/2$. For RBC, there are two different characteristic times used to measure the time needed to restore a deformation due to bending and shearing, respectively. That is

$$t^{\text{b}}_{\text{char}} = \frac{\eta^e R^3}{\kappa} \quad \text{and} \quad t^{\text{s}}_{\text{char}} = \frac{\eta^e R}{\mu_s}. \tag{5.14}$$

Taking the typical values of RBC, $R = 2.82\,\mu\text{m}$, $\eta^e = 1.2c$ Pa $= 1.2 \times 10^{-3}$ Pa s, $\kappa = 2.4 \times 10^{-19}$ J and $\mu_s = 5 \times 10^{-6}$N m^{-1}, we have $t^{\text{b}}_{\text{char}} \approx 112.13$ ms and $t^{\text{s}}_{\text{char}} \approx 0.68$ ms. The two typical *in vivo* shear rates, 270 and 1640 s^{-1}, which are considered as the avergae shear rate and the peak shear rate in human body. This defines the characteristic flow time (using the shear rate $\dot{\gamma}_c = \dot{\gamma}_{max}/\sqrt{2}$) $t^{\text{f}}_{\text{char}} = \dot{\gamma}_c^{-1} \approx 0.86$ ms [120, 155]. Similarly, the two characteristic force densities are

$$f^{\text{b}}_{\text{char}} = \frac{\kappa}{R^3} \quad \text{and} \quad f^{\text{s}}_{\text{char}} = \frac{\mu_s}{R}. \tag{5.15}$$

In this chapter, we use the characteristic values based on shear modulus as the reference values, that is $t_{\text{ref}} = t^{\text{s}}_{\text{char}}$ and $f_{\text{ref}} = f^{\text{s}}_{\text{char}}$, for all simulations of RBC. Whereas when these results are compared to those of the vesicle ($\mu_s = 0$), the time is re-scaled by the characteristic time defined by the bending modulus $t^{\text{b}}_{\text{char}}$ in post-processing.

5.4.1 RBC stretching

We first perform RBC stretching simulations and compare our numerical results with the experimental data of RBC deformations by optical tweezers [148]. In this example, an oblate with a reduced volume $\nu = 0.98$ is used as the stress-free shape in most of the cases, and $\kappa = 2.4 \times 10^{-19}$ J.

Figure 5.3 shows a sketch of RBC after deformation. The RBC membrane network is composed of N (= 642) vertices, which define the level of the membrane representation from the spectrin-level to the coarse-grained network of N vertices. The total stretching force F_s is applied to an area with diameter $d_c \approx 2\,\mu$m, along the negative and positive axial directions of x (drawn as black dots in Figure 5.3). Inspired by Sigüenza et al. [141], where

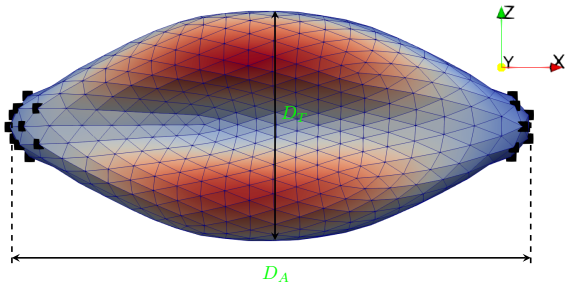

Figure 5.3: Schematic RBC deformation under the stretching force. The membrane is colored by the distance from the membrane to its symmetrical plane parallel to the plane Oxz, and black dots denote the vertices where the force is applied.

the stretching force is applied only to the nodes located on the edges delimiting the contact areas. The force applied here is proportional to $(|\boldsymbol{x} - \boldsymbol{x}_c|)^\alpha$, where $\boldsymbol{x}_c$ is the center of the contact area and $\alpha \in [1, 2]$, is used to control the variation of the stretching force. The axial diameter D_A is computed as $|x_{\max} - x_{\min}|$, where $x_{\max}$ and $x_{\min}$ are the maximum and the minimum x position of all vertices. The transverse diameter D_T is calculated as $2 \times \max_{i=1\ldots N} \sqrt{(y_i - c_y)^2 + (z_i - c_z)^2}$, where c_y and c_z are the coordinates of the y and z centers of mass.

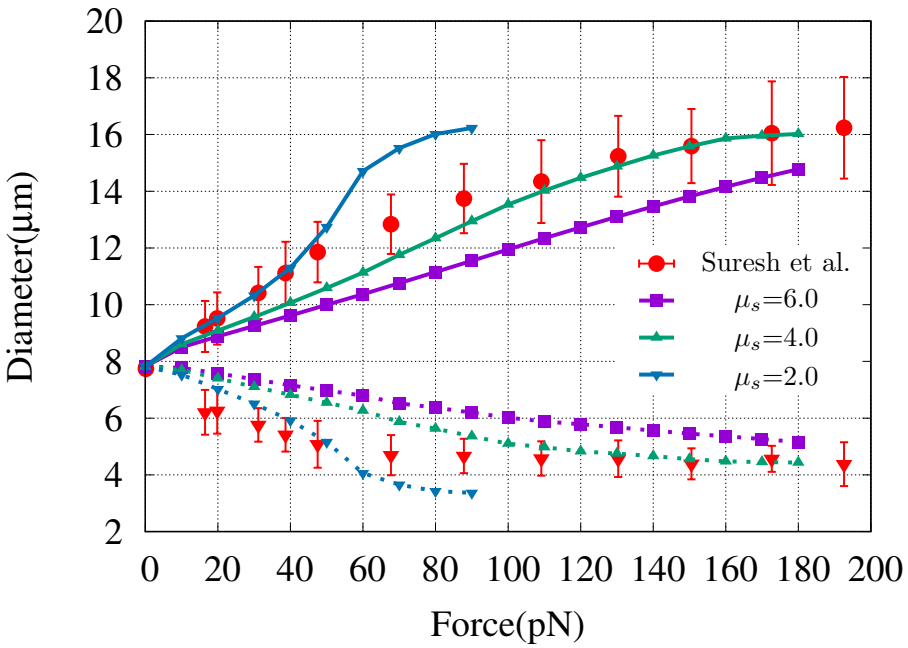

Figure 5.4: Comparison of the axial (D_A) and transverse (D_T) diameters of the RBC stretched by optical tweezers for different shear modulus and for the experimental results of Suresh et al. [148].

Figure 5.4 shows the change in RBC's axial and transverse diameters in response to the applied stretching forces with three different shear modulus, $\mu_s = 2.0, 4.0$ and $6.0\,\mathrm{pN\,\mu m^{-1}}$. These numerical predictions are compared to the experimental results given by Suresh et al. [148]. As the cell becomes more and more elongated by increasing the stretching force F_s, it is seen that the axial diameter D_A increases. This elongation induces a contraction of the cell in the orthogonal direction, which results in a decrease of the transverse diameter D_T.

As for the evolution of the axial and transverse diameters as a function of the stretching force, we should first be aware that the elastic shear modulus μ_s, measured experimentally, lies in the range of 4–12 μN/m, and the bending modulus in the range of $1\text{–}7\times10^{-19}$ J [52, 116], indicating a large-amount scatter in the measured values, as shown in Figure 5.4. As for our numerical results, it is seen that, as the stretching force increases, the RBC's axial diameter increases, while transverse one decreases from the initial value $D = 7.82\,\mu\mathrm{m}$. Given a relatively higher value of the shear modulus μ_s, a relatively smaller deformation is produced since the membrane is "harder". Our numerical results behave well in this way and vary around the experimental measurements. But interestingly, our hybrid approach gives a good prediction with a smaller μ_s (=2 $\mathrm{pN\,\mu m^{-1}}$) for the stretching force is not too strong, whereas, for a stronger stretching force, a good prediction is given with a higher shear modulus μ_s (=4 $\mathrm{pN\,\mu m^{-1}}$).

5.4.2 RBC in shear flow

As a second numerical example, we perform a preliminary study of RBC flows in a simple shear flow, $\boldsymbol{u}^\infty = \dot{\gamma} y \boldsymbol{e}_x$. The aim is to show that this hybrid approach can indeed reproduce the basic dynamics of the RBC in shear flow. In this example, the biconcave shape is the only used stress-free shape.

A general picture of the dynamics of a single RBC in a shear flow was proposed by Abkarian and Viallat [2], as shown in Figure 5.5. It is seen that the biconcave shape is preserved at low values of Ca, and conversely, the cell is deformed by hydrodynamic forces at high values of Ca. Compared to RBCs *in vivo*, one particularity of RBCs in diluted suspension is that the steady tank-treading (TT) motion occurs only for low viscosity ratios [2, 57, 91]. In this example, we are only interested in the tumbling and the tank-treading motions.

Before presenting the numerical results, it is useful to recall the relevant dimensionless parameters that we are using in this example, they are

(1) the viscosity ratio $\lambda = \eta^i/\eta^e$;

(2) the capillary number $Ca = t^\mathrm{s}_\mathrm{char}/t^\mathrm{f}_\mathrm{char} = \eta^e R\dot{\gamma}/\mu_s$, which is the ratio of the characteristic time to restore the membrane deformation and the characteristic time of the flow;

(3) the reduced bending number $C_\mathrm{b} = \kappa/(\mu_\mathrm{s} R^2)$, which is the ratio of the bending modulus and shearing modulus.

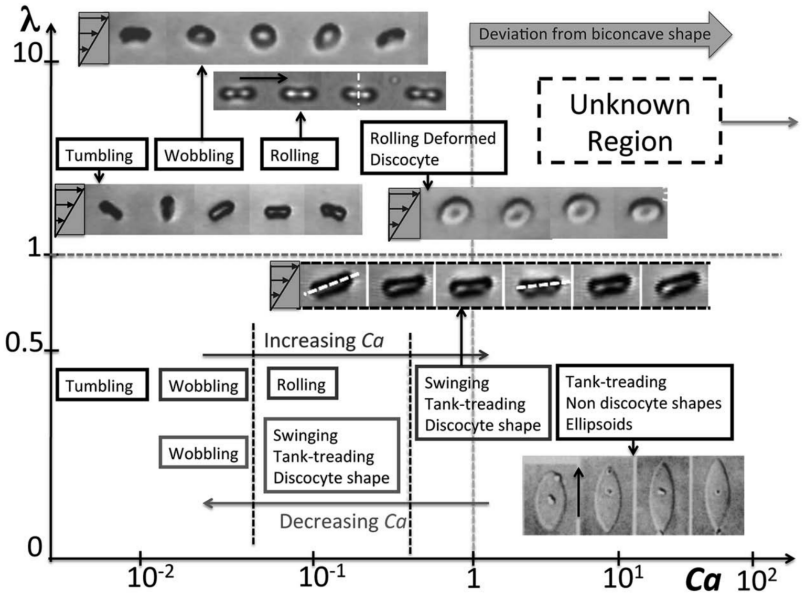

Figure 5.5: Phase diagram of the dynamics of a single RBC in shear flow in the plane of the capillary number Ca and the viscosity ratio λ (reproduced from [2]).

Tumbling

In order to reproduce the tumbling motion, a set of the three dimensionless parameters $\{\lambda, Ca, C_{\mathrm{b}}\}$ was selected and tested. The overall ranges of these dimensionless parameters are $\lambda \in \{0.2, 1.0, 5.0\}$, $Ca \in (0.034, 0.508)$ and $C_{\mathrm{b}} \in (0.003, 0.019)$. More specifically, the values of Ca and C_{b} for each λ are summarized in Table 5.2. For these selected parameters,

λ	Ca	C_{b}
0.2	0.034–0.169	0.003–0.015
1.0	0.034–0.508	
5.0	0.034–0.169	0.003–0.019

Table 5.2: Summary of the dimensionless numbers used in the tumbling motion example.

the tumbling motion only occurs for $\lambda = 5.0$, no matter the cell is discretized with 320 elements or 1280 elements. All simulations for $\lambda = 0.2$ and $\lambda = 1.0$ start with a tank-treading motion and may end up with a very deformed shape (a shape with a fixed inclination angle to the flow direction and without membrane tank-treading) if the capillary number Ca exceeds certain critical values.

Figure 5.6 shows the evolution of the inclination angle ϕ_y (the angle between the minor axis of the RBC and the Y axis, as shown in Figure 5.2) and the x component of the coordinates of the numerical probe (For Figure 5.6 (b), this probe is indicated by the black dot

shown in Figure 5.7) as a function of the dimensionless time $\dot{\gamma}t$ [1] for an RBC with $\lambda = 5.0$ flows in a simple shear flow with $Ca = 0.1$. From these figures, it can be seen that these

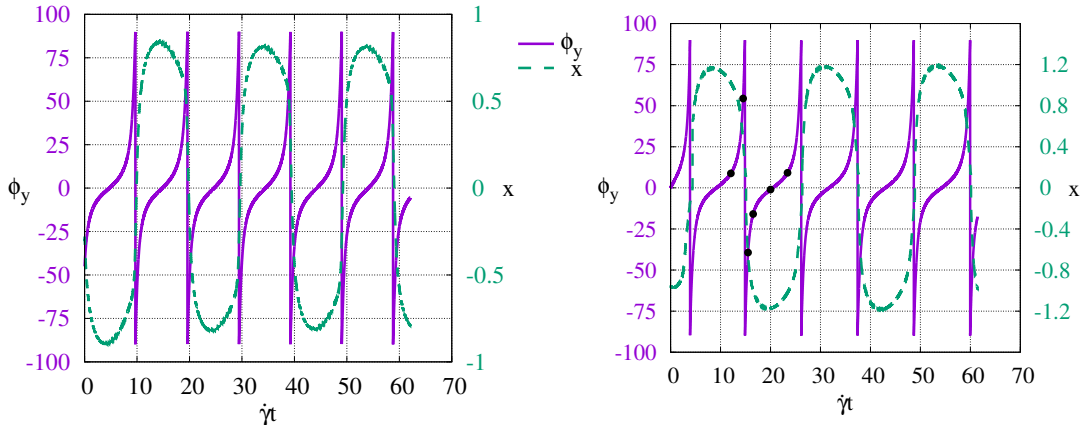

(a) $C_b = 0.0075, \theta_0 = 45°$ (b) $C_b = 0.003, \theta_0 = 0°$

Figure 5.6: Time histories of the inclination angle ϕ_y and the x-position of a numerical probe during the tumbling motion of an RBC flow in a simple shear flow with $\lambda = 5.0$ and $Ca = 0.1$.

two examples with a different reduced bending modulus C_b show a very similar behavior, the RBC periodically rotates in the shear plane, that is, a tumbling motion (some typical cell shapes are shown in Figure 5.7 for $C_b = 0.003$). The average period of this tumbling motion is 19.6 for $C_b = 0.0075$ and 22.5 for $C_b = 0.003$.

Figure 5.7 shows snapshots of the motion/deformation of RBC as well as the cell profiles in the $z = 0$ plane over one half oscillation cycle of the inclination angle ϕ_y for $C_b = 0.003$ (Figure 5.6 (b)). These figures show, in addition to the periodically flipping such as that for the vesicle (Figure 1.5), that their shapes also deform periodically. Moreover, the cross-section (cell profiles in the XY plane) alternates between the biconcave form and a reversed S-shape pattern, as reported by Pozrikidis [125] and Peng et al. [120]. A posteriori check shows that the volume and the global surface variations are about 0.013% and 0.1%, respectively, during such an oscillation circle.

The case with $C_b = 0.0075$ (Figure 5.6 (b)) is compared in detail with the predictions of Peng et al. [120], as shown in Figure 5.8, with same physical parameters $\mu_s = 3.0\,\text{pN}\,\mu\text{m}^{-1}$, $\kappa = 1.8 \times 10^{-19}$ J and initial condition $\phi_y = -45°$. The variation of the inclination angle ϕ_y during its first half circle is compared with those of Peng et al., which were obtained with the single-layer model (SLM) and the multiscale model (MSM). The two horizontal dashed lines mark the orientation levels $\phi_y = -45°$ and $\phi_y = 135°$. The time interval between the intersection points of these lines and the curves provides us the approximation of

[1] To compare with the existing results [120], the simulation time t, initially dimensionalized by t^s_{char}, is multiplied by the capillary number $Ca = t^s_{\text{char}}/t^{\text{flow}}_{\text{char}} = t^s_{\text{char}}/\dot{\gamma}^{-1}$. Thus the new dimensionless time is $t^* = \dot{\gamma}t$.

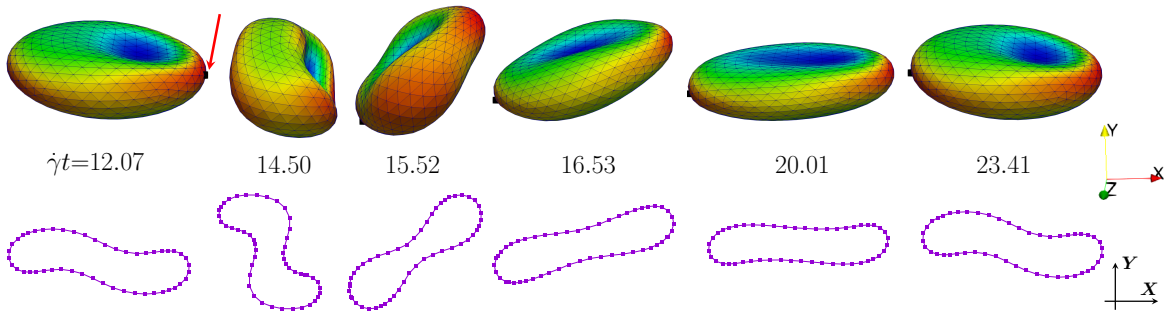

Figure 5.7: RBC shapes (top) and profiles in the XY plane (bottom) over one oscillation cycle of the inclination angle ϕ_y for $\lambda = 5$, $Ca = 0.1$ and $C_{\mathrm{b}} = 0.003$. Snapshots are taken at the time marked by the black dots as shown in Figure 5.6 (b). The black dot indicated by a red arrow is the numerical probe.

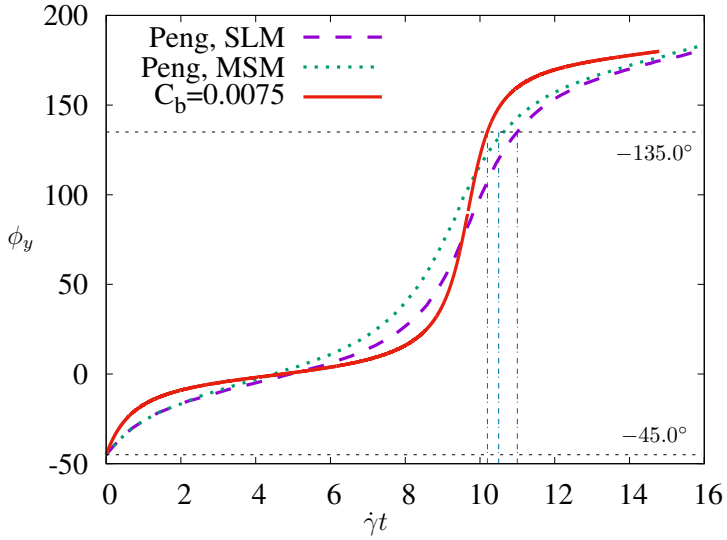

Figure 5.8: Evolution of the inclination angle ϕ_y for the case of $C_b = 0.075$ in Figure 5.6 (a). The result is compared with the predictions by Peng et al. [120].

a half-period of tumbling motion, $T/2$, they are 10.2, 10.5 and 11.0 for our simulation, for predictions given by MSM and SLM, respectively.

It can be seen, both for our simulation and the predictions of Peng, that the angular velocity has a minimum value when the flat side of RBC is parallel to the direction of flow ($\phi_y = 0°$) and reaches a maximum when the flat side is normal to the direction of flow ($\phi_y = 90°$), which are in agreement with the observation of Goldsmith and Marlow for RBCs in dilute suspensions of Poiseuille and Couette flow ($< 2\%$ haematocrit) [62]. Quantitatively, this variation of the angular velocity is stronger in our simulation than those of Peng.

By fitting the experimental data at the low shear rate ($\dot{\gamma} < 20\,\mathrm{s}^{-1}$, or $Ca < 0.05$), Goldsmith and Marlow proposed that the period of rotation can be well described by the Jeffery equation for prolate spheroids

$$T = \dot{\gamma}\Delta T = 2\pi\left(r_p + \frac{1}{r_p}\right), \tag{5.16}$$

where the dimensionless number $r_p \in (0.25, 0.51)$ [62, 125]. Substituting in Eq. (5.16) with the mean value 0.38, we find the period $T \approx 18.9$, which is close to our prediction of 20.4.

Tank-treading

We then show two cases with tank-treading motion under the following common conditions: $\lambda = 1$, $\dot{\gamma} = 100\,\mathrm{s}^{-1}$, and for two different shear moduli $\mu_s = 8.0\,\mathrm{pN\,\mu m^{-1}}$ ($Ca \approx 0.06$) and $\mu_s = 4.0\,\mathrm{pN\,\mu m^{-1}}$ ($Ca \approx 0.12$), in Figure 5.9.

In Figure 5.9 (a) and (c), the red horizontal lines show the inclination angle between the major axis of RBC and the flow direction, it has a value about 18° for $\mu_s = 8.0\,\mathrm{pN\,\mu m^{-1}}$ and 16° for $\mu_s = 4.0\,\mathrm{pN\,\mu m^{-1}}$ once the tank-treading movement becomes stable ($t^* > 60$). Whereas the black curve shows the time history of the angle between a numerical probe (a vertex of the mesh) and the flow direction, it varies periodically as the membrane takes the tank-treading motion. Due to the effect of remeshing, the frequency indicated by the inclination angle of the probe should be different from the actual tank-treading frequency. However, this effect must be subtracted in order to calculate the tank-treading frequency.

Figure 5.9 (b) and (d) show a snapshot (at $t^* \approx 131$) of the tank-treading motion of the RBC, respectively for Figure 5.9 (a) and (c). The RBCs are colored by the mean curvature and the membrane presented here was refined to have 1280 elements to better represent the shape. The arrows indicate the direction of the velocity on the membrane, they are in the range of $[-0.015, 0.015]$ [2] for $\mu_s = 8.0\,\mathrm{pN\,\mu m^{-1}}$ and of $[-0.033, 0.033]$ for $\mu_s = 4.0\,\mathrm{pN\,\mu m^{-1}}$ (at the instant $t^* \approx 131$) for the x component of the velocity, i.e., u_x. This means that periodic variation of the inclination angle of the probe has effect from the membrane tank-treading (and, not only because of remeshing). From the elongation of the shape, the effect of the shear modulus is also shown.

[2] $U_{\mathrm{ref}} = 391\,\mu\mathrm{m\,s}^{-1}$, thus the two speed ranges are about $[-6, 6]\,\mu\mathrm{m\,s}^{-1}$ and $[-13, 13]\,\mu\mathrm{m\,s}^{-1}$.

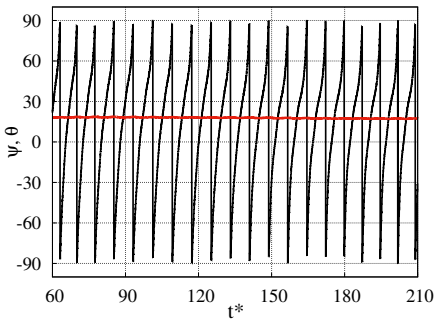

(a) $\mu_s = 8.0\,\mathrm{pN\,\mu m^{-1}}$

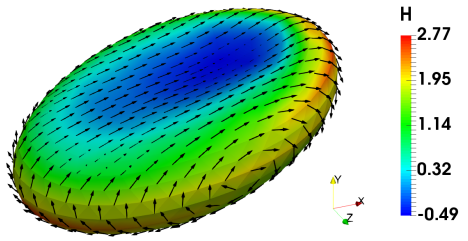

(b) $\mu_s = 8.0\,\mathrm{pN\,\mu m^{-1}}$, $t^* \approx 131$

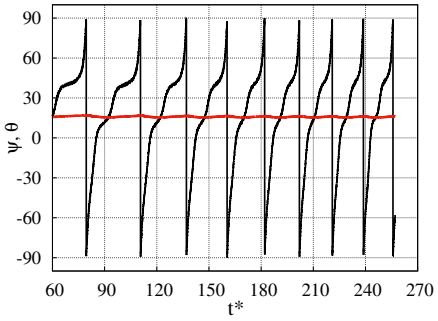

(c) $\mu_s = 4.0\,\mathrm{pN\,\mu m^{-1}}$

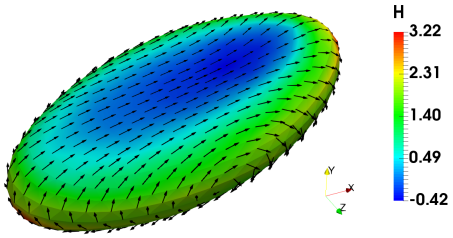

(d) $\mu_s = 4.0\,\mathrm{pN\,\mu m^{-1}}$, $t^* \approx 131$

Figure 5.9: (a) Time histories of the global inclination angle of the RBC (ψ, red line) and the inclination angle of a probe (θ, black curve) during tank-treading motion for $\mu_s = 8.0\,\mathrm{pN\,\mu m^{-1}}$, with 320 elements. (b) Snapshot shows the membrane tank-treading motion of (a) at $t^* \approx 131$, membrane is coded by the mean curvature. (c) Time histories of the two inclination angles for $\mu_s = 4.0\,\mathrm{pN\,\mu m^{-1}}$, with 320 elements. (d) Snapshot shows the membrane tank-treading motion of (c) at $t^* \approx 131$.

5.4.3 RBC in capillary flow

The third and the last simulation example concerns a single RBC in capillary flows with equal viscosities ($\lambda = 1$). Identical to the case of a vesicle flowing in capillary, the Poiseuille flow is given by Eq. (1.19), where $U_m = 0.032\,\text{cm s}^{-1}$ for all cases in this section[3], which lies in the range of $0.002\,\text{cm s}^{-1}$ to $2\,\text{cm s}^{-1}$ as exploited by Pozrikidis [126].

In this section, two different configurations are studied by varying the shear modulus μ_s, they are

A. $\beta = 0.5$, $H_0 = 0.0$ and $\theta_0 = -90°$ (see Figure 3.1);

B. $\beta = 0.4$, $H_0 = 0.3$ and $\theta_0 \approx -6°$.

Whereas the bending modulus is set to 2.4×10^{-19} J and the biconcave shape is used as the unstressed shape for both of these configurations. In this example, RBC with different shear moduli μ_s flowing in the capillary are studied numerically and the results are compared with those of the vesicle (RBC with $\mu_s = 0$). To show the evolution of the RBC's shapes under the effect of the shear modulus, and to compare it to that of vesicle, all results are re-scaled by the characteristic time based on the bending modulus t^b_{char} (Eq. (5.14)), namely, $t^* = t/t^b_{\text{char}}$.

Case A

First, we consider that RBCs are initially placed on the axis of the capillary ($H_0 = 0.0$) and that their flat surfaces are orthogonal to the flow ($\theta_0 = -90°$) for the proposed hybrid method with various elastic moduli $\mu_s = 0.0, 0.5, 5.0$ and $10.0\,\mu\text{N m}^{-1}$.

The evolution of the shape is first presented in Figure 5.10 for a vesicle ($\mu_s = 0.0$) and an RBC ($\mu_s = 5.0$). It can be seen that from a biconcave shape, they quickly deform into a parachute-like shape, with a rounded front and a concave rear face. During the evolution, they remain at the centerline with the axisymmetric shape, while the vesicle is more deformed due to the lack of elastic force generated by the cytoskeleton in the case of RBCs.

The evolution of the position of the rounded front and the upper bound are shown in Figure 5.11 (a), respectively by the maximum coordinate of the x component and y component of all vertices, $X_{\max}$ and $Y_{\max}$ (see Figure 5.11 (b)). It is seen that the shapes deform significantly from $t^* = 0$ to $t^* = 0.5$, and a visually quasi-steady shape is obtained at $t^* = 1.0$, as depicted in Figure 5.10. The final stable shapes of these different shear moduli μ_s are plotted in Figure 5.11 (b) for the cell profiles in XY plane (top) and in XZ plane (bottom). This shows that these shapes remain axisymmetric, at least visually, when they reach stable form. As for the effect of the elastic modulus μ_s, it is seen that the deformation is attenuated for an RBC with high resistance to elastic force. This is quite reasonable since an RBC with a higher shear modulus will have a greater ability to withstand hydrodynamic stresses.

The evolution of the additional pressure drop Δp^a (extra pressure needed to maintain the flux due to the presence of RBCs) adimensionned by $\eta^e \overline{U}/R_t$ for these different shear

[3] In this example, the reference length is taken as L_{ref}=R=$D/2$ = 3.91 μm. And, take the local shear rate $\dot{\gamma}(r)$=$\dot{\gamma}(\frac{D}{2})$ (see 1.3.4), the capillary number Ca=$\frac{\eta^e R\dot{\gamma}}{\mu_s}$=$\frac{\eta^e U_m \beta^2}{\mu_s}$ is 0.96 for $\mu_s = 0.1\,\mu\text{N m}^{-1}$ and 0.0192 for $\mu_s = 5.0\,\mu\text{N m}^{-1}$.

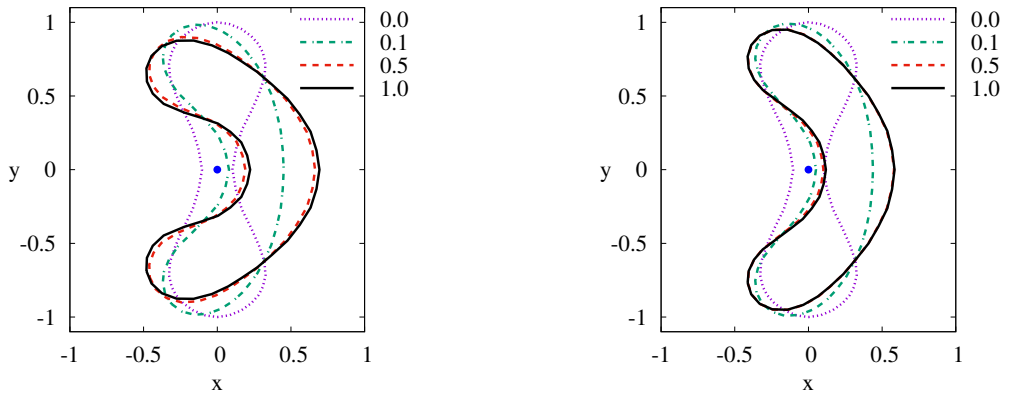

(a) $\mu_s = 0.0\,\mu\mathrm{N\,m^{-1}}$ (b) $\mu_s = 5.0\,\mu\mathrm{N\,m^{-1}}$

Figure 5.10: Cell profiles in the xy plane at times $t^* = 0.0, 0.1, 0.5$ and 1.0. All lengths are scaled by the cell radius $D/2 = 3.91\,\mu\mathrm{m}$.

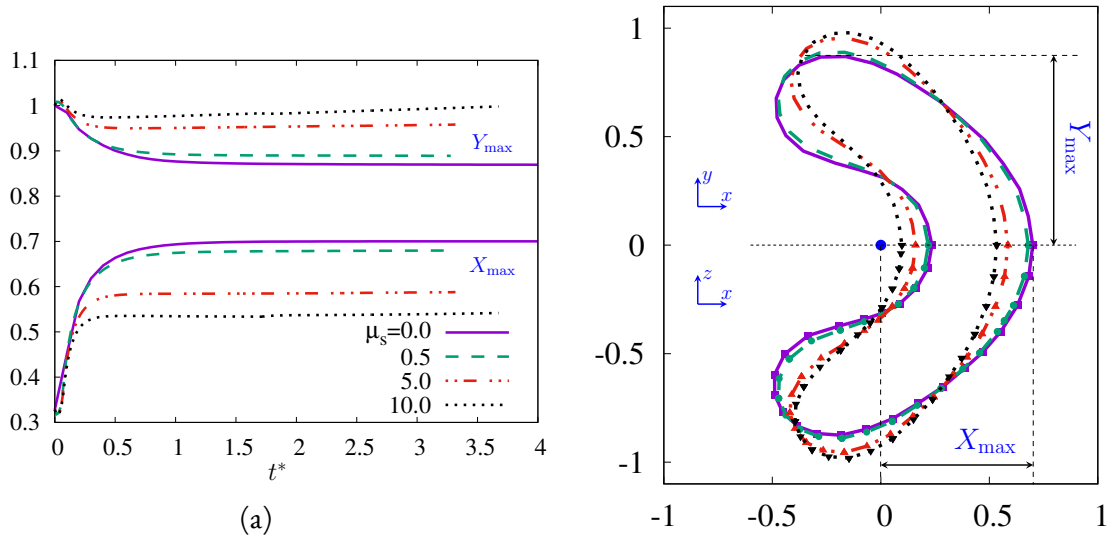

(a) (b)

Figure 5.11: (a) Evolution of the maximum coordinate of the x component of all the vertices and (b) the final stable cell profiles in the plane $z = 0$ (top) and in the plane $y = 0$ (bottom) for various shear modulus $\mu_s = 0.0, 0.5, 5.0$ and $10.0\,\mu\mathrm{N\,m^{-1}}$. All lengths are scaled by the cell radius $D/2 = 3.91\,\mu\mathrm{m}$.

moduli is illustrated in Figure 5.12 (a), where $\overline{U} = U_m/2$ is the mean velocity of unperturbed Poiseuille flow, R_t is the radius of the capillary. The horizontal blue segment on the right

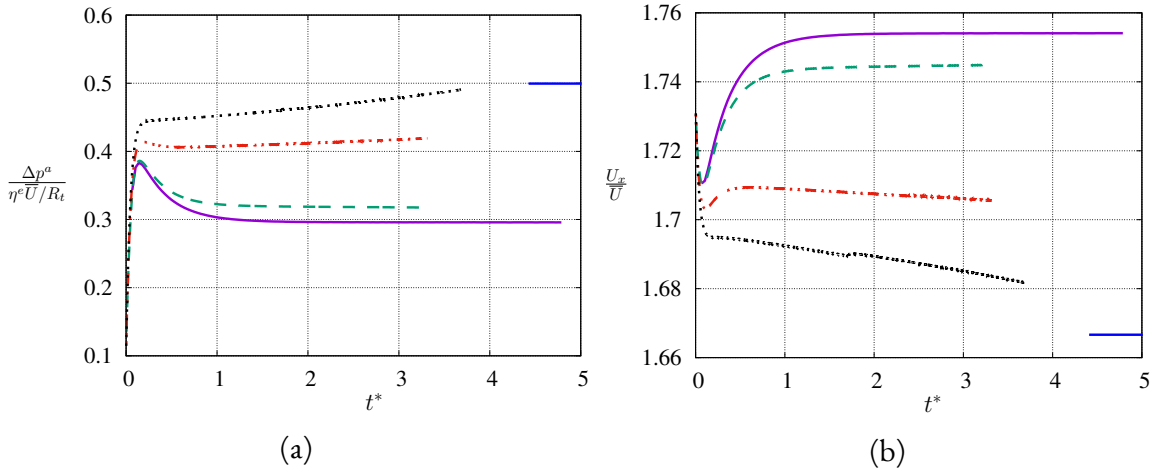

Figure 5.12: Evolution of (a) the additional pressure drop Δp^a adimensionned by $\eta^e \overline{U}/R_t$, and (b) the translational velocity $U_x/\overline{U}$, corresponding the RBCs with various shear moduli in Figure 5.11. The horizontal blue segments on the right of each graph represent the asymptotic predictions for small ($\beta \to 0$), neutrally-buoyant, freely-suspended solid spheres ($\lambda \to \infty$) [126].

illustrates the estimation by Eq. (2.68) with $\lambda \to \infty$, which corresponds to the asymptotic prediction of the additional pressure induced by a small solid sphere moving at the centerline. For these four cases, the additional pressure initially increases to a large value at a small time interval during which significant deformation occurs (see Figure 5.11 (a)), and then it settles to a nearly stable value. In general, by increasing the stiffness of the membrane, the numerical predictions given by the hybrid model converge to the asymptotic value 0.5, the asymptotical prediction for solid spheres.

The evolution of the axial velocity of the cell centroid is correspondingly illustrated in Figure 5.12 (b), and the horizontal blue segment shows the estimation by Eq. (2.67) with same approximation as for the additional pressure drop. This evolution of the translational velocity is similar and consistent with that for the additional pressure drop.

Case B

In this case, the flat plane of RBCs is not placed orthogonally to the flow direction, but only with a small inclined angle $\theta_0 \approx -6°$, and at a height of $H_0 = 0.3$ in a capillary with $R_t = 2.5$. By varying the shear modulus of the membrane μ_s from 0 (vesicle) to a relatively high value 8.0, it is found that a totally different shape evolution process depends upon the shear modulus, as demonstrated in Figure 5.13.

For $\mu_s = 0$, namely a vesicle, the capillary number Ca obtained with the local shear rate $\dot{\gamma}(r)$ computed at $r = L_{\text{ref}}/2$ is 1.0. The snapshots in the first row of Figure 5.13 show that an initially biconcave vesicle ($\nu \approx 0.64$) placed at $H_0 = 0.3$ deforms and evolves into a slipper shape. This process is similar to our previous results for an oblate vesicle, as shown in Figure 3.26 (the shape evolution) and 3.28 (the final stable shape), with $\nu = 0.65$. The

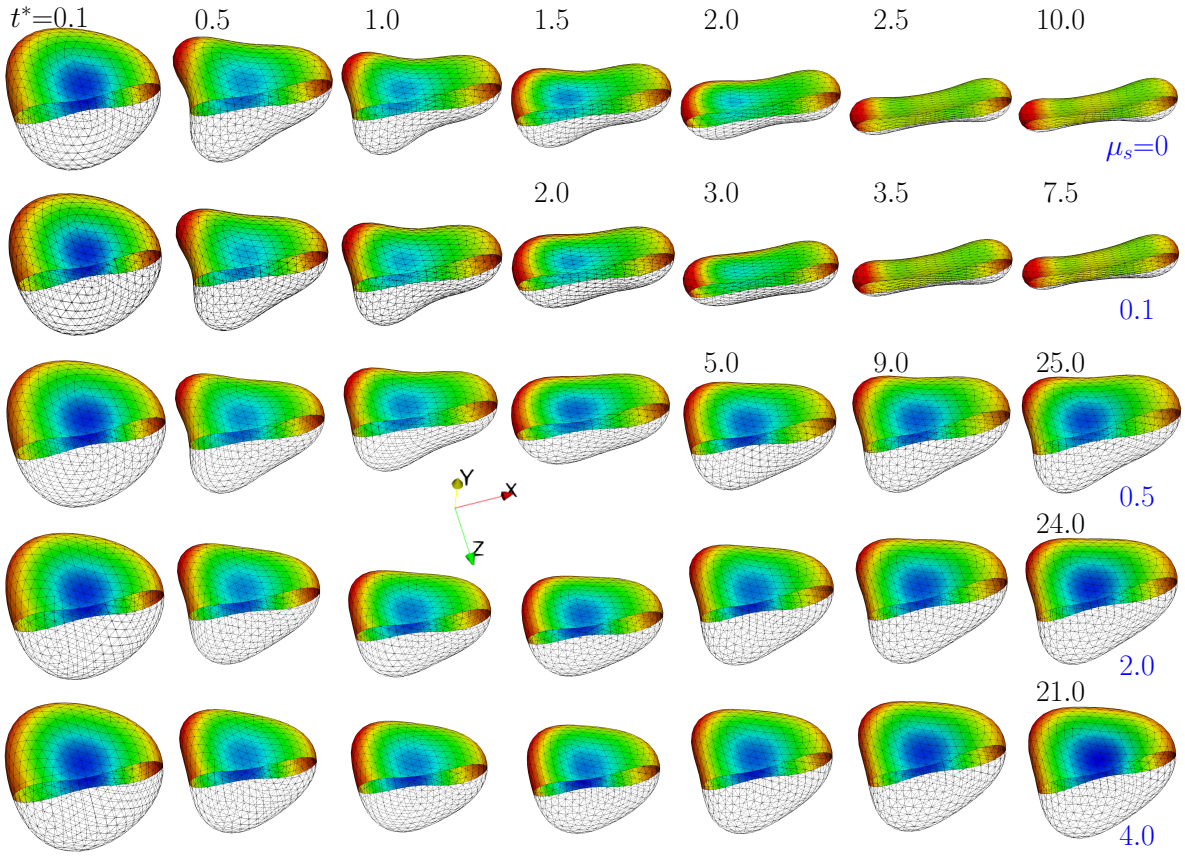

Figure 5.13: Evolution of the RBCs shape in a capillary flow ($\beta = 0.4$) for five different shear modulus $\mu_s = 0.0, 0.1, 0.5, 2.0$, and 4.0 with $H_0 = 0.3$ and $\theta_0 \approx -6°$. Membranes are colored by the mean curvature.

final stable shape remains unchanged to the slight increase of the shear modulus from 0.0 to 0.1, while the evolution process becomes slower due to the elasticity of the membrane, that is, more work is needed to deform an RBC than to deform a vesicle.

A different evolution occurs by increasing the shear modulus to 0.5, as indicated in the third row of Figure 5.13, a biconcave shape finally evolves into a biconcave-croissant shape, for which the two dimples are preserved during the deformation. This evolution remains globally the same by further increasing the shear modulus to 2.0 and then to 4.0. Morphologically, the biconcave shape is first stretched due to hydrodynamic stresses, but this stretched deformation is then relaxed due to a relatively high value of the shear modulus

($\mu_s \geq 0.5$). One of the minor differences lie in this common evolution process is that the deformation becomes more difficult for a higher value of the shear modulus.

Figure 5.14 shows the evolution of the lateral position of the centroid Y_g and the inclination angle θ of RBCs as function of the time t^* (Eq. (5.14)) dimensionless by characteristic time defined by the bending modulus t^b_{char}. It is seen that for the shear modulus those with

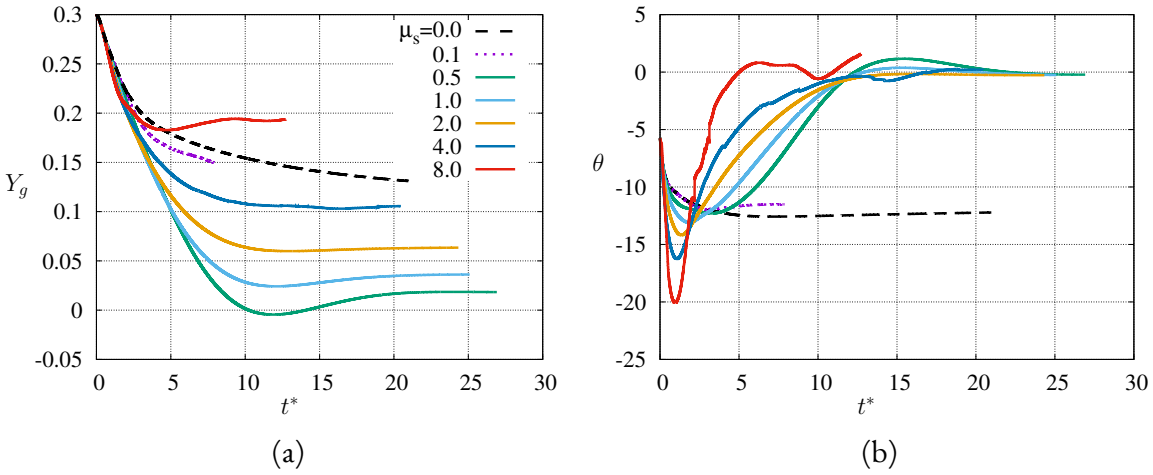

(a) (b)

Figure 5.14: Evolution of (a) the radial position of the centroid Y_g and (b) the inclination angle θ of a vesicle flowing in a capillary ($\beta = 0.4$) for various shear modulus μ_s, varying from 0.0 (a vesicle) to 8.0.

the biconcave-croissant shape as the final stable form (solid line), the stable lateral position Y_g^* increases with the shear modulus μ_s and the inclination angle θ has almost a zero value. That is, the stable biconcave-croissant shape has its flat plane parallel to the flow direction and its radial position increases with the shear modulus. While for the two cases with a slipper as final stable shape, the centroid Y_g is still evolving. For reference, the prediction of the stable lateral position, given by vesicles ($\nu = 0.65$, prolate or oblate), is about 0.04.

5.5 Summary

In this chapter, RBCs and in particular its membrane are first reviewed in Section 5.1. RBCs can generally be modeled as a hybrid of the vesicle and the capsule because of its composite bilayer-spectrin membrane. Two widely used approaches, the classical continuum approach and the discrete modeling (also the coarse-graining one) are then briefly reviewed.

The proposed hybrid continuum–coarse-grained approach, based on our previous vesicle model (as that used in Chapter 3), is then presented. This approach includes the essential mechanical properties of the RBC membrane, namely shearing resistance and bending rigidity, as well as the constraints of fixed surface area and fixed enclosed volume. Specifically, the

RBC membrane is modeled as a composite network, which consists of a dynamically triangulated surface as in a fluid vesicle model. The membrane is then coupled with an additional network of springs with fixed connectivity, representing the cytoskeleton. In this work, the coarse-grained FENE-POW spring model, as presented in Sec. 5.2, is used to describe the elastic cytoskeleton through Eq. (5.7). This force, which is embodied on each spring edge, is transmitted to the lipid bilayer in the normal direction directly and in the tangential plane indirectly via the drag forces $\boldsymbol{f}^d$ (Eq. (5.10)), as presented in Sec. 5.3. Compared to other two-component approaches, the mechanical interaction between the bilayer and the cytoskeleton is explicitly computed. Another advantage is that only one mesh is used both for the bilayer and the cytoskeleton, thus significantly reducing the computational complexity.

Following on from our previous work [105], we presented three simulation examples (with stationary and time-dependent shapes) to illustrate the effectiveness of our model in the isogeometric FEM-BEM framework. Our hybrid approach is first applied to the optical tweezers experiment (Sec. 5.4.1), and then the tumbling and the tank-treading motion are investigated in a linear shear flow (Sec. 5.4.2), and lastly, its dynamics in capillary flow is studied by varying the shear modulus μ_s (Sec. 5.4.3). Thanks to the subdivision representation, no local anomalous surface features (kinks) appear even in the case of large deformations such as the tumbling case, contrary to the previous work [105] with simple linear triangular elements.

6 Conclusions and Perspectives

6.1 Conclusions

The main objectives of this dissertation were to numerically investigate the dynamics of soft particles – lipid bilayer vesicles and red blood cells – in microchannel flows. To this end, the original code has been developed to account for microchannel walls of arbitrary cross-section and incorporated into a previous isogeometric boundary element method model for unbounded Stokes flows. The newly-developed code has been validated by two well-known examples – a clean liquid drop flowing in circular capillaries and a capsule moving in a rectangular microchannel. Moreover, it is shown that the numerical method preserves second-order convergence in both time and space. Subsequently, the code has been used to study the dynamics of a vesicle or a red blood cell that is transported through a circular tube in a pressure-driven flow.

The motion and deformation of a vesicle in tube flow with matched viscosity of inner and outer fluids are determined by three independent dimensionless parameters, namely, the vesicle's reduced volume, the flow confinement, and the capillary number. A deflated vesicle initially placed at an off-center position, is shown to migrate also perpendicular to the flow direction due to both the presence of the wall boundary and the curvature of the imposed flow profile. Three general migration modes have been clearly identified – migration to the flow centerline (i.e., inward migration), centered snaking, and migration to an off-center position – depending on these three control parameters. Simulation results revealed that during the lateral migration, the vesicle's shape undergoes continuous deformation due to the hydrodynamic stresses imposed by the flow onto the membrane. Once the lateral migration speed vanishes, a stable shape is obtained. In comparison with previous studies, various stable shapes have been reproduced, including bullet shape, parachute shape, peanut shape, croissant shape, slipper shape, and also a not well-documented one, namely the *biconcave-croissant* shape that has two biconcave flat surfaces (like the unstressed shape of RBCs) and has two planes of symmetry (like a croissant shape). A noticeable feature found is the membrane sliding (tank-treading motion) that occurs during the lateral migration or for the non-axisymmetric shapes. Furthermore, it is shown that the flow structure on the vesicle membrane of the slipper shape depends on the degree of confinement. Simulation results made it clear that upon increasing either the confinement or the capillary number, the stable shape tends to have more planes of symmetry – a stable form transition from non-axisymmetric one to axisymmetric one, or the centroid of the stable form tends to decrease to zero if the corresponding free space stable shape is a slipper (characterized with non-zero lateral position). Taken together, several phase diagrams of stable shapes for different re-

duced volumes have been built in the (confinement, capillary number) space, showing an extension of the set of vesicle morphologies and rich vesicle dynamics.

Under high confinement, it is expected that the vesicle shape preserves axisymmetry, which has allowed us to study vesicle hydrodynamics by means of the axisymmetric boundary element method. The geometric properties of a vesicle – fixed volume and surface area – yield critical flow confinement or a low limit to the radius of tubes through which a vesicle may pass intact. Simulation results have been obtained in a wide range of the reduced volume (i.e., $0.6 \leq \nu \leq 0.98$) for different degrees of confinement up to near critical value. Our high-fidelity BEM simulations have produced the prediction of the most important hydrodynamical quantities of interest – vesicle mobility and extra pressure drop, the latter having implication for the rheology of a vesicle suspension in tube flow. Being able to deal with a wider range of the reduced volume, this study has extended the previous numerical investigation of vesicle hydrodynamics in high confined flows. The numerical results, together with previous asymptotic theory and various scaling laws obtained herein, offer possibilities for tube-flow experiments to correlate easily accessible quantities such as vesicle velocity and its length to the extra pressure drop. Several other quantities of interest can also be accurately predicted, like the reduced volume, even the thickness of lubrication film from which maximal tension in the membrane can be inferred, too. It is our hope that the results presented this paper could serve as a benchmark for future studies and help devise and interpret tube-flow experiments.

By combining a continuum description of a lipid membrane with a discrete representation of cytoskeleton, we have presented an approach for modeling the membrane of red blood cells in the context of the prediction of red blood cells dynamics in a flow. Compared to other two-component approaches, we explicitly computed the mechanical interaction between the bilayer and the cytoskeleton by considering normal elastic spring and tangential friction force. Another advantage is only one mesh that is used both for the bilayer and the cytoskeleton, thus significantly reducing the computational complexity. The newly-developed model has offered the possibility of studying tank-treading and tumbling motions of an RBC immersed in a linear shear flow, and RBCs dynamics in tube flow. This work fills the gap between continuum mechanical modeling and coarse-grained modeling of RBC membranes by fusing these two approaches.

6.2 Perspectives

We outline below some improvements and future potential developments that are closely related to this work:

- *How to improve the efficiency of simulations?* BEM simulations of 3D vesicle dynamics are computationally challenging and time-consuming, particularly for highly deflated vesicles and under high flow confinement – it took several months (with 6 CPUs) to simulate a snaking dynamics with 1280 elements (Fig. 3.3). One of the major difficulties stems from the constraint of the vesicle's surface incompressibility that has to be satisfied at each time step. One possible way to overcome this hurdle would be to

implement a penalization method (or quasi-incompressibility method) that is widely employed in the numerical solution of the incompressible Navier-Stokes equations.

- We have almost the whole phase diagram of vesicle shapes in tube flow for the reduced volumes equal to 0.95, 0.9, and 0.85, it would be interesting to extend simulations to include smaller reduced volumes.

- The newly-developed code allows for the different cross-sections of conduit flow, it's natural to extend the study to square or rectangular section, or even convergent-divergent conduits. Such an extension would find direct applications to microfluidic experimentations.

- The proposed hybrid RBC model is a combination of the vesicle model with a network of springs with fixed connectivity, representing the cytoskeleton. Since the thin elastic membrane can also be modeled with a capsule model, a combination of vesicle and capsule models would constitute a new, more consistent approach to modeling the mechanical properties of the RBC membrane.

- Our code is currently written in Java (partially multithreading), it could be beneficial if it were re-coded into fully parallelized code, with C++ for example. A combination of OpenACC with CUDA-enabled GPUs computing (only partially available, up to now) would lead to a substantial improvement over the present version.

A Lubrication theory

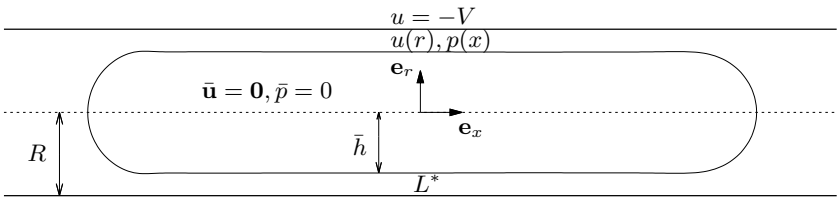

Figure A.1: Schematic of lubrication theory analysis for a steady, sphero-cylindrical vesicle moving along the axis of a circular tube of radius R. In a coordinate frame moving with the vesicle, there can be no flow and pressure gradient inside the vesicle. The vesicle has a cylindrical main body with a length L^*, assumed large compared to R. Plotted vesicle profile corresponds to a vesicle shape for $\nu = 0.6$, $\lambda = 1.92$ and $\mathrm{Ca_B} = 50$ (shown in Figure 4.3(d)); the tube wall is placed at more than 20% away from its actual place in order to amplify the width of the gap between the vesicle and the tube wall.

We combine previously reported results in the literature [9, 10, 27, 99, 136] to present an axisymmetric form of lubrication theory for a vesicle in tube flow. Our aim is not to numerically resolve the complete system of governing equations of the lubrication theory, as it was generally conducted by those authors. Instead, we make use of some asymptotic scaling laws established via lubrication theory analysis to help interpret the present simulation results when confinement is close to its maximum value (i.e., $\lambda \to \lambda_c$). The following paragraphs are an attempt to combine two approaches, one is based on parallel-flow approximation [9, 27, 136], the other is the small-gap theory in the singular limit $\lambda \to \lambda_c$ [10]. Starting from well-established theories developed in [71, 99], we show that the two approaches yield the same asymptotic behavior of the film thickness and vesicle velocity in the limit $\lambda \to \lambda_c$, and the film thickness is further controlled dynamically by the membrane tension.

A schematic description of lubrication theory analysis is shown in Figure A.1. The shape of the membrane is described by $r = \bar{h}(x)$, and the gap separating the vesicle membrane and tube wall has a typical film thickness h, which is defined at the vesicle's midplane, namely $h \equiv R - \bar{h}(0)$. At this stage, we assume that the thickness is small compared to the vesicle length L (but not necessarily small relative to the tube radius), as it is usually the case with high confinements (e.g., as illustrated in Figure 4.3). In the reference frame moving with a steady vesicle centered along the axis of the tube, the axial symmetry of the problem and the incompressibility of the vesicle membrane lead to

- the fluid inside the vesicle is stationary with no pressure gradient (for simplicity we set $\bar{p} = 0$) and behaves like a rigid-body ($\bar{\mathbf{u}} = \mathbf{0}$);

- the viscous normal stress on the membrane vanishes so that the net normal traction on the membrane is the hydrostatic pressure difference between the internal and external flows $\bar{p} - p$, which is equivalent to be $-p$;

- the net shear traction is the viscous shear stress τ due to the external fluid.

Then, in the lubrication approximation, the pressure p in the lubrication layer depends only on the axial position x, and the axial velocity field u is governed by the axial momentum equation and an equation of continuity

$$\frac{\eta}{r}\frac{\partial}{\partial r}\left(r\frac{\partial u}{\partial r}\right) = \frac{\mathrm{d}p}{\mathrm{d}x}, \tag{A.1a}$$

$$\int_{\bar{h}(x)}^{R} 2\pi u r \mathrm{d}r = \pi R^2(U - V) \equiv -2\pi R q, \tag{A.1b}$$

subject to boundary conditions

$$u = -V \qquad \text{at} \quad r = R, \tag{A.2a}$$

$$u = 0 \qquad \text{at} \quad r = \bar{h}(x), \tag{A.2b}$$

where q ($= \frac{1}{2}R(V - U)$) represents a rate per unit circumference of leakback of fluid past the vesicle.

Equations (A.1) with boundary conditions (A.2) yield the Reynolds lubrication equation [71] for the pressure gradient in terms of the azimuthal radius of curvature $r(x) = \bar{h}(x)$:

$$\frac{\mathrm{d}p}{\mathrm{d}x} = -\frac{8\eta U}{R^2(1-(r/R)^2)}\left[\left(\frac{1-(r/R)^2}{2\log(r/R)}\right)\frac{V}{U} - \frac{2q}{RU}\right]\left[1 + (r/R)^2 + \frac{1-(r/R)^2}{\log(r/R)}\right]^{-1}. \tag{A.3}$$

The shear stress exerted on the membrane due to the ambient flow is then given by

$$\tau(r) \equiv \eta\frac{\partial u}{\partial r} = -\frac{1}{4}\frac{\mathrm{d}p}{\mathrm{d}x}\left[2r + \frac{R^2 - r^2}{r\log(r/R)}\right] + \frac{\eta V}{r\log(r/R)}. \tag{A.4}$$

The normal and shear stress boundary conditions (4.4), together with (4.12), respectively, can now be approximated by

$$-p = -2\kappa\left[\frac{1}{g_s}\frac{\mathrm{d}}{\mathrm{d}x}\left(\frac{r^2}{g_s}\frac{\mathrm{d}H}{\mathrm{d}x}\right) + 2H(H^2 - K)\right] + 2\gamma H, \tag{A.5}$$

$$\tau = -\frac{r}{g_s}\frac{\mathrm{d}\gamma}{\mathrm{d}x}, \tag{A.6}$$

where $g_s = r\sqrt{1+(\mathrm{d}r/\mathrm{d}x)^2}$ is the surface metric. The mean and Gaussian curvatures can be written in terms of $r(x)$ and its derivatives:

$$H = \frac{1}{2}(c_1 + c_2), \qquad K = c_1 c_2, \tag{A.7a}$$

$$\text{with} \qquad c_1 = \frac{1}{g_s}, \quad c_2 = -\frac{r^3}{g_s^3}\frac{\mathrm{d}^2 r}{\mathrm{d}x^2}. \tag{A.7b}$$

Equations (A.3)–(A.6), together with the usual symmetry conditions at the front nose of the vesicle $x = L/2$ and at the rear tail of the vesicle $x = -L/2$, are solved numerically in [9, 136]. It is shown that the above axisymmetric lubrication equations yield effectively good approximations to the Stokes flow of a vesicle inside a circular tube if the membrane slope $|\mathrm{d}r/\mathrm{d}x|$ is sufficiently small.

To gain insight into the situation of narrow gaps, we now make an additional assumption that the thickness of the lubricating film between the membrane and inner tube wall is small relative to the tube radius. In this case, the leakback is also small compared with the total flow. Introducing a small parameter

$$\epsilon \equiv \frac{2q}{UR} = \frac{V}{U} - 1 \ll 1, \tag{A.8}$$

and a rescaled film thickness h^* such that

$$r = R(1 - \epsilon h^*), \tag{A.9}$$

we obtain approximate solutions for the pressure gradient and shear stress [71, 99] and their simplified forms in a lubrication layer of uniform thickness (h) with a pure shear flow:

$$\frac{\mathrm{d}p}{\mathrm{d}x} = -\frac{6\eta U}{(R\epsilon h^*)^2}\left[\frac{V}{U} - \frac{1}{h^*} + O(\epsilon h^*)\right] = -\frac{6\eta}{h^2}\left[V - \frac{2q}{h} + O(\epsilon)\right], \tag{A.10a}$$

$$\tau = \frac{\eta U}{R\epsilon h^*}\left[2\frac{V}{U} - \frac{3}{h^*} + O(\epsilon h^*)\right] = \frac{2\eta}{h}\left[V - \frac{3q}{h} + O(\epsilon)\right]. \tag{A.10b}$$

Hence, in this approximation, equations (A.10a) and (A.10b) show that

$$h^* = 1 + O(\epsilon), \qquad h/R = \epsilon + O(\epsilon)^2. \tag{A.11}$$

The range of validity of such a narrow approximation can be estimated from the balance of the axial forces on the vesicle, requiring in some average sense, $\mathrm{d}p/\mathrm{d}x < 0$ and $\tau < 0$. This means that the film thickness must lie in the following range:

$$2q/V < h < 3q/V, \tag{A.12a}$$

$$\text{or equivalently} \qquad 1 - \frac{U}{V} < \delta \equiv h/R < \frac{3}{2}\left(1 - \frac{U}{V}\right), \tag{A.12b}$$

for the clearance parameter δ. We will see that such conditions are always satisfied when $\lambda \to \lambda_c$.

Since we are mostly interested in the asymptotic behavior of quantities of interest established via a narrow-gap analysis, we consider the configuration close to maximal confinement (i.e., $\lambda \to \lambda_c$) in which a cylindrical vesicle with hemispherical ends is formed, nearly fitting the tube cross-section, as shown in Figure A.1. In this limit, a pure geometric consideration – constraints of vesicle surface area and enclosed volume – which are fixed, yields an expansion for the clearance parameter δ [10]:

$$\delta = 1 - \lambda/\lambda_c + O\left[(1 - \lambda/\lambda_c)^2\right]. \tag{A.13}$$

Using Eq. (A.8) in Eq. (A.11) gives an asymptotic behavior of the vesicle mobility, measured in the relative velocity

$$V/U = 1 + (1 - \lambda/\lambda_c) + O\left[(1 - \lambda/\lambda_c)^2\right]. \tag{A.14}$$

This is the same prediction of the small-gap theory in the singular limit $\lambda \to \lambda_c$) [10]

While these two asymptotic expansions are helpful to interpret the present numerical results regarding the film thickness and vesicle mobility, it remains unclear how the clearance parameter is precisely controlled dynamically by a quantity, like hydrodynamic pressure p in the lubrication layer or the membrane tension γ. To this end, by using (A.10), we further simplify the normal and shear stress boundary conditions, equations (A.5) and (A.6), which can be approximated by

$$p = \frac{\kappa}{2R^3} - \frac{\gamma}{R}, \tag{A.15a}$$

$$\frac{\mathrm{d}\gamma}{\mathrm{d}x} = -\tau = -\frac{2\eta V}{h} + \frac{6\eta q}{h^2}, \tag{A.15b}$$

$$\text{with} \qquad q = \left(\frac{6\eta V}{h^2} + \frac{\mathrm{d}p}{\mathrm{d}x}\right)\frac{h^3}{12\eta}. \tag{A.15c}$$

We then obtain a simple expression for the membrane tension gradient in the lubrication layer region

$$\frac{\mathrm{d}\gamma}{\mathrm{d}x} = \frac{\eta V}{h} + O(1), \tag{A.16}$$

thereby indicating that the thickness of the lubrication layer is inversely propositional to the tension gradient in the membrane. That equation gives

$$\gamma(x) = \gamma_R + \frac{\eta V}{h} x \tag{A.17}$$

with γ_R denoting the membrane tension of the rear endcap. Therefore, the tension of the vesicle increases linearly with distance and has a higher tension γ_F at the frontal endcap. The pressure in the lubrication layer, however, decreases with distance according to Eq. (A.15a). The pressure and membrane tension both are of the order of ϵ^{-1} and, therefore bending resistance has a negligible contribution to the hydrodynamic force balance in the lubrication layer. The rear tension γ_R of the vesicle is negligibly small compared to its frontal counterpart γ_F [27, 136] – the rear portion of the vesicle is nearly tensionless, we may estimate the frontal tension for the cylindrical portion having a length of L^*

$$\gamma_F \simeq \frac{\eta V}{\delta}(L^*/R). \tag{A.18}$$

A further overall asymptotic solution of Eqs. (A.15) near the front end of the vesicle has shown [27, 136] as

$$\gamma_F \simeq \eta V (\delta/c_0)^{-3/2}, \tag{A.19}$$

where c_0 is a constant. Finally, the clearance parameter is found to be controlled through a dynamical parameter – the vesicle tension-mobility-based capillary number $\mathrm{Ca_v} = \eta V/\gamma_F$

$$\delta \simeq c_0 {\mathrm{Ca_v}}^{2/3}. \tag{A.20}$$

The numerical prefactor c_0 differs slightly in the literature; $c_0 \simeq 2.123$ in Ref. [136] while $c_0 \simeq 2.05$ in Ref. [27].

B Shape functions

We have summarized here the shape functions used in this thesis.

B.1 Regular Loop Elements

For the regular Loop elements, 12 box-spline shape functions with the local numbering as shown in Figure B.1(a) are used [29].

$$
\begin{aligned}
N_1 &= \frac{1}{12}\left(u^4 + 2u^3v\right) \\
N_2 &= \frac{1}{12}\left(u^4 + 2u^3w\right) \\
N_3 &= \frac{1}{12}\left(u^4 + 2u^3w + 6u^3v + 6u^2vw + 12u^2v^2 + 6uv^2w + 6uv^3 + 2v^3w + v^4\right) \\
N_4 &= \frac{1}{12}\left(6u^4 + 24u^3w + 24u^2w^2 + 8uw^3 + w^4 + 24u^3v + 60u^2vw \right. \\
&\quad \left. + 36uvw^2 + 6vw^3 + 24u^2v^2 + 36uv^2w + 12v^2w^2 + 8uv^3 + 6v^3w + v^4\right) \\
N_5 &= \frac{1}{12}\left(u^4 + 6u^3w + 12u^2w^2 + 6uw^3 + w^4 + 2u^3v + 6u^2vw + 6uvw^2 + 2vw^3\right) \\
N_6 &= \frac{1}{12}\left(2uv^3 + v^4\right) \\
N_7 &= \frac{1}{12}\left(u^4 + 6u^3w + 12u^2w^2 + 6uw^3 + w^4 + 8u^3v + 36u^2vw + 36uvw^2 \right. \\
&\quad \left. + 8vw^3 + 24u^2v^2 + 60uv^2w + 24v^2w^2 + 24uv^3 + 24v^3w + 6v^4\right) \\
N_8 &= \frac{1}{12}\left(u^4 + 8u^3w + 24u^2w^2 + 24uw^3 + 6w^4 + 6u^3v + 36u^2vw \right. \\
&\quad \left. + 60uvw^2 + 24vw^3 + 12u^2v^2 + 36uv^2w + 24v^2w^2 + 6uv^3 + 8v^3w + v^4\right) \\
N_9 &= \frac{1}{12}\left(2uw^3 + w^4\right) \\
N_{10} &= \frac{1}{12}\left(2v^3w + v^4\right) \\
N_{11} &= \frac{1}{12}\left(2uw^3 + w^4 + 6uvw^2 + 6vw^3 + 6uv^2w + 12v^2w^2 + 2uv^3 + 6v^3w + v^4\right) \\
N_{12} &= \frac{1}{12}\left(w^4 + 2vw^3\right)
\end{aligned}
\tag{B.1}
$$

where the barycentric coordinates (u, v, w) obey the relation:

$$u + v + w = 1. \tag{B.2}$$

While the local curvilinear coordinates (s^1, s^2) for the element can be identified with the barycentric coordinates (v, w).

For irregular Loop elements, the irregular patch must be subdivided until the parameter value (s^1, s^2) of interest is within a regular patch, and then the regular shape functions apply again. Refer to [29] for details.

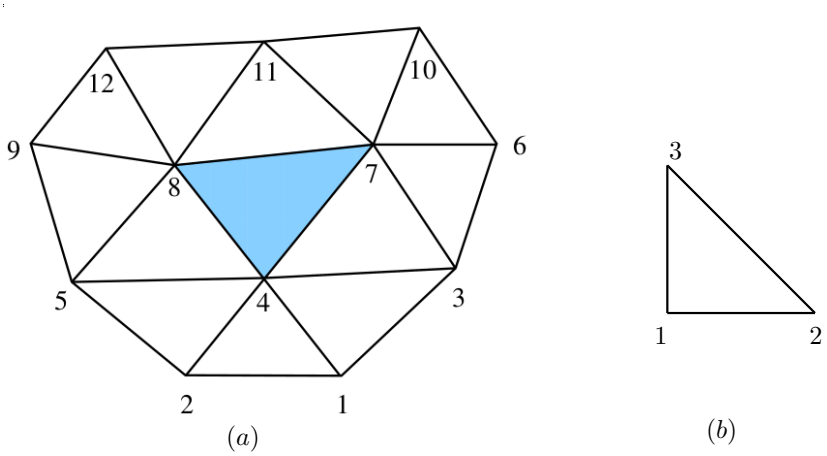

Figure B.1: Control points for (a) regular Loop elements and (b) T1 elements.

B.2 T1 ELEMENTS

The classical linear shape functions for T1 elements, triangles with 3 nodes, with the local numbering illustrated in Figure B.1(b), are

$$\begin{aligned} N_1 &= 1 - u - v \\ N_2 &= u \\ N_3 &= v \end{aligned} \quad . \tag{B.3}$$

C Computation of flow around vesicle

The fluid flow, in vesicle's reference frame, around the vesicle is computed by BIM in order to show its structure and to show its interplay with the shape of vesicles. To avoid interpolation and near-singularity, the fluid surface which corresponds to the vesicle membrane has the same mesh with that of the membrane. Namely, we create a fluid mesh which use exactly the vesicle mesh. The basic steps are,

1. From the mesh contained *vtk* file, generate the *msh* file by using the python package *meshio*[1]. *msh* is the standard mesh file of *Gmsh*[2]. An example script is shown in Listing C.1.

2. Convert the *msh* file to *geo* file in using another python package *pygmsh*[3]. *geo* is the standard geometry file of Gmsh. An example script is shown in Listing C.2.

3. Generate 3D fluid mesh with Gmsh based on the *geo* file with:
   `gmsh fluidmesh.geo -3 -o fluidMesh.msh`

```
""" use package mesoio to read vtk file, and
store the mesh in gmsh format.

NOTE: surface mesh physical tag is set to 0!!!
"""

import meshio
import sys

if len(sys.argv) != 3:
    print("Two parameters should be followed!!")
    exit()
#read vtk file
mesh = meshio.read(sys.argv[1])

mshfile = open(sys.argv[2], 'w')
print('$MeshFormat\n2.0 0 8\n$EndMeshFormat', file=mshfile)

```

[1] https://pypi.org/project/meshio/
[2] http://gmsh.info/
[3] https://pygmsh.readthedocs.io/en/latest/

```
#write vertices
print('$Nodes\n%d'%len(mesh.points), file=mshfile)
for node_id in range(0, len(mesh.points)):
    print(node_id+1, ' ', mesh.points[node_id][0], ' ', mesh.points[node_id][1], ' ', mesh.points[node_id][2], file=mshfile)
print('$EndNodes', file=mshfile)

#write cells
#only work for triangle surface mesh
#physical tag is set to 0
ele_type = 2
nb_tags = 2
print('$Elements\n%d'%len(mesh.cells['triangle']), file=mshfile)
for ele_id in range(0, len(mesh.cells['triangle'])):
    print(ele_id+1, ' ', ele_type, ' ', nb_tags, ' ', 1, ' ', 0, ' ',
          mesh.cells['triangle'][ele_id][0]+1, ' ', mesh.cells['triangle'][ele_id][1]+1, ' ', mesh.cells['triangle'][ele_id][2]+1, file=mshfile)
print('$EndElements', file=mshfile)
```

Listing C.1: vtk2msh: convert the vtk file to msh file

```
from pygmsh import *
import sys
import os

if len(sys.argv) != 3:
    print("Two parameters should be followed!!")
    exit()

#read vtk file
m = GmshMesh(sys.argv[1])
m.write_geo(sys.argv[2])

#add surface loop for inner surface boundary
#bashCommand = "sed -i '/Point/s/}}/\,3.0}}/' {0}".format(sys.argv[2])
lc0 = 3.0
bashCommand = "sed -i '/Point/s/}}/\,{1}}}/' {0}".format(sys.argv[2],lc0)
os.system(bashCommand)
bashCommand = "sed -i '/Physical Surface/p;s//Surface Loop/' {0}".format(sys.argv[2])
os.system(bashCommand)
bashCommand = "sed -i '/Physical Surface/s/Physical Surface(/Physical Surface(\"Soft\"\, /' {0}".format(sys.argv[2])
os.system(bashCommand)


XM = 5.0
YM = 2.0
```

```
ZM = 2.0
lc1 = 0.3
startIdx = 10000
geofile = open(sys.argv[2], 'a')

#write box structure
geofile.write('Point(%d) = {%f,%f,%f,%f};\n'%(startIdx+1, -XM, -YM, ZM, lc1))
geofile.write('Point(%d) = {%f,%f,%f,%f};\n'%(startIdx+2, XM, -YM, ZM, lc1))
geofile.write('Point(%d) = {%f,%f,%f,%f};\n'%(startIdx+3, XM, -YM, -ZM, lc1))
geofile.write('Point(%d) = {%f,%f,%f,%f};\n'%(startIdx+4, -XM, -YM, -ZM, lc1))
geofile.write('Point(%d) = {%f,%f,%f,%f};\n'%(startIdx+5, -XM, YM, ZM, lc1))
geofile.write('Point(%d) = {%f,%f,%f,%f};\n'%(startIdx+6, XM, YM, ZM, lc1))
geofile.write('Point(%d) = {%f,%f,%f,%f};\n'%(startIdx+7, XM, YM, -ZM, lc1))
geofile.write('Point(%d) = {%f,%f,%f,%f};\n'%(startIdx+8, -XM, YM, -ZM, lc1))

geofile.write("Line(%d) = {%d,%d};\n"%(startIdx+1, startIdx+1, startIdx+2))
geofile.write("Line(%d) = {%d,%d};\n"%(startIdx+2, startIdx+2, startIdx+3))
geofile.write("Line(%d) = {%d,%d};\n"%(startIdx+3, startIdx+3, startIdx+4))
geofile.write("Line(%d) = {%d,%d};\n"%(startIdx+4, startIdx+4, startIdx+1))
geofile.write("Line(%d) = {%d,%d};\n"%(startIdx+5, startIdx+5, startIdx+6))
geofile.write("Line(%d) = {%d,%d};\n"%(startIdx+6, startIdx+6, startIdx+7))
geofile.write("Line(%d) = {%d,%d};\n"%(startIdx+7, startIdx+7, startIdx+8))
geofile.write("Line(%d) = {%d,%d};\n"%(startIdx+8, startIdx+8, startIdx+5))
geofile.write("Line(%d) = {%d,%d};\n"%(startIdx+9, startIdx+1, startIdx+5))
geofile.write("Line(%d) = {%d,%d};\n"%(startIdx+10, startIdx+2, startIdx+6))
geofile.write("Line(%d) = {%d,%d};\n"%(startIdx+11, startIdx+3, startIdx+7))
geofile.write("Line(%d) = {%d,%d};\n"%(startIdx+12, startIdx+4, startIdx+8))

geofile.write("Line Loop(%d) = {%d,%d,%d,%d};\n"%(startIdx+1, startIdx+1, startIdx+2, startIdx+3, startIdx+4))
```

```
55  geofile.write("Line Loop(%d) = {%d,%d,%d,%d};\n"%(startIdx+2,
     startIdx+5, startIdx+6, startIdx+7, startIdx+8))
56  geofile.write("Line Loop(%d) = {%d,%d,%d,%d};\n"%(startIdx+3,
     startIdx+1, startIdx+10, -startIdx-5, -startIdx-9))
57  geofile.write("Line Loop(%d) = {%d,%d,%d,%d};\n"%(startIdx+4,
     startIdx+2, startIdx+11, -startIdx-6, -startIdx-10))
58  geofile.write("Line Loop(%d) = {%d,%d,%d,%d};\n"%(startIdx+5,
     startIdx+3, startIdx+12, -startIdx-7, -startIdx-11))
59  geofile.write("Line Loop(%d) = {%d,%d,%d,%d};\n"%(startIdx+6,
     startIdx+4, startIdx+9, -startIdx-8, -startIdx-12))
60
61  geofile.write("Plane Surface(%d) = {%d};\n"%(startIdx+1, startIdx
     +1))
62  geofile.write("Plane Surface(%d) = {%d};\n"%(startIdx+2, startIdx
     +2))
63  geofile.write("Plane Surface(%d) = {%d};\n"%(startIdx+3, startIdx
     +3))
64  geofile.write("Plane Surface(%d) = {%d};\n"%(startIdx+4, startIdx
     +4))
65  geofile.write("Plane Surface(%d) = {%d};\n"%(startIdx+5, startIdx
     +5))
66  geofile.write("Plane Surface(%d) = {%d};\n"%(startIdx+6, startIdx
     +6))
67
68  geofile.write("Physical Surface(\"Box\", %d) = {%d,%d,%d,%d,%d,%d
     };\n"%(10, startIdx+1, startIdx+2, startIdx+3, startIdx+4,
     startIdx+5, startIdx+6))
69
70  geofile.write("Surface Loop(%d) = {%d,%d,%d,%d,%d,%d};\n"%(
     startIdx+1, startIdx+1, startIdx+2, startIdx+3, startIdx+4,
     startIdx+5, startIdx+6))
71  geofile.write("Volume(%d) = {%d,%d};\n"%(startIdx+1, 1, startIdx
     +1))
72  geofile.write("Volume(%d) = {%d};\n"%(startIdx+2, 1))
73  geofile.write("Physical Volume(\"oFluid\", %d) = {%d};\n"%(
     startIdx+1, startIdx+1))
74  geofile.write("Physical Volume(\"iFluid\", %d) = {%d};\n"%(
     startIdx+2, startIdx+2))
75
76  geofile.close()
```

Listing C.2: msh2geo: convert the msh file to geo file

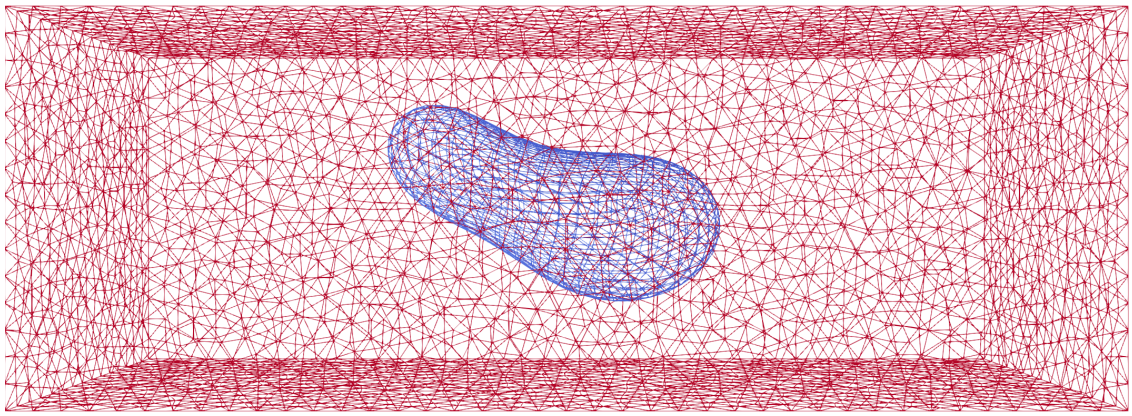

Figure C.1: An example of fluid mesh generated by the aforementioned procedure.

D Support materials

D.1 Accelerate convergence by manually alerting radial position

Here, some numerical examples are presented to show that the acceleration strategy of manual *alert* (a small value in compared with Y_g^c) of the radial position of the centroid of vesicles does not alert the final stable state. The radial position adjustment (δY) is done by inspecting the lateral migration speed U_y, that is, when $U_y > 0$ (such as Figure 3.10 (b) and D.1 (b)), a positive adjustment $\delta Y > 0$ is applied, and otherwise, a negative adjustment is applied.

Figure D.1–D.3 show three different cases in which the results with adjustment of the centroid position are compared to those without adjustment. From these plots, it is seen that the convergence becomes very time consuming for simulations with 1280 elements when Y_g is close to Y_g^c. And the converged values Y_g (with $U_t \approx 0$) with adjustment are consistent with those without adjustment (errors of coarse mesh are responsible for the small discrepancy of results between 320 elements and 1280 elements). This manual alter of the radial position of the centroid of the vesicles should be beneficial in searching the stable radial position of a slipper.

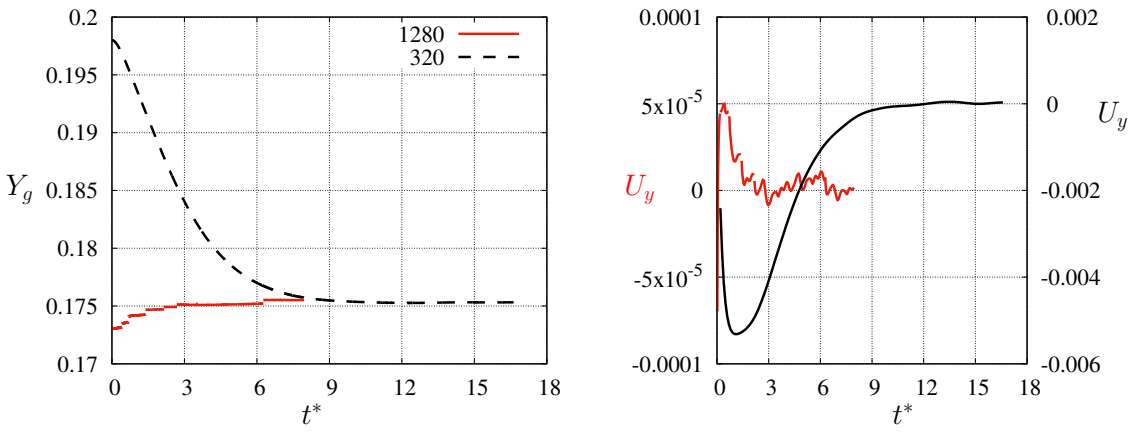

(a) Y_g (b) U_y

Figure D.1: Evolution of (a) the radial centroid position Y_g and (b) the lateral migration speed U_y for $Ca = 1, \nu = 0.9, R_t = 5.0$. Where 320 and 1280 represent the number of elements used in the discretization of the vesicles.

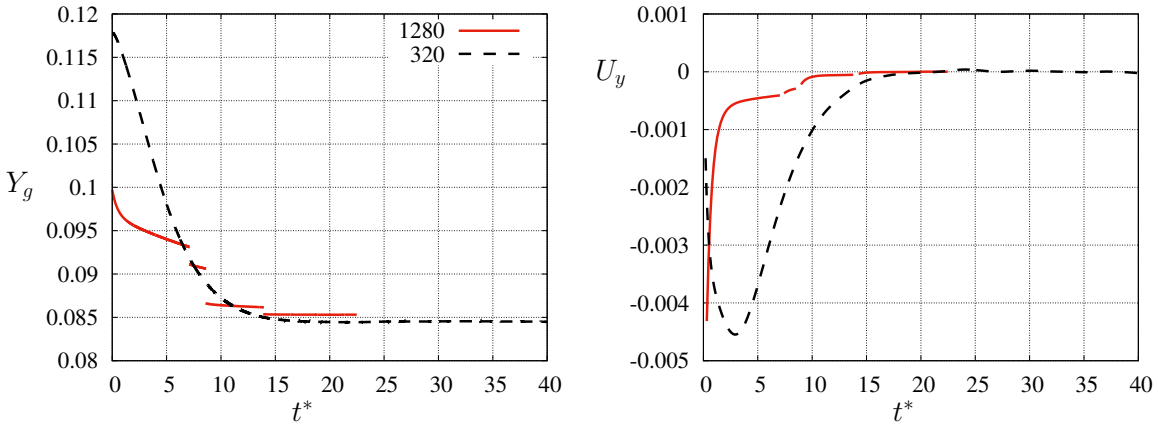

(a) Y_g (b) U_y

Figure D.2: Evolution of (a) the radial centroid position Y_g and (b) the lateral migration speed U_y for $Ca = 1, \nu = 0.9, R_t = 3.7$.

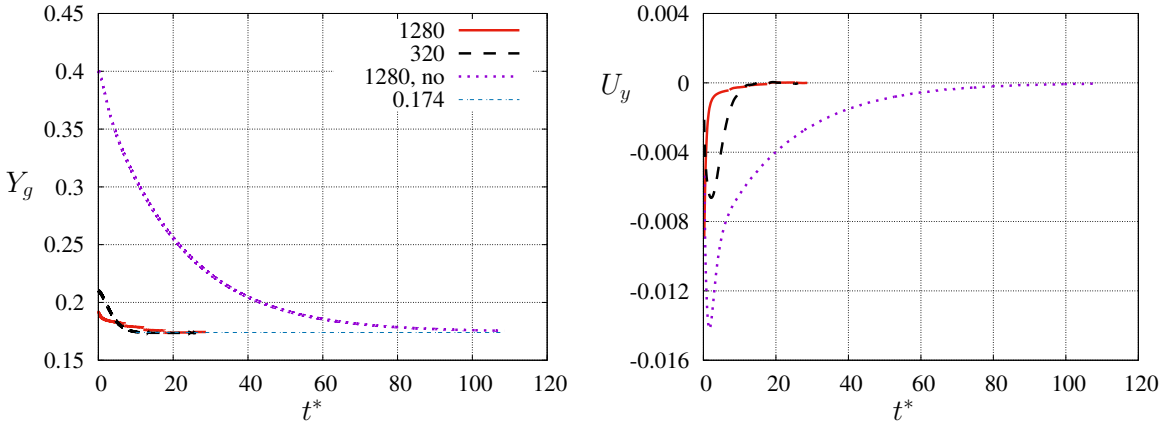

(a) Y_g (b) U_y

Figure D.3: Evolution of (a) the radial centroid position Y_g and (b) the lateral migration speed U_y for $Ca = 1, \nu = 0.85, R_t = 4.0$. Where *no* means that *no* adjustment is applied.

D.2 Unbounded cases

Figure D.4 shows a vesicle ($\nu = 0.85$) flowing in an unbounded Poiseuille flow ($Ca = 1$) with two different initial lateral positions $H_0 = 0.5582$ and 0.05. It is seen that without the capillary wall, the vesicle migrates to a stable position Y_g^* about 0.54 even for $H_0 = 0.05$, unlike those in the Figure 3.22.

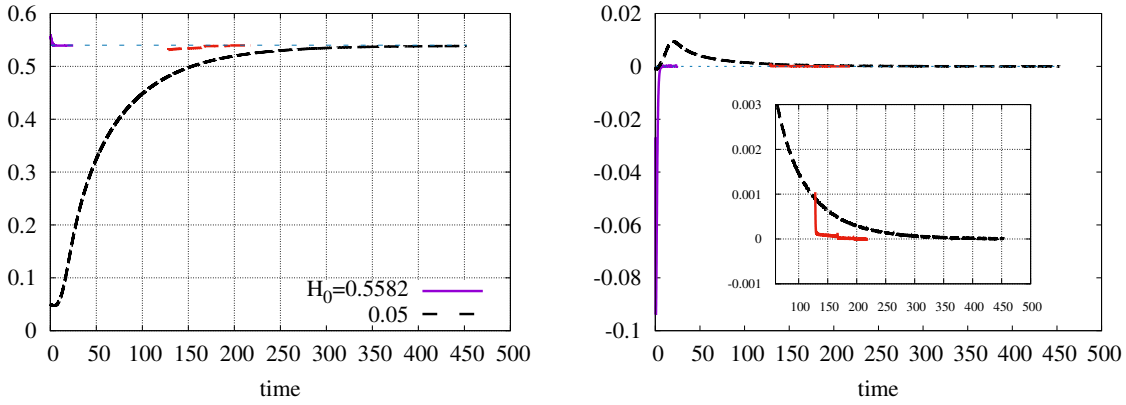

(a) Y_g (b) U_y

Figure D.4: Evolution of (a) the lateral position Y_g of the centroid and (b) the lateral migration speed U_y in an unbounded Poiseuille flow with $Ca = 1, \nu = 0.85$, and two initial lateral positions H_0. The red curves represent simulations with manual adjustment of the lateral position of the vesicle (case $H_0 = 0.05$).

Figure D.5 shows an initial oblate vesicle ($\nu = 0.65$) flowing in an unbounded Poiseuille flow ($Ca = 1$) under three different initial conditions $(H_0, \theta_0) = (0.05, 0.0)$, $(0.05, -0.15)$ and $(0.35, -0.15)$. Unlike the examples presented in sec. 3.3.7 (such as Figure 3.27), in which an initial oblate veiscle (following in a bounded Poiseuille flow) can transform either into an elongated slipper shape or a biconcave-croissant shape, depending on the initial conditions (H_0, θ_0). While the three cases illustrated in Figure D.5 first transform into the biconcave-croissant shape, but this form seems unstable in the unbounded Poiseuille flow, and it continues to evolve into a slipper shape, as illustrated by the insets. More precisely, in the case where $H_0 = 0.35$, the initial oblate shape first evolves into the biconcave-croissant shape (in a damped oscillation way), whereas this latter becomes unstable (at the time about 100) and rapidly transforms into a slipper shape. The unstable originates from one of the convex rear ends (in the Oxz plane), which is accompanied by a significant increase in lateral position Z_g of the centroid.

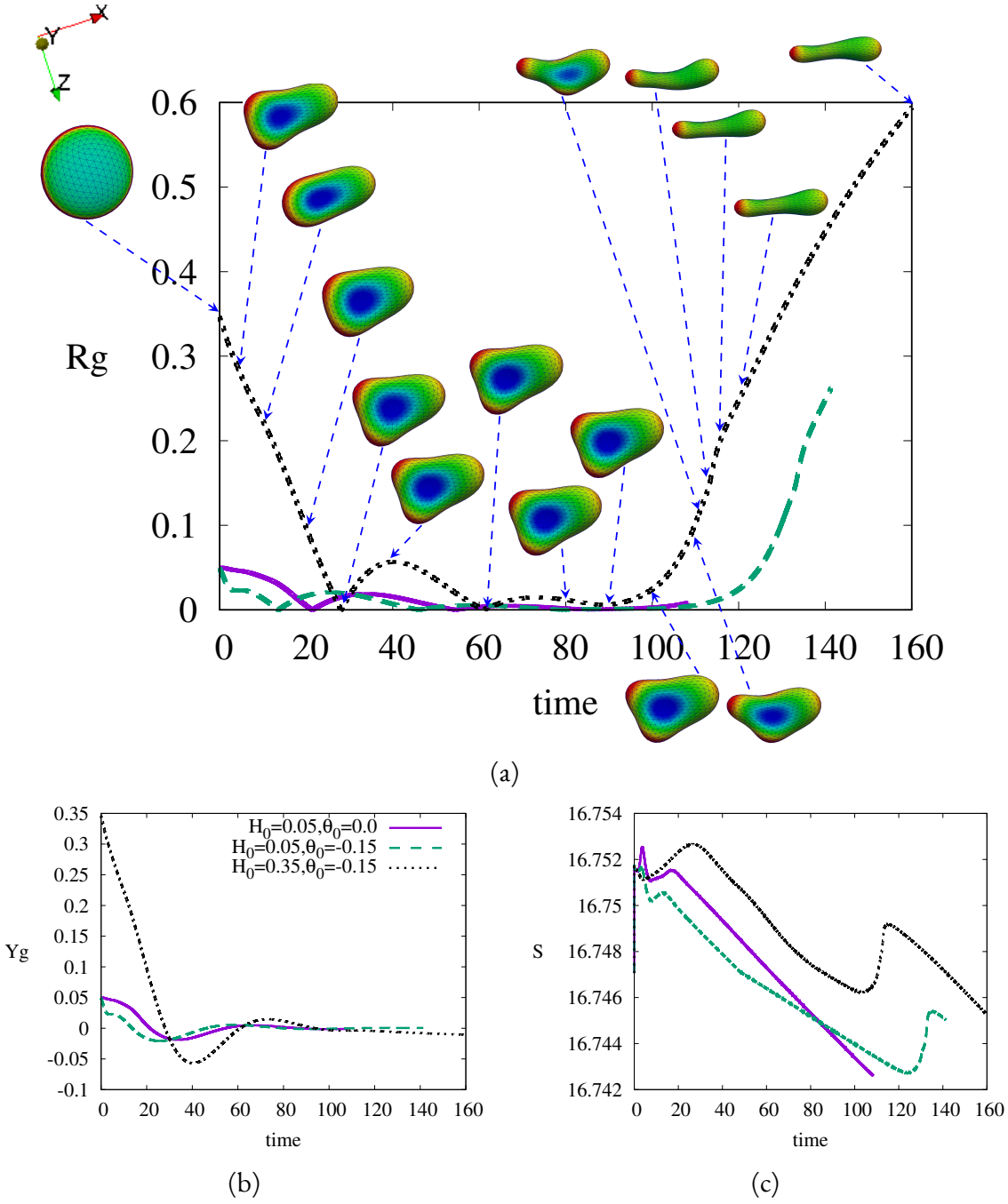

Figure D.5: Evolution of (a) $R_g = \sqrt{Y_g^2 + Z_g^2}$ of the centroid, (b) Y_g of the centroid, and (c) the membrane area S of an initial oblate vesicle in an unbounded Poiseuille flow with $Ca = 1$ and $\nu = 0.65$. The insets are instantaneous vesicle shapes of the case $H_0 = 0.35$, colored by the mean curvature of the membrane.

Bibliography

1. M. Abkarian, C. Lartigue, and A. Viallat. "Tank Treading and Unbinding of Deformable Vesicles in Shear Flow: Determination of the Lift Force". *Phys. Rev. Lett.* 88, 2002, p. 068103. DOI: 10.1103/PhysRevLett.88.068103 (cit. on pp. 7, 57).
2. M. Abkarian and A. Viallat. "On the Importance of the Deformability of Red Blood Cells in Blood Flow". In: *Fluid-Structure Interactions in Low-Reynolds-Number Flows*. Royal Society of Chemistry, 2015, pp. 347–462 (cit. on pp. 6, 122, 124, 126–127).
3. D. Abreu, M. Levant, V. Steinberg, and U. Seifert. "Fluid vesicles in flow". *Advances in colloid and interface science* 208, 2014, pp. 129–141. DOI: 10.1016/j.cis.2014.02.004 (cit. on pp. 3, 15, 29, 57).
4. C. K. Aidun and J. R. Clausen. "Lattice-Boltzmann Method for Complex Flows". *Annual Review of Fluid Mechanics* 42, 2010, pp. 439–472. DOI: 10.1146/annurev-fluid-121108-145519 (cit. on p. 14).
5. O. Aouane, M. Thiébaud, A. Benyoussef, C. Wagner, and C. Misbah. "Vesicle dynamics in a confined Poiseuille flow: from steady state to chaos". *Physical Review E* 90, 2014, p. 033011. DOI: 10.1103/PhysRevE.90.033011 (cit. on p. 12).
6. F. Aydin, X. Chu, J. Greenstein, and M. Dutt. "A review on phospholipid vesicles flowing through channels". *MRS Communications* 8, 2018, pp. 718–726. DOI: 10.1557/mrc.2018.118 (cit. on p. 15).
7. P. Bagchi, P. C. Johnson, and A. S. Popel. "Computational fluid dynamic simulation of aggregation of deformable cells in a shear flow". *Journal of biomechanical engineering* 127, 2005, pp. 1070–1080. DOI: 10.1115/1.2112907 (cit. on p. 14).
8. P. Bagchi and R. M. Kalluri. "Dynamic rheology of a dilute suspension of elastic capsules: effect of capsule tank-treading, swinging and tumbling". *Journal of Fluid Mechanics* 669, 2011, 498–526. DOI: 10.1017/S0022112010005161 (cit. on p. 14).
9. J. M. Barakat and E. S. Shaqfeh. "Stokes flow of vesicles in a circular tube". *Journal of Fluid Mechanics* 851, 2018, pp. 606–635. DOI: 10.1017/jfm.2018.533 (cit. on pp. 107, 143, 145).
10. J. M. Barakat and E. S. Shaqfeh. "The steady motion of a closely fitting vesicle in a tube". *Journal of Fluid Mechanics* 835, 2018, pp. 721–761. DOI: 10.1017/jfm.2017.743 (cit. on pp. 106, 109–110, 113–115, 143, 146).
11. D. Barthès-Biesel. "Motion of a spherical microcapsule freely suspended in a linear shear flow". *Journal of Fluid Mechanics* 100, 1980, pp. 831–853. DOI: 10.1017/S0022112080001449 (cit. on p. 12).
12. D. Barthès-Biesel. "Motion and Deformation of Elastic Capsules and Vesicles in Flow". *Annual Review of Fluid Mechanics* 48, 2016, pp. 25–52. DOI: 10.1146/annurev-fluid-122414-034345 (cit. on pp. 2, 11–12, 14–15).
13. N. Beams, L. Olson, and J. Freund. "A Finite Element Based P^3M Method for N-Body Problems". *SIAM Journal on Scientific Computing* 38, 2016, A1538–A1560. DOI: 10.1137/15M1014644 (cit. on p. 14).
14. M Behr. "GMRES Usage". URL: http://citeseerx.ist.psu.edu/viewdoc/download?doi=10.1.1.606.972&rep=rep1&type=pdf (cit. on p. 35).

15. M. Belkin, J. Sun, and Y. Wang. "Discrete laplace operator on meshed surfaces". In: *Proceedings of the twenty-fourth annual symposium on Computational geometry*. ACM. 2008, pp. 278–287. DOI: 10.1145/1377676.1377725 (cit. on pp. 15–16).

16. T. Biben and C. Misbah. "Tumbling of vesicles under shear flow within an advected-field approach". *Phys. Rev. E* 67, 2003, p. 031908. DOI: 10.1103/PhysRevE.67.031908 (cit. on p. 13).

17. T. Biben, A. Farutin, and C. Misbah. "Three-dimensional vesicles under shear flow: Numerical study of dynamics and phase diagram". *Phys. Rev. E* 83, 2011, p. 031921. DOI: 10.1103/PhysRevE.83.031921 (cit. on pp. 7–8, 57).

18. T. Biben, K. Kassner, and C. Misbah. "Phase-field approach to three-dimensional vesicle dynamics". *Phys. Rev. E* 72, 2005, p. 041921. DOI: 10.1103/PhysRevE.72.041921 (cit. on p. 13).

19. G. Boëdec. "Modélisation d'une vésicule sous forçage hydrodynamique". PhD thesis. Aix-Marseille 3, 2011 (cit. on pp. 4, 10, 119).

20. G. Boëdec, M. Jaeger, and M. Leonetti. "Settling of a vesicle in the limit of quasispherical shapes". *Journal of Fluid Mechanics* 690, 2012, pp. 227–261. DOI: 10.1017/jfm.2011.427 (cit. on p. 7).

21. G. Boëdec, M. Leonetti, and M. Jaeger. "3D vesicle dynamics simulations with a linearly triangulated surface". *Journal of Computational Physics* 230, 2011, pp. 1020–1034. DOI: 10.1016/j.jcp.2010.10.021 (cit. on pp. 12–14, 22, 57, 95–97, 121).

22. G. Boëdec, M. Leonetti, and M. Jaeger. "Isogeometric FEM-BEM simulations of drop, capsule and vesicle dynamics in Stokes flow". *Journal of Computational Physics* 342, 2017, pp. 117–138. DOI: 10.1016/j.jcp.2017.04.024 (cit. on pp. 7, 11–16, 21–22, 24, 26, 28–29, 38, 45, 54–57, 119, 121).

23. Z. Boujja, C. Misbah, H. Ez-Zahraouy, A. Benyoussef, T. John, C. Wagner, and M. M. Müller. "Vesicle dynamics in confined steady and harmonically modulated Poiseuille flows". *Phys. Rev. E* 98, 2018, p. 043111. DOI: 10.1103/PhysRevE.98.043111 (cit. on p. 62).

24. H. Brenner. "Pressure Drop Due to the Motion of Neutrally Buoyant Particles in Duct Flows. II. Spherical Droplets and Bubbles". *Industrial & Engineering Chemistry Fundamentals* 10, 1971, pp. 537–543. DOI: 10.1021/i160040a001 (cit. on p. 109).

25. F. P. Bretherton. "The motion of long bubbles in tubes". *Journal of Fluid Mechanics* 10, 1961, pp. 166–188. DOI: 10.1017/S0022112061000160 (cit. on p. 105).

26. F. L. Brown. "Elastic Modeling of Biomembranes and Lipid Bilayers". *Annual Review of Physical Chemistry* 59, 2008. PMID: 18173377, pp. 685–712. DOI: 10.1146/annurev.physchem.59.032607.093550 (cit. on pp. 13, 30).

27. R. Bruinsma. "Rheology and shape transitions of vesicles under capillary flow". *Physica A: Statistical Mechanics and its Applications* 234, 1996, pp. 249–270. DOI: 10.1016/S0378-4371(96)00358-5 (cit. on pp. 94, 104–105, 143, 147).

28. P. B. Canham. "The minimum energy of bending as a possible explanation of the biconcave shape of the human red blood cell". *Journal of theoretical biology* 26, 1970, pp. 61–81. DOI: 10.1016/S0022-5193(70)80032-7 (cit. on pp. 5, 15).

29. F. Cirak, M. Ortiz, and P. Schröder. "Subdivision surfaces: a new paradigm for thin-shell finite-element analysis". *International Journal for Numerical Methods in Engineering* 47, 2000, pp. 2039–2072. DOI: 10.1002/(SICI)1097-0207(20000430)47:12<2039::AID-NME872>3.0.CO;2-1 (cit. on pp. 15, 22–23, 27, 149–150).

30. D. Cordasco, A. Yazdani, and P. Bagchi. "Comparison of erythrocyte dynamics in shear flow under different stress-free configurations". *Physics of Fluids* 26, 2014, p. 041902. DOI: 10.1063/1.4871300 (cit. on p. 124).

31. G.-H. Cottet, E. Maitre, and T. Milcent. "Eulerian formulation and level set models for incompressible fluid-structure interaction". *ESAIM: Mathematical Modelling and Numerical Analysis* 42, 2008, 471–492. DOI: 10.1051/m2an:2008013 (cit. on p. 14).

32. G. Coupier, A. Farutin, C. Minetti, T. Podgorski, and C. Misbah. "Shape Diagram of Vesicles in Poiseuille Flow". *Phys. Rev. Lett.* 108, 2012, p. 178106. DOI: 10.1103/PhysRevLett.108.178106 (cit. on pp. 8, 57–58, 99, 101, 115).

33. G. Coupier, B. Kaoui, T. Podgorski, and C. Misbah. "Noninertial lateral migration of vesicles in bounded Poiseuille flow". *Physics of Fluids* 20, 2008, p. 111702. DOI: 10.1063/1.3023159 (cit. on pp. 8, 58).

34. M. C. Cross and P. C. Hohenberg. "Pattern formation outside of equilibrium". *Reviews of modern physics* 65, 1993, p. 851. DOI: 10.1103/RevModPhys.65.851 (cit. on p. 80).

35. G. Danker and C. Misbah. "Rheology of a Dilute Suspension of Vesicles". *Phys. Rev. Lett.* 98, 2007, p. 088104. DOI: 10.1103/PhysRevLett.98.088104 (cit. on pp. 7, 57).

36. P.-G. De Gennes. "Soft matter". *Rev. Mod. Phys.* 64, 1992, pp. 645–648. DOI: 10.1103/RevModPhys.64.645 (cit. on p. 1).

37. J. Deschamps, V. Kantsler, E. Segre, and V. Steinberg. "Dynamics of a vesicle in general flow". *Proceedings of the National Academy of Sciences* 106, 2009, pp. 11444–11447. DOI: 10.1073/pnas.0902657106 (cit. on p. 7).

38. J. Deschamps, V. Kantsler, and V. Steinberg. "Phase Diagram of Single Vesicle Dynamical States in Shear Flow". *Phys. Rev. Lett.* 102, 2009, p. 118105. DOI: 10.1103/PhysRevLett.102.118105 (cit. on pp. 7–8).

39. P. Dimitrakopoulos. "Interfacial dynamics in Stokes flow via a three-dimensional fully-implicit interfacial spectral boundary element algorithm". *Journal of Computational Physics* 225, 2007, pp. 408–426. DOI: 10.1016/j.jcp.2006.12.004 (cit. on p. 22).

40. I. K. Dimov, L. Basabe-Desmonts, J. L. Garcia-Cordero, B. M. Ross, A. J. Ricco, and L. P. Lee. "Stand-alone self-powered integrated microfluidic blood analysis system (SIMBAS)". *Lab Chip* 11, 2011, pp. 845–850. DOI: 10.1039/C0LC00403K (cit. on pp. 2, 4).

41. R. Dimova, S. Aranda, N. Bezlyepkina, V. Nikolov, K. A. Riske, and R. Lipowsky. "A practical guide to giant vesicles. Probing the membrane nanoregime via optical microscopy". *Journal of Physics: Condensed Matter* 18, 2006, S1151. DOI: 10.1088/0953-8984/18/28/S04 (cit. on p. 4).

42. V. Doyeux, Y. Guyot, V. Chabannes, C. Prud'homme, and M. Ismail. "Simulation of two-fluid flows using a finite element/level set method. Application to bubbles and vesicle dynamics". *Journal of Computational and Applied Mathematics* 246, 2013. Fifth International Conference on Advanced COmputational Methods in ENgineering (ACOMEN 2011), pp. 251 –259. DOI: 10.1016/j.cam.2012.05.004 (cit. on p. 14).

43. Doyeux, Vincent, Chabannes, Vincent, Prud´homme, Christophe, and Ismail, Mourad. "Simulation of vesicle using level set method solved by high order finite element". *ESAIM: Proc.* 38, 2012, pp. 335–347. DOI: 10.1051/proc/201238018 (cit. on p. 13).

44. E. A. Evans and R. Skalak. *Mechanics and thermodynamics of biomembranes*. CRC Press, 1980 (cit. on p. 123).

45. A. Farutin, T. Biben, and C. Misbah. "Analytical progress in the theory of vesicles under linear flow". *Phys. Rev. E* 81, 2010, p. 061904. DOI: 10.1103/PhysRevE.81.061904 (cit. on pp. 7–8, 58).

46. A. Farutin, T. Biben, and C. Misbah. "3D numerical simulations of vesicle and inextensible capsule dynamics". *Journal of Computational Physics* 275, 2014, pp. 539–568. DOI: 10.1016/j.jcp.2014.07.008 (cit. on pp. 12, 14–16, 22, 35).

47. A. Farutin and C. Misbah. "Symmetry breaking of vesicle shapes in Poiseuille flow". *Phys. Rev. E* 84, 2011, p. 011902. DOI: 10.1103/PhysRevE.84.011902 (cit. on pp. 8, 58).

48. A. Farutin and C. Misbah. "Analytical and Numerical Study of Three Main Migration Laws for Vesicles Under Flow". *Phys. Rev. Lett.* 110, 2013, p. 108104. DOI: 10.1103/PhysRevLett.110.108104 (cit. on pp. 8, 58, 60, 65).

49. A. Farutin and C. Misbah. "Symmetry breaking and cross-streamline migration of three-dimensional vesicles in an axial Poiseuille flow". *Phys. Rev. E* 89, 2014, p. 042709. DOI: 10.1103/PhysRevE.89.042709 (cit. on pp. 8, 57–58, 66, 81, 83).

50. D. A. Fedosov. "Multiscale modeling of blood flow and soft matter". PhD thesis. Brown University, 2010. URL: http://citeseerx.ist.psu.edu/viewdoc/download?doi=10.1.1.715.6978&rep=rep1&type=pdf (cit. on p. 30).

51. D. A. Fedosov, B. Caswell, and G. E. Karniadakis. "A Multiscale Red Blood Cell Model with Accurate Mechanics, Rheology, and Dynamics". *Biophysical Journal* 98, 2010, pp. 2215 –2225. DOI: 10.1016/j.bpj.2010.02.002 (cit. on pp. 13, 15, 22, 30).

52. D. A. Fedosov, B. Caswell, and G. E. Karniadakis. "Systematic coarse-graining of spectrin-level red blood cell models". *Computer Methods in Applied Mechanics and Engineering* 199, 2010, pp. 1937–1948. DOI: 10.1016/j.cma.2010.02.001 (cit. on pp. 13, 118, 120–122, 126).

53. D. A. Fedosov and G. E. Karniadakis. "Triple-decker: interfacing atomistic–mesoscopic–continuum flow regimes". *Journal of Computational Physics* 228, 2009, pp. 1157–1171. DOI: 10.1016/j.jcp.2008.10.024 (cit. on p. 13).

54. D. A. Fedosov, H. Noguchi, and G. Gompper. "Multiscale modeling of blood flow: from single cells to blood rheology". *Biomechanics and Modeling in Mechanobiology* 13, 2014, pp. 239–258. DOI: 10.1007/s10237-013-0497-9 (cit. on p. 13).

55. E. Fehlberg. "Low-order classical Runge-Kutta formulas with stepsize control and their application to some heat transfer problems", 1969 (cit. on p. 36).

56. R Finken, S Kessler, and U Seifert. "Micro-capsules in shear flow". *Journal of Physics: Condensed Matter* 23, 2011, p. 184113. DOI: 10.1088/0953-8984/23/18/184113 (cit. on p. 15).

57. T. M. Fischer, M Stohr-Lissen, and H. Schmid-Schonbein. "The red cell as a fluid droplet: tank tread-like motion of the human erythrocyte membrane in shear flow". *Science* 202, 1978, pp. 894–896. DOI: 10.1126/science.715448 (cit. on p. 126).

58. J. Freund and H Zhao. "A high-resolution fast boundary-integral method for multiple interacting blood cells". *Computational Hydrodynamics of Capsules and Biological Cells*, 2010, p. 71 (cit. on p. 14).

59. J. B. Freund. "Numerical Simulation of Flowing Blood Cells". *Annual Review of Fluid Mechanics* 46, 2014, pp. 67–95. DOI: 10.1146/annurev-fluid-010313-141349 (cit. on pp. 12–15, 21, 29, 117).

60. G. Ghigliotti, A. Rahimian, G. Biros, and C. Misbah. "Vesicle Migration and Spatial Organization Driven by Flow Line Curvature". *Phys. Rev. Lett.* 106, 2011, p. 028101. DOI: 10.1103/PhysRevLett.106.028101 (cit. on pp. 60, 65).

61. E. Gibaud. "Numerical simulation of red blood cells flowing in a blood analyzer". PhD thesis. Université Montpellier, 2015 (cit. on p. 12).

62. H. Goldsmith, J. Marlow, and F. C. MacIntosh. "Flow behaviour of erythrocytes-I. Rotation and deformation in dilute suspensions". *Proceedings of the Royal Society of London. Series B. Biological Sciences* 182, 1972, pp. 351–384. DOI: 10.1098/rspb.1972.0084 (cit. on p. 130).

63. G Gompper, T Ihle, D. Kroll, and R. Winkler. "Multi-particle collision dynamics: A particle-based mesoscale simulation approach to the hydrodynamics of complex fluids". In: *Advanced computer simulation approaches for soft matter sciences III*. Springer, 2009, pp. 1–87. DOI: 10.1007/978-3-540-87706-6_1 (cit. on pp. 13, 15).

64. G Gompper and D. Kroll. "Random surface discretizations and the renormalization of the bending rigidity". *Journal de Physique I* 6, 1996, pp. 1305–1320. DOI: 10.1051/jp1:1996246 (cit. on pp. 15–16).

65. J Gounley, G Boedec, M. Jaeger, and M Leonetti. "Influence of surface viscosity on droplets in shear flow". *Journal of Fluid Mechanics* 791, 2016, pp. 464–494. DOI: 10.1017/jfm.2016.39 (cit. on p. 38).

66. L. Greengard and V. Rokhlin. "A fast algorithm for particle simulations". *Journal of computational physics* 73, 1987, pp. 325–348. DOI: 10.1016/0021-9991(87)90140-9 (cit. on p. 14).

67. R. D. Groot and P. B. Warren. "Dissipative particle dynamics: Bridging the gap between atomistic and mesoscopic simulation". *The Journal of chemical physics* 107, 1997, pp. 4423–4435. DOI: 10.1063/1.474784 (cit. on p. 13).

68. A. Guckenberger, M. P. Schraml, P. G. Chen, M. Leonetti, and S. Gekle. "On the bending algorithms for soft objects in flows". *Computer Physics Communications* 207, 2016, pp. 1–23. DOI: 10.1016/j.cpc.2016.04.018 (cit. on pp. 15, 56, 94).

69. W. Helfrich. "Elastic properties of lipid bilayers: theory and possible experiments". *Zeitschrift für Naturforschung C* 28, 1973, pp. 693–703. DOI: 10.1515/znc-1973-11-1209 (cit. on pp. 5, 15, 93).

70. G. Hetsroni, S. Haber, and E. Wacholder. "The flow fields in and around a droplet moving axially within a tube". *Journal of Fluid Mechanics* 41, 1970, 689–705. DOI: 10.1017/S0022112070000848 (cit. on p. 109).

71. R. Hochmuth and S. Sutera. "Spherical caps in low Reynolds-number tube flow". *Chemical Engineering Science* 25, 1970, pp. 593–604. DOI: 10.1016/0009-2509(70)85091-6 (cit. on pp. 143–145).

72. X.-Q. Hu, A.-V. Salsac, and D Barthès-Biesel. "Flow of a spherical capsule in a pore with circular or square cross-section". *Journal of Fluid Mechanics* 705, 2012, pp. 176–194. DOI: 10.1017/jfm.2011.462 (cit. on pp. 52–53).

73. X.-Q. Hu, B. Sévénié, A.-V. Salsac, E. Leclerc, and D. Barthès-Biesel. "Characterizing the membrane properties of capsules flowing in a square-section microfluidic channel: Effects of the membrane constitutive law". *Phys. Rev. E* 87, 2013, p. 063008. DOI: 10.1103/PhysRevE.87.063008 (cit. on pp. 52–53).

74. T. J. Hughes, J. A. Cottrell, and Y. Bazilevs. "Isogeometric analysis: CAD, finite elements, NURBS, exact geometry and mesh refinement". *Computer methods in applied mechanics and engineering* 194, 2005, pp. 4135–4195. DOI: 10.1016/j.cma.2004.10.008 (cit. on p. 22).

75. Y. Kantor and D. R. Nelson. "Phase transitions in flexible polymeric surfaces". *Phys. Rev. A* 36, 1987, pp. 4020–4032. DOI: 10.1103/PhysRevA.36.4020 (cit. on p. 15).

76. V. Kantsler and V. Steinberg. "Orientation and Dynamics of a Vesicle in Tank-Treading Motion in Shear Flow". *Phys. Rev. Lett.* 95, 2005, p. 258101. DOI: 10.1103/PhysRevLett.95.258101 (cit. on pp. 7, 57).

77. V. Kantsler and V. Steinberg. "Transition to Tumbling and Two Regimes of Tumbling Motion of a Vesicle in Shear Flow". *Phys. Rev. Lett.* 96, 2006, p. 036001. DOI: 10.1103/PhysRevLett.96.036001 (cit. on pp. 7, 57).

78. B. Kaoui, G. H. Ristow, I. Cantat, C. Misbah, and W. Zimmermann. "Lateral migration of a two-dimensional vesicle in unbounded Poiseuille flow". *Phys. Rev. E* 77, 2008, p. 021903. DOI: 10.1103/PhysRevE.77.021903 (cit. on pp. 8, 58).

79. B. Kaoui, N. Tahiri, T. Biben, H. Ez-Zahraouy, A. Benyoussef, G. Biros, and C. Misbah. "Complexity of vesicle microcirculation". *Phys. Rev. E* 84, 2011, p. 041906. DOI: 10.1103/PhysRevE.84.041906 (cit. on pp. 8, 57–58, 62).

80. B. Kaoui, G. Biros, and C. Misbah. "Why Do Red Blood Cells Have Asymmetric Shapes Even in a Symmetric Flow?" *Phys. Rev. Lett.* 103, 2009, p. 188101. DOI: 10.1103/PhysRevLett.103.188101 (cit. on pp. 8–9, 57–58, 62, 69, 75, 80).

81. B. Kaoui, J. Harting, and C. Misbah. "Two-dimensional vesicle dynamics under shear flow: Effect of confinement". *Physical Review E* 83, 2011, p. 066319. DOI: 10.1103/PhysRevE.83.066319 (cit. on p. 14).

82. S. R. Keller and R. Skalak. "Motion of a tank-treading ellipsoidal particle in a shear flow". *Journal of Fluid Mechanics* 120, 1982, pp. 27–47. DOI: 10.1017/S0022112082002651 (cit. on pp. 7, 57–58).

83. S Kessler, R Finken, and U Seifert. "Swinging and tumbling of elastic capsules in shear flow". *Journal of Fluid Mechanics* 605, 2008, pp. 207–226. DOI: 10.1017/S0022112008001493 (cit. on pp. 22, 30).

84. Y. Kim and M.-C. Lai. "Numerical study of viscosity and inertial effects on tank-treading and tumbling motions of vesicles under shear flow". *Phys. Rev. E* 86, 2012, p. 066321. DOI: 10.1103/PhysRevE.86.066321 (cit. on pp. 7, 57).

85. L. af Klinteberg, D. S. Shamshirgar, and A.-K. Tornberg. "Fast Ewald summation for free-space Stokes potentials". *Research in the Mathematical Sciences* 4, 2017, p. 1. DOI: 10.1186/s40687-016-0092-7 (cit. on p. 14).

86. D. A. Knoll and D. E. Keyes. "Jacobian-free Newton–Krylov methods: a survey of approaches and applications". *Journal of Computational Physics* 193, 2004, pp. 357–397. DOI: 10.1016/j.jcp.2003.08.010 (cit. on p. 38).

87. T. Krüger, B. Kaoui, and J. Harting. "Interplay of inertia and deformability on rheological properties of a suspension of capsules". *Journal of Fluid Mechanics* 751, 2014, 725–745. DOI: 10.1017/jfm.2014.315 (cit. on p. 14).

88. A. Kumar and M. D. Graham. "Accelerated boundary integral method for multiphase flow in non-periodic geometries". *Journal of Computational Physics* 231, 2012, pp. 6682 –6713. DOI: 10.1016/j.jcp.2012.05.035 (cit. on p. 14).

89. S. Kuriakose and P. Dimitrakopoulos. "Motion of an elastic capsule in a square microfluidic channel". *Phys. Rev. E* 84, 2011, p. 011906. DOI: 10.1103/PhysRevE.84.011906 (cit. on pp. 30, 51).

90. E. Lac and J. Sherwood. "Motion of a drop along the centreline of a capillary in a pressure-driven flow". *Journal of Fluid Mechanics* 640, 2009, pp. 27–54. DOI: 10.1017/S0022112009991212 (cit. on pp. 43–44, 48, 50, 97).

91. L. Lanotte, J. Mauer, S. Mendez, D. A. Fedosov, J.-M. Fromental, V. Claveria, F. Nicoud, G. Gompper, and M. Abkarian. "Red cells' dynamic morphologies govern blood shear thinning under microcirculatory flow conditions". *Proceedings of the National Academy of Sciences* 113, 2016, pp. 13289–13294. DOI: 10.1073/pnas.1608074113 (cit. on pp. 13–14, 122, 126).

92. V. V. Lebedev, K. S. Turitsyn, and S. S. Vergeles. "Dynamics of Nearly Spherical Vesicles in an External Flow". *Phys. Rev. Lett.* 99, 2007, p. 218101. DOI: 10.1103/PhysRevLett.99.218101 (cit. on pp. 7, 57).

93. V. Lebedev, K. Turitsyn, and S. Vergeles. "Nearly spherical vesicles in an external flow". *New journal of Physics* 10, 2008, p. 043044. DOI: 10.1088/1367-2630/10/4/043044 (cit. on pp. 7–8, 57).

94. R. LeVeque and Z. Li. "Immersed Interface Methods for Stokes Flow with Elastic Boundaries or Surface Tension". *SIAM Journal on Scientific Computing* 18, 1997, pp. 709–735. DOI: 10.1137/S1064827595282532 (cit. on p. 14).

95. J Li, M Dao, C. Lim, and S Suresh. "Spectrin-level modeling of the cytoskeleton and optical tweezers stretching of the erythrocyte". *Biophysical journal* 88, 2005, pp. 3707–3719. DOI: 10.1529/biophysj.104.047332 (cit. on pp. 13, 118).

96. X. Li, Z. Peng, H. Lei, M. Dao, and G. E. Karniadakis. "Probing red blood cell mechanics, rheology and dynamics with a two-component multi-scale model". *Phil. Trans. R. Soc. A* 372, 2014, p. 20130389. DOI: 10.1098/rsta.2013.0389 (cit. on p. 118).

97. X. Li, P. M. Vlahovska, and G. E. Karniadakis. “Continuum- and particle-based modeling of shapes and dynamics of red blood cells in health and disease”. *Soft Matter* 9, 2013, pp. 28–37. DOI: 10.1039/C2SM26891D (cit. on pp. 13, 15, 22, 29, 117).

98. Z. Li, K. Ito, and M.-C. Lai. “An augmented approach for Stokes equations with a discontinuous viscosity and singular forces”. *Computers & Fluids* 36, 2007, pp. 622 –635. DOI: 10.1016/j.compfluid.2006.03.003 (cit. on p. 14).

99. M. Lighthill. “Pressure-forcing of tightly fitting pellets along fluid-filled elastic tubes”. *Journal of Fluid Mechanics* 34, 1968, pp. 113–143. DOI: 10.1017/S0022112068001795 (cit. on pp. 143, 145).

100. R. Lipowsky. “The conformation of membranes”. *Nature* 349, 1991, p. 475. DOI: 10.1038/349475a0 (cit. on p. 98).

101. R. Lipowsky. “Coupling of bending and stretching deformations in vesicle membranes”. *Advances in colloid and interface science* 208, 2014, pp. 14–24. DOI: 10.1016/j.cis.2014.02.008 (cit. on p. 105).

102. N Liron and R Shahar. “Stokes flow due to a Stokeslet in a pipe”. *Journal of Fluid Mechanics* 86, 1978, pp. 727–744. DOI: 10.1017/S0022112078001366 (cit. on p. 95).

103. S.-C. Liu, L. H. Derick, and J. Palek. “Visualization of the hexagonal lattice in the erythrocyte membrane skeleton.” *The Journal of cell biology* 104, 1987, pp. 527–536. DOI: 10.1083/jcb.104.3.527 (cit. on p. 118).

104. C. Loop. “Smooth subdivision surfaces based on triangles”. MA thesis. 1987 (cit. on pp. 22–23).

105. J. Lyu, P. G. Chen, G. Boëdec, M. Leonetti, and M. Jaeger. “Hybrid continuum–coarse-grained modeling of erythrocytes”. *Comptes Rendus Mécanique* 346, 2018, pp. 439–448. DOI: 10.1016/j.crme.2018.04.015 (cit. on pp. 13, 122, 137).

106. R. M. Macmeccan, J. R. Clausen, G. P. Neitzel, and C. K. Aidun. “Simulating deformable particle suspensions using a coupled lattice-Boltzmann and finite-element method”. *Journal of Fluid Mechanics* 618, 2009, 13–39. DOI: 10.1017/S0022112008004011 (cit. on p. 14).

107. E. Maitre, C. Misbah, P. Peyla, and A. Raoult. “Comparison between advected-field and level-set methods in the study of vesicle dynamics”. *Physica D: Nonlinear Phenomena* 241, 2012, pp. 1146 –1157. DOI: 10.1016/j.physd.2012.03.005 (cit. on p. 13).

108. E. Maitre, T. Milcent, G.-H. Cottet, A. Raoult, and Y. Usson. “Applications of level set methods in computational biophysics”. *Mathematical and Computer Modelling* 49, 2009. Trends in Application of Mathematics to Medicine, pp. 2161 –2169. DOI: 10.1016/j.mcm.2008.07.026 (cit. on p. 14).

109. J. L. McWhirter, H. Noguchi, and G. Gompper. “Flow-induced clustering and alignment of vesicles and red blood cells in microcapillaries”. *Proceedings of the National Academy of Sciences* 106, 2009, pp. 6039–6043. DOI: 10.1073/pnas.0811484106 (cit. on pp. 13, 15).

110. S. Mendez, E. Gibaud, and F. Nicoud. “An unstructured solver for simulations of deformable particles in flows at arbitrary Reynolds numbers”. *Journal of computational physics* 256, 2014, pp. 465–483. DOI: 10.1016/j.jcp.2013.08.061 (cit. on pp. 13–14, 22).

111. M. Meyer, M. Desbrun, P. Schröder, and A. H. Barr. “Discrete Differential-Geometry Operators for Triangulated 2-Manifolds”. In: *Visualization and Mathematics III*. Ed. by H.-C. Hege and K. Polthier. Springer Berlin Heidelberg, Berlin, Heidelberg, 2003, pp. 35–57. ISBN: 978-3-662-05105-4 (cit. on p. 15).

112. C. Misbah. “Vacillating Breathing and Tumbling of Vesicles under Shear Flow”. *Phys. Rev. Lett.* 96, 2006, p. 028104. DOI: 10.1103/PhysRevLett.96.028104 (cit. on pp. 7, 57).

113. C. Misbah. “Vesicles, capsules and red blood cells under flow”. In: *Journal of Physics: Conference Series*. Vol. 392. IOP Publishing. 2012, p. 012005. DOI: 10.1088/1742-6596/392/1/012005 (cit. on p. 12).

114. K. Müller, D. A. Fedosov, and G. Gompper. "Smoothed dissipative particle dynamics with angular momentum conservation". *Journal of computational physics* 281, 2015, pp. 301–315. DOI: 10.1016/j.jcp.2014.10.017 (cit. on p. 13).

115. H. Noguchi and G. Gompper. "Dynamics of fluid vesicles in shear flow: Effect of membrane viscosity and thermal fluctuations". *Phys. Rev. E* 72, 2005, p. 011901. DOI: 10.1103/PhysRevE.72.011901 (cit. on pp. 7, 57).

116. H. Noguchi and G. Gompper. "Shape transitions of fluid vesicles and red blood cells in capillary flows". *Proceedings of the National Academy of Sciences* 102, 2005, pp. 14159–14164. DOI: 10.1073/pnas.0504243102 (cit. on pp. 118, 122, 126).

117. H. Noguchi and G. Gompper. "Swinging and Tumbling of Fluid Vesicles in Shear Flow". *Phys. Rev. Lett.* 98, 2007, p. 128103. DOI: 10.1103/PhysRevLett.98.128103 (cit. on pp. 7, 57).

118. P. Olla. "The behavior of closed inextensible membranes in linear and quadratic shear flows". *Physica A: Statistical Mechanics and its Applications* 278, 2000, pp. 87–106. DOI: 10.1016/S0378-4371(99)00563-4 (cit. on p. 57).

119. N. Pamme. "Continuous flow separations in microfluidic devices". *Lab Chip* 7, 2007, pp. 1644–1659. DOI: 10.1039/B712784G (cit. on p. 2).

120. Z. Peng, R. J. Asaro, and Q. Zhu. "Multiscale modelling of erythrocytes in Stokes flow". *Journal of Fluid Mechanics* 686, 2011, pp. 299–337. DOI: 10.1017/jfm.2011.332 (cit. on pp. 122, 124, 128–129).

121. Z. Peng, X. Li, I. V. Pivkin, M. Dao, G. E. Karniadakis, and S. Suresh. "Lipid bilayer and cytoskeletal interactions in a red blood cell". *Proceedings of the National Academy of Sciences* 110, 2013, pp. 13356–13361. DOI: 10.1073/pnas.1311827110 (cit. on p. 122).

122. Z. Peng, A. Mashayekh, and Q. Zhu. "Erythrocyte responses in low-shear-rate flows: effects of non-biconcave stress-free state in the cytoskeleton". *Journal of Fluid Mechanics* 742, 2014, pp. 96–118. DOI: 10.1017/jfm.2014.14 (cit. on p. 124).

123. I. V. Pivkin and G. E. Karniadakis. "Accurate coarse-grained modeling of red blood cells". *Physical review letters* 101, 2008, p. 118105. DOI: 10.1103/PhysRevLett.101.118105 (cit. on p. 15).

124. A. S. Popel and P. C. Johnson. "Microcirculation and hemorheology". *Annual Review of Fluid Mechanics* 37, 2005, pp. 43–69. DOI: 10.1146/annurev.fluid.37.042604.133933 (cit. on p. 1).

125. C Pozrikidis. "Numerical simulation of the flow-induced deformation of red blood cells". *Annals of biomedical engineering* 31, 2003, pp. 1194–1205. DOI: 10.1114/1.1617985 (cit. on pp. 128, 130).

126. C Pozrikidis. "Numerical simulation of cell motion in tube flow". *Annals of Biomedical Engineering* 33, 2005, pp. 165–178. DOI: 10.1007/s10439-005-8975-6 (cit. on pp. 32, 34, 42, 95–96, 132, 134).

127. C. Pozrikidis. *Boundary integral and singularity methods for linearized viscous flow*. Cambridge University Press, 1992 (cit. on pp. 10, 14, 30–33, 95).

128. C. Pozrikidis. *A practical guide to boundary element methods with the software library BEMLIB*. CRC Press, 2002 (cit. on p. 14).

129. C. Pozrikidis. "Interfacial dynamics for Stokes flow". *Journal of Computational Physics* 169, 2001, pp. 250–301. DOI: 10.1006/jcph.2000.6582 (cit. on pp. 12, 14).

130. A. R. Pries, D. Neuhaus, and P. Gaehtgens. "Blood viscosity in tube flow: dependence on diameter and hematocrit". *American Journal of Physiology-Heart and Circulatory Physiology* 263, 1992. PMID: 1481902, H1770–H1778. DOI: 10.1152/ajpheart.1992.263.6.H1770 (cit. on pp. 98, 113–114).

131. A. Rahimian, I. Lashuk, S. Veerapaneni, A. Chandramowlishwaran, D. Malhotra, L. Moon, R. Sampath, A. Shringarpure, J. Vetter, R. Vuduc, D. Zorin, and G. Biros. "Petascale Direct Numerical Simulation of Blood Flow on 200K Cores and Heterogeneous Architectures". In: *Proceedings of the 2010 ACM/IEEE International Conference for High Performance Computing, Networking, Storage and Analysis*. SC '10. IEEE Computer Society, Washington, DC, USA, 2010, pp. 1–11. ISBN: 978-1-4244-7559-9. DOI: 10.1109/SC.2010.42 (cit. on p. 14).

132. A. Rahimian, S. K. Veerapaneni, D. Zorin, and G. Biros. "Boundary integral method for the flow of vesicles with viscosity contrast in three dimensions". *Journal of Computational Physics* 298, 2015, pp. 766–786. DOI: 10.1016/j.jcp.2015.06.017 (cit. on pp. 12–13).

133. A. Rahimian, S. K. Veerapaneni, and G. Biros. "Dynamic simulation of locally inextensible vesicles suspended in an arbitrary two-dimensional domain, a boundary integral method". *Journal of Computational Physics* 229, 2010, pp. 6466–6484. DOI: 10.1016/j.jcp.2010.05.006 (cit. on p. 40).

134. D. A. Reasor Jr, J. R. Clausen, and C. K. Aidun. "Coupling the lattice-Boltzmann and spectrin-link methods for the direct numerical simulation of cellular blood flow". *International Journal for Numerical Methods in Fluids* 68, 2012, pp. 767–781. DOI: 10.1002/fld.2534 (cit. on p. 14).

135. Y. Saad and M. H. Schultz. "GMRES: A generalized minimal residual algorithm for solving nonsymmetric linear systems". *SIAM Journal on scientific and statistical computing* 7, 1986, pp. 856–869. DOI: 10.1137/0907058 (cit. on p. 35).

136. T. W. Secomb, R Skalak, N Özkaya, and J. Gross. "Flow of axisymmetric red blood cells in narrow capillaries". *Journal of Fluid Mechanics* 163, 1986, pp. 405–423. DOI: 10.1017/S0022112086002355 (cit. on pp. 94, 98, 104, 107–109, 112–114, 143, 145, 147).

137. U. Seifert. "Fluid membranes in hydrodynamic flow fields: Formalism and an application to fluctuating quasispherical vesicles in shear flow". *The European Physical Journal B - Condensed Matter and Complex Systems* 8, 1999, pp. 405–415. DOI: 10.1007/s100510050706 (cit. on pp. 7, 57).

138. U. Seifert. "Configurations of fluid membranes and vesicles". *Advances in physics* 46, 1997, pp. 13–137. DOI: 10.1080/00018739700101488 (cit. on pp. 5, 12, 57).

139. U. Seifert, K. Berndl, and R. Lipowsky. "Shape transformations of vesicles: Phase diagram for spontaneous-curvature and bilayer-coupling models". *Physical Review A* 44, 1991, p. 1182. DOI: 10.1103/PhysRevA.44.1182 (cit. on pp. 6–7, 98).

140. J Sigüenza, S. Mendez, D. Ambard, F. Dubois, F. Jourdan, R. Mozul, and F. Nicoud. "Validation of an immersed thick boundary method for simulating fluid–structure interactions of deformable membranes". *Journal of Computational Physics* 322, 2016, pp. 723–746. DOI: 10.1016/j.jcp.2016.06.041 (cit. on pp. 14, 30).

141. J. Sigüenza, S. Mendez, and F. Nicoud. "How should the optical tweezers experiment be used to characterize the red blood cell membrane mechanics?" *Biomechanics and modeling in mechanobiology* 16, 2017, pp. 1645–1657. DOI: 10.1007/s10237-017-0910-x (cit. on p. 124).

142. R. Van der Sman and S Van der Graaf. "Emulsion droplet deformation and breakup with lattice Boltzmann model". *Computer Physics Communications* 178, 2008, pp. 492–504. DOI: 10.1016/j.cpc.2007.11.009 (cit. on p. 13).

143. J. Stam. "Evaluation of loop subdivision surfaces". In: *SIGGRAPH'98 CDROM Proceedings*. Citeseer. 1998 (cit. on p. 23).

144. H. A. Stone. "Dynamics of Drop Deformation and Breakup in Viscous Fluids". *Annual Review of Fluid Mechanics* 26, 1994, pp. 65–102. DOI: 10.1146/annurev.fl.26.010194.000433 (cit. on p. 2).

145. H. A. Stone and C. Duprat. "CHAPTER 2 Low-Reynolds-Number Flows". In: *Fluid-Structure Interactions in Low-Reynolds-Number Flows*. The Royal Society of Chemistry, 2016, pp. 25–77. ISBN: 978-1-84973-813-2. DOI: 10.1039/9781782628491-00025 (cit. on p. 58).

146. S. H. Strogatz. *Nonlinear Dynamics and Chaos with Student Solutions Manual: With Applications to Physics, Biology, Chemistry, and Engineering*. CRC Press, 2018. DOI: 10.1201/9780429399640 (cit. on p. 85).

147. Y. Sui, Y. T. Chew, P. Roy, Y. P. Cheng, and H. T. Low. "Dynamic motion of red blood cells in simple shear flow". *Physics of Fluids* 20, 2008, p. 112106. DOI: 10.1063/1.3026569 (cit. on p. 14).

148. S. Suresh, J Spatz, J. Mills, A. Micoulet, M Dao, C. Lim, M Beil, and T Seufferlein. "Connections between single-cell biomechanics and human disease states: gastrointestinal cancer and malaria". *Acta biomaterialia* 1, 2005, pp. 15–30. DOI: 10.1016/j.actbio.2004.09.001 (cit. on pp. 123–126).

149. V. P. Torchilin. "Recent advances with liposomes as pharmaceutical carriers". *Nature reviews Drug discovery* 4, 2005, p. 145. DOI: 10.1038/nrd1632 (cit. on p. 57).

150. R. Trozzo, G. Boëdec, M. Leonetti, and M. Jaeger. "Axisymmetric Boundary Element Method for vesicles in a capillary". *Journal of Computational Physics* 289, 2015, pp. 62–82. DOI: 10.1016/j.jcp.2015.02.022 (cit. on pp. 12, 22, 95–97, 119).

151. V. Vitkova, M Mader, and T. Podgorski. "Deformation of vesicles flowing through capillaries". *EPL (Europhysics Letters)* 68, 2004, p. 398. DOI: 10.1209/epl/i2004-10211-9 (cit. on pp. 91, 102, 109).

152. P. M. Vlahovska, D. Barthès-Biesel, and C. Misbah. "Flow dynamics of red blood cells and their biomimetic counterparts". *Comptes Rendus Physique* 14, 2013, pp. 451–458. DOI: 10.1016/j.crhy.2013.05.001 (cit. on p. 117).

153. P. M. Vlahovska, T. Podgorski, and C. Misbah. "Vesicles and red blood cells in flow: From individual dynamics to rheology". *Comptes Rendus Physique* 10, 2009, pp. 775–789. DOI: 10.1016/j.crhy.2009.10.001 (cit. on pp. 3–4, 117).

154. J. Walter. "Couplage intégrales de frontières–éléments finis: application aux capsules sphériques et ellipsoïdales en écoulement." PhD thesis. Université de Technologie de Compiègne, 2009. URL: https://tel.archives-ouvertes.fr/tel-00454538/document (cit. on pp. 11, 29).

155. A. Z. Yazdani and P. Bagchi. "Phase diagram and breathing dynamics of a single red blood cell and a biconcave capsule in dilute shear flow". *Physical Review E* 84, 2011, p. 026314. DOI: 10.1103/PhysRevE.84.026314 (cit. on pp. 13, 121–122, 124).

156. J. Zhang, P. C. Johnson, and A. S. Popel. "Red blood cell aggregation and dissociation in shear flows simulated by lattice Boltzmann method". *Journal of Biomechanics* 41, 2008, pp. 47 –55. DOI: 10.1016/j.jbiomech.2007.07.020 (cit. on p. 14).

157. H. Zhao, A. H. Isfahani, L. N. Olson, and J. B. Freund. "A spectral boundary integral method for flowing blood cells". *Journal of Computational Physics* 229, 2010, pp. 3726–3744. DOI: 10.1016/j.jcp.2010.01.024 (cit. on pp. 22, 30).

158. H. Zhao and E. S. Shaqfeh. "The dynamics of a vesicle in simple shear flow". *Journal of Fluid Mechanics* 674, 2011, pp. 578–604. DOI: 10.1017/S0022112011000115 (cit. on pp. 7, 12, 57).

159. O.-Y. Zhong-Can and W. Helfrich. "Bending energy of vesicle membranes: General expressions for the first, second, and third variation of the shape energy and applications to spheres and cylinders". *Physical Review A* 39, 1989, p. 5280. DOI: 10.1103/PhysRevA.39.5280 (cit. on p. 94).

160. L. Zhu, C. Rorai, D. Mitra, and L. Brandt. "A microfluidic device to sort capsules by deformability: a numerical study". *Soft Matter* 10, 2014, pp. 7705–7711. DOI: 10.1039/C4SM01097C (cit. on p. 12).

Résumé

Une vésicule est un système modèle utilisé pour comprendre le comportement dynamique en écoulement d'une particule molle fermée telle qu'un globule rouge. La membrane bicouche lipidique inextensible d'une vésicule admet une résistance d'élasticité en flexion. Lorsque dégonflée, c'est-à-dire pour un grand rapport surface sur volume, une vésicule présente des changements de formes remarquables. Des progrès significatifs ont été réalisés au cours des dernières décennies dans la compréhension de leur dynamique en milieu infini. Ce manuscrit s'intéresse à la transition de formes et à la migration latérale d'une vésicule dans des écoulements confinés. L'approche est numérique, basée sur une méthode aux éléments finis de frontière (BEM) isogéométrique. Partant d'une version existante pour les écoulements de Stokes non confiné, un code original est développé pour prendre en compte les parois de microcanaux de section transversale arbitraire. L'essentiel des études porte sur la dynamique d'une vésicule transportée par un écoulement de Poiseuille dans une conduite de section circulaire. Tout d'abord, nous examinons les formes typiques des vésicules, les différents modes de migration latérale et la structure de l'écoulement des lipides dans la membrane, en fonction des trois paramètres sans dimension caractéristiques : le volume réduit, le confinement et le nombre capillaire (de flexion). Les transitions de forme et le diagramme de phase de formes stables pour plusieurs volumes réduits sont obtenus dans l'espace (confinement, nombre capillaire). Ils montrent une extension de l'ensemble des morphologies de la vésicule. L'interaction complexe entre la paroi du tube, les contraintes hydrodynamiques et l'élasticité de flexion de la membrane conduit à une dynamique bien plus riche. Nous étudions ensuite, via une version axisymétrique du modèle, le comportement de la vésicule lorsque des conditions de confinement deviennent sévères et imposent des formes de vésicule axisymétriques. Un accent particulier est mis sur la prédiction de la mobilité de la vésicule et de la perte de charge additionnelle induite par la présence de la vésicule. Cette dernière est importante pour comprendre la rhéologie d'une suspension diluée. De plus, sur la base des résultats numériques du comportement proche du confinement maximal, nous établissons plusieurs lois d'échelle portant sur la vitesse de la vésicule et sa longueur, ainsi que sur l'épaisseur du film de lubrification. Enfin, nous présentons un modèle hybride BEM–coarse-graining permettant d'adjoindre un cytosquelette à une vésicule pour étendre nos études au cas des globules rouges. La modélisation coarse-graining du cytosquelette repose sur un réseau de ressorts identifié à l'ensemble des arêtes du maillage d'éléments finis de la membrane de la vésicule. Les résultats numériques montrent que ce modèle à deux composants vésicule–cytosquelette est capable d'extraire les propriétés mécaniques des globules rouges et de prédire sa dynamique dans les écoulements de fluide.

Mots-clés: Interaction fluide-cellule, Vésicules, Globules rouges, Méthode des éléments de frontière, Transition de formes, Théorie de lubrification.